Linking confined electron spins through coherent light-matter interaction.

Candidate Robert H. J. Stockill

Supervisor Prof. Mete Atatüre

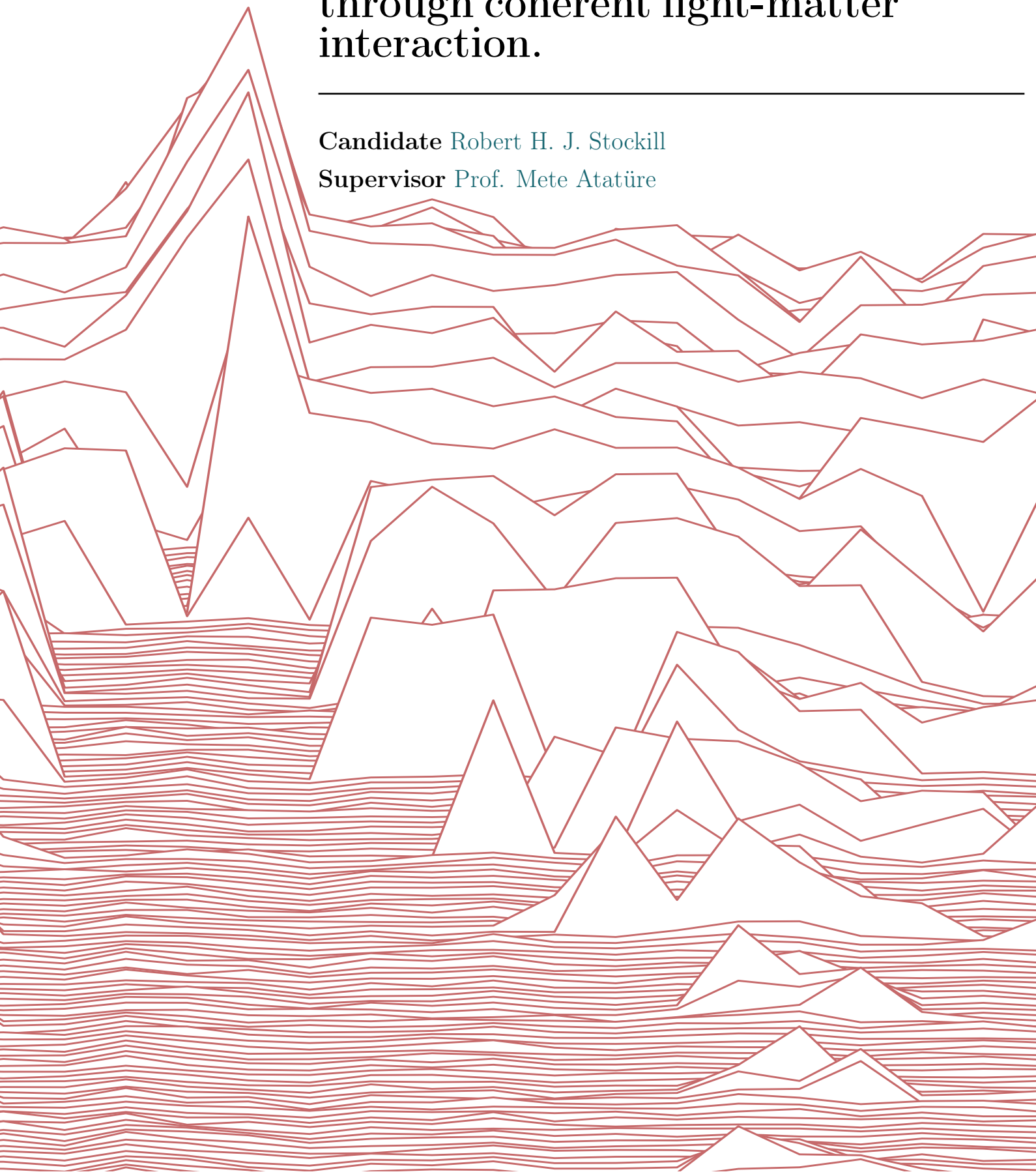

This dissertation is submitted for the degree of *Doctor of Philosophy*

King's College, University of Cambridge

Cover illustration:

transpose of data in figure 2.4.

Linking confined electron spins through coherent light-matter interaction.

Robert H. J. Stockill

Electron spins confined to self-assembled quantum dots are considered as nodes for a coherent optical network capable of supporting distributed quantum states. Through a series of experiments, the work contributing to this dissertation examines some of the key criteria for constructing such a network.

First, the ability to optically extract a coherent spin state from the quantum dot without perturbing the nuclear environment is explored: nuclear feedback is an issue that has frustrated previous studies into electron spin coherence in these systems. With the novel techniques we develop, we identify and characterise the previously undetermined intrinsic mechanisms that govern the coherence of the central spin. We show how the coherence of the electron spin is intimately related to the growth of these strained nanostructures. Second, a model network is constructed in which two spins confined to separate quantum dots are projected into a highly entangled state. This is the first time electron spins in distant quantum dots have been entangled, and in doing so we demonstrate controllable entanglement generation at the highest rates recorded for optically accessible qubit definitions.

We investigate the realisation of a hybrid quantum network by demonstrating the first interconnect between wholly different single quantum systems: a semiconductor quantum dot and a trapped ytterbium ion. In forming an optical link between these two complementary qubit definitions, we show that we can circumvent their intrinsic optical differences through coherent photon generation at the quantum dot. A network built from these diverse constituents could combine the ultrafast operations self-assembled quantum dots enable with the long coherence times states in trapped ions experience. Finally, in a step towards truly scalable entanglement generation between quantum dot spins, we design minimally invasive structures that will funnel large proportions of the optical dipole field from the optically dense

material that surrounds the quantum dot.

The techniques developed in this work and the knowledge gained from their operation should enable the demonstration the creation of high-order nonlocal states between quantum dot spins, single photons and trapped ions, as well as the development of new optically active systems that will benefit from enhanced spin coherence.

DECLARATION

This dissertation is the result of my own work and includes nothing which is the outcome of work done in collaboration except as declared in the Preface and specified in the text.

It is not substantially the same as any that I have submitted, or, is being concurrently submitted for a degree or diploma or other qualification at the University of Cambridge or any other University or similar institution except as declared in the Preface and specified in the text. I further state that no substantial part of my dissertation has already been submitted, or, is being concurrently submitted for any such degree, diploma or other qualification at the University of Cambridge or any other University or similar institution except as declared in the Preface and specified in the text.

It does not exceed the prescribed word limit of 60,000 words, including summary, tables, footnotes and appendices.

Robert H. J. Stockill

March 2017

For Jack Stockill

(Durham Physics 1947-1953)

ACKNOWLEDGEMENTS

This dissertation exists due to the contributions of many people and they have to be held accountable. First I must express my gratitude to Prof. Mete Atatüre for supervising me through this work. He has constructed a fantastic environment to work and research in, and keeps it fueled with ambition and commitment. His unshakable enthusiasm runs through all the work here.

Special mention must go to Clemens Matthiesen and Claire Le Gall for their modelling of the nuclear spectra in chapter 3, as well as Claire's modelling of quantum-dot emission spectra for chapter 5. Aside from this, through our work in the lab together they taught me just about everything I know. Both posses an ideal combination of expertise and patience.

Megan Stanley and Lukas Huthmacher measured the entangled electron spins with me in chapter 4. They each deserve extra individual credit for the interferometer stabilisation (Megan) and the data sorting (Lukas). They were also high quality office-mates in room 967 (coincidence?).

I would like to express particular appreciation to Matthias Steiner, Hendrik Meyer and Professor Michael Köhl for our work together on the quantum dot-ion experiment in chapter 5. It was my first experiment in Cambridge and their last and they taught me a lot.

The success of the experiments presented in this dissertation relied on high-quality quantum dot samples, which were grown by Maxime Hugues and Edmund Clarke in the EPSRC national centre for III-V technologies in Sheffield, and by Arne Ludwig

at the Ruhr-Universität Bochum. The in-house sample processing was performed by Clemens Matthiesen, Carsten Schulte and Lukas Huthmacher.

I must acknowledge Dhiren Kara for teaching me so much about spin coherence through countless snatched conversations. Although we sadly never shared a publication, Jack Hansom and Carsten Schulte were fine companions through the first 3 years, either in the pub or the lab. A special thank-you and the promise of booze is extended to Claire, Lukas, Clemens and Dhiren for their careful reading and invaluable feedback on this dissertation.

Whether they work(ed) on NVs (Helena, Jan, Ben, Lucio, Josh, Yury, David, Lina), SiVs (Ben, Camille, Mustafa, Jeff, Tina, Christian) or 2D-QDs (Carmen, Alejandro, Matteo) the AMOP-MESS group as a whole continue to provide a stimulating group to spend time with and a rare collection of 'local knowledge'. Particular thanks go to those who came to Green Man festival 2014 or 2016 (extra point for both, Megan), to Carmen for navigating the organisation with me in 2016 and to Mete for making sure it happened at all.

I look forward to working with Gabriel and Dorian and am grateful to be able to stay on in the group for a year for a few more explorations with the quantum dots.

Pam Smith is the one who actually made it all work. I also thank Stephen Topliss for his construction of the custom electronics we needed, including the phase-locked loop used for chapter 2 and the pulse counters for chapter 4.

Without the steady support of my family I wouldn't have even started this degree or, quite frankly, the previous one. Nel was always there for me through the degree and is now here as well, which is very nice indeed. I would make a joke about entanglement now but she wouldn't get it.

CONTENTS

1. Introduction - Quantum dots for quantum networks **1**

1.1. InGaAs quantum dots 3

1.2. Confined excitons 5

1.3. Coherent light-matter interaction in the solid state 8

1.3.1. Population transfer 9

1.3.2. Emission properties 10

1.3.3. AC - Stark effect 11

1.4. Quantum dot device 12

1.4.1. Charge control 12

1.4.2. Stark-shift tuning 14

1.4.3. Photon extraction 15

1.5. Resonant confocal microscopy 18

1.6. Quantum dot spectroscopy 20

1.6.1. Absorption scan 22

1.6.2. Course emission properties 22

1.6.3. Time resolved dynamics 23

1.6.4. Spectral coherence 24

1.7. Spin 26

1.7.1. The hyperfine interaction 26

1.7.2. Nuclear dynamics 29

1.8. Optical spin interactions . . . 31
1.8.1. State preparation & readout . . . 32
1.8.2. Optical spin rotations . . . 33
1.8.3. Full control . . . 37
1.8.4. Realistic spin rotations . . . 39
1.9. Conclusion (of the Introduction) . . . 42

2. Nuclear dynamics during coherent electron control 45
2.1. Ramsey interferometry . . . 46
2.1.1. Method . . . 46
2.1.2. Results . . . 47
2.2. Bias modulation . . . 51
2.2.1. Time-resolved dynamics . . . 52
2.2.2. Free induction decay . . . 56
2.3. DNSP suppression . . . 57
2.4. Conclusions & outlook . . . 62

3. Nuclear dynamics-dominated electron spin coherence 65
3.1. Spectrally filtering environment noise . . . 66
3.2. Electron spin Hahn-echo . . . 73
3.3. Hahn-echo visibility . . . 74
3.4. Nuclear-dominated electron spin coherence . . . 76
3.4.1. Nuclear spectra . . . 78
3.4.2. On-axis components: $B_{\mathrm{OH}}^{\parallel}$ . . . 79
3.4.3. Perpendicular components: $\left(B_{\mathrm{OH}}^{\perp}\right)^2/2B_{\mathrm{ext}}$ . . . 82
3.4.4. Total coherence . . . 83
3.5. Dynamical decoupling . . . 85
3.6. Conclusions & outlook . . . 88

4. Entanglement of distant electron spins 91
4.1. Entanglement by single photon measurement . . . 92

4.2. Spin-photon interface . . . 96
4.2.1. Control sequence . . . 97
4.2.2. Single spin recovery. . . . 99
4.3. Forming a network . . . 100
4.3.1. Interferometer delay . . . 102
4.3.2. Raman photon statistics . . . 106
4.4. State reconstruction . . . 110
4.4.1. Joint spin-state population . . . 110
4.4.2. Transverse spin measurements . . . 112
4.5. Controllable entangled state generation . . . 118
4.6. Experimental details . . . 120
4.6.1. Dynamic nuclear spin polarisation . . . 120
4.6.2. Data filtering . . . 121
4.7. Conclusions & outlook . . . 123

5. Direct coupling of a quantum dot to a single ion 127
5.1. A single $^{174}Yb^{+}$ ion . . . 129
5.2. A common resonance . . . 131
5.3. A photonic link . . . 134
5.4. Interaction properties . . . 136
5.5. Electron spin-ion state correlations . . . 139
5.6. Conclusions & outlook . . . 143

6. Collection efficiency strategies 147
6.1. Dipole collection strategies . . . 148
6.2. A dipole in a 1D heterostructure . . . 150
6.2.1. Boundary conditions . . . 152
6.2.2. Far-field approximations . . . 153
6.3. Quantum dot device structure . . . 154
6.3.1. Structure design . . . 155

6.3.2. Device construction 158
6.4. Conclusions & outlook 159

Conclusions & further work **163**

A. Pulse sequence construction **165**
A.1. Version 1 - Basic readout suppression 166
A.2. Version 2 - Modulation > 76 MHz 167
A.3. Version 3 - High suppression 169
A.4. Version 4 - Spin-spin entanglement 171

B. Buried dipole boundary conditions **173**
B.1. Polarisation decoupling 173
B.2. Trial solutions 174
B.3. Matrix methods 175

References **179**

LIST OF FIGURES

1.1. InGaAs quantum dot energy levels 6
1.2. Single quantum dot spectrum 7
1.3. Coherent 2-level system dynamics 9
1.4. Quantum dot device 13
1.5. Photoluminescence spectra 14
1.6. Solid immersion lenses 16
1.7. DBR reflectivity 18
1.8. Confocal microscope 19
1.9. A coherent two-level system 21
1.10. High frequency electron and nuclear processes 29
1.11. Nuclear spin dragging 31
1.12. Electron spin pumping 32
1.13. Growth-axis and field-axis level structure 34
1.14. Coherent spin-state rotation 36
1.15. Spin-Rabi oscillation bias voltage dependence 37
1.16. Control-pulse Michelson interferometer 38
1.17. Full control 39
1.18. Small-delay Ramsey interference power dependence 40
1.19. Rabi and Ramsey amplitudes 41

2.1. Ramsey interference 47

2.2. Ramsey interference transition dependence 48
2.3. Overhauser shift-Ramsey signal relation 49
2.4. Gate modulation Ramsey interference 51
2.5. Nuclear spin recovery in Ramsey interferometry 52
2.6. Time-resolved nuclear polarisation 54
2.7. Ramsey signal decay rates 55
2.8. 2-T free-induction decay measurement 56
2.9. Alternating sequence 58
2.10. Ramsey interference with variable repump 59
2.11. Alternating sequence free-induction decay 60
2.12. Fourier analysis of free-induction decay 61

3.1. Hahn-Echo 67
3.2. Spin Coherence Filter Functions 71
3.3. Hahn-Echo Pulse Sequence and Spin Population 72
3.4. Dynamic Nuclear Polarisation under Hahn-Echo 74
3.5. Hahn-Echo Visibility 75
3.6. Overhauser Field Projections 77
3.7. Overhauser Field Power Spectral Densities 80
3.8. Split Hahn-Echo Response 84
3.9. High-field Hahn-echo 85
3.10. Electron Spin Dynamical Decoupling Oscillations 86
3.11. Dynamical Decoupling Visibilities 87

4.1. Entangling optical Λ-systems 93
4.2. Λ-Scheme with transition resolving etalon 96
4.3. Quantum-dot pulse-sequence fluorescence 98
4.4. Raman-photon spin heralding 99
4.5. Matched quantum dot energetics 101
4.6. Entanglement setup 103

4.7. Interferometer-delay measurement traces . . . 105
4.8. Reconstructed interferometer delay . . . 106
4.9. Raman photon intensity autocorrelation . . . 107
4.10. Hong-Ou-Mandel interference of Raman photons . . . 108
4.11. Entanglement pulse-sequence fluorescence . . . 110
4.12. Joint spin-state population . . . 111
4.13. Single spin heralding in transverse basis . . . 114
4.14. Stabilised Rayleigh photon interference . . . 115
4.15. Transverse spin measurements . . . 116
4.16. Controllable entangled state generation . . . 119
4.17. Detuned-quantum dot interference . . . 122
4.18. Entanglement comparison . . . 123

5.1. Single $^{174}Yb^{+}$ ion in a fibre-based cavity . . . 130
5.2. QD resonance magnetic field dependence . . . 131
5.3. Resonant transitions . . . 132
5.4. Pulse-sequence fluorescence trace . . . 133
5.5. Atomic state transfer by quantum dot photons . . . 135
5.6. Ion state transfer dependence on QD driving intensity . . . 136
5.7. Spectral dependence of the per-photon ion state change probability . 138
5.8. Quantum dot spin in Faraday geometry . . . 140
5.9. Spin pumping in Faraday geometry . . . 141
5.10. Ion state-transfer correlated to quantum dot spin . . . 142
5.11. Hybrid entanglement from a direct interface . . . 144

6.1. Collection efficiency strategies . . . 149
6.2. Dipole in 1-D dielectric stack . . . 151
6.3. Dipole far-field comparison . . . 153
6.4. Sub-quantum dot reflections . . . 155
6.5. Integrated dipole intensities . . . 156

6.6. Free-space collection efficiencies 157
6.7. Partially under-etched sample 158
6.8. Under-etched photoluminescence 159
6.9. SIL mounting-gap collection efficiency 160

A.1. Basic pulse sequence for modulating readout 167
A.2. Delay tuning of the Version 1 pulse sequence 167
A.3. PLL-triggered PPG 168
A.4. PPG pulse sequence and fluorescence 168
A.5. Hahn-echo hardware 169
A.6. Long time readout suppression 170
A.7. Entanglement experiment electrical hardware 172

CHAPTER

ONE

INTRODUCTION - QUANTUM DOTS FOR QUANTUM NETWORKS

Realising useful quantum information requires linking together coherent components (generally two-level qubits) into large-scale entangled states. This entanglement provides the resource to process and communicate information in entirely new ways [1–4] as well as effectively simulate previously inaccessible quantum dynamics [5]. Just as importantly, certain entangled states have emerged as the host for a single distributed qubit that is robust against errors acting on the individual components [6, 7].

Highly entangled states could be formed entirely through nearest-neighbour interactions, as in the chequerboard surface code proposal for quantum computing [8, 9]. A particularly attractive alternative merges the fields of quantum communication and computation in constructing a network of optically linked qubits [10]. Such a network would combine the coherent optical manipulation common to many quantum systems with the ability of single photons to faithfully transmit quantum states.

As well as providing flexible architectures for information processing [11, 12] networks of interlinked qubits can increase the range of an entangled qubit pair through

intermediate quantum repeaters [13]. A coherent network of optically active qubits could also be used to generate entangled optical cluster states as the input for measurement based computing [14, 15].

In finding ingredients for such a network, single atoms held in high vacuum were the first focus owing to their natural isolation from environmental interactions [16]. A branch of study that has received intense experimental and theoretical scrutiny is the role of solid-state defects, where a confined carrier experiences energetic isolation from the surrounding host. Although generally requiring cryogenic temperatures to function, these systems relax the need for ultra-high vacuum and laser cooling techniques. If we control their formation they enable the possibility of chip-production scalability [17]. They also allow provide a natural integration for on-chip routing of optical signals [18–20].

The particular physical system studied here is an electron spin confined to a self-assembled indium-gallium-arsenide (InGaAs) quantum dot. The creation of confined excitons provides an ultrafast interface between a confined spin and a well-defined optical mode [21, 22], and as such these systems are an attractive host for high-frequency entanglement distribution.

We can only begin to access quantum information in the abstract sense with a full understanding the specific physics of the host. For quantum dots this means that any demonstration of a particular protocol is rooted in an understanding of the dynamics of the confined charge we manipulate and the role of the semiconductor lattice. Similarly, efforts towards developing highly entangled networks of spins have enabled new understanding of how these highly unique systems behave. In particular, we can explore subtle features of coherent light-matter interaction previously inaccessible with single atoms, such as the generation of squeezed light in resonance fluorescence [23].

This dissertation contains a selection of experiments which all share the common goal of networking individual spins in quantum dots. First we look in detail at the specific properties of a coherent electron spin confined to a self-assembled InGaAs

quantum dot. We establish the regimes that allow for a protected electron spin state, and how they emerge from dynamics intrinsic to the quantum dot. Building from this work, in combination with studies on the optical-frequency coherence of excitons [22, 24], we then move to demonstrate entanglement between two non-interacting electron spins.

As research concentrates on truly scalable quantum network implementations, there is a growing attention in hybrid architectures [25–27]. By liberating ourselves from a single physical representation of a quantum state, we could combine the diverse advantages different systems provide. This field, very much in its infancy, is a focus of one of the chapters in this dissertation, where we demonstrate an optical link between a quantum dot spin and a single ytterbium ion.

1.1. InGaAs quantum dots

If a wavefunction is confined in three dimensions, its density of states transforms from a continuum to a discrete set of energies. For excitons in III-V semiconductors, the length scale for this effect is set by the Bohr-radius which extends over many lattice sites [28]. In this way, a three-dimensional potential well containing $\sim 10^5$ atoms can provide an atomic-like density of states for confined excitations. What results is a mesoscopic system embedded in the solid state with intrinsic spectral features typically found in atomic energy levels, referred to as a quantum dot (QD).

Quantum dots emerge through modulation of the semiconductor heterostructure on a sufficiently small length scale. This can be achieved multiple ways, for instance by forming nano-scale clusters in solution [29], or by patterning depletion regions in a two-dimensional electron gas [30]. The quantum dots we focus on in this work are formed from the interplay between the band gaps of indium arsenide (InAs) and gallium arsenide (GaAs). The two materials are qualitatively similar direct band-gap semiconductors with zincblende crystal structure [31], however their band gaps differ by 1.07 eV (0.36 eV for InAs and 1.43 eV for GaAs at 300 K) [32]. A small

sample of InAs embedded in GaAs forms three-dimensional potential wells in both the conduction and valence bands, confining both electrons and holes.

The quantum dots form spontaneously by self-assembly during Molecular Beam Epitaxy (MBE), through a process known as Stranski-Krastanov growth [33, 34]. With advances in MBE, we have atom layer-level control over the growth of high-purity InAs and GaAs crystals [35]. When attempting to grow InAs on top of a GaAs substrate the 6% mismatch in the lattice constants of the two (6.06 Å for InAs and 5.65 Å for GaAs) induces strain at the interface. To find the lowest energy arrangement, after ~ 1.6 monolayers of growth further material nucleates into small islands about 20 nm wide and 5 nm tall. After capping the layer with GaAs, we are left with a two-dimensional array of clusters containing $\sim 10^4 - 10^5$ atoms which provide our desired three-dimensional band modulation, sat on a thin wetting layer [36].

Dot nucleation occurs at the transition between two growth regimes, where the InAs either strains to match the GaAs lattice or adapts over multiple layers to its relaxed spacing. The quantum dots that form then feature significant, inhomogeneous strain [37]. For the samples used in this work, confined excitons feature energies around 1.3 eV (950 nm). This value is set by the balance of the electron-hole binding energy, the band gap of the alloyed InGaAs and the confinement energy provided by the QD. The dot size is uniform to $\sim 10\%$ [38], resulting in confined exciton energies typically distributed over a 40 meV range. The central energy can be controlled through the growth parameters or by an additional annealing step [39]. Our samples contain densities on the order of 1 QD per μm^2, which is low enough to preserve the optical quality of the quantum dots, yet high enough to find a dot with desired spectral properties within the sample.

The small QD height strongly confines excitons along the growth direction. The weaker lateral confinement allows for a shell-structure in the exciton wavefunction. Excitons in the higher-order shells quickly decay non-radiatively to the ground state, which then optically recombines in less than an nanosecond. In confining charges

and excitations, the quantum dot provides isolation from external interactions that would decohere their wavefunction. This results in highly coherent optical excitonic transitions capable of interacting with a well-defined optical mode. Similarly, a single charge can be trapped in the dot. The spin of this additional carrier can then be studied as an optically accessible qubit definition.

1.2. Confined excitons

The constituents of an exciton confined to the quantum dot are inherited from the bulk band structure. Lowest energy electrons in the conduction band are s-shell, and holes in the valence band p-shell. Due to spin orbit coupling [32] and the presence of uniaxial strain in the quantum dot, the contributing hole states at lowest energy are heavy holes with $j = 3/2, j_z = \pm 3/2$ (with a slight mixing of the light holes with $j = 3/2, j_z = \pm 1/2$). We can form four possible exciton combinations from the s-shell electrons and the heavy holes, $|\uparrow\Uparrow\rangle, |\downarrow\Downarrow\rangle, |\uparrow\Downarrow\rangle$ & $|\downarrow\Uparrow\rangle$, where $\uparrow, \downarrow$ refers to the spin of the electron, and $\Uparrow, \Downarrow$ the pseudo-spin of the $j_z = \pm 3/2$ hole. The first two combinations have an angular momentum of $\pm\, 2\hbar$, which prevents recombination by a single photon. They are then known as 'dark' excitons and are long lived ($\sim \mu s$ [40]). The latter two with momentum $\pm\, 1\hbar$ can recombine through a single photon and are the 'bright' excitons with a lifetime ~ 0.7 ns. We restrict our studies to the optically-active bright excitons (X^0).

Owing to a lack of in-plane symmetry, the exchange interaction between the electron and the hole mixes the two bright excitons into the linear combinations $\frac{1}{\sqrt{2}}(|\downarrow\Uparrow\rangle \pm |\uparrow\Downarrow\rangle)$, polarised along the major and minor axes of the ellipse [41]. These states are split in energy by the fine structure splitting, Δ_{FS}, which is typically 20-28 μeV in our samples. The bright exciton level structure is displayed in figure 1.1a.

For a quantum dot charged with a single electron, the excited state is no longer the exciton but rather the trion (X^{1-}), which consists of two electrons and a heavy hole. The electrons form an anti-symmetric singlet ($\frac{1}{\sqrt{2}}(|\uparrow\downarrow\rangle - |\downarrow\uparrow\rangle)$), which we will denote

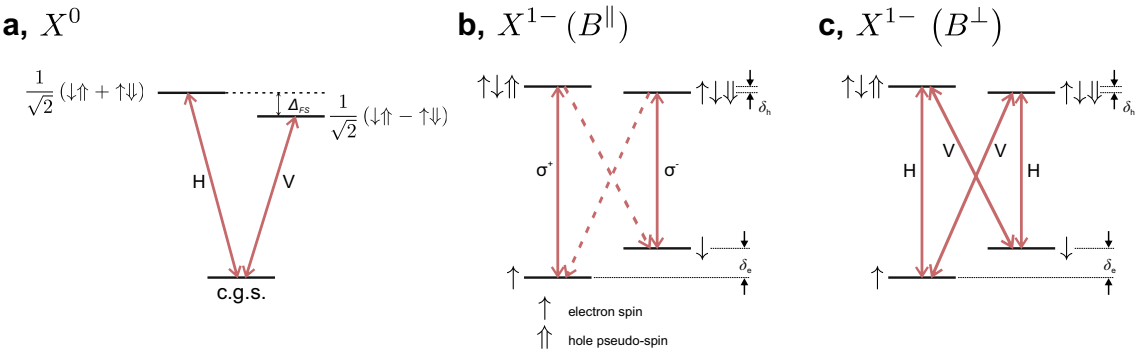

Figure 1.1.: **InGaAs quantum dot energy levels** Figure displays the neutral exciton (X^0), and the charged trion (X^{1-}) for an external magnetic field parallel to the growth axis (Faraday geometry, $B^{\parallel}$) and perpendicular (Voigt geometry, $B^{\perp}$) The dashed lines in Faraday geometry depict the weakly allowed transitions owing to slight light-hole mixing.

as $\uparrow\downarrow$. The angular momentum of the trion is then set by the heavy hole. We will interact with charged quantum dots under an external magnetic field which splits the electron spin states by δ_e, and the hole by δ_h. There are two key geometries for this field: Faraday geometry where the optical axis, growth direction and magnetic field all coincide (figure 1.1b), and Voigt geometry, where the magnetic field is transverse to the other two (1.1c). In Faraday geometry ($B^{\parallel}$), angular momentum permits two spin-conserving transitions: between $|\uparrow\rangle \leftrightarrow |\uparrow\downarrow\Uparrow\rangle$ and $|\downarrow\rangle \leftrightarrow |\uparrow\downarrow\Downarrow\rangle$, with circular polarisation ($\sigma^{+/-}$), as displayed in figure 1.1b. Non-spin conserving transitions are slightly allowed to $\sim 2\%$ due to the mixing of the $j_z = 1/2$ light hole [42] (see chapter 5).

A transverse magnetic field (Voigt geometry) mixes the ground and excited states, which now permits four transitions as sketched in figure 1.1c. This now forms two equal strength Λ-schemes with rectilinear polarisation (H/V) from the sum or difference of the Faraday geometry transitions. This field geometry is employed through a large amount of this dissertation as it now forms a coherent interface between the ground state spin and the optical transitions, enabling coherent optical control of the electron spin [21], and spin-photon entanglement [43–45].

In figure 1.2, we display the photolumiscence spectrum of a single quantum dot at 4.2 K. The photon-generation process is depicted in the figure inset. We excite

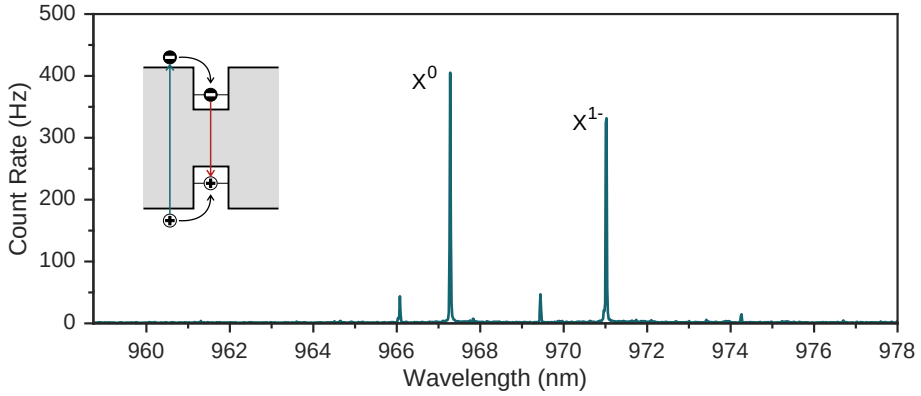

Figure 1.2.: **Single quantum dot spectrum** Recorded with spectrometer during above-band gap excitation. The form of the main peaks are labelled. The inset displays the carrier generation and relaxation process.

the sample at 780 nm, which pumps carriers into the conduction band of the bulk GaAs. The carriers then relax non-radiatively into the quantum dot and recombine through a photon emission. We detect the fluorescence from the dot on a spectrometer. The two bright peaks at 967 nm and 971 nm are the recombination of the neutral exciton (X^0) and charged trion (X^{1-}) within the same quantum dot. We observe them simultaneously due to the optical generation of additional charges in the dot. The trion peak is red-shifted by four nanometres by the balance of additional Coulomb attraction between the hole and the extra electron combined with the confinement energy for the extra charge [46]. The narrow lines are limited by the 10-GHz resolution of the spectrometer, which prevents us from observing the X^0 fine-structure splitting Δ_{FS}.

Photoluminescence spectroscopy allows us to determine the course features of a single quantum dot, and align our microscope optics to maximise the proportion of photons we collect from the exciton recombination. For more in-depth studies and control of exciton and spin dynamics, we interact resonantly with the discrete exciton energies.

1.3. Coherent light-matter interaction in the solid state

At its simplest, the important aspects of our optical interaction with neutral or charged excitons can be understood through a dissipative two level system interacting with a near-resonant classical driving field, provided in our experiments by a coherent laser pulse. In this case the Hamiltonian for the two level system consisting of a ground state ($|1\rangle$) and an excited state ($|2\rangle$) is [47]:

$$\hat{H} = \frac{\hbar}{2}\left(\Omega\,|2\rangle\langle 1| + \Omega^*\,|1\rangle\langle 2| + \Delta\left(|1\rangle\langle 1| - |2\rangle\langle 2|\right)\right). \tag{1.1}$$

The Hamiltonian is expressed in a frame rotating at the laser frequency, detuned from the transition by Δ in the rotating wave approximation. The optical field couples to the two level system with a Rabi frequency $\Omega = \mu_{12}|\mathbf{E}|/\hbar$, where μ_{12} is the transition matrix element linking the ground and excited state and $|\mathbf{E}|$ the size of the driving field. The relevant structure is plotted in figure 1.3a.

For a quantum dot the levels represent either the crystal ground state and a single exciton, or a single electron and a trion in the case of a charged dot. A key parameter in determining the coupling frequency is the dimensionless oscillator strength, which compares the transition dipole moment against a single electron oscillating at the resonance frequency. This value is typically an order of magnitude larger for InGaAs quantum dots than in single atoms [48–50].

The coupling of the exciton to the vacuum modes of the optical field results in spontaneous decay of population in state 2 over a time T_1. The state decoheres in a time T_2, which is given by:

$$\frac{1}{T_2} = \frac{1}{2T_1} + \gamma, \tag{1.2}$$

where we have included additional pure decoherence at a rate γ. In the absence of any pure dephasing, $T_2 = 2T_1$ and the transition is said to be transform limited

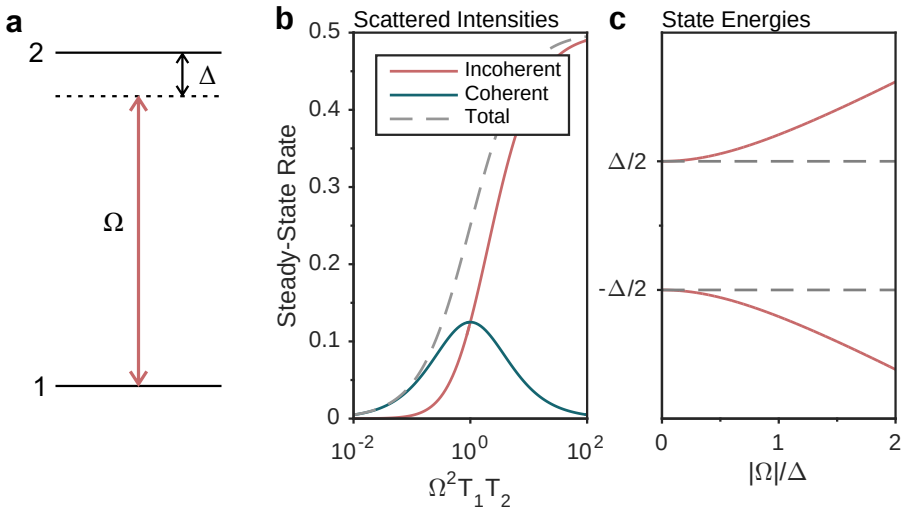

Figure 1.3.: **Coherent 2-level system dynamics a** Two level system driven at Rabi frequency Ω at a detuning Δ. **b** Evolution of incoherent, coherent and total scattering rates as a function of Rabi Frequency. **c** AC-Stark shift of levels under a detuned coherent drive.

[51].

Combining the unitary Hamiltonian in equation 1.1 with the incoherent relaxation, we can find the dynamics of the two-level density matrix in the rotating frame [47]:

$$\dot{\rho}_{22} = -\dot{\rho}_{11} = \frac{i\Omega}{2}\left(\rho_{21} - \rho_{12}\right) - \frac{\rho_{22}}{T_1}, \tag{1.3}$$

$$\dot{\rho}_{12} = \left(\dot{\rho}_{21}\right)^* = -i\Delta\rho_{12} + \frac{i\Omega}{2}\left(\rho_{11} - \rho_{22}\right) - \frac{\rho_{21}}{T_2}. \tag{1.4}$$

These dynamics form the Optical Bloch equations for a three-dimensional vector in the two-state Bloch sphere [52].

1.3.1. Population transfer

The intensity of the light scattered by the transition is proportional to the excited state population, ρ_{22} [53]. The optical drive coherently transfers population between the ground and excited state, which is balanced by the incoherent decay processes. In general we work in the long-time limit where the system has reached a steady

state which we find by setting the time-derivatives in equations 1.3 and 1.4 to 0. In this case the population we create is given by:

$$\rho_{22} = \frac{1}{2}\frac{|\Omega|^2}{\Delta^2\frac{T_2}{T_1} + \frac{1}{T_1T_2} + |\Omega|^2}. \tag{1.5}$$

The excited state follows a Lorentzian with a width $\Delta_{\mathrm{FWHM}} = 2/T_2\sqrt{1 + T_1T_2|\Omega|^2}$. For strong driving ($|\Omega|^2 \gg 1/T_1T_2$ for $\Delta = 0$), the excited population saturates at a value of $1/2$, as stimulated emission and absorption rates dominate over the spontaneous emission. We can normalise the Rabi frequency against the environmental coupling of the transition to gain a dimensionless parameter that characterises the response of the system, $s = T_1T_2|\Omega|^2$. This sets a saturation intensity I_{sat}, where we drive the transition at $s = 1$. On resonance, this corresponds to a steady-state excited state population of $1/4$. For all excitation intensities, the transition can only support one excitation at a time, and the scattered intensity is, naturally, antibunched over the system re-excitation time [54].

1.3.2. Emission properties

We can split the light scattered from the two level system into two main components: the coherent response of the transition dipole to the driving field, and incoherent decay from coupling to the sum of vacuum modes. While the total intensity is given by the excited state population, the fraction of the coherently scattered light is related to the purity of the steady-state density matrix, $F_{\mathrm{coh}} = |\rho_{12}|^2/\rho_{22}$ [55]. For the case of exact resonance ($\Delta = 0$) from equations 1.3 and 1.4 we find the intensity of the coherently scattered light to be:

$$I_{\mathrm{coh}} \propto F_{\mathrm{coh}} \times \rho_{22} = \left(\frac{T_2/2T_1}{1 + |\Omega|^2T_1T_2}\right) \times \frac{1}{2}\left(\frac{|\Omega|^2}{\frac{1}{T_1T_2} + |\Omega|^2}\right) \tag{1.6}$$

This coherently scattered intensity reaches a limit $I_{\mathrm{coh}}^{\mathrm{max}} \propto T_2/8T_1$ for driving at the saturation intensity ($\rho_{22} = 1/4$). This scattering is coherent with the optical drive field [24], and is only observable due to the lack of significant pure decoher-

ence for the confined exciton. For a drive with a sub-linewidth spectral width, the scattered spectrum is similarly narrow [22], and pinned to the laser frequency [56]. At high-powers ($I > I_{\text{sat}}$) incoherent excited state decay with a spectral width set by the dephasing rate of the transition is the dominant emission process, and the coherently scattered intensity reduces to zero ($|\rho_{12}|^2 \to 0$). The proportions of coherent, incoherent and total scattering are plotted against the dimensionless drive in figure 1.3b for the case of $T_2 = 2T_1$.

While this is the classical response of the transition dipole to the driving field, the two level system restricts further excitation, and the intensity of the light field is still anti-bunched [22]. In this low power regime, the full scattering is a squeezed mode, as the limited availability of states restricts the population from following the coherent drive in phase space [23]. This scattering, which is pinned to the laser frequency, offers some protection against small spectral wandering of the exact resonance frequency, although the phase of the scattering is still sensitive to frequency shifts (as we discuss in chapter 4).

1.3.3. AC - Stark effect

Finally, we look at the response of the transition energy to the drive field. Rediagonalising the Hamiltonian in equation 1.1 under the coherent mixing of the states, we find new eigenenergies, $\lambda_{+/-}$ given by:

$$\lambda_{+/-} = \pm\frac{\hbar}{2}\sqrt{|\Omega|^2 + \Delta^2}. \tag{1.7}$$

The eigenenergies in the rotating frame are plotted against the normalised Rabi frequency in figure 1.3c, for a fixed detuning Δ.

On resonance ($\Delta = 0$), this splits the degenerate states by $\pm(\hbar/2)|\Omega|$, as the optical field dresses the system. This splitting is observed as either the Autler-Townes doublet for weak-probe absorption in the presence of a strong drive [57, 58], or in the forming of a Mollow triplet in emission spectra [59–62].

Another important limit is large detuning, where $\Delta \gg \Omega$. In this limit no significant excited state population is created, according to equation 1.5. Nonetheless the transition receives an energy shift of $\approx \hbar|\Omega|^2/2\Delta$. We use the transition-selective phase acquired by this shift to optically rotate the ground state spin projection in a charged quantum dot, as we will discuss in section 1.8.2.

1.4. Quantum dot device

In addition to the GaAs host, our sample comprises a layered stack of MBE-compatible dielectric materials. Figure 1.4a shows the geometry of the different materials that form the device and their core function. The device provides three main functions: control over charge occupation of the quantum dot, DC stark-shift tuning of the exciton/trion resonance and improved photon extraction efficiency.

1.4.1. Charge control

Before growing the quantum dots, we first deposit a 40-nm of heavily n-doped GaAs, with a free-charge density of 2×10^{18} cm^{-3}. The carriers are provided by electron-contributing substitutional silicon introduced in the growth process [63]. This forms a Fermi-reservoir of free electrons, with the energy pinned close to the conduction band. We then grow a 35 nm tunnel barrier of un-doped GaAs, and the quantum dot layer on top of that. 10 nm above the quantum dot layer, we grow 50 nm of $Al_{0.3}Ga_{0.7}As$. This larger band gap material provides a barrier layer that blocks current flow through the device. After a final 100 nm of GaAs, we cap with 6-nm of Titanium. This top metal-semiconductor interface forms a Schottky gate with the semiconductor, bending the conduction and valence bands as shown in figure 1.4b.

The doped layer and the quantum dot are separated by only a short, triangular potential barrier. Applying a field across the device alters the band bending and shifts the relative height of the confined states and the pinned Fermi-level in the doped layer. If the field is high enough to compensate the in-built bias in the device and

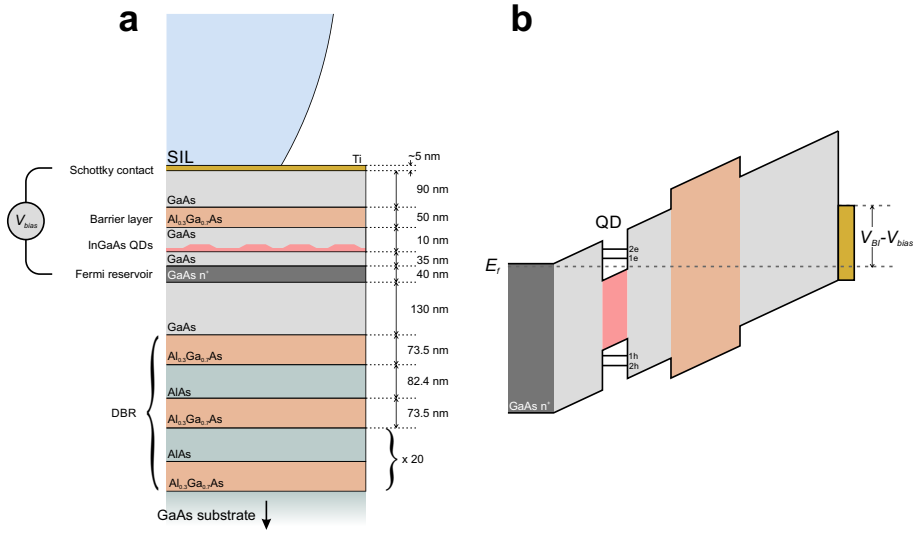

Figure 1.4.: **Quantum dot device a** Sample layer materials, thickness and function. **b** Approximate band energies between the doped layer and the top contact.

pull the bound-electron energy below the pinned Fermi-level one electron will tunnel into the quantum dot. The Coulomb-interaction between two electrons confined to the dot provides an energy cost for an extra charge of 25 meV. If cold enough, this will prevent multiple charge occupation until the interaction is compensated by a larger field, referred to as a Coulomb blockade [64, 65].

At each bias voltage, a certain charge occupation will be the lowest energy state of the combined reservoir-dot system, forming bias voltage-dependent plateaus of long-lived charge occupation (up to $\sim$ ms). At specific gate values different charge occupations become degenerate. At this point fast, second order cotunneling processes across the tunnel barrier occur between the degenerate charge states, which thermalises the spin orientation in single-ns [66, 67]. For most experiments we work far from this region, however this interaction is useful as the controllable spin lifetime gives us a mechanism to thermalise the nuclear bath via electron-spin dependent hyperfine interactions [68], where the broad electron spin energy allows for non-energy conserving nuclear spin flips. This will be examined in greater detail in chapter 2.

Figure 1.5 shows photoluminescence spectra from a quantum dot sample under different applied bias voltages. The marked regions of high intensity correspond to

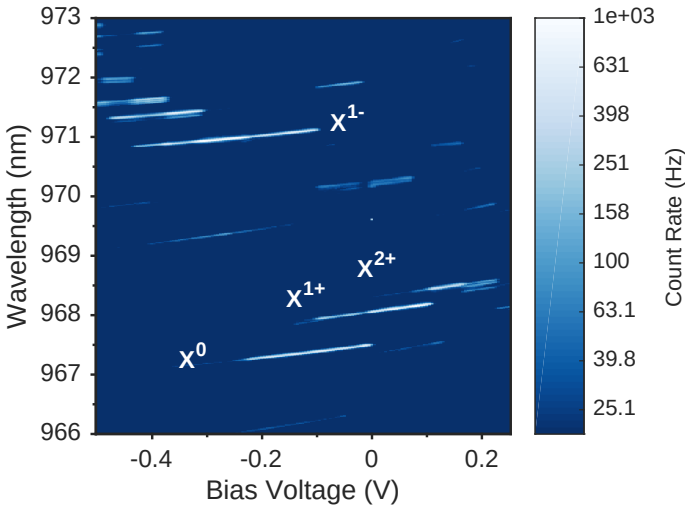

Figure 1.5.: **Photoluminescence spectra** 2D map of photoluminescence as a function of applied bias voltage demonstrating Stark-shift tuning and shifting charge occupation.

different charge occupations of the same QD. The spectral lines overlap at certain gate-bias regions here due to optically created charge states.

1.4.2. Stark-shift tuning

In controlling the charge occupation of our quantum dots, we apply large electric field values across the sample. The exact size of the stability plateau can vary, but typically, for our ∼35 nm tunnel barriers, it corresponds to a range of 5 kV cm^{-1}.

This field, **F**, induces a dipole moment between the electron and the hole, set by the polarisability of the material, β. In addition, a permanent dipole moment, $\mathbf{p}_0$, exists due to the localisation of the hole wavefunction in the indium-rich quantum dot apex [69]. These in turn couple to the electric field to shift the excitonic energy from its zero-field value by ΔE [70]:

$$\Delta E = -\mathbf{p}_0 \cdot \mathbf{F} - \beta F^2. \tag{1.8}$$

The in-built permanent exciton dipole [71], and the plateau widths are such that we measure a linear response to an applied DC bias, corresponding to ∼28 μeV

cm kV^{-1} ($\sim$350 MHz mV^{-1}). This allows us to match the quantum dot optical transition with an atomic transition (chapter 5) or another quantum dot (chapter 4). The Stark shift tuning is visible in the gradients of the spectral lines in the photoluminescence map displayed in figure 1.5.

The bandwidth of any electrical operation on the quantum dot is limited by the RC constant of the device. In our devices we employ a single gate for the whole centimetre-scale sample, which limits our bandwidth to kHz values. As we will discuss in chapter 2, this is still fast enough to resolve dynamics of the quantum dot nuclear spin bath. It is also fast enough to feedback against electrical noise in the surrounding host [72]. That being said, much higher bandwidths approaching the GHz regime have been reported in samples that miniaturise the gate features to limit the capacitance of the device [73].

1.4.3. Photon extraction

The last main function of the device is to extract as much of the dipolar field pattern scattered by the quantum dot transition out of the top of the sample and funnel it into a mode compatible with a single-mode fibre. Efficiently extracting the fluorescence from a two-level system requires conversion of the dipolar emission pattern to a mode that can be focussed into an optical fibre. To compound this, at QD wavelengths gallium-arsenide presents a particularly high refractive index, n = 3.44 [74, 75]. In the absence of any collection strategy, the combination of total internal reflection at the sample surface and the loss of emission into the lower half-space limits the possible collectable emission in free space to 2% with a numerical aperture of unity [76].

A method for countering the large losses due to the refractive index contrast between GaAs and air is to introduce a solid immersion lens (SIL) at the collection interface [77]. If the SIL is in close contact to the surface of the Gallium Arsenide (sub - wavelength) it can reduce losses due to total internal reflection, as well as funnel the light into our collection optics.

a Hemispherical SIL **b** Superhemispherical SIL

Figure 1.6.: **Solid immersion lenses** The path of an incident ray at θ_{sub} is traced through each form of lens, emerging at θ_{out} from vertical.

Solid immersion lenses are used in two main geometries, hemispherical (hSIL) and superhemispherical (SSIL, often referred to as the Weierstrass geometry). These are shown in figure 1.6, with the paths taken for a light beam incident at the centre of the SIL contact at angle θ_{sub}. The refractive indices of the lenses are chosen at a value between that of air and the sample (Cubic Zirconia at n = 2.3 is used in this work), but they are most effective for photon extraction if the indices of the lens and sample match. Solid immersion lenses also play a role in forming a stable focus at the emitter in the substrate, as the magnification they provide reduces the effect of sample motion on the collected intensity [78, 79].

If index-matching ($n_{\text{SIL}} = n_{\text{SUB}}$), the hSIL maps the angles of the emission in the bulk to air ($\theta_{\text{out}} = \theta_{\text{SIL}} = \theta_{\text{sub}}$), as all rays are normal to the curved surface of the lens. Total internal reflection is avoided, yet the emission is still spread over a 2π solid angle. The lack of refraction at the surface of a hSIL forms an image without chromatic aberration. This is of great use for white light microscopy [80], though aberration is not a concern to mono-chromatic photon collection.

The SSIL is similar to the hSIL, however the additional focussing due to the super-hemispherical geometry funnels the available emission into a smaller solid angle, suitable for a more modest collection numerical aperture. The out-coupling angle, θ_{out} is related to the angle in the substrate, θ_{sub} by:

$$\theta_{\text{out}} = \arcsin\left[\frac{n_{\text{sub}}}{n_{\text{SIL}}^2}\sin\theta_{\text{sub}}\right], \tag{1.9}$$

funnelling the light by a factor of $n_{\mathrm{SIL}}^2/n_{\mathrm{sub}}$. Orthogonal emission in the substrate will therefore be refracted to an angle of $\arcsin(n_{\mathrm{sub}}/n_{\mathrm{SIL}}^2)$. For an index matched GaAs SSIL, this corresponds to all the upper half-space emission within an NA of 0.3.

In this work we use super-hemispherical polished Cubic-Zirconia SILs (2-mm diameter), which provide a large active area within which we can find a quantum dot to suit our requirements. The lens is suction-held to the sample by evaporating water from underneath and secured with mounting wax. The bottleneck of this technique is mounting the lens with a sub-wavelength gap to the material beneath, which we require to avoid reflections at the interface for high incidence angles.

A well-contacted SIL can increase the fraction of emitted photons out of the sample by an order of magnitude. At the same time, half of the emission is still below the quantum dot. We introduce a reflective surface to access this portion. This can be constructed from a stack of dielectrics with alternating refractive index (see figure 1.4), which forms a distributed Bragg reflector [81]. If the lengths of the layers are chosen correctly (quarter-wavelength), the Fresnel reflections at each interface constructively interfere to form a stop band. The wavelength dependence of the reflectivity at normal incidence for the DBR used in our samples is shown in figure 1.7, featuring a stop-band from 910 to 1025 nm. This DBR contains 20 repetitions of 73.5 nm of $Al_{0.2}Ga_{0.8}As$ and 82.4 nm of AlAs, which is grown during the epitaxy process before the quantum dot layer. For comparison, the dashed curve in figure 1.7 shows the reflectivity of a 10-repetition stack, featuring a broader, yet less well defined stop band. These curves are calculated from transfer matrices for the interfaces between the dielectric layers, described in Appendix B. Although the DBR is highly reflective for normal incidence rays, the interference condition is lost for larger angles, ($> 20°$), losing signifiant proportions of the emission to the substrate.This loss will be examined in greater detail in chapter 6.

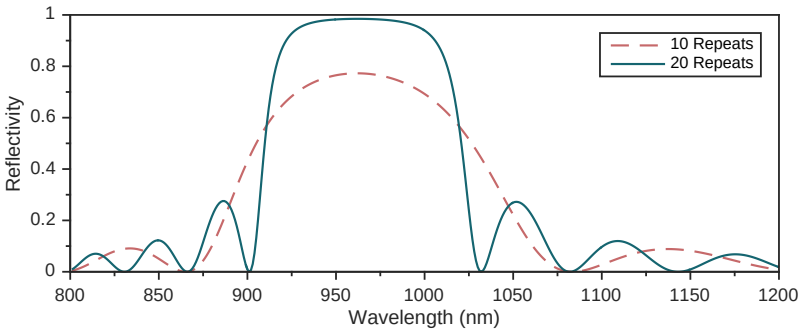

Figure 1.7.: **DBR reflectivity** Normal incidence reflectivity for $Al_{0.2}Ga_{0.8}As$/AlAs DBR used in this work, for both 10 layer repeats (dashed curve) and 20 layer repeats (solid curve). Calculated using transfer matrices described in appendix B.

1.5. Resonant confocal microscopy

Figure 1.8 displays the important elements of the microscopy setup we build to interact with the energy levels of a single quantum dot. The sample is held at 4.2 K in a liquid bath cryostat to prevent thermal occupation of levels ($k_BT = 0.4$ meV at 4.2 K) and provide a controllable QD charge state. The suppression of available phonon modes is necessary for coherent interaction between the exciton and a single optical mode [82].

The cryostat contains a superconducting coil capable of generating magnetic fields up to 9 Tesla parallel to the main optical axis. In figure 1.8, the quantum dot is mounted with the field perpendicular to the growth axis (Voigt geometry). This field defines the quantisation axis for a confined electron spin, and shifts the quantum dot transition energies through the combination of Zeeman splitting and quadratic diamagnetic interaction [83].

The sample is mounted on three independent slip-stick piezo stacks (Attocube) to provide nanometre-resolution position control for aligning on single quantum dots. A 0.5 NA single-piece aspheric lens, sufficient for the super-hemispherical SIL geometry we use, is held a few mm above the SIL surface to focus the collimated excitation and collection paths.

Optical access is provided by a fibre-based confocal microscope resting on top of the cryostat. The microscope has two inputs and one output, sharing an imbalanced

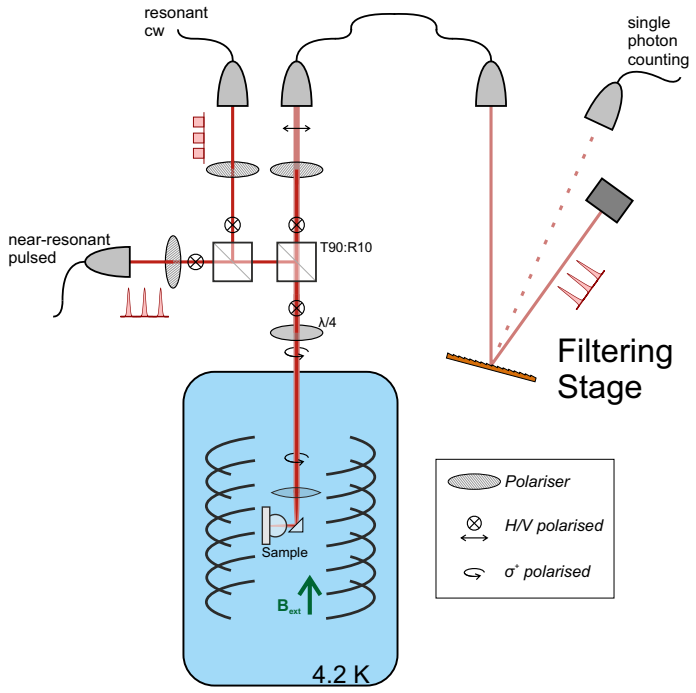

Figure 1.8.: **Confocal microscope** Main components of confocal microscope setup, including polarisation and spectral filtering of scattered laser photons. The symbols mark the polarisation at each point in the microscope. The resonant, photons are filtered out by polarisation and the detuned, pulsed laser is additionally filtered using the single diffraction grating displayed to the right of the figure.

beam-splitter that directs 10% of the excitation down to the quantum dot, and passes 90% of the emission up to the collection fibre. The two inputs are assigned to resonant quasi-continous pulses and the detuned spin control pulses (more details in section 1.8). Splitting the inputs this way allows for independent polarisation and position control between the two.

Resonant interaction with the quantum dot energy levels is the least invasive spectroscopic probe available, and generates single photons with the highest purity. This technique requires that we distinguish the quantum dot photons from the frequency-matching excitation laser scatter, which we achieve through polarisation filtering [84]. Operating successfully requires that the polariser in the collection arm suppresses laser scatter by factor of 10^7 to achieve a signal to background rate of > 100, sufficient for our experiments. Achieving rejection to this level then neces-

sitates careful tracking of birefringence through the cryostat optical elements, as well as any spatial mode distortion. The best combination of polariser positions is empirically found after aligning the quantum dot sample using non-resonant Photoluminescence. The rejection can be frequency dependent to the single GHz level, so generally requires fixed excitation conditions.

Experimental runs require intermittent checks of the background level to identify any drifts in the excitation beam position or polarisation which necessitates a slightly altered combination of polariser positions. A quarter wave plate sits in the optical path, common to both the excitation and detection arms. This element provides the interconversion between linear and circular polarisation which we require to meet the selection rules for our optical spin control (as will be discussed in section 1.8.2). In addition, the wave-plate provides an extra degree of freedom for fine-tuning excitation-laser rejection through the system.

The high-power, detuned control pulses we use to rotate the spin state are poorly suppressed by the polariser pair, due to their spectral separation and broad bandwidth. They are then rejected by a holographic diffraction grating after the microscope (1600 lines per mm) filtering over a 25-GHz bandwidth and featuring a 90% first-order efficiency. The single photon stream from the quantum dot is then counted with either an avalanche-photodiode or a fibre-coupled superconducting nanowire detector.

The whole system is very stable if supplied with enough liquid helium and periodically re-aligned. This allows for the continual study of a single quantum dot for an extended period of time (current PhD record: 474 days).

1.6. Quantum dot spectroscopy

There are a host of techniques to characterise the absorption and emission properties of a resonantly driven quantum dot transition in both the time and frequency domain, some of which are exhibited in figure 1.9 and outlined below. The data

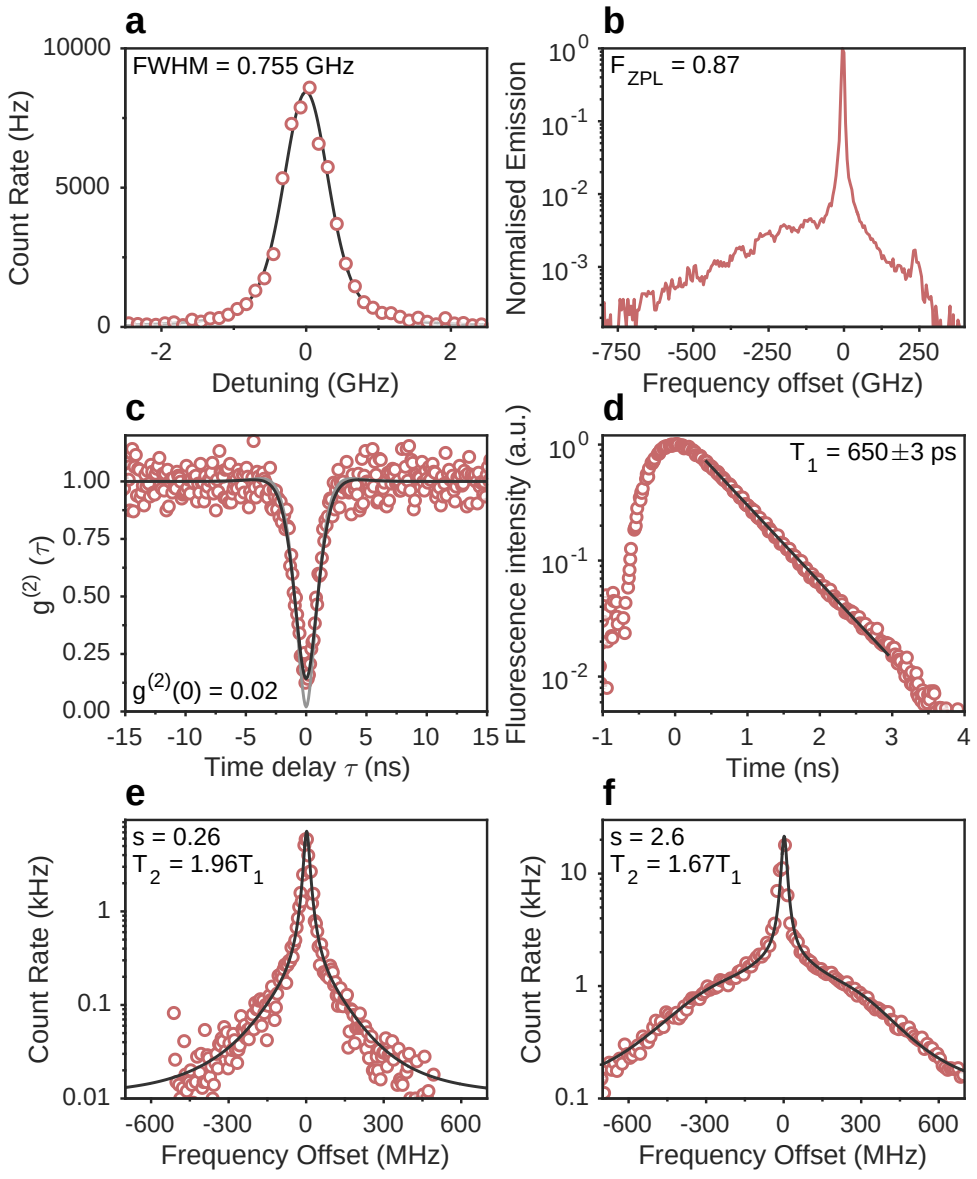

Figure 1.9.: **A coherent two-level system** Characterisation measurements of a quantum dot optical transition including. **a** Resonant absorption scan. **b** Course emission spectrum. **b** Photon autocorrelation. **d** Lifetime measurement. **e** Low power fine emission spectrum. **f** High power fine emission spectrum.

in this section are taken from the quantum dot we couple to an ytterbium ion in chapter 5.

1.6.1. Absorption scan

The response to resonant driving can be observed by monitoring the fluorescence rate from the quantum dot as its transition frequency, ω_{QD} is electrically tuned across a fixed frequency laser at ω_{L}. The recorded count rates against detuning ($\Delta = \omega_{\mathrm{QD}} - \omega_{\mathrm{L}}$) are displayed in figure 1.9a. The fluorescence follows the excited state population ρ_{22}, which, for an ideal two-level system follows a Lorentzian function of detuning, Δ as in equation 1.5.

The resonance frequency of the transition is sensitive to the presence of local charge traps in the surrounding material. The discrete charge occupation of nearby defects introduce a random telegraph signal to the resonance frequency [85–87].

For the data in figure 1.9a, the quantum dot is subject to an external noise source in the lattice featuring fluctuations faster than our scan rate. This is reflected in the emission rate function: a Lorentzian describing the two level system convolved with a Gaussian for the spectral wandering. We extract a total transition width of 755 $\pm$ 15 MHz, containing a Lorentzian width of 345 $\pm$ 35 MHz. We drive the quantum dot at $I = 0.1 I_{\mathrm{sat}}$, which according to equation 1.5 predicts a lifetime-limited width of $1.05/(2\pi T_1) = 260$ MHz. Another broadening effect is the dragging of the resonance condition via the non-collinear hyperfine interaction with the nuclear bath in the quantum dot. This effect will be discussed in more detail in section 1.7.2. We take the scan at a high stepping rate (12.5 MHz ms^{-1}) to limit this effect.

1.6.2. Course emission properties

Rather than simply count the total photon rate, with a spectrometer we can resolve the course features of the quantum dot emission. The spectrum for the resonantly driven quantum dot is displayed in figure 1.9b, offset by the probe frequency.

The spectrum features a sharp peak at the quantum dot resonance, providing 87% of the area, and a broad low background containing the other 13%. The broad background is a result of phonon assisted decay in the quantum dot, sitting predominantly to the red side of the transition. This imbalance is due to the lack of occupied phonon modes at 4.2 K, as the blue sideband requires the absorption of a phonon as part of the decay process [88]. This 13% of emission does not generate a photon within a well-defined mode, and cannot be used for tasks like entanglement distribution and state transfer. On the other hand, if filtered and collected, as in reference [72], the phonon-assisted emission rate provides a reference for the resonance condition. The signal can be used to form a feedback loop to compensate low-frequency environmental noise. It is worth noting the phonon-assisted proportion of emission is significantly smaller than the 97% reported for Nitrogen Vacancy Centres at similar temperatures [89], a key factor contributing to the high-frequency entanglement distribution we report in chapter 4.

1.6.3. Time resolved dynamics

By passing single photon detection events to a time-to-digital converter (quTAU) we generate time stamps with a resolution accurate to the 100 ps level. We can exploit this timing accuracy to observe the dynamics of the quantum dot population as we excite the optical transitions, either through correlations between multiple events or with the clock for a set optical sequence.

Figure 1.9c displays the normalised autocorrelation of scattered photons for a time delay τ, $g^{(2)}(\tau)$ as we continuously drive the quantum dot transition resonantly at low power. We split the fluorescence into two detectors to measure multiple events within the dead-time of each. The pronounced dip in correlation events around $\tau = 0$ is the hallmark of a single photon emitter [90], confirming we are interacting with a single two-level system. The black curve is the two-time correlator of the excited state population, convolved with the detector response, revealing a value of $g^{(2)}(0) = 0.14$, well below the limit of 0.5 required for a single emitter. Deconvolving

from the detector response (grey curve) reveals a zero-time autocorrelation value of $g^{(2)}(0) = 0.02$. We drive the quantum dot at low intensity for this measurement, as a high Rabi frequency will modulate the coincidence rate and obscure the dip at $\tau = 0$ [54].

An alternative time-domain measurement is presented in figure 1.9d. We excite the quantum dot with short (few-nanosecond) optical pulses created with a high-bandwidth electro-optic modulator and correlate the emission events with the short pulses. To correct for the non-square profile of the excitation pulse we then record the same pattern with the quantum dot off-resonance but an equivalent photon detection rate from the excitation laser. Figure 1.9d contains the normalised difference of these two measurements at the end of the excitation pulse. After the excitation pulse any remaining excited state population will relax over the emission lifetime, which we can directly measure. The curve is an exponential fit, revealing an excited state lifetime of $T_1 = 650 \pm 3$ ps.

1.6.4. Spectral coherence

Finally, in figure 1.9e&f we present two fine spectral measurements of the quantum dot emission. In each we drive the quantum dot at a fixed, continuous intensity and record the count rate through a free-space Fabry-Pérot cavity scanned across the resonance frequency. The cavity has a linewidth of 20 MHz and reveals the structure in the response of the quantum dot transition that is unavailable in absorption scans. More details of the technique can be found in reference [91]

For a low driving intensity ($I = 0.26\ I_{\mathrm{sat}}$), the emission is narrow and limited by the width of the cavity transmission. This peak is the coherent response of the transition dipole to the near-monochromatic driving field, as introduced in section 1.3.2 [22]. From the Wiener-Khintchine theorem, we can relate this sharp spectrum to the coherence of the quantum dot dipole in this limit, which exhibits minimal pure decoherence. We can estimate $T_2 = 1.96 T_1$ here. The curve is the theoretically expected emission spectra for the transition driven at resonance, following [22].

In figure 1.9f, we display the emission spectra from driving the quantum dot at $I = 2.6\ I_{\text{sat}}$. This significantly higher intensity generates an average excited state population of 0.36. The broad feature is a consequence of the incoherent decay of this excited state population. The sharp peak is the remaining coherent scattering at this power, contributing 23% of the total photon rate. Supplementing these data with further measurements at higher excitation intensity, we could approximate the pure decoherence rate of the transition, γ, as $\gamma = 2\pi \times (I/I_{\text{sat}}) \times 9.3MHz$, such that $T_2 = 1.67\ T_1$ here. If we drive the quantum dot at higher powers, such that the optical Rabi frequency significantly exceeds the incoherent decay rate we would resolve the Mollow sidebands of the dressed system [84].

With these minimal measurements, we have already determined the key population dynamics for the exciton, and established the coherence of the state, confirming the applicability of the coherent, driven two-level system picture in section 1.3.

1.7. Spin

The exciton decays in ∼700 ps. For a quantum memory, we require long-lived, controllable levels that can encode and store state amplitudes [92]. This is provided by the Zeeman-split spin-1/2 states of a single electron confined to the dot.

A particular focus of this work will be the identification of intrinsic processes that govern the evolution of the spin state. Under a reasonably-large external magnetic field ($B_{\text{ext}} > 100$ mT), and outside a cotunneling bias region, the population of the electron spin is long lived (as discussed in section 1.4.1). For vanishing cotunneling with the Fermi reservoir, the spin lifetime is limited by phonon interactions, which are enabled by the spin-orbit coupling present in crystal structures lacking an inversion symmetry [93, 94]. In the absence of thermally populated phonon states at the Zeeman energy the phonon-assisted spin flip transition rate follows a B_{ext}^5 dependence, due to the product of the available phonon density of states ($\propto B_{\text{ext}}^2$), the squared matrix element for the phonon-induced spin flip ($\propto B_{\text{ext}}^4$), and the electric field strength of the piezoelectric phonon ($\propto B_{\text{ext}}^{-1}$) [95]. The inclusion of thermally populated phonon states modifies the dependence to B_{ext}^4. This behaviour has been confirmed in both self-assembled QDs [96] and larger electrostatically defined dots [97]. For the QDs studied in this work, relaxation times approaching ms have been observed [98]. In the field ranges we use and our particular sample design cotunneling is likely to limit the lifetime first to the few-hundred μs value. Theoretical investigations have shown the phonon interaction to purely induce population relaxation, and have no additional effects on the coherence of the state [99]. These timescales are all long enough that from this point we can neglect the relaxation of the spin, and focus on other mechanisms that disturb its coherence.

1.7.1. The hyperfine interaction

The critical interaction for understanding the storage of a quantum state in the electron spin is the Fermi-contact hyperfine interaction with the host nuclear spins

that form the quantum dot. In addition to its relevance to quantum information storage, the interaction between a single spin and a mesoscopic host, referred to as the central spin problem, is a particularly rich source for emergent dynamics [100] unique to the scale of the quantum dots we examine. Here we present the elements that underpin the processes we observe.

Compared to solid-state qubit representations in silicon or diamond that experience a dipolar interaction due to nearby isotropic impurities [101, 102], self-assembled InGaAs quantum dots are made from purely III-V materials, such that every atomic site contains a nuclear spin. The Fermi-contact hyperfine interaction between an electron and nuclear spin occurs when the electronic orbital has a non-zero wavefunction at the site of the nucleus [103]. This condition is satisfied for every nuclear spin within the wavefunction envelope of the s-shell electron spin we consider. The contact hyperfine interaction between the electron spin $\hat{S}^{\mathrm{e}}$ and the nuclear spins $\hat{I}^i$ can then be expressed as the following:

$$\hat{H}_{\mathrm{fc}} = \frac{\nu_0}{8} \sum_i A_i |\psi(\mathbf{r}_i)|^2 \left(\hat{I}^i_z \hat{S}^{\mathrm{e}}_z + \frac{1}{2} \left[\hat{I}^i_+ \hat{S}^{\mathrm{e}}_- + \hat{I}^i_- \hat{S}^{\mathrm{e}}_+ \right] \right) \tag{1.10}$$

Here, the sum is over every nuclear site, where $|\psi(\mathbf{r}_i)|^2$ is the normalised electron wave function at site i, $A_i \sim 45\mu$eV is the contact hyperfine strength set by the particular isotope and ν_0 is the 8-atom unit cell volume. In equation 1.10, the isotropic interaction has been re-expressed, where $\hat{I}^i_{+/-} = 1/\sqrt{2}\left(\hat{I}^i_x \pm \hat{I}^i_y\right)$ ($\hat{S}^{\mathrm{e}}_{+/-} = 1/\sqrt{2}\left(\hat{S}^{\mathrm{e}}_x \pm \hat{S}^{\mathrm{e}}_y\right)$), where $\hat{I}^i_{+/-}$ ($\hat{S}^{\mathrm{e}}_{+/-}$) are the nuclear spin (electron spin) raising and lowering operators. This divides the interaction into terms that alter the precession frequencies along one axis ($\hat{I}^i_z \hat{S}^{\mathrm{e}}_z$) and terms that enable flip-flop interactions around the other two ($\hat{I}^i_{\pm} \hat{S}^{\mathrm{e}}_{\mp}$). Under an external field along some direction, z, the large mismatch between the electron and nuclear splittings frustrates the latter type of interaction.

It is useful to re-express the interaction semi-classically as an effective field acting upon the electron spin, the Overhauser field $\mathbf{B}_{\mathrm{OH}}$ [104], where we normalise the average hyperfine energy against the electron Zeeman coupling $g_{\mathrm{e}}\mu_{\mathrm{B}}$:

$$\mathbf{B}_{\mathrm{OH}} = \frac{\nu_0}{8 g_{\mathrm{e}} \mu_{\mathrm{B}}} \sum_i A_i |\psi(\mathbf{r}_i)|^2 \left\langle \hat{I}^i \right\rangle \tag{1.11}$$

The variance of the Overhauser field magnitude, σ^2_{OH}, is a direct consequence of the mesoscopic scale of the spin confinement: for a large wavefunction envelope the contribution at each site becomes minimal ($|\psi(\mathbf{r}_i)|^2 \to 0$), and for a wavefunction approaching a single nuclear site the interaction can be expressed as a coherent exchange between the electron and a nuclear spin. Treating the electron wave function as a uniform distribution over N lattice sites, the standard deviation follows a $1/\sqrt{N}$ dependence. For the quantum dots in this work, the relatively small number of nuclear spins (∼30,000) sets this value at $\sigma_{\mathrm{OH}} \sim 30$ mT [105, 106]. In comparison larger, electrostatically defined dots containing 10^6 atoms feature a standard deviation at the single mT level [107]. A symmetric field is experienced by each nuclear spin due to the portion of the electron wave function at that site, referred to as the Knight field.

The first consequence of the large Overhauser field variance is the requirement that the external magnetic field must dominate in order to provide a well-defined basis for the electron spin [108], corresponding to a suppression of the flip-flop terms in equation 1.10. For much larger external fields, the Overhauser field acts as a perturbation to the spin splitting: the predominant source of dephasing between the electron spin states. We depict this process in figure 1.10a, where the spin ($\mathbf{S}^{\mathrm{e}}$) precesses in the vector sum of the external and Overhauser fields. Further details of the way in which different field components couple to the electron precession are provided in chapter 3, where we find that each component plays a unique role in determining the retrieval of central spin coherence.

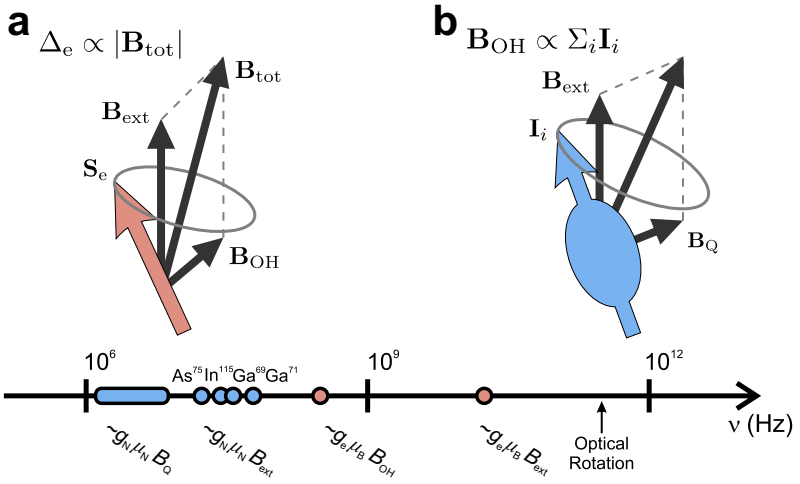

Figure 1.10.: **High Frequency Electron and Nuclear Processes** The arrows display the electron spin ($\mathbf{S}_e$) and nuclear spin ($\mathbf{I}_i$) vectors. The timeline displays the typical values for electon and nuclear processes in a few-Tesla external magnetic field.

1.7.2. Nuclear dynamics

In the same way that accounting for the hyperfine interaction is necessary to understand the electron spin dynamics in the quantum dot, the quadrupolar interaction of the nuclear spins needs to be taken into account to understand the dynamics of the nuclear bath. All the constituent isotopes in the quantum dot (In^{115}, Ga^{69}, Ga^{71} and As^{75}) posses a nuclear spin greater than 1/2 (9/2 for indium, 3/2 for the rest). The higher order components of these spins correspond to non-spherical nuclear charge distributions which can couple to electric field gradients [104]. This coupling is particularly important for InGaAs quantum dots because the strain-driven self-assembly process leads to signifiant, inhomogeneous local field gradients throughout the QD [37]. The random alloying of indium and gallium throughout is another key source for these gradients. The quadrupolar interaction has a strength of $\sim$ 1-5 MHz, comparable to the four nuclear Zeeman splittings: $g_N \mu_N$ = 9.33, 10.22, 12,98 and 7.22 MHz T^{-1} for In^{115}, Ga^{69}, Ga^{71} and As^{75}.

For magnetic fields in the few Tesla range, the quadrupolar coupling tips the nuclear quantisation axis away from the external field direction [109]. This is depicted in figure 1.10b where the quadrupolar interaction is represented as an effective

magnetic field $\mathbf{B}_{\mathrm{Q}}$. As we will discuss in chapter 3, this tilted quantisation axis generates large, high frequency terms along the external field direction, which dominate electron spin dynamics for fields up to $\sim$4 T.

Another consequence of this tilting is the ability to induce a nuclear spin flip without flipping an electron spin, which emerges from a basis change in the hyperfine interaction described in equation 1.10 owing to the fact that $\hat{I}_z^i$ is no longer a good quantum number [109].

Perhaps the most striking result of this interaction is the dragging (pushing) of optical resonances with a detuned probe when driving the high (low) frequency Zeeman transition under magnetic field [110]. Depending on the detuning of the probe optical excitation enables nuclear spin flips to higher or lower energy, inducing a non-zero mean Overhauser field value that either brings the transition to resonance for the high frequency Zeeman branch, or increases the detuning for the low frequency transition. This interaction, while slow [110], is ever-present for experiments with InGaAs quantum dots under magnetic field, and must be taken into account when we design control sequences. For the high frequency transition, the effect can feedback to reduce electrical noise down to the sub-ms level (at the cost of an altered electron splitting). For the low frequency transition, the exact resonance is an unstable condition, and small detunings will cause a run-off of the frequency (referred to as anti-dragging).

Two resonance scans of the high-frequency neutral exciton (blue Zeeman branch) under an external 4-T field are displayed in figure 1.11. In the top scan, the transition is swept quickly (12.5 MHz ms^{-1}) across a low power ($I = 0.1I_{\mathrm{sat}}$) probe. In the bottom scan, the same transition is probed at higher power ($I = I_{\mathrm{sat}}$) at a lower rate (0.125 MHz ms^{-1}). In the fast scan we recover a broadened Lorentzian (as discussed in section 1.6.1), while in the slow scan we find a flat top extending for 10 GHz around the central transition frequency, as the nuclear bath compensates for the detuned probe. The Lorentzian curves depict the underlying scanning transition centre.

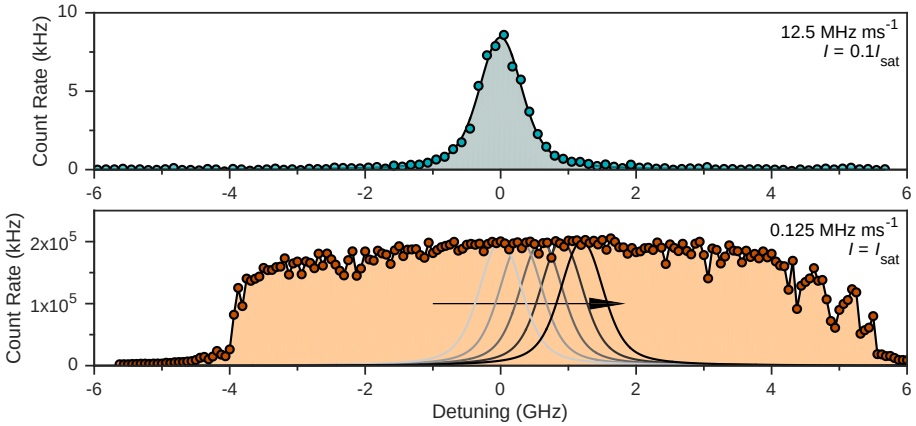

Figure 1.11.: **Nuclear spin dragging** Fast (top) and slow (bottom) resonant scans of the high-frequency neutral exciton under a 4-T external magnetic field. For the slow scan nuclear spin-flips compensate for the detuned resonant probe, generating a top-hat response.

Through the quadrupolar interaction, the strain fields in the quantum dot produce local shifts in the transition energies of the nuclei. This suppresses resonant spin-spin interactions, such that the bath remains coherent for longer than unstrained systems [111–113], and can retain a polarisation for many hours in the absence of an electron [68].

Bringing these high-frequency electronic and nuclear processes together, the logarithmic frequency axis at the base of figure 1.10 contains the rates of the different processes for a few-Tesla magnetic field. Included is the frequency of our coherent electron control, which exceeds every other process by at least an order of magnitude.

1.8. Optical spin interactions

Optical interaction with the ground-state spin can be grouped into two main techniques: quasi-continuous excitation for spin initialisation and readout and detuned, pulsed interaction for coherent spin control. In the first case we create excitonic population to link the ground state spin to the optical reservoir, pumping the spin and simultaneously providing optical readout. For most of our experiments we consider this interaction to be incoherent, however in chapter 4 we will discuss how it can be

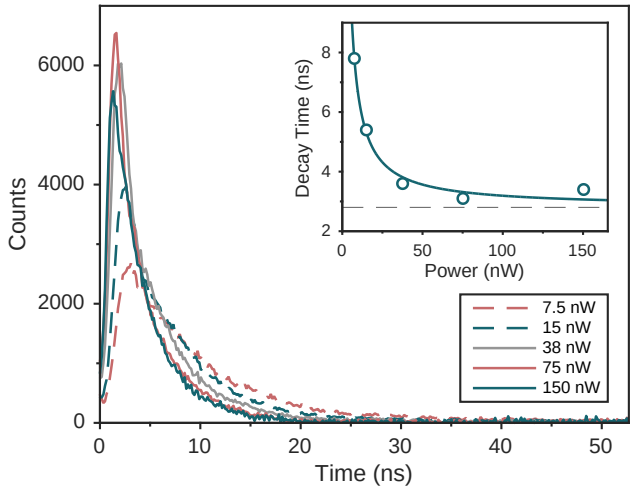

Figure 1.12.: **Electron spin pumping** Correlated counts from optical pumping for a range of resonant powers. The inset displays the exponential decay time for each power.

used to generate an entangled spin state. In the second case we pulse the transition far red detuned from the resonance. This detuning ensures that we prevent the build up of excited state population, so that ideally we preserve the coherence of the ground state and rotate the orientation of the spin via the AC-Stark shift.

1.8.1. State preparation & readout

At 4.2 Kelvin, for all reasonable magnetic fields, the electron spin is sat in a thermal mixture [114], and the first task of any of any experiment involving coherent spin-state manipulation is to prepare a well-defined ground state population. If we drive a single transition, say from the spin up ground state, the electron is exponentially shelved into the spin down state. The time required is set by the excited state population (ρ_{ee}) and the branching ratio. In chapter 5 we will discuss spin preparation in Faraday geometry [42]. In Voigt geometry, the equal-weighted lambda system permits spin preparation in a few excited state lifetimes [115].

Figure 1.12 contains time-correlated emission events for spin pumping in Voigt geometry for different laser powers (7-150 nW), resonant with the highest-frequency

Zeeman-split transition. At zero time, we start with a spin-up state. The exponential decay of the fluorescence follows the emptying spin-up population. The inset of the figure 1.12 displays the fitted exponential decay times for the different power drives. The solid curve is a fit to the decay time calculated from the excited state population for zero detuning in equation 1.5, neglecting the modulated population of the excited state [116]. The dashed horizontal line at 2.8 ns marks the limit of above-saturation pumping, at four times the lifetime ($\rho_{ee} = 1/2$).

The high preparation rate means we can prepare the spin to a reasonable fidelity within the 13-ns repetition time of our pulsed rotation laser. In general, we find a preparation fidelity of $\geq 95\%$ is achievable.

The photon generation during spin preparation forms a natural optical readout of the spin population, although this is limited to an average of two photons for a bright spin in the Voigt geometry, which then prohibits single shot readout for any realistic collection efficiency [117]. There are proposed schemes to optically switch the basis, through the AC-Stark shift [118], or alternatively, readout through electrically induced spin-to-charge conversion is possible in diode structures [119].

1.8.2. Optical spin rotations

After state preparation and readout, we now discuss how we can control the ground-state spin orientation. In the majority of solid-state qubit definitions, spin states are manipulated by electron-spin-resonance (ESR) with a driving microwave pulse that extends far beyond the precession time of the spin [120, 121]. We work in the opposite limit, where we use the strong coupling of the optical transitions to a coherent optical pulse to reorient the spin in a fraction of its Larmor period [21].

We can coherently rotate the spin projection with a single, circularly polarised pulse, detuned from the optical resonance. To understand the operating principle, we consider the relationship between the spin states and the optical selection rules in both the direction of the applied field and the optical axis. The left of figure 1.13 shows the level structure of the charged quantum dot in a transverse field. The

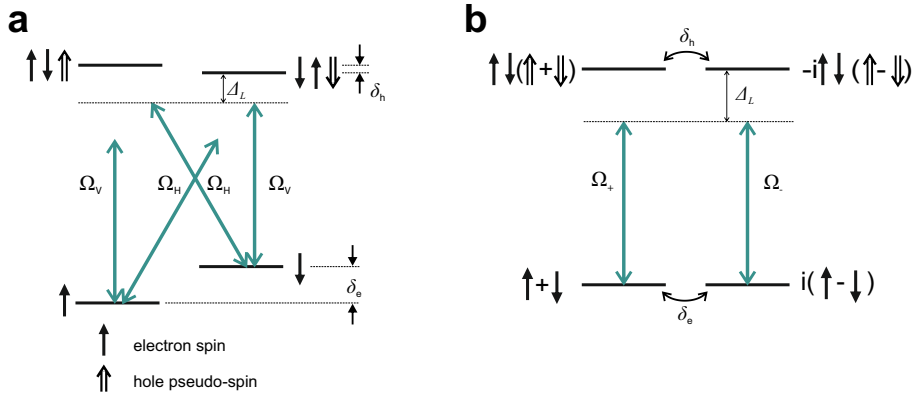

Figure 1.13.: **Growth-axis and field-axis level structure a** Spin states and allowed transitions in Voigt geometry. **b** Spin projections along optical axis.

ground and excited states are split by δ_e and δ_h respectively. A laser, detuned from the excited state by Δ_L couples to the four transitions by its linear polarisation components, Ω_H and Ω_V.

The right of figure 1.13 shows the same level structure but along the optical axis. The degenerate ground and excited states are coherent superpositions of the Zeeman eigenstates, and are mixed at the splitting frequency. In this geometry the pulse only couples to the two circularly polarised allowed transitions by the projections, Ω_+ & Ω_-. In the limit $\Delta_L \gg \Omega$ the pulse does not produce excited state population, but alters the transition frequency through the AC Stark shift, as described in section 1.3.3. The pulse then splits the degenerate ground states by $\hbar(\Omega_-^2 - \Omega_+^2)/2\Delta_L$ [47]. Afterwards an integrated phase θ will have been accumulated between the states, which maps into a population rotation in the basis of the external field:

$$|\downarrow\rangle = \frac{1}{2}(|\uparrow\rangle + |\downarrow\rangle) - \frac{1}{2}(|\uparrow\rangle - |\downarrow\rangle) \xrightarrow[shift]{Stark} \frac{1}{2}e^{i\theta}(|\uparrow\rangle + |\downarrow\rangle) - \frac{1}{2}(|\uparrow\rangle - |\downarrow\rangle) \tag{1.12}$$

$$= \frac{1}{2}|\uparrow\rangle\left(e^{i\theta} - 1\right) + \frac{1}{2}|\downarrow\rangle\left(e^{i\theta} + 1\right) \tag{1.13}$$

In this way our spin rotations emerge from the AC Stark shift, requiring a circularly polarised pulse to induce a significant phase difference. The full Hamiltonian can be treated analytically, by adiabatically eliminating the excited state population

[122] to recover the effective two-dimensional Hamiltonian:

$$\hat{H}_{2D} = \frac{\hbar}{2}\left(\Omega_{\text{eff}}\left|\uparrow\right\rangle\left\langle\downarrow\right| + \Omega_{\text{eff}}\left|\downarrow\right\rangle\left\langle\uparrow\right| + \delta_{\text{e}}\left(\left|\uparrow\right\rangle\left\langle\uparrow\right| - \left|\downarrow\right\rangle\left\langle\downarrow\right|\right)\right) \tag{1.14}$$

where Ω_{eff} is given by:

$$\Omega_{\text{eff}} = \frac{\Omega_{-}^{2} - \Omega_{+}^{2}}{2}\left(\frac{1}{2\Delta_{\text{L}}} + \frac{1}{2\left(\Delta_{\text{L}} - \delta_{\text{h}}\right)}\right) \approx \frac{\Omega_{-}^{2} - \Omega_{+}^{2}}{2\Delta_{\text{L}}} \tag{1.15}$$

In addition a small phase-shift is induced between the spin states due to the non-zero excited state splitting which accumulates at a negligible rate $\sim \Omega_{+}\Omega_{-}\delta_{\text{h}}/\Delta_{\text{L}}^{2}$ [21]. The Hamiltonian of equation 1.14 is for a two-level system subject to a DC transverse field. Rather than working in a frame that rotates at a frequency close to the spin splitting, we work directly in the laboratory frame. Inverting the electron spin this way then requires that our rotation pulses are much shorter than the spin precession time. The optical rotation pulses we use in this work are provided by a modelocked laser (Coherent MIRA 900), which results in very large instantaneous optical Rabi frequencies in few-picosecond bursts. The effect of the non-zero spin precession during our rotation pulses will be assessed in section 1.8.4.

To measure the effect of our optical spin rotations we combine continuous, resonant spin readout and preparation with the ps-long rotation pulses. The pulse scheme, which repeats at 76 MHz, is shown in the left of figure 1.14. The control pulses are red-detuned by ~ 1 THz from the excitonic resonance. In principle, the scheme would work equally well for a blue-detuned pulse, however phonon assisted processes would populate the excited state [123].

The right of the figure shows the recorded count rate when we vary the power of the rotation pulses. The time-averaged power at the cryostat forms the horizontal axis of the figure. The readout pulse, resonant with the $\left|\uparrow\right\rangle \leftrightarrow \left|\uparrow\downarrow\Uparrow\right\rangle$ transition prepares the spin in $\left|\downarrow\right\rangle$. Every 13.1 nanoseconds the rotation pulse reorientates the spin vector. We then recover high-visibility effective spin-Rabi oscillations as a function of the average rotation power. The Bloch sphere on the left displays an

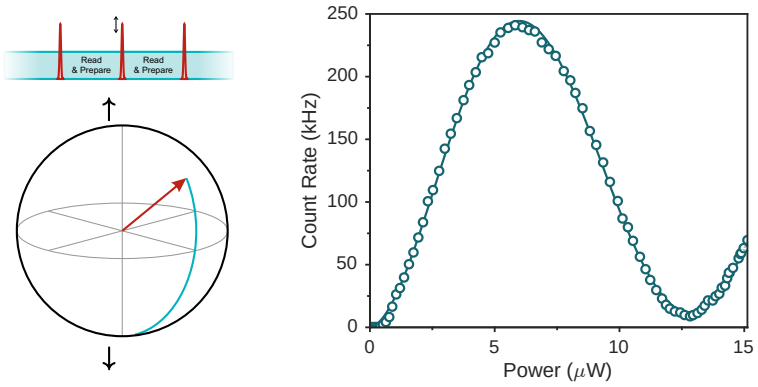

Figure 1.14.: **Coherent spin-state rotation** Pulse sequence, approximate Bloch sphere trajectory and average readout count-rate for single-pulse spin control.

approximation of the trajectory the spin takes, where the resonant readout produces an amount of fluorescence proportional to the height of the state vector in the sphere after rotation.

The return to a minimal count rate is evidence of the coherence of our spin rotations. Decoherence between the spin states leads to shrinking of the state vector away from the Bloch sphere preventing the count rate from returning to zero [21]. The lead source of decoherence for this process is excitonic dephasing due to coupling to acoustic phonons [124, 125], which contributes to $< 5\%$ decay for a 2π-rotation here. For a full calibration of errors, we would need to perform benchmarking over the Bloch sphere [126, 127]. At the same time, the return to a minimal count rate, and the limited number of pulses we require is such that for the rest of the work we will consider these rotations effectively coherent, and focus on the geometry of the state trajectory on the surface of the Bloch sphere.

In figure 1.14, we only show one full oscillation of the spin state. Our ability to probe the spin for rotation angles far beyond 2π is limited by a large shift of the resonance condition in the sample owing to local charge build-up induced by the high-power optical rotation pulses. This 'heating' of the sample shifts the resonant bias voltage in the quantum dot by $\sim$4 mV for a π rotation, and decays on a 10 millisecond timescale [91]. Accordingly, for the experiments in this work, the required bias voltage is found for the particular set of rotation pulses used. Figure

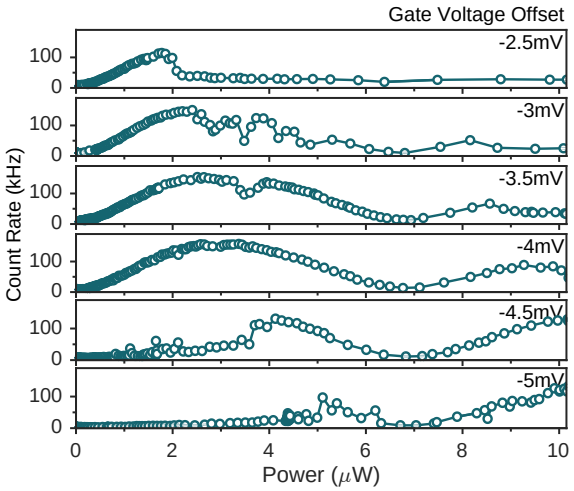

Figure 1.15.: **Spin-Rabi oscillation bias voltage dependence** Gate voltage offset relative to resonant value without the rotation laser.

1.15 demonstrates this sample heating effect: each panel is a spin-Rabi oscillation recorded at a different bias. For small offsets from the unperturbed bias (-2 to -3 mV) we only see the small angle rotations before the optically-induced shift prevents state readout and preparation. Alternatively for large offsets (-4 to -5 mV) we only observe the oscillations at $> \pi$ rotation. It is worth noting here that by using the high frequency transition in the quantum dot, DNSP works to counteract this power-dependent shift and provide a stable resonance over a wider range of rotation powers.

1.8.3. Full control

To move beyond the single-axis control presented in figure 1.14, we need to introduce another rotation axis. This is provided by the coupling to the external magnetic field. By chaining together control pulses with wait periods, we can achieve arbitrary rotations around the Bloch sphere [128].

We then require multiple optical rotations with a well-defined delay. We realise this by passing the pulsed control laser through an unstabilised Michelson interferometer, which is sketched in two forms in figure 1.16. At the output of the laser we split the pulse train into two with a 50:50 beam splitter, transmitting through

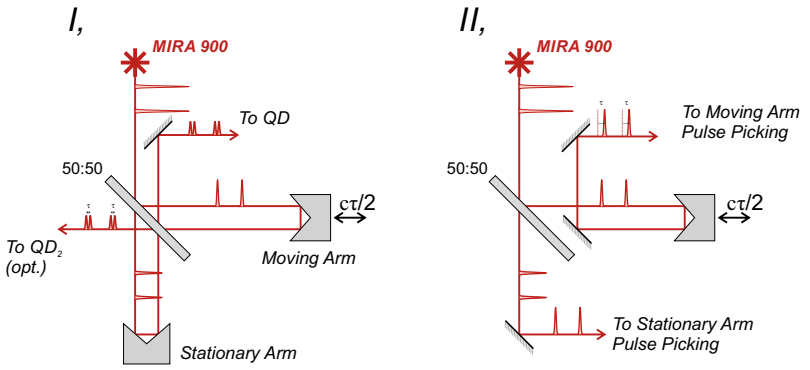

Figure 1.16.: **Control-pulse Michelson interferometer** Two forms are shown, either for producing pairs of pulses with a controlled delay (**I**) or pulse-picking each arm individually (**II**).

to the 'stationary arm' and reflecting to the 'moving arm'. In the most basic form (figure 1.16I), we recombine these arms on the same beam-splitter with two retroreflectors. The reflector in the moving arm is mounted on a piezo-controlled delay stage (Nanomotion FB150), which provides a controllable delay, τ, to an accuracy $\ll$ ps. The two outputs, at a quarter of the initial power, contain pairs of rotations with a delay up to 1.2 ns. We send one to the quantum dot we control, with the second available for a second quantum dot (as in chapter 4). In the second form, (figure 1.16II) we pick off the reflected beams to recombine at a point later in the setup. This way we can pulse pick each arm independently, required for operating the more complex control sequences in chapter 3. For both forms of the setup, we characterise the delay between the arms by scanning the delay stage and observing the unstabilised interference between the pulses when τ is smaller than the ps-pulse duration.

By applying two $\pi/2$ rotations to the QD, we form a Ramsey interference sequence and can observe the spin precession in the external magnetic field. The final spin population depends on the angle the spin state forms with the rotation axis as it precesses in the equator. To demonstrate this we sweep the delay between the two constant-power pulses. Figure 1.17 contains a sketch of the pulse sequence, an illustration of the three-part trajectory around the Bloch sphere and the recorded count rate. The count rate oscillates sinusoidally with high visibility (97$\pm$1%) at the

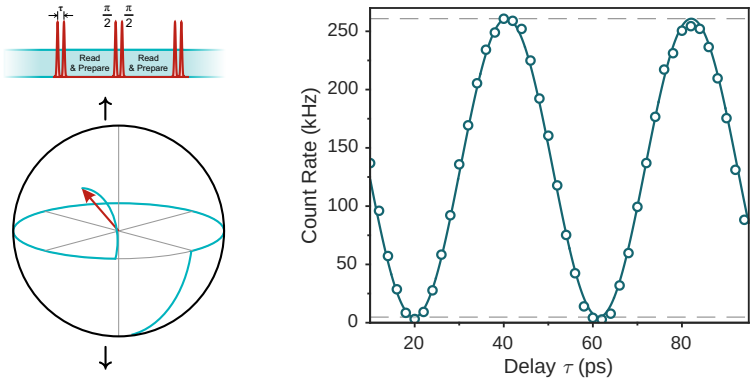

Figure 1.17.: **Full control** Pulse sequence, approximate Bloch-sphere trajectory and recorded count rates as a function of delay, τ. The curve is a sinusoidal fit, revealing a visibility of 97±1%.

25.1 GHz spin precession frequency in the 4-T external field. The fidelity of these rotations is limited by the dephasing of the electron. Our measurements presented in chapter 2 show that for one spin precession this value is given by $e^{-(0.04/1.93)^2} = 0.9996$. As we increase the delay between the rotations beyond a single precession, the function of the double-rotation sequence moves from controlling the spin to measuring the uncertainty in its splitting in the time-averaged visibility.

1.8.4. Realistic spin rotations

During the control pulse the spin is oscillating in both the effective field generated by the AC Stark shift and the orthogonal external field, B_{ext}. Ideal rotations perpendicular to the quantisation axis are then only available for vanishingly short pulses, requiring very high pulse energies to effect a spin rotation. For this work, the few-picosecond pulses we use to rotate the spin take up a non-negligible fraction of the spin precession time (40 ps for a $B_{\text{ext}} = 4$ T field). In this section, we characterise the effect of the finite duration optical pulses and track the geometry of our rotations on the Bloch sphere.

We determine the direction of our rotation axis by referencing it against the electron spin quantisation axis. We do this by performing a variant on the Ramsey interference sequence, where we sweep the height of the two rotations together as

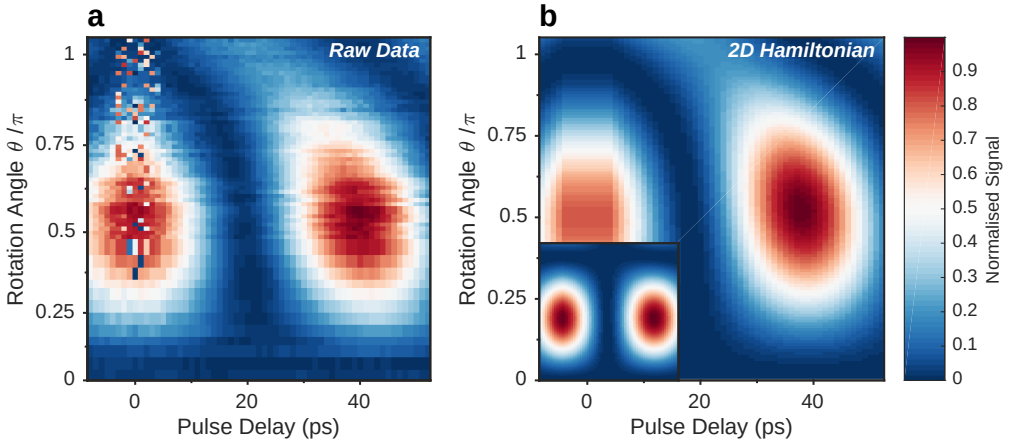

Figure 1.18.: **Small-delay Ramsey interference power dependence a** Recorded count rates for varying delay and rotation angle for two-pulse sequence. **b** Modelled signal from the Hamiltonian in equation 1.14 with a square, 4.5-ps rotation pulse. Inset shows the same modelling for a 0.5-ps pulse.

well as their delay. The count rates we record are displayed in the intensity plot in figure 1.18a. We recover large contrast oscillations for a pair of $\pi/2$ rotations and a reduced, but non-zero amplitude oscillation for two π rotations. The noise around 0-ps delay is a consequence of the unstabilised interference between the overlapping rotations.

Figure 1.18b contains the calculated signal for the same pulse sequence developed from the Hamiltonian in equation 1.14. We evolve the spin with a square 4.5-ps long rotation pulse, approximating a 4-ps wide sech^2 intensity profile. The Hamiltonian reproduces the features of we observe, including the non-zero amplitude oscillations for a pair of π pulses and the phase-shift of the oscillation fringes for rotations $> \pi/2$. The pulse length used in this model is longer than the 2-ps envelope we record in field autocorrelation measurements, most likely due to dispersion between the spectral components of the pulse. For comparison, the sub-panel in figure 1.18b contains the same calculation but for 0.5-ps pulse lengths, showing no phase shift, and a complete suppression of the count-rate for π rotations.

For a more quantitative comparison, figure 1.19 contains the oscillation amplitudes due to the variable power Ramsey sequence (red points), and the results from the

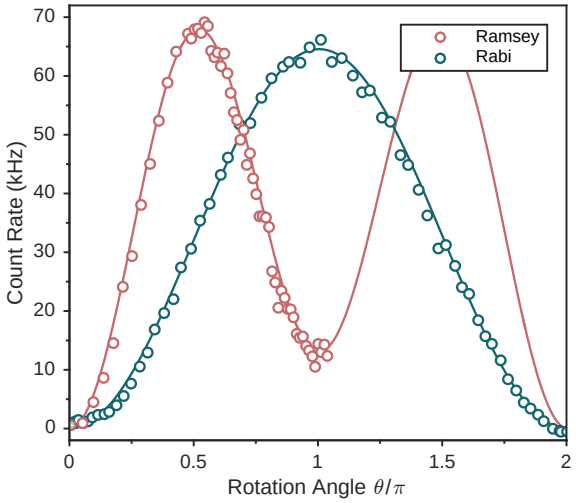

Figure 1.19.: **Rabi and Ramsey amplitudes** Ramsey interference amplitudes fitted from figure 1.18, with Rabi oscillation count rates for comparison. The curves are modelled for the two sequences assuming for a 4-ps sech^2 pulse with an electron precession frequency of 25 GHz

model Hamiltonian (red curve). In addition, the figure contains the recorded and calculated count rates for a single-pulse Rabi sequence (corrected for the few-percent decoherence at $\theta = 2\pi$). These results are consistent with a constant deviation in the rotation axis of 12.5° away from the equator. The oscillation amplitude for a pair of π rotations is a particularly sensitive measurement of this angle, as the normalised height corresponds to $1/2\,(1 - \cos 4\alpha)$, where α is the rotation axis deviation from the equator.

An interesting feature of the data in figure 1.19 is the difference in the maximum heights of the double and single-pulse measurements. We can gain a more full inversion through using a composite pair of $\pi/2$ rotations rather than a single pulse [129]. The extreme example of this would be if the rotation axis were deviated by 45°, and an inversion would require a pair of Hadamard gates (π rotations) spaced by half a precession. The use of composite pairs to correct for imperfect rotation angles will be revisited in chapter 4 to perform tomography on the electron spin. In particular, long rotation pulses are advantageous, as the smaller splitting limits the phonon-induced excitonic dephasing rate.

1.9. Conclusion (of the Introduction)

This introductory chapter has presented a high speed tour through the methods by which we access the spin of a self-assembled quantum dot through its coherent optical transitions, and some key electronic and nuclear dynamics.

Self-assembled InGaAs quantum dots and their variants have been the subject of intense experimental and theoretical study for over 20 years. This has produced a large body of knowledge, multiple textbooks ([46, 130] for examples), a number of review articles [104, 124, 131–136], a biennial international conference and numerous national meetings. It is important to understand the state of this busy field and the context of this work within the many advances so far.

First: spin control and coherence. Controllable charge occupation was demonstrated in 2000 [137] and single spin storage in 2004 [96]. State preparation and all-optical control were demonstrated by 2008 [21, 42], and Hahn echo used to extend the coherence to 3 μs in 2010 [138]. At the same time, the irreversible decoherence processes for the electron spin have been largely undetermined to this point, specifically the extent to which we can protect a spin state from the large hyperfine interaction through dynamical decoupling.

As for the optical networking of single spins, interference between separate quantum dots was demonstrated by 2010 [139, 140], spin-photon entanglement was demonstrated in 2012-2013 by three independent groups [43–45], and photon to spin teleportation in 2013 [141]. As a complement to the work presented in chapter 4, nonlocal state creation was demonstrated between hole spins in 2016 [142].

This dissertation can be roughly divided into two halves. In the first half (chapters 2 and 3), we examine in detail the how we can determine the coherence of the electron spin: a surprisingly non-trivial task owing to phase-sensitive feedback with the nuclear environment. By either dissipating or preventing unwanted nuclear polarisation we access the full timescale of spin coherence and determine the intrinsic processes that irreversibly govern the spin coherence.

In the second half we move from single spin studies to direct demonstrations of

optical networking between single quantum systems. In chapter 4 we demonstrate the realisation of an entangled state between two distant electron spins. This experiment uses the coherent spin-photon interface the provided by the QD to distribute a nonlocal state between noninteracting ground state spins through the measurement of a single photon. The technique we demonstrate enables the generation of entangled states at the highest rate reported so far for optically active qubit definitions, with a controllable phase set by the interference of their indistinguishable emission.

In looking to the possible construction of hybrid quantum networks, in chapter 5 we demonstrate the direct coupling of a quantum dot and a single ion. This is the first demonstration of a link between single, wholly different quantum systems. We explore how the different optical properties limit the efficiency of the hybrid interface, and investigate routes to circumvent this based on the coherence of the excitonic transition in the quantum dot.

Finally, in chapter 6 we briefly assess how we to extract larger proportions of the quantum dot dipole field out of the optically dense gallium arsenide host. The developments we investigate will be crucial to demonstrating higher-order nonlocatlity between multiple quantum dots, as they should improve the outcoupling by an order of magnitude, while still preserving the clean electrostatic environment we require.

CHAPTER

TWO

NUCLEAR DYNAMICS DURING COHERENT ELECTRON CONTROL

We can use the coherent optical transitions provided by a self-assembled quantum dot to generate and manipulate arbitrary superpositions of the ground-state electron spin. In order to use the spin for information processing and communication, the state coherences need to be preserved for a sufficiently long time before dephasing through environmental interactions. While the hyperfine interaction with the nuclear bath is known to provide the significant source of dephasing, these interactions are correlated in time and can be effectively suppressed through dynamical decoupling [143] as observed in electrostatically defined GaAs quantum dots [144]. A key motivation for our development of coherent electron spin control is to establish the extent to which we can use decoupling schemes to protect the electron spin state.

The first step is to observe the free evolution of a coherent electron spin, which we achieve through Ramsey interference of the spin-basis states. We discussed how we construct the interference sequence in section 1.8.3 of the previous chapter. For longer delays between the two $\pi/2$ rotations environmental interactions lead to uncertainty in the energy difference between the spin states which then maps to a loss of visibility in the time-averaged signal.

As this chapter covers, extraction of spin coherence through resonance fluorescence is not a trivial process: phase-sensitive readout forms a feedback loop with the nuclear spins in the quantum dot. This process induces delay-sensitive polarisation of the bath, which in turn prevents the measurement of the spin state.

We show how we can study the electron free from this polarisation. We achieve this first by dissipating the nuclear polarisation through electron cotunneling with the back reservoir and then by altering our control sequence to frustrate the phase-dependent feedback loop. With these techniques we gain access to the unperturbed dynamics of the electron-nuclear system under resonant optical excitation and achieve reliable extraction of the spin-state coherence. In the next chapter we will extend these methods to incorporate dynamic decoupling and explore how nuclear bath dynamics are imprinted on the evolution of the electron spin.

A side-note: the data presented in this chapter were taken from three quantum dots from the same sample at a variety of field values between 1.5 and 4 T. The dynamics were found to be consistent between the QDs studied, and qualitative features independent of external field for these values. Indeed, they match dynamics recovered for quantum dots studied in multiple research groups [145, 146].

The data presented in this chapter were taken with Claire Le Gall, except for the final free-induction decay measurement in figure 2.11 which was performed with Lukas Huthmacher.

2.1. Ramsey interferometry

2.1.1. Method

To operate coherent control sequences much longer than a single Larmor precession we must suppress the spin readout and preparation laser: with the repump on the spin lifetime is reduced to 2.8 ns. We use an electro-optic modulator (EOM) formed from a $LiNbO_3$ waveguide Mach-Zehnder interferometer which provides rise times $\sim$ 200 ps, suitable for modulating the readout within the 13-nanosecond rotation pulse

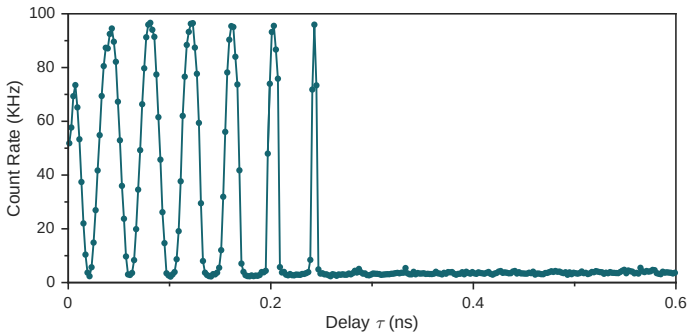

Figure 2.1.: **Ramsey interference** Count rates for delay τ between two $\pi/2$ rotations in a 4-T external magnetic field.

repetition time. The interferometric suppression of the laser is sensitive to thermal drifts in the waveguide, so we monitor the time-averaged output and feedback to a DC compensation offset to ensure that modulation is between maximally destructive and constructive interference. This way we can achieve suppression ratios between 300 and 600, with the exact ratio depending on the pulse sequence duty cycle.

The resonant laser modulation must be synchronised with the rotation pulses, which can be achieved a number of ways. Details are provided in appendix A which covers the construction of the various pulse sequences used in this work. Suffice to say, for the first measurements the laser is extinguished for 2.5 ns around the spin rotations. The remaining 11 ns provides enough time to prepare the electron spin to a reasonable fidelity, so the Ramsey measurement can be performed at 76 MHz without any pulse-picking of the rotation laser.

2.1.2. Results

When we apply the correct modulation to the spin readout and sweep the delay between the $\pi/2$ rotations, τ, we record the quantum dot fluorescence rates shown in figure 2.1. For short delays, $\tau \leq 200$ ps, the signal is very much as expected. The electron spin precesses in the external 4-T field at 24.8 GHz, and we record high visibility fringes. After this point the signal collapses to zero. This is in contrast to the behaviour we would expect for spin relaxation or time-averaged dephasing which would cause the fringes to continuously decay to their mean value.

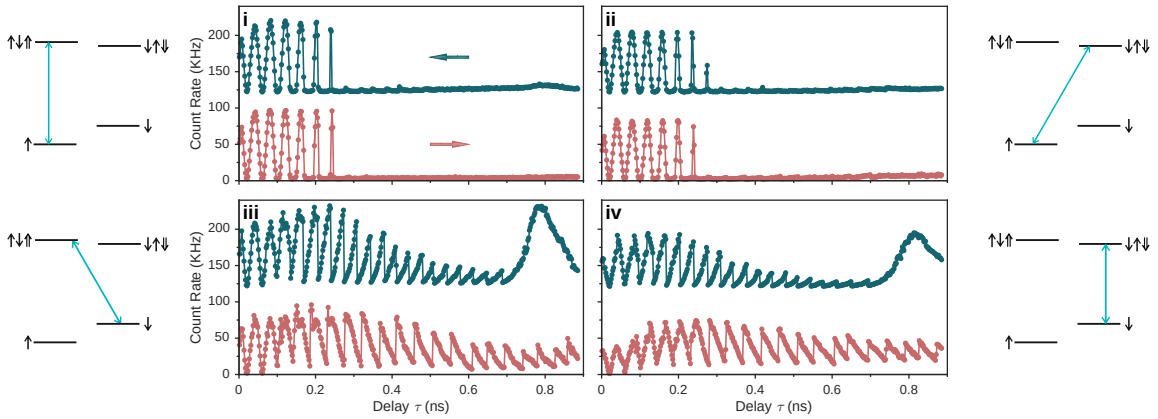

Figure 2.2.: **Ramsey interference transition dependence** Count rates as a function of delay for different scan directions and probed transition. The level structures adjacent to each axis display the used transition.

If we include both increasing and decreasing delay scans, and additionally use all four of the available optical transitions for readout and preparation, we record the count rates in figure 2.2. When probing either of the high-frequency transitions emerging from the spin-up ground state (i&ii), we observe this collapsing signal. Alternatively, when we probe the lower frequency transitions (iii&iv), a qualitatively different behaviour emerges: a direction-dependent sawtooth pattern [145]. The behaviour of the Ramsey interference for all transitions points to a phase acquisition by the electron spin which is non-linear as a function of τ, emerging from optically-induced dynamic polarisation of the nuclear bath (DNSP).

A net polarisation of the nuclear bath affects our measurement in two ways. First, a shift of the Overhauser field will introduce a detuning between our probe laser and the excitonic resonance. This reduces the photon rate we record and the fidelity with which we initialise the electron spin between rotations. Second, a polarisation alters the electron spin precession frequency. This will change the population at the end of the Ramsey sequence, and the amount by which we have to repump the spin.

The signal we generate from the quantum dot, $C(\omega_0, \omega_{\mathrm{OH}}, \tau)$, is set by the following [145]:

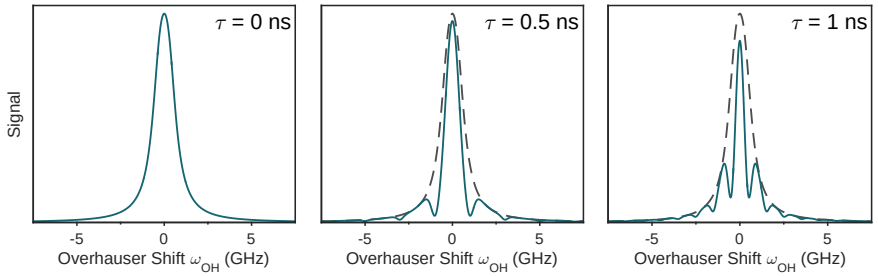

Figure 2.3.: **Overhauser shift-Ramsey signal relation** The transition is modelled as a Lorentzian with a 700-ps excited state lifetime. The transition is driven at twice the saturation intensity with a spin readout/preparation time of 13 ns, and the Larmor frequency is set at 10 GHz. For non zero Overhauser shifts, $\omega_{\mathrm{OH}} \neq 0$, the signal decreases as the laser becomes non-resonant, but for longer delays, the effect of changing the electron precession is also observed. The dashed lines for $\tau \neq 0$ mark the optical transition.

$$C\left(\omega_0, \omega_{\mathrm{OH}}, \tau\right) \propto \frac{\left(1 - e^{-\beta(\omega_{\mathrm{OH}})T_{\mathrm{P}}}\right)\left(1 + \cos\left[\left(\omega_0 + \omega_{\mathrm{OH}}\right)\tau\right]\right)}{1 + \cos\left[\left(\omega_0 + \omega_{\mathrm{OH}}\right)\tau\right] e^{-\beta(\omega_{\mathrm{OH}})T_{\mathrm{P}}}}. \tag{2.1}$$

This form can be found by solving the spin-pumping differential equation and the Ramsey interference transformation self-consistently. Here, $\beta(\omega_{\mathrm{OH}})$ is the spin pumping rate, set by the excited state population (as discussed in section 1.8.1), T_{P} is the spin pumping time, ω_0 is the Zeeman splitting of the electron spin, ω_{OH} the mean Overhauser shift and τ the delay between the $\pi/2$ rotations. Figure 2.3 displays the predicted readout signal as a function of Overhauser shift for a Zeeman splitting of 10 GHz at delays of $\tau = 0$, 0.5 and 1 ns. We have sampled over the finite width of the Overhauser field determined from the ensemble dephasing time of the electron spin [106]. For $\tau = 0$, the readout follows the natural transition width. As we increase the delay the signal modulates owing to the phase acquisition of the electron spin. The readout signal then becomes sensitive to a small, sub-linewidth nuclear polarisation. This additional element now forms a feedback loop between the electron spin and the nuclear bath polarisation. This increased sensitivity at longer delays explains why the nuclear feedback has increasingly strong effects in the Ramsey data as τ is increased.

In references [145] and [147], the authors captured the dynamics that result from

probing the lower frequency Zeeman branches ($|\downarrow\rangle$ population). They considered how the short excitonic lifetime enables flip-flop transitions with the nuclear bath. This in turn allows for an unbiased random walk of nuclear spin flips. This diffusive process will on average favour spin flips that increase the probability of exciting the quantum dot, forming a positive feedback loop. This loop then results in the sharp signal pick-up that we observe when probing the low-energy transitions in panels iii&iv of figure 2.2, as the nuclear bath polarises to ensure constructive Ramsey interference. A similar random-walk mechanism was attributed to nuclear focussing effects studied in references [148] & [149]. This mechanism leads to a polarisation of the Overhauser field of the form:

$$\frac{\partial \omega_{\mathrm{OH}}}{\partial t} = -\kappa \omega_{\mathrm{OH}} + \alpha \frac{\partial C}{\partial \omega_{\mathrm{OH}}} \tag{2.2}$$

Here, κ is the dissipation rate of a finite nuclear polarisation, and α is the polarisation rate. A positive feedback loop emerges when $\alpha > 0$. We will see in section 2.2.1 that dynamics of this form are consistent with our observations, however the transition dependence we observe is not reproduced by this random walk. For the high frequency transitions, the polarisation serves to minimise the creation of excited state population, forming a negative feedback loop (equivalent to $\alpha < 0$). An interesting feature of these data is the opposite spin dependence to the DNSP introduced in section 1.7.2 where probing spin-up population would lock the resonance condition.

This nuclear feedback is a fascinating manifestation of particular mechanisms unique to an electron and nuclear spins in a self-assembled dot. At the same time for our purposes, it is an effect we want to avoid. The delay dependence prevents us from obtaining time-averaged measurements of the electron dynamics without inducing a pulse-scheme dependent feedback loop with the nuclear environment. The rest of this chapter covers the ways we avoid this effect and the dynamics we can then resolve.

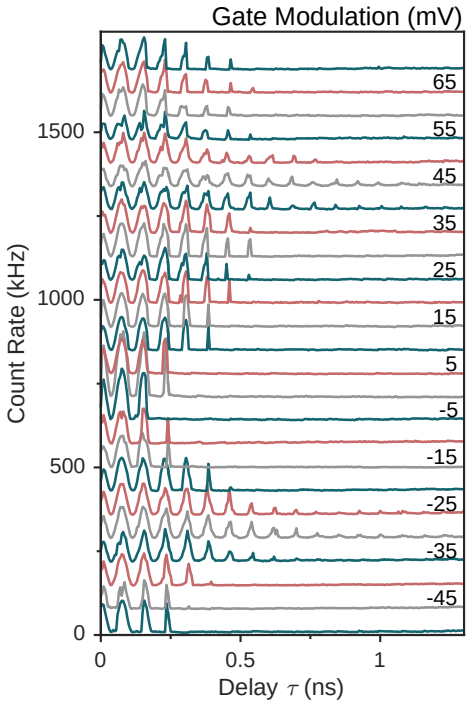

Figure 2.4.: **Gate modulation Ramsey interference** Signal for different modulation amplitudes from the resonance condition, offset for clarity. A plot of the transpose of these data forms the cover image for this dissertation.

2.2. Bias modulation

When we probe the high-frequency transitions, the steady state nuclear polarisation suppresses the signal from the spin readout. This loss of signal provides a straightforward signature of the polarisation process, which we can use to study the dynamics of the system as we perform the interferometry sequence.

In the first experiment, we run the Ramsey sequence at 76 MHz, and simultaneously apply a low frequency square-wave modulation at 700 Hz to the bias across the quantum dot sample. The modulation brings the optical transition off resonance, so we record half the average photon rate. The Ramsey interference signal we recover for varying the modulation step between -50 and +70 mV are displayed as offset curves in figure 2.4. Strikingly, when we apply modulation of ≈ -30 or $+45$ mV the beating persists for much longer, extending up to delays of a nanosecond.

By comparing the applied modulation with maps of quantum dot charge occu-

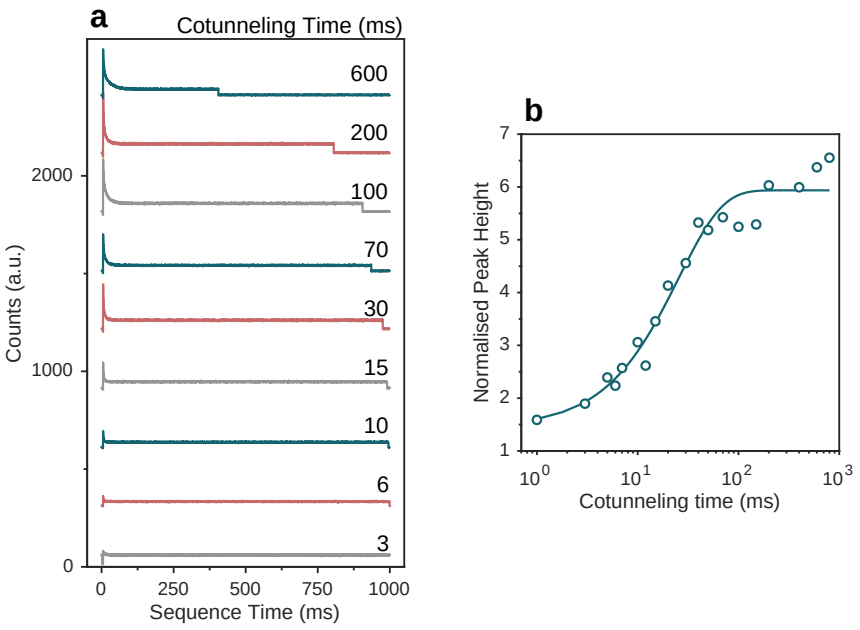

Figure 2.5.: **Nuclear spin recovery in Ramsey interferometry a** Correlated counts from the pulse sequence. The full sequence lasts for 1 s. The text labels mark the amount of time spent in a region of fast electron cotunneling. **b** Extracted peak heights, normalised to the polarised counts. The curve is an exponential fit to the data.

pation, we see that we are extending the Ramsey signal by modulating into bias regions of fast electron cotunneling with the back contact. The short spin lifetime allows for fast decay of nuclear polarisation through the hyperfine interaction [68]. In this way 1.4 ms in the cotunneling region partially reinitialises the system when we return to resonance. We observe the interference signal from the portion of time when the bath hasn't been polarised yet, becoming smaller for larger values of τ.

2.2.1. Time-resolved dynamics

The evolution of fluorescence as the bias voltage is switched allows us to observe in detail how the nuclear polarisation is created and lost. We keep the delay between the $\pi/2$ pulses fixed to 0.6 ns, where without nuclear polarisation Ramsey interference should give a maximal signal. We then pulse the bias voltage into the cotunneling region for a variable time, from 1 to 800 ms. A selection of the resulting time traces

are shown in figure 2.5a. The fast decay within the first 100 ms corresponds to the build-up of nuclear polarisation, which suppresses the signal to the constant, low value we find in time-averaged measurements. As we spend longer at the cotunneling bias the height of the initial peak increases as the system recovers [150]. We take this height normalised to the steady-state fluorescence rate as a measure of the recovery from DNSP. The extracted values are plotted in figure 2.5b. The curve is a single exponential fit to the signal height with a 25.6-ms recovery time constant. A full model would reproduce the exact response of the signal to a dissipating nuclear polarisation, although this captures the short-time return very well.

The nuclear spin polarisation is being effectively dissipated through the short electron spin lifetime. The energetically forbidden flip-flop terms in the fermi-contact hyperfine interaction we introduced in section 1.7.1 ($\hat{I}^i_{\pm}\hat{S}^{\mathrm{e}}_{\mp}$) are re-enabled when the spin decorrelation rate approaches the electron Zeeman splitting [104, 151]. We record cotunneling limited spin lifetimes down to single ns, however this would induce a loss of nuclear polarisation through this mechanism at a sub Hertz rate, orders of magnitude slower than we observe.

An alternative loss of polarisation is enabled by the large quadrupolar coupling, which tilts the nuclear quantisation axis resulting in an interaction of the form [109]:

$$\hat{H}^{nc}_{hf} = \sum_i A^{\mathrm{nc}}_i \hat{I}^i_x \hat{S}^{\mathrm{e}}_z. \tag{2.3}$$

Here, A^{nc}_i is set by the tilting of the nuclear quantisation axis, which we expect to be significant for the size and geometry of the magnetic field we apply ($\sim 0.2A_i$). This interaction, which conserves the electron spin, only requires that the electron lifetime is short enough to compensate for a nuclear spin flip. For a few-ns correlation time, this then enables the millisecond timescale relaxation we observe [68].

Similarly, if we allow sufficient time in the cotunneling region for the nuclear bath to recover, we can study the loss of signal due to DNSP. We operate an asymmetric pulse sequence of 22.5 ms in the cotunneling region and 2.5 ms on resonance. When we step the delay between the $\pi/2$ pulses, we record the time resolved fluorescence

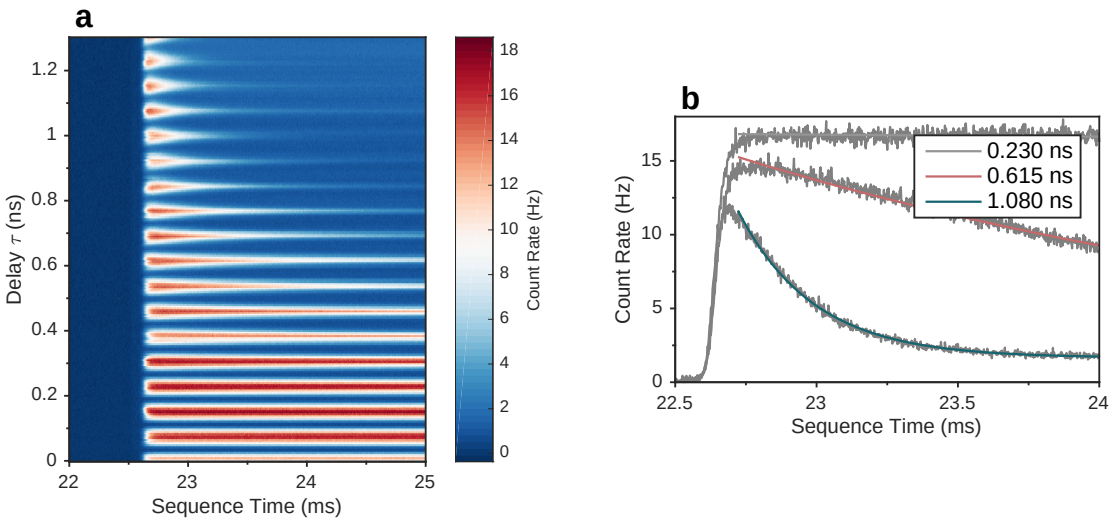

Figure 2.6.: **Time-resolved nuclear polarisation a** Full map of fluorescence when pulsing the bias into the cotunelling region for 22.5 ms, and back to resonance for 2.5 ms. The first 22 ms are not plotted as they produce no fluorescence. **b** Samples of the signal trace at $\tau = 0.230$, 0.615 & 1.080 ns. The coloured curves are exponential fits to the signal from the Ramsey sequence.

map displayed in figure 2.6a. The gate is switched back to resonance at 22.5 ms yet we observe signal from 22.65 ms onwards due to the low electrical bandwidth of the device. For the first few periods of electron spin precession ($\tau \leq 0.3$ ns), we recover a constant signal without polarisation-induced loss, consistent with the time-averaged measurements in figure 2.1. For longer delays the modulated signal starts to decay at an increasing rate.

Figure 2.6b displays the count rates after the gate returns to resonance for delays of $\tau = 0.230$, 0.615 and 1.080 ns. The coloured curves are exponential fits to the decreasing count rate. Although we don't expect the decay to be truly exponential, again the function captures the rate at which we lose signal. In this approximation, the count rate is described by $C = C_0 \exp(-\kappa_R t)$, where C_0 is our unperturbed signal, κ_R a constant decay rate, and t the time we spend on resonance. The fitted rates κ_R are then plotted as a function of rotation delay in figure 2.7. We find a quadratic dependence of the decay rate on the delay τ, with additional modulation at the electron precession frequency, with a maximum rate at delays that provide

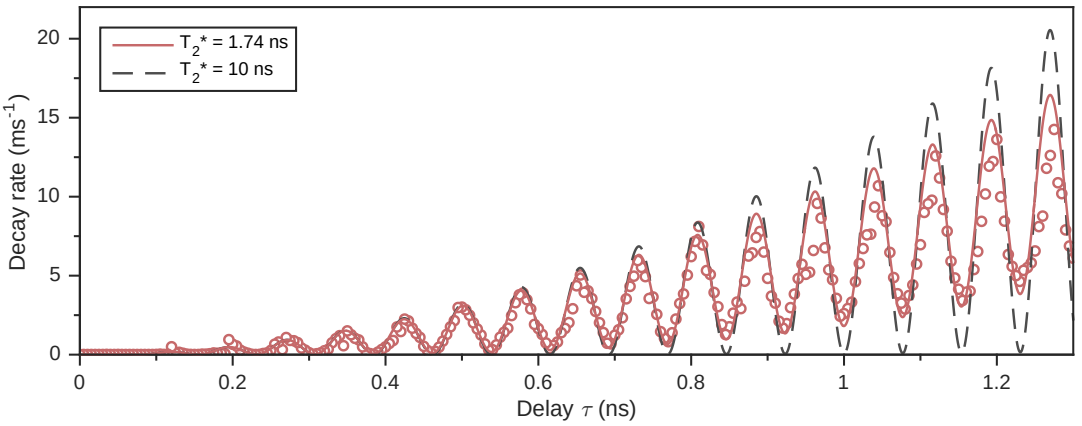

Figure 2.7.: **Ramsey signal decay rates** Points: extracted decay rates from figure 2.6. Solid (dashed) curve: estimated decay rates from equation 2.5 for $T_2^* = 1.74$ ns ($T_2^* = 10$ ns).

minimum count rate (destructive interference). The figure features curves following the functional form we outline below.

Motivated by reference [145], we take the polarisation rate to follow, $\partial\omega_{\mathrm{OH}}/\partial t = \alpha\partial C/\partial\omega_{\mathrm{OH}}$, as in equation 2.2, with the negative feedback condition, $\alpha < 0$. We neglect the additional relaxation rate, κ during the short timescales we study. This then allows us to extract an approximate decay rate of the Ramsey signal from the relationship between the count rate and an induced Overhauser polarisation:

$$\kappa_{\mathrm{R}} = -\frac{1}{C}\frac{dC}{dt} = -\frac{1}{C}\frac{\partial C}{\partial\omega_{\mathrm{OH}}}\frac{\partial\omega_{\mathrm{OH}}}{\partial t} = -\alpha\frac{1}{C}\left(\frac{\partial C}{\partial\omega_{\mathrm{OH}}}\right)^2. \tag{2.4}$$

We determine the form of this expression from the count-rate dependence in equation 2.1. We assume that our spin preparation is independent of Overhauser shift, appropriate for small deviations from the optical resonance condition. We then find the following, where the average is taken over the unperturbed configurations of the Overhauser field:

$$\kappa_{\mathrm{R}} \propto \left\langle \tau^2 \frac{\sin^2\left[\left(\omega+\omega_{\mathrm{OH}}\right)\tau\right]}{1+\cos\left[\left(\omega+\omega_{\mathrm{OH}}\right)\tau\right]} \right\rangle_{\Delta\omega_{\mathrm{OH}}}. \tag{2.5}$$

We assume the Overhauser field takes the form $\omega_{\mathrm{OH}} = \omega_{\mathrm{OH}}^{\mathrm{C}} + \Delta\omega_{\mathrm{OH}}$, where $\Delta\omega_{\mathrm{OH}}$ follows a Gaussian probability distribution. We then set the standard deviation of

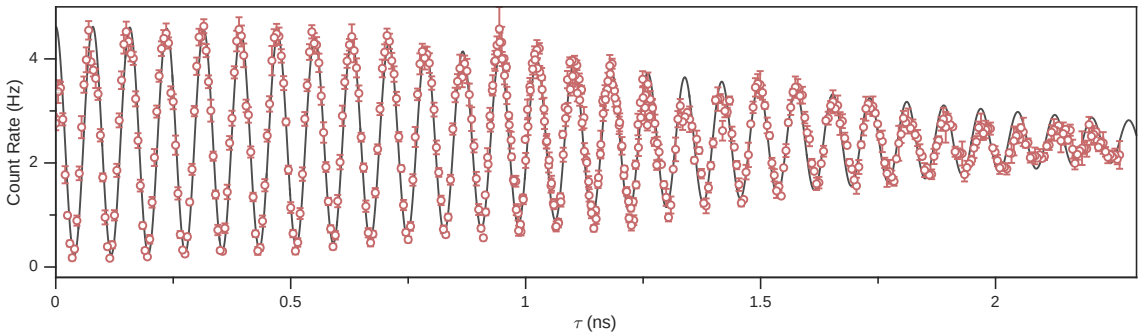

Figure 2.8.: **2-T free-induction decay measurement** The data is stitched from two measurements covering 0 to 1.28 ns and 0.914 to 2.264 ns. The count rate is the average of the first 10 μs after returning to a resonant gate voltage, determined from 150 s of acquisition at each delay. The error bars are the standard deviation in the first 10 μs.

the distribution to $2\pi\times129$ MHz determined from the free induction decay measurement presented in section 2.2.2. We evaluate for κ_{R} at no net nuclear polarisation ($\omega_{\mathrm{OH}}^{\mathrm{C}} = 0$), for which we retrieve the solid curve in figure 2.7. This model quantitatively reproduces all the key features in our loss of signal, including both the quadratic increase in rate and the modulated decay rate at a limited visibility. The dashed curve in figure 2.7 is the predicted decay rate for an Overhauser standard deviation of $2\pi\times23$ MHz. The narrower Overhauser distribution increases the visibility of the oscillations, showing that our loss of signal at all values of τ is a consequence of sampling over a range of Overhauser configurations.

2.2.2. Free induction decay

In order to measure a DNSP-free signal at larger delays, we need to spend increasing amounts of time recovering in the cotunneling bias region to ensure a more complete relaxation of the nuclear polarisation. Figure 2.8 displays the count rate we record in the first 10 μs after we return to resonance from spending 79.5 ms depolarising the nuclear bath, before staying on resonance for 0.5 ms. This highly-asymmetric duty cycle is sufficient to measure delays up to the dephasing time of the electron. The lack of significant nuclear polarisation is evidenced by the symmetric loss of contrast in the count rate.

The curve in figure 2.8 is a direct fit to the extracted count rate: a modulating signal at 12.8 GHz with a Gaussian envelope. This fit provides a dephasing time $T_2^* = 1.75 \pm 0.08$ ns. This is an expected timescale, given the large value of the Overhauser field variance, and consistent with previous measurements of the effective field width [119, 138, 146, 152]. More quantitative analysis will be provided in section 2.3. Importantly, here we have shown that we can recover the unperturbed dynamics of the electron spin through the dissipation of nuclear polarisation.

2.3. DNSP suppression

By erasing an unknown polarisation in the nuclear bath we can recover the full dynamics of the electron spin coherence. This method is limited by the rate at which we can depolarise the bath compared to how quickly the polarisation prevents state readout. For the full free-induction decay measurement in figure 2.8 >99% of the sequence time is spent resetting the system rather than producing information on the electron spin. While the Ramsey interferometry sequence can repeat at 76 MHz, another solution is required to prevent signal rates from becoming prohibitively low for longer, more complex rotation sequences. One option is to shepherd the nuclear bath to a desired polarisation with another optical feedback loop, such as through a dark-state double resonance [148, 153]. This option has the potential advantage of preparing the nuclear spins in a state with reduced fluctuations along the external field direction [100], increasing the ensemble dephasing time, albeit requires careful tracking of the position of the optical resonances at each step to ensure the bath polarisation returns to a pre-determined value.

Another option is to actively avoid the state-dependent feedback. When subjected to a control sequence repeating at 76 MHz, the interaction with the nuclear bath is, at fastest, on the microsecond timescale. The bath responds to the time-averaged signal from the electron spin, specifically the sensitive dependence of the state read-out on the phase acquired during the control sequence. We can remove this feature

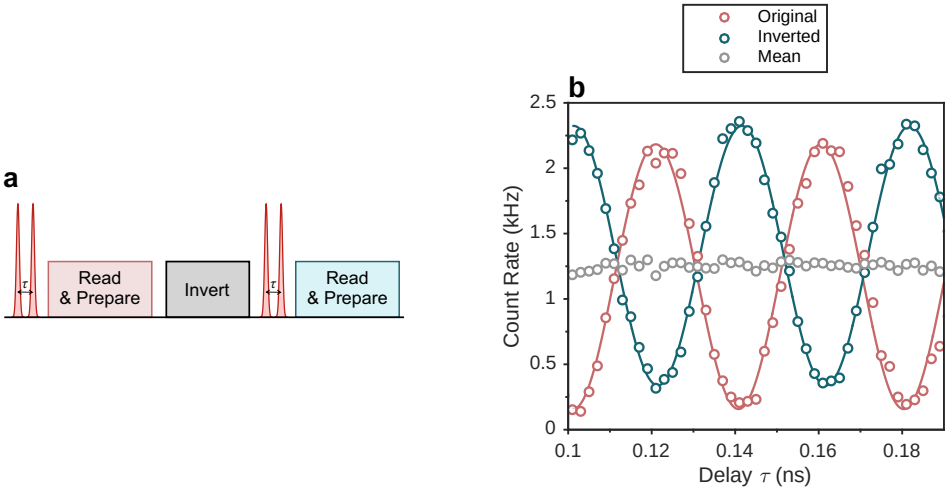

Figure 2.9.: **Alternating sequence a** Pulse sequence for nuclear-polarisation suppression. The inversion can be achieved either through a coherent rotation or an incoherent repumping step. **b** Count rates emerging from alternating initial spin states. The blue (red) points are the Ramsey sequence with (without) an initial inversion. The grey points are the average of the two sequences. The offset in heights is a consequence of the tilted optical rotation axis in the Ramsey sequence, while the inversion is complete.

by alternating the initial state of the electron before every repeat. These two initial states produce oscillatory signals with a π phase shift, and the average of the two should contain no phase dependence. Correlating the state readouts from two sequences with a time-to-digital converter (or a radio-frequency switch), allows us to extract the oscillating Ramsey interference signal.

We can invert the spin either through a coherent rotation, or by optical pumping. The main spin readout and preparation step that occurs every sequence is kept to a high-frequency transition (probing the population in $|\uparrow\rangle$) to ensure a stable resonance condition under DNSP [110]. The pulse sequence is sketched in figure 2.9a, where the two different colour pulses are state readouts on the same transition with opposite initial spin. To operate this sequence, we now pick a subset of the modelocked rotations with either an EOM or a high-frequency acousto-optic modulator. We then record the count rates shown in figure 2.9b. The grey points are the mean of the two repetitions, and exhibit no dependence on the rotation-delay, τ.

Figure 2.10 shows the two spin readout signals when we perform the Ramsey

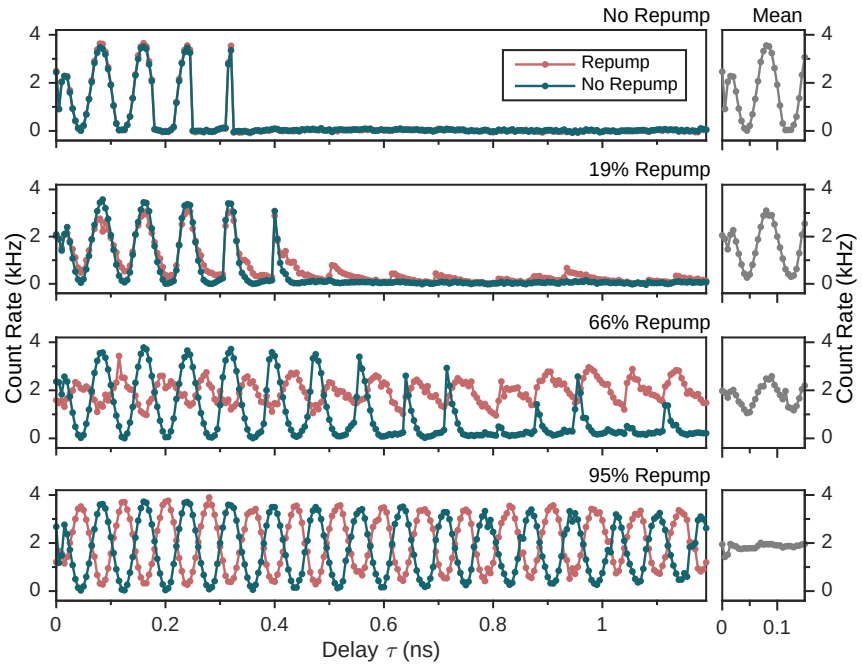

Figure 2.10.: **Ramsey interference with variable repump** The four panels show the alternating sequence for varying amounts of repump, as labelled. The red (blue) curves are the pulse sequence with (without) the variable repump. The subpanels to the right display the mean of the two readouts. As the repump approaches 100%, nuclear polarisation is suppressed and the sinusoidal behaviour extends up to the maximum delay here.

interference sequence, reading out with a high-frequency transition, and change the amount by which we repump the spin before every second repetition. The text above each panel contains an estimate of the amount of spin population returned in this variable repump step. The small panels to the right display the mean count rate from the two readouts for $\tau \leq 150$ ps.

For no repump, the two readouts are equal and the signal vanishes for $\tau > 300$ ps. As we increase the difference between the initial populations, the mean visibility is reduced and the traces extend due to suppressed nuclear feedback. For a 95% spin repump, the Ramsey interference patterns are now equal and opposite, the mean is flat, and the traces continue to oscillate up to the largest measured delays, showing that we have successfully prevented the build-up of measurement-disturbing nuclear polarisation.

In the 95% repump panel for $\tau > 1$ ns a slight non-sinusoidal behaviour is visible

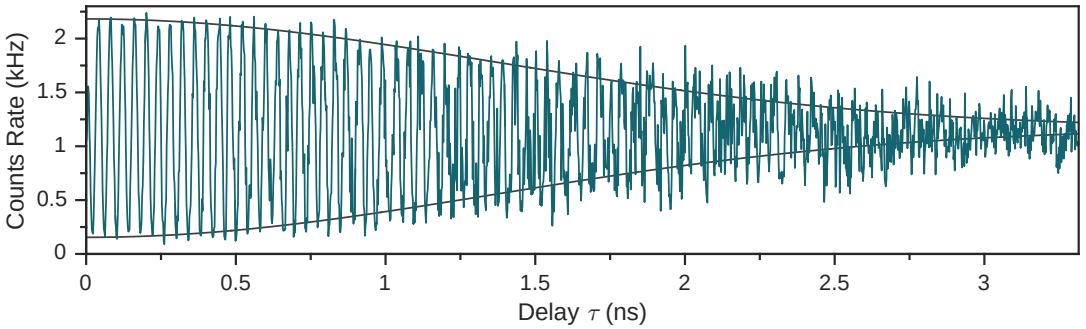

Figure 2.11.: **Alternating sequence free-induction decay** The non-inverting half of the full sequence is displayed. The grey curves are a gaussian envelope with a decay time $T_2^* = 1.93$ ns, which is determined by a scanning Fourier window. The non-sinusoidal behaviour at long delays is a consequence of slight nuclear spin polarisation.

in the two readouts, indicating a non-constant phase acquisition owing to a small polarisation. This is due to the fact that exact resonance with the lower frequency transition we use for the alternating repump step is an unstable condition due to DNSP [109].

For a high-fidelity, reliable inversion we combine a coherent π rotation with a resonant repump step. As discussed in section 1.8.4, precession in the external field prevents the π pulse from completely inverting the spin state so we use the incoherent repump to 'clean up' remaining spin population. The coherent rotation reduces the amount by which we drive the low-frequency transition by over an order of magnitude, reducing instability in the resonance condition.

Figure 2.11 contains the readout from the non-inverting half of the sequence for delays up to 3.2 ns. As can be seen, we have now sufficiently prevented the build-up of nuclear polarisation to recover the full free induction decay of the electron spin. Small shifts in the nuclear polarisation are still visible for $\tau \geq 1.5$ ns in the non-sinusoidal behaviour of the fringes, however an extraction of the ensemble dephasing time is still possible. The probable cause of this polarisation is sub-optical linewidth, low frequency electrical noise in the sample, compensated by an additional nuclear polarisation which in turn alters the electron splitting [110].

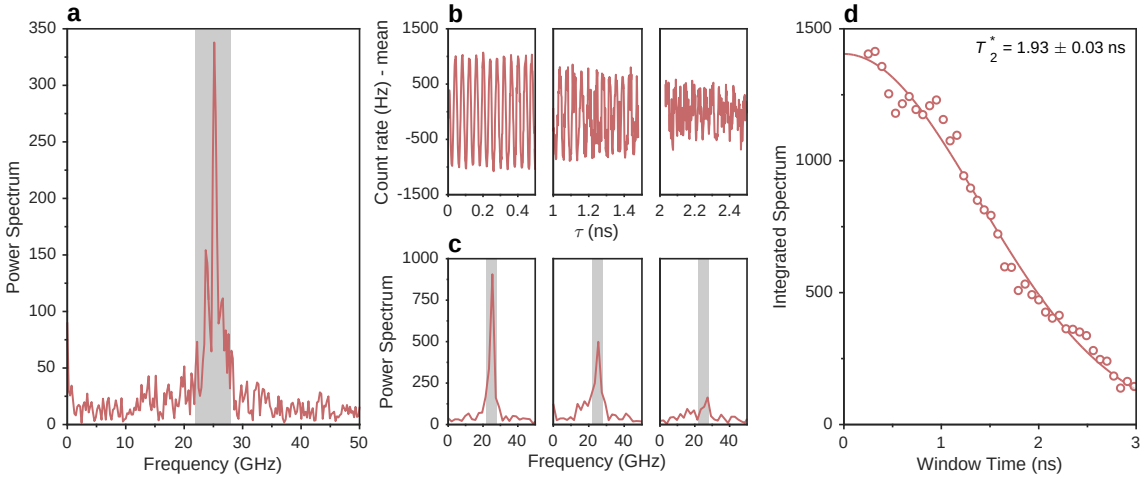

Figure 2.12.: **Fourier analysis of free-induction decay a** Power-spectrum of free-induction decay signal. **b** 0.5-ns windows of FID measure starting at τ = 0,1&2 ns. **c** Power spectra of windows in **b**. The rectangle marks the region of interest for extracting the oscillating component. **d** Filtered power around 26 GHz for swept central window position.

For this measurement, we perform Fourier analysis on the modulating spin population to extract the dephasing time of the electron. The results of this are displayed in figure 2.12. Panel a displays the fast Fourier transform (FFT) of the trace in figure 2.11 with mean count rate subtracted. The beat note at $\sim$ 26 GHz corresponds to the electron spin precession owing to the 4-T external magnetic field.

To fit the decay we find the spectrum of a 0.5-ns window of the data and step the window offset by 70 ps. Figure 2.12b&c show the counts and FFT spectra for windows centred around 0.25, 1.25 and 2.25 ns. We extract the amplitude of the beating by integrating a 6 GHz frequency band around the central tone, highlighted in the FFT spectra. The amplitudes are displayed in the panel to the right of the figure. Fitting these amplitudes with the function $\mathrm{A}e^{-(T/T_2^*)^\alpha}$ provides a value of $\alpha = 2.03 \pm 0.11$, consistent with a Gaussian decay of coherence. The non-zero size of the scanning window produces a slight overshoot in the decay time, which if compensated for reveals a T_2^* of 1.93 $\pm$ 0.03 ns. We note that these data were taken for a different QD than in figure 2.8.

As we will discuss in the next chapter, a Gaussian free-induction decay envelope

corresponds to a Gaussian noise source which can be considered static on the scale of T_2^*. The dephasing time is set by the noise amplitude, such that a simple relation can be found: $T_2^* = \sqrt{2}/\sigma_\mathrm{n}$, where σ_n is the standard deviation of the noise source [154]. This measurement sets $\sigma_\mathrm{n} = 2\pi\times(116 \pm 2)$ MHz. With the electron spin g-factor measured to be 0.43, this corresponds to an effective magnetic field width of 19.3 ± 0.3 mT. If we assume the electron spin is only sensitive to noise along the external field direction, we can recover the total three-dimensional Overhauser width by $\sigma_\mathrm{OH} = \sqrt{3}\sigma_\mathrm{n}$, providing a value of 33.6 ± 0.5 mT, in direct agreement with other work on similar InGaAs QDs [106, 108, 155]. For an indium concentration of 0.5 this is the variance emerging from a thermal mixed state of ∼33,000 nuclear spins

For the continued use of the alternating technique in the next chapter, we will only use a coherent π-rotation for the inversion step: the reduced average visibility is sufficient to prevent nuclear polarisation for small amounts of electron-spin phase acquisition. It is only the free-induction decay measurements that feature such large phase accumulation that the nuclear bath becomes sensitive to small oscillations in the time-averaged signal. The advantage of directly preventing state-dependent polarisation is apparent in the count rates of the two Free-Induction Decay measurements. Compared with running the Ramsey sequence at the original 76 MHz rate, hardware dead-time means we lose a factor of ~ 50 in running the alternating sequence. This technique still provides a spin measurement rate over a factor of 1000 higher than through erasing nuclear bath polarisation.

2.4. Conclusions & outlook

In this chapter we have demonstrated the extraction of spin coherence from a self-assembled quantum dot in the presence of significant feedback interactions with the nuclear bath. This has allowed us to retrieve high-accuracy measurements of the ensemble dephasing of the central spin through resonance fluorescence.

Recently, other routes to accessing electron spin coherence have been developed, in spin-to-charge measurements [119], or through measuring the coherence of spin-flip Raman scattering [146]. These both avoid a phase-dependent optical interaction rate, and consequentially seem to be free of significant polarisation.

The exact mechanism for the feedback loop deserves some more attention, as its dependence on the ground state spin seems contradictory to polarisation mechanisms in the literature. In the Voigt geometry the same dragging and anti-dragging dependence is observed for sequences with no phase dependence, albeit with a smaller width than in Faraday geometry owing to the high rate of electron spin flip induced nuclear diffusion [109].

Resonance fluorescence provides a minimally invasive, spin-selective interaction process which we can use to link the ground state spin with other nodes in an optical network, either through joint measurement [156] or a direct link [157]. For the spin-spin entanglement experiment in chapter 4, the specific operation sequence does not feature electron-phase dependent readout, and the polarisation processes explored in this chapter do not need to be accounted for. At the same time, more complex sequences will require careful tracking of where polarisation could emerge. This is not only to ensure the electron precession is well-known through multiple repetitions, but also that the detuning of the optical drive from the excitonic transition is fixed. In particular, the creation of highly entangled photon states from a quantum dot [158] will generally feature repeating sections of spin evolution and excited state creation, so would be particularly vulnerable to nuclear polarisation of the form discussed here.

CHAPTER

THREE

NUCLEAR DYNAMICS-DOMINATED ELECTRON SPIN COHERENCE

In the previous chapter we investigated methods to extract electron spin coherence free from a polarised nuclear environment. In this chapter we now use these techniques to examine the evolution of electron spin coherences, and the extent to which we can actively protect a coherent spin-state from the interaction with the nuclear bath.

By measuring the unperturbed electron-nuclear system, we recovered a T_2^* for the electron spin of 1.93 ± 3 ns. The Gaussian form of the decay informs us that this is due to large-amplitude, low frequency noise in the nuclear bath. Over this timescale the state evolves at a fixed but uncertain rate. While we can directly extract a value for the variance of the Overhauser field, the loss of electron spin coherence here is not sensitive to the dynamics of the environment.

The coherence time can be extended beyond T_2^* by using patterns of inversion pulses to decouple the state from the spin-dependent hyperfine interaction. To remove uncontrolled phase acquisition, temporally separate periods of spin evolution need to destructively interfere. The extent to which we can protect a state is now set by the environmental dynamics and their correlation time. As a consequence

by filtering noise decoupling schemes provide a sensitive spectroscopic probe of the nuclear bath, accessed through the time-averaged electron coherence [154, 159].

In this chapter we first introduce how electron-spin control sequences form spectral filters of environment dynamics. We then examine coherence of the spin under Hahn-echo decoupling [160]. We demonstrate how the behaviour we observe is governed by the high-frequency dynamics of the nuclear bath, and in this way determine the intrinsic mechanisms that irreversibly affect electron-spin coherence in self-assembled quantum dots. Finally, we present multi-pulse decoupling of the electron spin, and show that in certain cases protection beyond the Hahn-echo coherence time can be realised.

The mechanisms that could limit electron spin coherence in self-assembled quantum dots are topics that have received significant experimental and theoretical attention. One particular feature of these investigations has been the role of the significant, growth-induced strain fields. Nuclear magnetic resonance (NMR) studies of InGaAs quantum dot nuclei have shown the variation of spin splittings through the quantum dot preserves the coherence of the bath through protection from resonant spin-spin interactions between nuclei [161, 162]. This has led to speculation on how exactly the electron spin loses coherence, and why times up to the ms coherence times of the bath haven't been observed [138], in line with the times reported for electrostatically-defined quantum dots [144].

A note on contributions: The modelling of the nuclear spectra we present in this chapter was performed by Clemens Matthiesen and Clare Le Gall. The data were taken with Clemens Matthiesen and Lukas Huthmacher.

3.1. Spectrally filtering environment noise

Spin-dependent environmental interactions lead to the accumulation of an unknown phase difference between the two spin eigenstates. If, after some evolution time the state amplitudes are swapped, the same interaction will cause the phase-difference

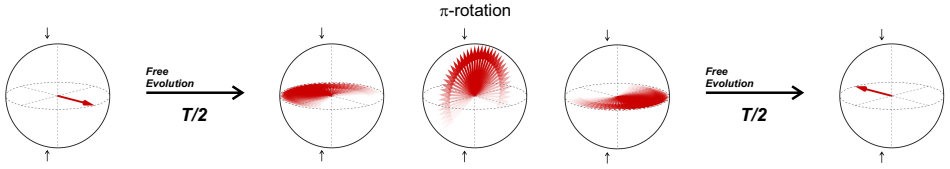

Figure 3.1.: **Hahn-Echo** Evolution of spin-state vector under an unknown environment with Hahn-echo. The state starts on the equator in an even superposition. After $T/2$, the orientation has been smeared out by the unknown evolution. The π rotation inverts the amplitudes. After another $T/2$ free precession the different trajectories have caught-up or lagged enough to converge on one point at the opposite side of the sphere.

to unwind. Erasing this unknown phase leads to a refocussing of the average state projection when the evolution time before and after the inversion are the same [160], at which point the electron state can be accessed. This process is sketched out on the Bloch sphere in figure 3.1. The shaded arrows represent the uncertainty in the state vector.

For a static environment, a single inverting pulse will completely refocus a dephased state. In the presence of a fluctuating environment the spin will only partially recover, in which case closer spaced inversion pulses can better protect the spin. This now requires that the environment is correlated on the timescale of the pulse separations, rather than the total sequence time, as in the case of a single echo pulse [143, 163].

The interplay between noise dynamics and the evolution of coherences can be viewed in multiple ways, for instance by developing the unknown environment in the time domain as a power series [164], or through the eigenvalues of a transfer matrix [165, 166] (important for considering a highly interacting nuclear environment). Here, we present one realisation which focusses on the spectral properties of the noise, appropriate for the dynamics of the nuclear bath in self-assembled quantum dots. Control sequences are treated as spectral filters through which the electron phase acquires noise from the environment [167]. To show how this emerges we follow reference [154], although equivalent derivations can be found in [168–170]. We derive in full how free-induction decay emerges from a dynamic environment, and

show how it can be extended to any pattern of inversion pulses.

We restrict ourselves to the case of a Gaussian noise source, valid for the Overhauser field emerging from a large ensemble of non-interacting nuclear spins. This limit is of interest as all environmental dynamics can be encapsulated in two-time correlation functions or equivalently a single spectrum filtered by our pulse sequence. In general this approximation might not be appropriate, if one considers linear coupling to an interacting bath or nonlinear coupling to a highly correlated environment [144, 171]. The validity of this approximation for the particular processes in self-assembled quantum dots will be discussed later.

We consider the spin subject to the Hamiltonian:

$$\hat{H} = \frac{\hat{\sigma_x}}{2} \left(B_{\text{ext}} + \hat{\eta}_x \right), \tag{3.1}$$

which contains both the coupling to the external field, B_{ext} and a noise source along the external quantisation direction, $\hat{\eta}_x$. We assume here that the variable field follows a Gaussian distribution with width Δ:

$$P\left[\hat{\eta}_x = \eta'\right] = \frac{1}{\sqrt{2\pi}\Delta} e^{\frac{-\eta'^2}{2\Delta^2}} \tag{3.2}$$

The corresponding propagator from time 0 to T for the hamiltonian in equation (3.1) is given by:

$$\begin{aligned} \hat{U}_\eta \left(T, 0\right) &= \exp\left(-i \frac{\hat{\sigma_x}}{2} \left(B_{\text{ext}} T + \int_0^T \eta'\left(t\right) \mathrm{d}t \right) \right) \\ &= \exp\left(-i \frac{\hat{\sigma_x}}{2} \left(B_{\text{ext}} T + X_\eta\left(T\right) \right) \right), \end{aligned} \tag{3.3}$$

including the linear phase accumulation from the external field , $B_{ext}T$, and the integral of the stochastic term η, $X_\eta\left(T\right)$. The resulting density matrix at time T is then the average over all realisations of the noise operator:

$$\rho\left(T\right)=\sum_{\eta}p_{\eta}U_{\eta}\left(T,0\right)\rho(0)U_{\eta}^{\dagger}\left(T,0\right) \tag{3.4}$$

The coherence of the density matrix can be found by measuring the double average of the operator σ_+:

$$\begin{aligned}\left\langle\left\langle\sigma_{+}\right\rangle\right\rangle &= \mathrm{Tr}\left\{\sigma_{+}\rho\left(T\right)\right\}\\ &= \sum_{\eta}p_{\eta}\mathrm{Tr}\left\{\hat{U}_{\eta}^{\dagger}\left(T,0\right)\sigma_{+}\hat{U}_{\eta}\left(T,0\right)\rho(0)\right\}\\ &= e^{iB_{\mathrm{ext}}T}\sum_{\eta}p_{\eta}e^{iX_{\eta}(T)}\mathrm{Tr}\left\{\sigma_{+}\rho(0)\right\}\\ &= e^{iB_{\mathrm{ext}}T}\left\langle e^{iX_{\eta}(T)}\right\rangle\mathrm{Tr}\left\{\sigma_{+}\rho(0)\right\}.\end{aligned} \tag{3.5}$$

This double average describes the projection operator acting on the density matrix found by averaging U_η over the noise distribution via p_η. By commuting the propagator through the expression and using the cyclic nature of the trace, we have linked this value to the expectation of $e^{iX_\eta(T)}$.

The phase acquired, X_η, is itself a Gaussian variable, being a linear combination of Gaussian noise, and accordingly the expectation value of $e^{iX_\eta(T)}$ can be expressed as:

$$\begin{aligned}\left\langle e^{iX_{\eta}(T)}\right\rangle &= \int_{-\infty}^{\infty}\frac{1}{\sqrt{2\pi}\sigma_{T}}e^{\frac{-X^{2}}{2\sigma_{T}^{2}}}e^{iX}\mathrm{d}X\\ &= e^{\frac{-\sigma_{T}^{2}}{2}}.\end{aligned} \tag{3.6}$$

The variance of X_η, σ_T is a time dependent function, which can be related back to the autocorrelation of η, $S\left(t\right)$ by a change in variables:

$$\begin{aligned}\sigma_T^2 &= \left\langle X^2(T)\right\rangle \\ &= \int_0^T t\mathrm{d}t_1 \int_0^T \mathrm{d}t_2 \left\langle \eta'(t_1)\,\eta'(t_2)\right\rangle \\ &= 2\int_0^T \mathrm{d}t \int_{\frac{t}{2}}^{T-\frac{t}{2}} \mathrm{d}t' \left\langle \eta'\left(t'+\frac{t}{2}\right)\eta'\left(t'-\frac{t}{2}\right)\right\rangle \\ &= 2\int_0^T \mathrm{d}t\,(T-t)\,S(t)\,.\end{aligned} \tag{3.7}$$

These steps take into account the time symmetry of η_x and the assumption of its stationary behaviour, such that $\langle\eta'(t)\eta'(0)\rangle = \langle\eta'(t+t'')\eta'(t'')\rangle$.

The Wiener-Khinchin theorem allows us to view the noise in the spectral domain, by relating the power spectral density (PSD) of the noise, $\tilde{S}(\omega)$ to the lag-covariance:

$$S(t) \equiv \int_{-\infty}^{\infty} e^{-i\omega t}\tilde{S}(\omega)\,\mathrm{d}\omega. \tag{3.8}$$

With this definition, we can re-express the definite time interval in equation (3.7), and as such find the variance of X_η, σ_T from an integral over the spectral density of noise processes:

$$\begin{aligned}\sigma_T^2 &= 2\int_0^T \mathrm{d}t \int_{-\infty}^{\infty} e^{-i\omega T}\tilde{S}(\omega)\,(T-t)\,\mathrm{d}\omega \\ &= 4\int_{-\infty}^{\infty} \tilde{S}(\omega)\,\frac{\sin^2\left(\frac{\omega T}{2}\right)}{\omega^2}\mathrm{d}\omega.\end{aligned} \tag{3.9}$$

The coherence of the spin-qubit is now encapsulated as:

$$\langle\langle\sigma_+\rangle\rangle = \exp\left\{-\int_{-\infty}^{\infty}\tilde{S}(\omega)\,\mathcal{F}_{\mathrm{FID}}(T,\omega)\,\mathrm{d}\omega\right\}, \tag{3.10}$$

where:

$$\mathcal{F}_{\mathrm{FID}}(T,\omega) = \frac{1}{2}\frac{\sin^2(\omega T/2)}{(\omega/2)^2}. \tag{3.11}$$

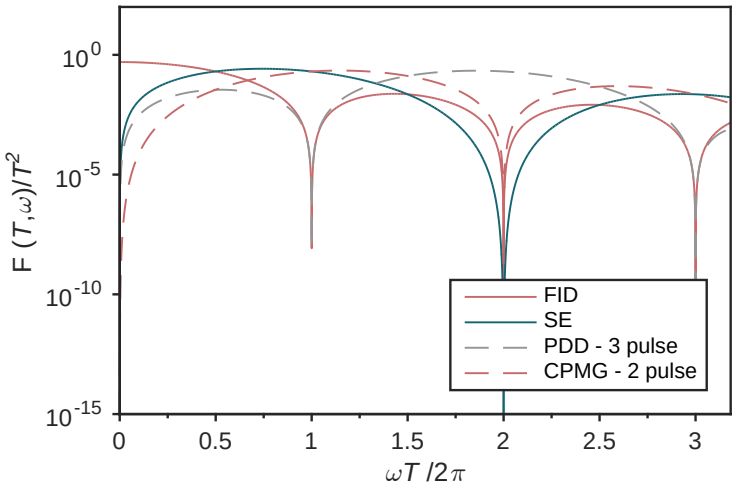

Figure 3.2.: **Spin Coherence Filter Functions** Filter functions for Free-Induction Decay, Hahn-Echo, two-pulse CPMG and three-pulse Periodic Dynamic Decoupling, plotted from refs. [169] & [154].

The coherence is determined by the integral of a filter-function, $\mathcal{F}_{\mathrm{FID}}(T,\omega)$, and the Gaussian noise PSD, $\tilde{S}(\omega)$. Inversion pulses can be incorporated by adding rotations at points in the propagator $\hat{U}(T,0)$, which leads to an additional term, $s(t) = \pm 1$ in the integral $X_\eta(T)$. For Hahn-echo this results in the filter function:

$$\mathcal{F}_{\mathrm{HE}}(T,\omega) = \frac{1}{2}\frac{\sin^4(\omega T/4)}{(\omega/4)^2}. \tag{3.12}$$

This picture allows for intuition on the loss of coherence in limiting cases of noise dynamics. For white noise ($\tilde{S}(\omega) \to \tilde{S}$) the power spectral density can be factored out of the integral. For all decoupling sequences, the filter function integrates to the state storage time, resulting in an exponential loss of coherence at the same rate for any order of decoupling. This will be important for assessing the extent to which different schemes can further protect coherence. At the other limit, for quasi-stationary noise, $\mathcal{F}_{\mathrm{FID}}(T,0) \to T^2/2$ which results in a Gaussian loss of coherence for free induction decay, the same form we observed for the measurements presented in chapter 2.

The filter functions $\mathcal{F}(T,\omega)$ for free-induction decay and Hahn-echo are plot-

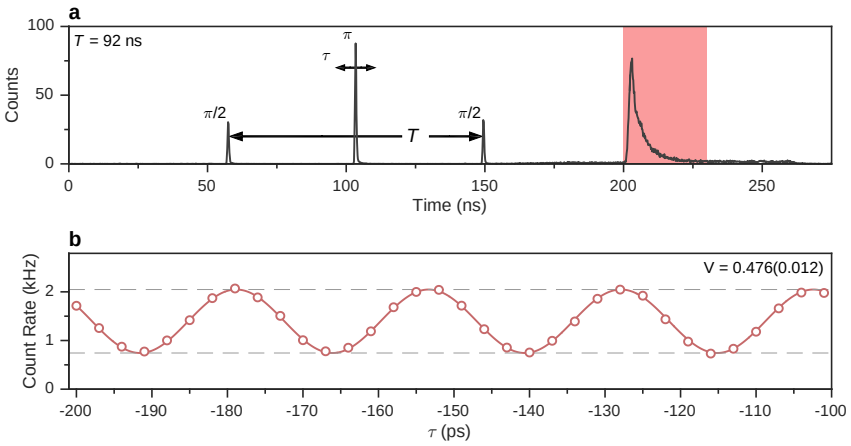

Figure 3.3.: **Hahn-Echo Pulse Sequence and Spin Population a** Rotation pulses and spin readout for a $T = 91.2$ ns Hahn-echo sequence with highlighted spin readout region of interest. **b** Modulated spin readout for relative delay of the central π rotation, τ.

ted in figure 3.2 against the noise frequency-time product. For comparison, three-pulse periodic dynamic decoupling (PDD) and two-pulse Carr-Purcell-Meiboom-Gill (CPMG) filter functions are displayed. The smaller the value of $\mathcal{F}(T, \omega)$, the less noise will contribute to decoherence at that frequency-time product.

The behaviour at low frequency ($\omega \ll 1/\mathrm{T}$) is the crucial parameter for most systems, where the qubit decoherence time is shorter than the correlation time of the environment. As expected, free-induction decay lets through all low frequency noise, while decoupling filters these terms. The advantage of PDD and CPMG over Hahn-Echo are clear from the better suppression of noise at higher frequencies. For $\omega \sim 1/T$, the pass-bands of the filter functions allow us to perform spectroscopy on high-frequency environment dynamics, without the loss of coherence being dominated by large low-frequency noise terms [159]. An intuitive analogy is provided in this picture: piecewise decoupling is equivalent to an optical grating, with a central frequency set by the periodic spacing, and a larger number of periods allowing for a sharper pass band [172].

3.2. Electron spin Hahn-echo

To perform Hahn-echo on the single spin we space the two $\pi/2$ rotations of our Ramsey sequence by $T > T_2^*$ and add a single π pulse at $T/2$. We split the 78 MHz modelocked pulse train into two, as described in section 1.8.3, and pulse-pick each half separately. We select the $\pi/2$ pulses from the same arm of the split pulse train, constraining T to a multiple of the 13-ns pulse repetition time. The π rotation is picked from the other arm. The pulse sequence trace and spin readout is displayed in figure 3.3a for $T = 92$ ns. We pick the rotation pulses and form the readout pulse using high-frequency waveguide electro-optic modulators. The electrical pattern is generated by two Stanford Research Systems DG645 Pulse Delay Generators, triggered by the modelocked source. An additional AOM envelope around the sharp EOM readout/state-preparation pulse improves our resonant probe on-off suppression ratio from 500 to 6300. These suppression ratios, combined with using a sub-saturation readout power prevent unwanted spin pumping during the echo sequence. Additional details and characterisation of the pulse sequence are provided in appendix A.

Selecting the π rotation from the moving arm of our split pulse (figure 1.16 in section 1.8.3) allows us to scan the relative delay of the rotations to $T/2 \pm \tau$ for $\tau \leq 0.7$ ns. An additional controllable delay allows us to set the separation of the two arms to 0 or 6.6 ns, for measuring Hahn-echo at even and odd multiples of the pulsed laser repetition. When we sweep the central delay, τ, by less than the electron ensemble dephasing time we record an oscillatory readout signal, as in figure 3.3b [138]. The two periods of evolution differ by $(T/2+\tau)-(T/2-\tau) = 2\tau$, and as such the state we recover oscillates at twice the spin splitting, as evident here for a magnetic field of 3 T with a spin splitting of 19.6 GHz. In the limit of perfect rotations the visibility of this trace provides a measure of the coherence of the electron spin, corresponding here to V = 0.476 ± 0.012. The finite duration of our rotation pulses, as discussed in section 1.8.4, is such that this measurement corresponds to a slight underestimate of the state coherence.

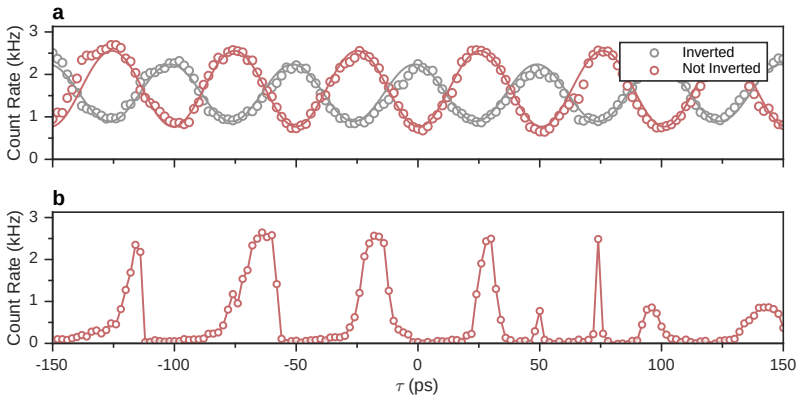

Figure 3.4.: **Dynamic Nuclear Polarisation under Hahn-Echo** The two panels differ by the addition of an initial spin inversion to prevent nuclear polarisation. **b** Spin readout for scanning the central π pulse by delay $\tau < T_2^*$. **c** Spin readout without alternating initial state. The nuclear polarisation results in the non-oscillatory trace.

As for the Ramsey interference measurements in the previous chapter, we use an alternating sequence to prevent the buildup of state-dependent nuclear polarisation, which would disturb the phase-sensitive spin readout. The two panels in figure 3.4 contain the spin readout for a 13.14-nanosecond echo sequence at a 1.5-Tesla external field with and without alternating initial states. In panel a, the imperfect inversion a single π rotation results in the lower visibility of the inverted readout signal. In comparison, however, in panel b where we remove the alternation the non-sinusoidal behaviour follows the build up of polarisation, preventing the extraction of state-coherence.

3.3. Hahn-echo visibility

Figure 3.5 displays the recovered visibility through Hahn-echo for storage time T up to 1.2 μs for four external magnetic field values: 2, 3, 4 & 5 Tesla. This figure contains a large amount of information, and it is worth discussing it in some detail. The figure is divided to focus on the short term behaviour for T up to 340 nanoseconds on the left, and the full behaviour up to 1.2 μs on the right. The data points are the average of 5 measurements at a particular delay and field value. The curves are calculated

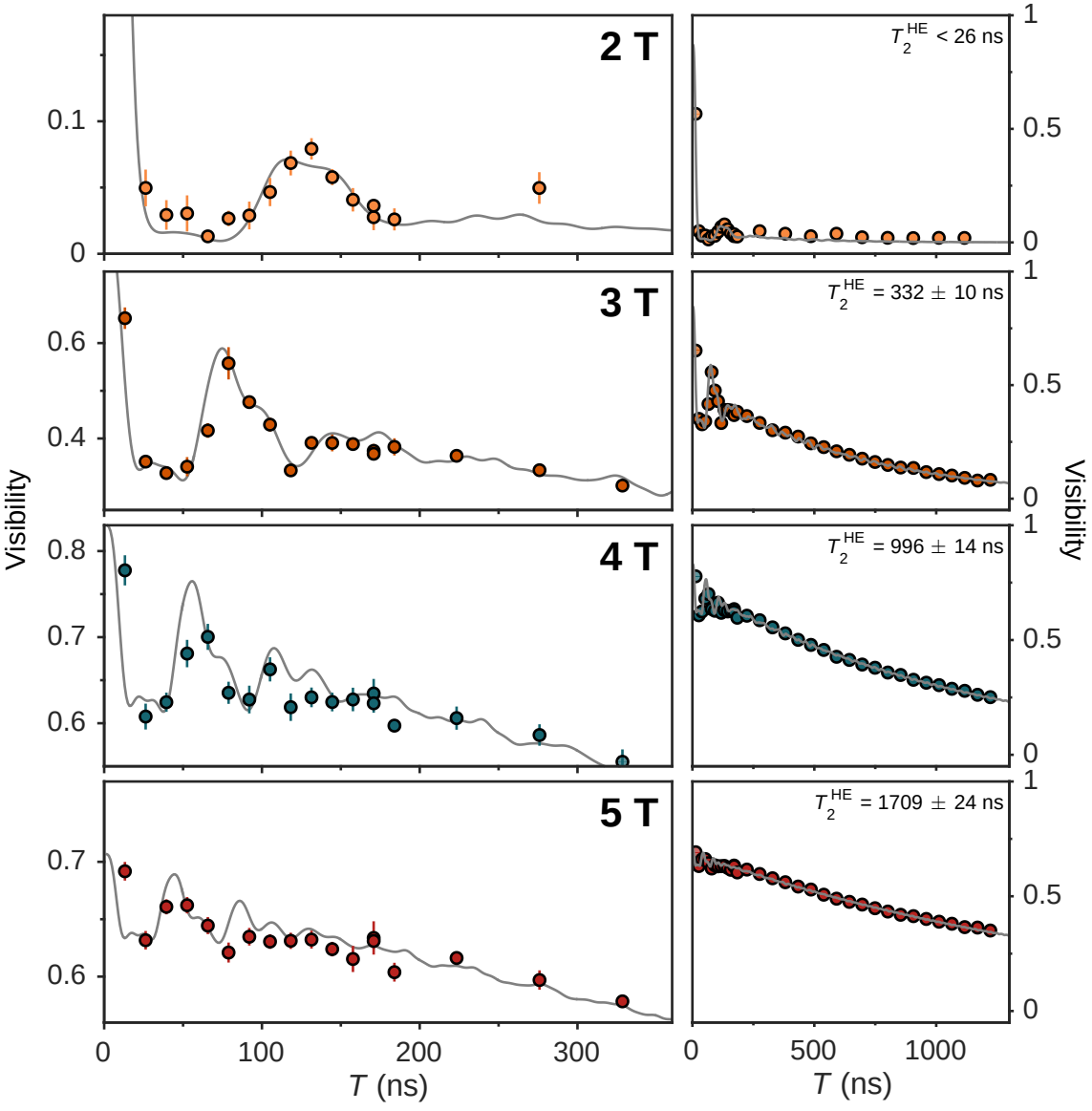

Figure 3.5.: **Hahn-Echo Visibility** Extracted visibilities for varying storage time, T, and external field values. The visibilities are drawn from the readout without initial inversion. Error bars show the standard error of the mean for repeated measurements. The curve is the result of modelling the echo sequence as a filter of the nuclear spectra. Right-hand panels show zoomed-out traces of long storage times, showing the exponential visibility decay and the fitted decay times.

by treating the sequence as a spectral filter on the high frequency nuclear processes we will discuss in section 3.4.

First we can focus on the global magnetic field dependence presented in the zoomed-out plots to the right of the figure. For an external field of 2 Tesla the visibility is strongly suppressed for $T > 13$ ns. This low field suppression of coherence had tentatively been attributed to occur as a consequence of dynamic nuclear polarisation [43], which our measurements are now to a large extent free from. Increasing the field to 3 Tesla induces a dramatic lift in short-time visibility to $\sim$ 50%, with an exponential tail dropping to the $1/e$ value at 332 ± 10 ns. Increasing the field further to 4 Tesla, the visibility rises, and similarly the length of the tail approaches a microsecond. At 5 Tesla, the short time visibility has saturated. At this field, our spin rotation axis starts to deviate by a large amount. Accordingly the extent to which the central π rotation inverts the state amplitudes is reduced, as well as the estimate of state-coherence from the spin visibility. The exponential tail, however, is still longer, and the visibility falls to the 1/e value at 1709 ± 24 ns.

The short-time behaviour ($T < 300$ ns) is particularly rich, and is highlighted in the left panels of the figure. All data sets feature a modulating visibility at a rate increasing with magnetic field, which damps within $\sim$ 150 ns. The depth of the oscillations decreases with increasing external field. The visibility dependence on storage time emerges from a spectrally broad, precessing environment. We will discuss in the next section how all of these experimental features can be understood and reproduced by considering the filtered spectra of high-frequency nuclear processes in the quantum dot.

3.4. Nuclear-dominated electron spin coherence

We introduced the basic features of the hyperfine interaction in chapter 1 (section 1.7.1), however to understand how the Hahn-echo response emerges from the electron-nuclear system, we need to consider in more detail how different dynamics

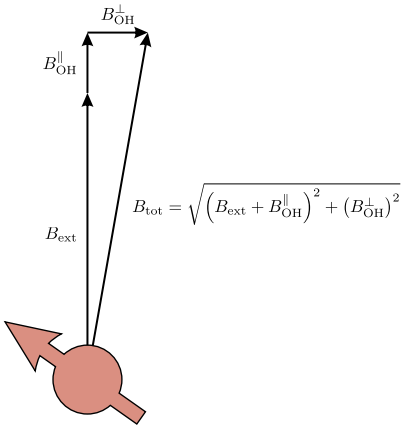

Figure 3.6.: **Overhauser Field Projections**

in the Overhauser field couple to the electron spin. In general the electron precesses around the axis $\mathbf{B}_{\mathrm{tot}}$, the vector sum of the external field ($\mathbf{B}_{\mathrm{ext}}$) and the Overhauser field $\mathbf{B}_{\mathrm{OH}}$, which we can split into components parallel ($B_{\mathrm{OH}}^{\parallel}$) and perpendicular ($B_{\mathrm{OH}}^{\perp}$) to the external field direction:

$$B_{\mathrm{tot}} \equiv |\mathbf{B}_{\mathrm{tot}}| = \sqrt{\left(B_{\mathrm{ext}} + B_{\mathrm{OH}}^{\parallel}\right)^2 + \left(B_{\mathrm{OH}}^{\perp}\right)^2}. \tag{3.13}$$

The geometry of the coupling is presented in figure 3.6. These measurements all take place in the limit $B_{\mathrm{ext}} \gg B_{\mathrm{OH}}$, such that we can make the approximation:

$$B_{\mathrm{tot}} \approx B_{\mathrm{ext}} + B_{\mathrm{OH}}^{\parallel} + \frac{\left(B_{\mathrm{OH}}^{\perp}\right)^2}{2B_{\mathrm{ext}}}. \tag{3.14}$$

In this way, Overhauser field projections couple in distinctly different ways to the electron spin, depending on the relation to the external field. Terms along the external field direction are mapped directly onto the electron spin splitting and contain the full Overhauser field variance. It is low-frequency noise components in this direction emerging from nuclear spin-spin interactions that dephase the electron in < 2 ns. These terms are effectively filtered by the Hahn-echo sequence. The perpendicular components, $B_{\mathrm{OH}}^{\perp}$, provides a much smaller perturbation, by a factor of $B_{\mathrm{OH}}^{\perp}/2B_{\mathrm{ext}}$ (~ 100). The quadratic dependence results in a spectral character set by the relative frequencies of nuclear processes [144]. To understand the coherence

we recover, we must consider how dynamics in these directions emerge from high frequency processes within the nuclear bath.

3.4.1. Nuclear spectra

As introduced in section 3.1, we can relate the coherence recovered through Hahn-echo to the power spectral density of the noise environment, in this case, the Overhauser field. The Gaussian distribution of Overhauser field amplitude follows from considering a large collection of non-interacting nuclear spins, valid for the high frequencies we consider. Following the definition of the power spectral density in equation 3.8, we can find the spectrum of the Overhauser field along some axes, $\alpha = x, y, z$ from the Fourier transform of two-time nuclear spin correlators:

$$\tilde{S}_\alpha(\omega) \propto \sum_j A_j^2 \int_{-\infty}^{\infty} e^{-i\omega\tau} \left\langle \hat{I}_\alpha^j(\tau)\, \hat{I}_\alpha^j(0) \right\rangle \mathrm{d}\tau, \tag{3.15}$$

where the sum is over every nuclear site, j. If $\hat{I}_\alpha^j$ commutes with the nuclear Hamiltonian, then the correlator $\left\langle \hat{I}_\alpha^j(\tau)\, \hat{I}_\alpha^j(0) \right\rangle$ is time-independent and the power spectral density only contains components at $\omega = 0$. Alternatively, for a direction where the operator no longer commutes, the spectrum will contain components at the frequency difference between the states linked by the Hamiltonian. For example, a magnetic field along x will generate terms such as $\left\langle \hat{I}_z^j(\tau)\, \hat{I}_z^j(0) \right\rangle \propto \cos\omega_{\mathrm{L}}^j\tau$, where ω_{L}^j is the Larmor precession frequency of the nuclear spin j, while $\left\langle \hat{I}_x^j(\tau)\, \hat{I}_x^j(0) \right\rangle$ would be constant in τ.

In order to determine the weight of these noise components, we note from the definition in equation 3.8 that the variance of a stationary random process is simply the zero-delay component of the lag-covariance; the integral of the power spectral density, $\tilde{S}_\alpha(\omega)$ [173]:

$$\sigma_\alpha^2 = S_\alpha(0) = \frac{1}{2\pi} \int_{-\infty}^{\infty} \tilde{S}_\alpha(\omega)\, \mathrm{d}\omega. \tag{3.16}$$

For a thermal mixture, the value of σ_α^2 is set by the hyperfine constant, the nuclear

spin quantum numbers and the size of the electron wavefunction, and therefore fixed for our specific quantum dot. The nuclear Hamiltonian then determines how the variance is distributed over different frequencies. We have accurately determined the width of the Overhauser field through our ensemble dephasing measurements of T_2^* to be $\sigma_\alpha = 33/\sqrt{3}$ mT in each direction, assuming the Overhauser field amplitudes are isotropic over sufficiently long times. Equivalently, over the timescales measured for free-induction decay the filter function is flat up to hundreds of MHz, which encapsulates the highest frequency nuclear processes we consider.

As a final point, we note that zero-frequency components in the nuclear spectra are shifted to a finite frequency due to inter-nuclear interactions and coupling out of the dot. We assume these processes occur faster than our measurement time for free-induction decay, yet slow enough that they are effectively filtered by our Hahn-echo decoupling schemes. As such we limit ourselves to high-frequency terms that emerge from the Zeeman and quadrupolar couplings. In particular, our measurements predict an upper bound on any of these other effects of 100 kHz, which is consistent with recent measurements of nuclear bath coherence in a charged quantum dot [174].

With these tools to link the nuclear Hamiltonian to the noise spectrum we can consider the specific details of the nuclear dynamics our electron spin is subject to.

3.4.2. On-axis components: $B_{\mathrm{OH}}^{\parallel}$

The quadrupolar interaction to strain induced field gradients is of such a strength that for a few-Tesla external field the nuclear quantisation axis is tilted by a significant amount. We introduced how this leads to new electron-nuclear dynamics in section 1.7.2. A particular consequence for the Overhauser field is the generation of high-frequency components in $B_{\mathrm{OH}}^{\parallel}$ up to high-external fields. These oscillatory dynamics couple strongly to the electron spin splitting and influence the evolution of coherences over short storage times (< 100 ns).

Following section 3.4.1 we model the spectra of the Overhauser field components for a nuclear spin j from a Hamiltonian containing the Zeeman and quadrupolar

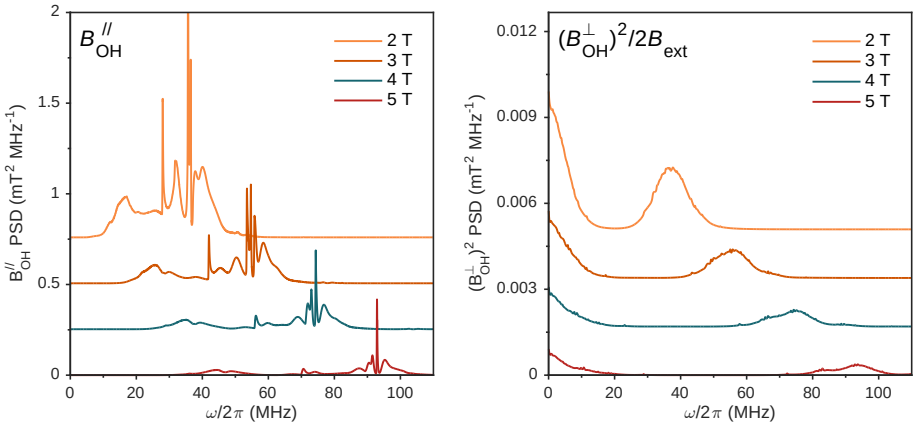

Figure 3.7.: **Overhauser Field Power Spectral Densities** Linearly coupled (left panel) and quadratically coupled (right panel) Overhauser field power spectral densities owing to processes in equation 3.17. Filtering these spectra result in the curves in figure 3.5. Note the difference in the vertical scale between the projections.

interactions:

$$\hat{H}^j_{\text{nuc}} = g_j \mu_N B_{\text{ext}} \hat{I}^j_x + \frac{h\nu_Q}{6}\left(3\hat{I}^{j2}_{z'} - \hat{I}^{j2} + \eta\left(\hat{I}^{j2}_{x'} - \hat{I}^{j2}_{y'}\right)\right) \tag{3.17}$$

Here, the external field acts along a direction x, while the quadrupolar interaction, with strength ν_Q is in a coordinate frame set by x', y', z'. The major axis of the quadrupolar interaction is along z', which deviates from the growth axis for isotope k by θ_k, with an additional biaxiality parameter η_k set by the asymmetry of the strain fields. We use values for the strength, direction and symmetry of the interaction motivated from reference [37], which uses atomistic simulations to determine the electric field gradients present. The validity of this model has been confirmed in measurements of quadrupolar-enabled DNSP [109] and NMR studies of the nuclear bath [175].

The quadrupolar strength and direction are modelled as Gaussian distributions around their central values to approximate the large inhomogeneity in the strain throughout the QD. The parameters we use are listed in table 3.1, labelled according to isotope k, where σ_{ν_Q} is the width of the quadrupolar interaction strength and σ_{θ_k} the width of the major quadrupolar axis tilt from the growth direction. This

	^{115}In & ^{113}In	^{75}As	^{69}Ga	^{71}Ga
I_k	9/2	3/2	3/2	3/2
$g_k\mu_N$ (MHz T^{-1})	9.33	10.22	12.98	7.22
ν_Q (MHz)	3	5	3.3	3.3
σ_{ν_k} (MHz)	0.9	3	1.65	1.65
η_k	0.315	0.5	0.358	0.358
$\theta_{k,1}$	15°	20°	11.3°	11.3°
$\sigma_{\theta_{k,1}}$	5°	10°	5°	5°
$\theta_{k,2}$	52.5°	-	-	-
$\sigma_{\theta_{k,2}}$	12°	-	-	-

Table 3.1.: Parameters used to form the Overhauser-field spectra displayed in figure 3.7.

is a simplification of more detailed structure in the geometry of the quadrupolar interaction [175]. For indium, we include a second axis at angle, $\theta_{k,2}$. Owing to their high quantum number indium spins form a major contribution to the Overhauser field spectra, and we need to include this additional feature to our approximation to reproduce the particular Hahn-echo response we observe. The important feature of interest in the values listed in table 3.1 is their relative strength. Not only is the size of the quadrupolar interaction appreciable to the Zeeman coupling, but its variance in magnitude and orientation also take up a significant fraction of the central values.

The left panel of figure 3.7 contains the high-frequency on-axis Overhauser field spectra, offset for clarity, calculated from $\left\langle \hat{I}_x^j(\tau)\,\hat{I}_x^j(0)\right\rangle$ for the four external field values studied in our Hahn echo experiment. For these spectra we assume an indium concentration of 0.5. The nuclear bath is taken as a thermal mixed state, correct for our 4.2-Kelvin measurement temperature. The components visible here at all fields are enabled by the quadrupolar interaction. As the field increases, the features move to higher frequency due to increased Zeeman splitting, and lose amplitude as the nuclear bath dynamics become dominated by the external field.

We can attribute our short term behaviour to these high-frequency, large amplitude terms. The evolution in the range 10-100 MHz gives rise to the modulation

we see in our Hahn echo visibility between 10 and 100 ns as the pass-band of the Hahn-echo sequence moves through the nuclear spectra. The large width of these spectral features, however damps the oscillations within one or two revivals. The relative size of the width and central frequency of the on-axis nuclear fluctuations prevent the nuclear bath from re-phasing, responsible for the constant drop in visibility, especially visible in the 2-T data were the spin never recovers to more than 10% of the original coherence. The suppression of these terms with external field results in the global lift of visibility we observe between 2 and 3 T as well as the reduction in the amplitude of the short-time oscillations at higher fields.

3.4.3. Perpendicular components: $\left(B_{\mathrm{OH}}^{\perp}\right)^2/2B_{\mathrm{ext}}$

After the high-strength on-axis fluctuations, we now examine the perpendicular components of the Overhauser field. These quadratically-coupled terms are a much smaller perturbation to the spin splitting.

The crucial parameter for understanding how these terms influence spin coherence is the width of the quadrupolar interaction. To model the quadratic coupling, we consider the auto-convolution of the noise processes in the frequency domain. The resulting spectra are plotted in the right panel of figure 3.7. The large spread of quadrupolar energies forms a continuous band of frequencies to $>$ 10 MHz, with a decreasing value at higher fields due to the $1/(2B_{\mathrm{ext}})$ coupling. In comparison to the on-axis fluctuations, these terms extend to zero frequency, capable of inducing a continuous decay of the electron spin coherence to zero. The small strength of these contributions affect the spin coherence at long times ($>$ 100 ns), such that they present a quasi-white noise spectrum. This then results in a field-dependent exponential loss of coherence for the electron spin, which we observe in the tails of the visibility in figure 3.5. In this way, we can see that the inhomogeneity of the quadrupolar interaction is responsible for the irreversible loss of spin coherence on a microsecond timescale, set by the relative strength of these quadratically coupled components and the external field.

It is important to mention that in general we cannot use the filter-function formalism to consider Overhauser field components that quadratically couple to the electron spin splitting [176, 177]. as the derivation in section 3.1 relies on a linear mapping from the Gaussian noise amplitude to the phase acquired by the spin. For self-assembled dots, however, the storage time at which these terms affect the central spin compared with their correlation time ensures the Gaussian-distribution of state phase is a valid approximation [171].

3.4.4. Total coherence

The total state visibility plotted in figure 3.5 is the product of the parallel and perpendicular Overhauser field contributions. They are found from the parameters listed in table 3.1. We require Overhauser field standard deviations of 40 and 28 mT for the linearly and quadratically coupled components to reproduce our extracted coherence. Our ensemble dephasing time suggested a standard deviation of 33 mT, supporting the validity of the model. We require an constant, field dependent scaling factor to account for our imperfect rotation axis (87%, 85%, 83% & 71% for 2, 3, 4 and 5 T). Importantly, the filtered spectra quantitatively support the features of our Hahn-echo response, showing that we can evaluate the evolution of electron spin coherence in its entirety from the nuclear Zeeman and quadrupolar interactions.

To clarify their individual roles, figure 3.8 displays the recovered coherence due to each term, and their product (dashed line). This shows the drop and modulation due to the linearly coupled terms, which dominate at low field, and the continuous, external field dependent decay stemming from the quadratically coupled terms. The panels display our imperfect visibility estimation due to the tilted optical rotation axis, plotted as the black dash-dotted curve for each magnetic field.

To what extent can we further protect the electron coherence with a multi-pulse decoupling sequence? Multi-pulse schemes protect coherence by inverting the spin state in timescales on the order of the environment correlation. Inversions would need to be separated by the nuclear correlation time (< 100 ns) to protect spin

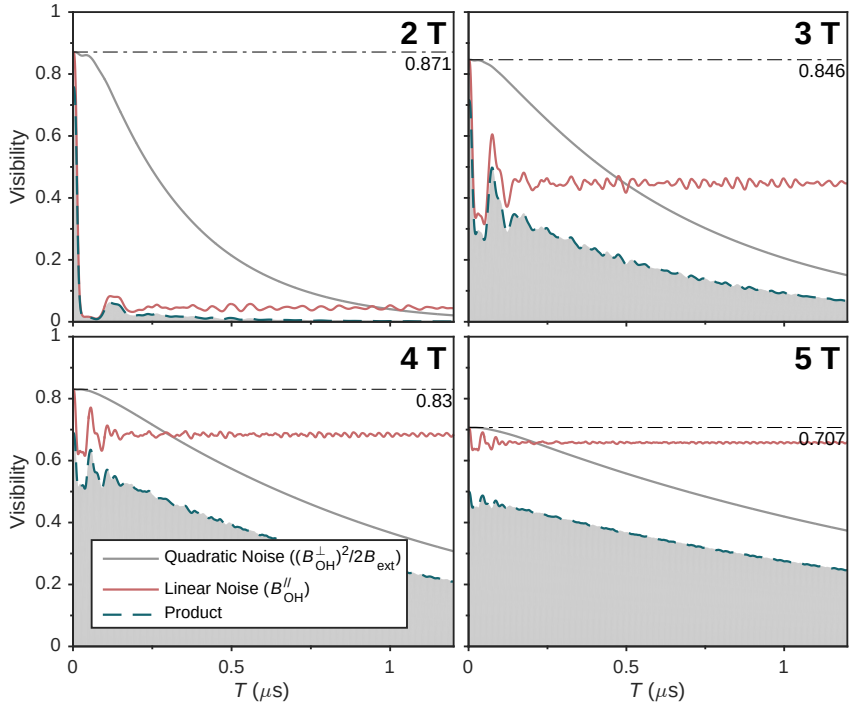

Figure 3.8.: **Split Hahn-Echo Response** Modelled Hahn echo visibilities for the linearly and quadratically coupled Overhauser field components at the four magnetic fields investigated. The dashed line - their product - is the total spin visibility we extract. The dash-dot line marks the limit of visibility we can extract due to our tilted optical rotation axis.

coherence from these transverse components. In order to see an appreciable improvement over the single microsecond values recorded for Hahn-echo at high field, a large number of pulses would then be required. The number of rotations possible would be limited by the irreversible coupling of the excitonic transitions to acoustic phonon modes in the quantum dot [124, 125], such that for any realistic scheme, the high-field values we record provide a bound to electron spin coherence in these strained systems.

Figure 3.9 offers support to our expected magnetic field dependence. The figure contains the Hahn-echo visibility for a separate quantum dot from the same sample at an external field of 7 T. At this field value the short time oscillations have reduced to a negligible value, and the exponential tail has increased to 2.70 ± 0.04 μs, consistent with a perturbation from quadratically coupled terms which decreases with larger external field.

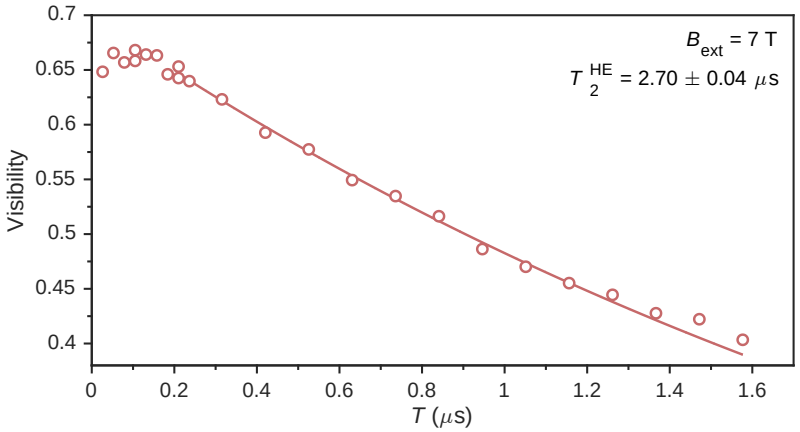

Figure 3.9.: **High-field Hahn-echo** Echo visibilities retrieved for a separate quantum dot from the same sample at an external field of 7 T. The curve is an exponential fit to the data, with a decay time of 2.70 ± 0.04 μs.

3.5. Dynamical decoupling

In the high-field limit ($>$ 4 T), extension beyond the Hahn-echo measurements is challenging, as the loss of coherence is caused by noise frequencies that extend far beyond the inverse state storage time ($\omega T \gg 1$). At low field ($B_{\text{ext}} < 3$ T), however, the non-exponential fast reduction in visibility informs us that higher order pulse sequences could further extend the accessible coherence time. From the nuclear spectra in figure 3.7, we see that this drop is due to the broad, large amplitude noise in the range $\omega/2\pi$ = 20-50 MHz. These frequencies then correspond to a time-frequency product ωT = 0.25-0.6 when combined with our observed loss of coherence in $\sim$ 20 ns. This intermediate time-frequency product is the region where it is possible to outperform Hahn-echo with higher order decoupling (see figure 3.2)

To investigate this we perform periodic dynamic decoupling of the electron spin at B_{ext} = 1.5 T. The repetition of our optical control pulses are such that we cannot fit an arbitrary number of rotations within this short time. Rather, we set the $\pi/2$ separation at a multiple of 13 ns (the pulse repetition time) and add a π rotations every 6.5 ns. In this way we can probe the coherence at 26 ns with three π pulses, 39 ns with 5 and so on.

The pulse sequences are depicted in the left of figure 3.10. For a sequence con-

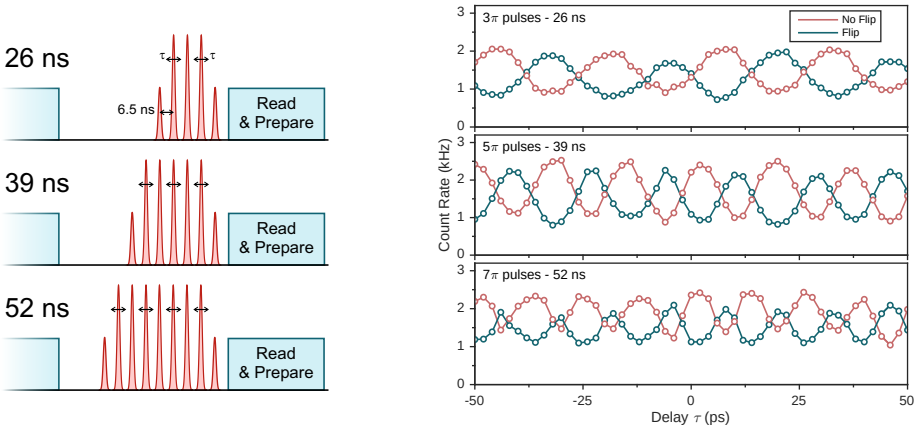

Figure 3.10.: **Electron Spin Dynamical Decoupling Oscillations left** Pulse sequences for measuring electron spin decoupling for 3, 5 & 7 inversion pulses. The sequence is repeated with an inverted initial state to prevent nuclear polarisation. **right** Extracted counts for decoupling with n = 3,5 & pulses when sweeping the location of $(n{+}1)/2$ inversions by τ.

taining n π-rotations the $\pi/2$ rotations and $(n-1)/2$ inversions are drawn from the arm of the split pulsed laser without the scanning stage, while $(n+1)/2$ are picked from the scanning arm, which features a 6.5-ns offset. This allows us to measure the coherence remaining after this dense sequence by scanning the relative positions of $(n+1)/2$ pulses and recording the final population in the same way as for Hahn echo. By sweeping the location of multiple pulses, the phase offsets accumulate, and the signal we record oscillates at $(n{+}1)$ times the spin splitting.

The spin population modulation we recover for $n = 3$, 5 and 7 ($T = 13$, 26 and 39 ns) sequences are displayed in the right of figure 3.10, which feature the increasing oscillation rate with rotation number. As for all the coherent control experiments, we repeat each sequence with an inversion to prevent nuclear polarisation, resulting in the lower visibility 'flip' trace in the figure.

We fit the oscillations and extract visibilities to estimate the electron spin coherence, which are displayed in figure 3.11. To the left of the figure the Hahn-echo visibility extracted for $T = 13$ and 26 ns are plotted in red. To the right the Periodic Dynamical Decoupling visibilities up to $T = 65$ ns (9 π-pulses) are displayed. The dashed line marks the fitted visibilities and the solid line links the values corrected

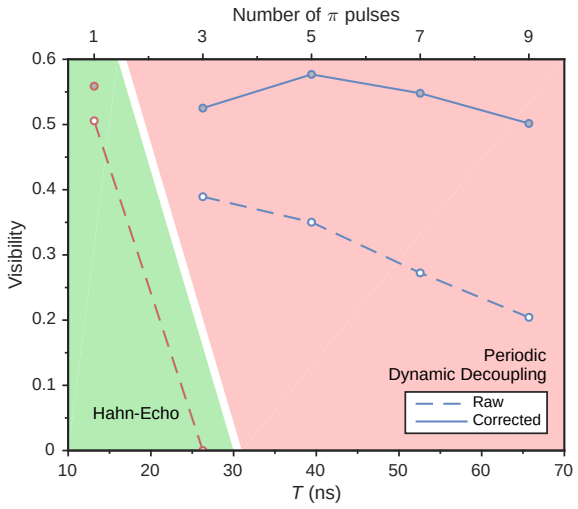

Figure 3.11.: **Dynamical Decoupling Visibilities** Extracted visibility from Hahn-echo (red points), and multi-pulse decoupling (blue points). The solid curve links visibilities corrected for the imperfect inversion. The top axis labels the number of π-rotations that protect the spin state at a particular value of T.

for the incomplete inversions, a factor of 0.905 for every π pulse. This only corrects for the mapping of visibility to coherence, rather than the imperfect protection of the spin.

The first striking feature is the retention of coherence beyond the Hahn-echo limit, through better filtering of the low-to-mid frequency components of $B_{OH}^{\parallel}$. A large proportion of the loss of visibility can be attributed to the accumulated error in multiple π rotations.

These data show that in certain limits, the spin coherence can be extended through multi-pulse decoupling. The timescale here, however, is only a small fraction of the microsecond coherence times measured at higher field, and it would take a large number of inversions to reach these times. That being said, the increase in coherence we observe through multi-pulse decoupling could make the critical difference in entangling small collections of spins at low field, increasing the coherence length from 3.9 m to over 15 m.

3.6. Conclusions & outlook

By suppressing nuclear bath polarisation in our quantum dot, we have been able to observe the full evolution of the electron-nuclear system, and establish the key timescales for central spin coherence in these structures. We have found that intrinsic high-frequency nuclear processes are sufficient to explain the rich, field-dependent dynamics we recover. The growth-induced strain variance throughout the dot disperses the nuclear evolution to provide a weak-irreversible loss of electron spin coherence. In particular, the high strength of the quadrupolar interaction provides a lower bound of $\sim$3 T on external field values for retaining coherence for appreciable lengths of time.

Our ability to diagnose the nuclear processes affecting spin coherence through Hahn-echo is closely related to spectroscopic work with bulk electron spin resonance: electron spin echo envelope modulation (ESEEM) [178, 179]. For these experiments, it is often the hyperfine interaction that alters the nuclear-spin quantisation axis, rather than the tilted quadrupolar interaction in our case.

A partner to this work which has not yet been discussed yet is capability of a heavy hole pseudo-spin as a spin-qubit. A confined heavy hole, which has a predominantly p-shell atomic orbital, offers an instant reduction in the hyperfine coupling strength [133]. This reduction has been observed as an order-of-magnitude improvement in ensemble dephasing times, observed either through optical Λ-scheme coherence [142, 146, 180] or coherent manipulation [181–183]. At the same time, coherence times exceeding those for decoupled electron spins have not yet been recorded. Unless another mechanism is responsible, one would expect an immediate improvement in coherence retention. One of the motivations for studying the electron spin qubit in detail is the high-optical quality n-doped samples allow. Recent results demonstrating small linewidth p-doped samples are very promising for marrying hole-spin coherence with coherent optical transitions [184].

This direct link between the strain-driven assembly and the central spin coherence motivates the investigation of other routes to improved coherence, specifically

through an engineered quadrupolar interaction. This could be achieved either in a system without quadrupolar nuclear moments, such as in II-VI quantum dots [150]. An alternative is to host a spin qubit in a quantum dot formed in a strain-free growth method [185, 186]. GaAs/AlGaAs quantum dots grown strain-free by droplet epitaxy have already demonstrated significantly different nuclear dynamics [187].

It can be interesting to compare our spin-state evolution with electrostatically-defined GaAs quantum dots. These much larger systems feature significantly less strain, and an isotopically simpler environment (in particular featuring no $I = 9/2$ indium). This has allowed for retention of electron spin coherence for times approaching a ms through dynamic decoupling [144, 177]. Quadrupolar effects still play a role in the evolution of spin coherence [176], however only for certain geometries and external field values. These systems cannot be viewed in the same spectral formalism as our self-assembled quantum dots, owing to the long correlation times and larger interaction strengths between the individual spins of the nuclear bath.

Similar dynamics have been obtained for electron spins confined to InGaAs quantum dots in references [138] and [119], which provide comparisons to the results in this chapter. Both references feature an increased coherence with external magnetic field. The coherence in each of these works is normalised, however, which prevents full, quantitative comparison. That aside, both show an increase in electron coherence at lower magnetic field than we observe. The suppression of quadrupolar-enabled fluctuations occurs between one and two Tesla in reference [119], and the exponential tail reaches 2 μs at 4 T in reference [138]. A lower field coherence pick-up is consistent with a smaller indium fraction in the quantum dot. This is exhibited in an accompanying reduction in both the strength of the Overhauser field and quadrupolar interaction [37], consistent with the longer ensemble dephasing time in reference [119] (we note that quantum dots studied in this work feature optical resonances at 904 nm, compared with 967 nm in our case).

With this understanding of the processes that dominate electron spin coherence,

in the next chapter we will move on to direct networking demonstrations between multiple self-assembled quantum dots.

CHAPTER

FOUR

ENTANGLEMENT OF DISTANT ELECTRON SPINS

The qualifying feature of a quantum network is the ability to distribute and support entanglement between the constituent nodes [10]. This single capability provides the resource behind provably secure communication [3, 4] and‘ the teleportation of quantum states [188], in addition to linking locally interacting clusters in a networked quantum computing architecture [189, 190].

In general, quantifying the degree of entanglement between systems is a nontrivial process with many metrics to determine the ‘quantum-ness’ of the shared state, based on the entropy of the individual and combined systems or the separability of the state [191, 192]. For pairs of qubits, a simple limit is available: the four Bell states [193]. These states form a maximally entangled basis of the two qubit system, and accordingly their generation is of particularly interest for quantum networks.

Up till now in this dissertation, optical spin measurement has been an end point to unitary control processes, forming an average population measure through multiple sequence repetitions. Measurement, however is an active process, and if conducted in the right mode can project a system of multiple qubits into a highly entangled state [194]. Such a process requires careful tracking of coherences and optical dispersion between the two qubits up to the measurement apparatus. In addition, evaluating the effects of a projective measurement necessitates that we move from time-averaged

population measurements to multi-photon project and read coincidence events in the same sequence cycle, the scaling of which places taxing requirements on our detection efficiency.

This chapter covers how we realise a highly-entangled state between two non-interacting electron spins resident in separate quantum dots. We first discuss how a single-photon measurement can project optically-active spins into an entangled state. Following that, we experimentally asses the capability of electron spins confined to self-assembled quantum dots to meet the requirements of this technique. We then move on to project two spins into a nonlocal state and demonstrate how our projection method in particular provides control over the entangled state we generate.

This demonstration involved large amounts of equipment and time to setup and complete, and the participants must be credited for their hard work. Megan Stanley, Lukas Huthmacher, Dr. Claire Le Gall and Dr. Clemens Matthiesen were all integral to the development, construction and operation of this experiment.

4.1. Entanglement by single photon measurement

Systems can become entangled through direct interaction as a local '2-qubit gate' [195] or by entangling a stationary superposition with a travelling photon and mapping from the optical channel at another site [10, 16, 157]. An important alternative is entanglement distribution via projective measurement of one or two photons [189, 194, 196–198]. These methods all consider measuring single photons from multiple systems in such a way that the detection events collapse the non-interacting ground states into a particular entangled state. Rather than by direct mapping, which requires high levels of cooperativity between the the stationary qubits and single photons, these techniques take advantage of the high single-photon detection efficiencies available, and automatically provide an electrical herald for state creation. As a consequence entanglement-by-measurement techniques have attracted great ex-

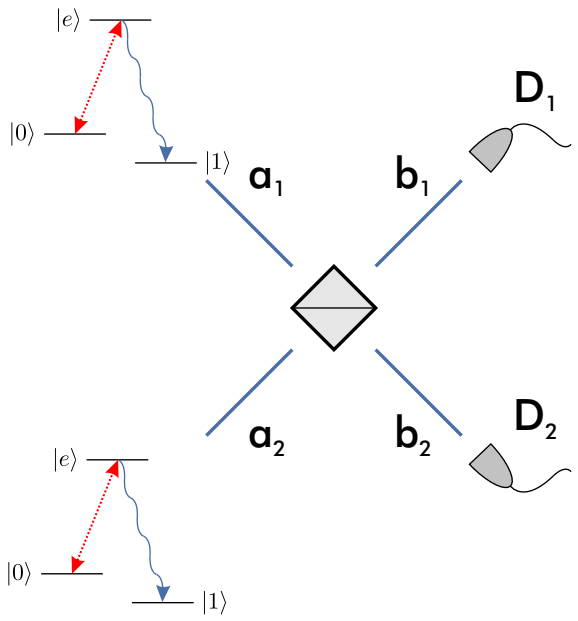

Figure 4.1.: **Entangling optical Λ-systems.** Two Λ-systems emit spin-flip Raman photons into modes $a_{1/2}$ which are mixed on a 50:50 beam-splitter into modes $b_{1/2}$ and passed to detectors $D_{1/2}$.

perimental attention, and have been used to realise entangled states of trapped ions [156, 199–201], neutral atoms [202], negatively charged NV centres [89, 203, 204] and more recently superconducting qubits [205] and single hole spins [142].

The method to entangle distant systems by measurement of a single photon was first investigated in a seminal paper from Cabrillo et al. [194], and is of particular interest to us due to the linear scaling of success rate with photon loss, albeit at the cost of requiring operation at a low generation probability. This is in comparison to other techniques, which generally require two-photon detection events to project the state and hence scale quadratically [206].

To understand the basic mechanism behind how a photon detection event can entangle two systems, we present a derivation that follows reference [207]. The necessary elements are displayed in figure 4.1. We consider two Λ-schemes, each consisting of ground states $|0\rangle$ & $|1\rangle$ and an excited state $|e\rangle$. The $|1\rangle \leftrightarrow |e\rangle$ transition in each couple to well-defined optical modes $a_{1/2}$, which are mixed on a 50:50 beam splitter. The two output modes $b_{1/2}$ can be detected by two single photon detectors,

$D_{1/2}$.

We begin with both systems prepared in the $|0\rangle$ state, and coherently transfer an amplitude $\sqrt{p}$ to $|e\rangle$, after which the state of each, $|\psi\rangle_i$, can be written as:

$$|\psi\rangle_i = \sqrt{1-p}\,|0\rangle_i + \sqrt{p}\,|e\rangle_i\,, \tag{4.1}$$

and the product state of the two systems, $|\Psi\rangle$:

$$|\Psi\rangle = |\psi\rangle_1 \otimes |\psi\rangle_2 = (1-p)\,|00\rangle + \sqrt{p\,(1-p)}\,(|0e\rangle + |e0\rangle) + p\,|ee\rangle\,. \tag{4.2}$$

The detection of a spin-flipping Raman photon is described by the jump operator $\mathcal{J}_i(\cdot) = \sigma_i^-(\cdot)\sigma_i^+$, where $\sigma_i^- = |1\rangle_i\langle e|_i$. The detectors D_i operate on the optical modes b_i. By mixing the paths from the two quantum dots on a 50-50 beam splitter, we can express the photon creation operators after the beam splitter, $\hat{b}_i^\dagger$ as coherent mixtures of operators in the two quantum dot modes, $\hat{a}_i^\dagger$:

$$\hat{b}_1^\dagger = \frac{1}{\sqrt{2}}\left(i\hat{a}_1^\dagger + \hat{a}_2^\dagger\right) \qquad \text{and} \qquad \hat{b}_2^\dagger = \frac{1}{\sqrt{2}}\left(\hat{a}_1^\dagger + i\hat{a}_2^\dagger\right). \tag{4.3}$$

Applying this transformation to the jump operator for detector D_1 results in:

$$\mathcal{J}_1(\cdot) = \frac{1}{2}\left(i\sigma_1^- + \sigma_2^-\right)(\cdot)\left(-i\sigma_1^+ + \sigma_2^+\right) \tag{4.4}$$

In this way the jump operator corresponding to a click on D_1 acts on the joint state of the two Λ-schemes leaving the pure conditional state $|\Psi_{D_1}\rangle$:

$$|\Psi_{D_1}\rangle = \frac{1}{\sqrt{2}}\left(i\sqrt{(1-p)}\,(|01\rangle + i\,|10\rangle) + \sqrt{p}\,(|e1\rangle + i\,|1e\rangle)\right). \tag{4.5}$$

We assume that the detectors are not capable of registering the double excitation events that occur with a probability p^2. These parts of the state which still contain population in $|e\rangle$ then decay incoherently to $|1\rangle$ and we recover the density matrix ρ_{D_1}:

$$\rho_{\mathrm{D}_1} = \frac{1}{2}\left[(1-p)\left(|01\rangle + i\,|10\rangle\right)\left(\langle 01| - i\,\langle 10|\right) + 2p\,|11\rangle\,\langle 11|\right] \tag{4.6}$$

This density matrix demonstrates that a single photon detection has projected the two systems into an entangled state, $\left(|01\rangle + i\,|10\rangle\right)/\sqrt{2}$, with a fidelity of $(1-p)$. For comparison, a click on the other detector D_2 would correspond to the state ρ_{D_2}:

$$\rho_{\mathrm{D}_2} = \frac{1}{2}\left[(1-p)\left(i\,|01\rangle + |10\rangle\right)\left(-i\,\langle 01| + \langle 10|\right) + 2p\,|11\rangle\,\langle 11|\right], \tag{4.7}$$

which differs from ρ_1 by a π phase shift owing to the difference between the beam splitter transformations.

This derivation covers the basic mechanism by which the detection of a single photon can herald the creation of an entangled state between two systems. In its simplicity, however it contains many implicit relationships that must be met. First, we have assumed complete mixing of the Raman photon modes a_1 and a_2 at the beam-splitter with a constant phase. This requires indistinguishability between the modes from the two emitters.

Assuming indistinguishable Raman photons, the detection then imprints the phase of the two modes onto the phase of the joint spin state. In general the state we recover is given by:

$$\rho_\phi = \frac{1}{2}\left[(1-p)\left(|01\rangle \pm e^{i\Delta\phi}\,|10\rangle\right)\left(\langle 01| \pm e^{-i\Delta\phi}\,\langle 10|\right) + 2p\,|11\rangle\,\langle 11|\right], \tag{4.8}$$

where the value of $\Delta\phi$ is set by the accumulated phase between the two inputs including both the Λ-scheme excitation and mode propagation to the beam-splitter, and the sign depends on the detector that registers the Raman photon.

In this way we require phase-coherent excitation and path-length stability between the systems on the level of an optical cycle. At the same time, in controlling the optical phase we gain an ability to project the two spins into a controllable entangled state.

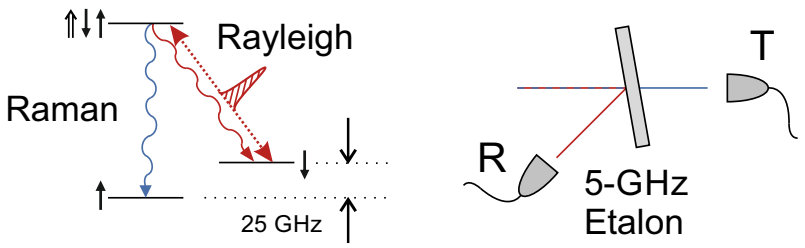

Figure 4.2.: **Λ-Scheme with transition resolving etalon** Only transitions with one excited state are considered. The pulse marks the excitation for our state projection. An angled Fabry-Pérot etalon transmits the Raman mode and reflects the Rayleigh scattering.

4.2. Spin-photon interface

In this section we discuss the most basic requirement our experiment needs to fulfil: the ability to optically project and recover a spin state from the quantum dot. This process is enabled by the spin-photon interface sketched in figure 4.2. A 4-T magnetic field perpendicular to the quantum dot growth axis provides four spectrally-resolvable transitions. For the following discussion we can restrict ourselves to two that form a Λ-scheme with the split ground state spin and a single excited state. The two equal-strength transitions are separated by the 25-GHz ground state spin-splitting and have orthogonal, linear polarisation. When the quantum dot is excited, it can decay along either optical path with equal probability, entangling the spin state with the optical frequency and polarisation of the emitted photon [43–45].

For all of these state-projecting experiments, we consider exciting the quantum dot with the low-frequency transition, as shown by the pulse in figure 4.2. The lower-frequency photons (red) from this pulse are the spin-conserving Rayleigh scattering, and higher-frequency (blue) the spin-flipping Raman scattering.

The equal strength of the Rayleigh and Raman scattering requires that we separate out the two branches to project the spin state. We detect quantum dot fluorescence in a single circularly-polarised mode, erasing any polarisation information. Using a free-space Fabry-Pérot etalon with a 5-GHz transmission window (Manx Optics) we can spectrally distinguish the two components, as shown in the right of figure 4.2. The higher-frequency Raman photons are transmitted through the etalon to

the 'T' detector, while the lower-frequency Rayleigh photons (and any remaining background laser scatter) are reflected to the 'R' detector. In this way, after a short pulse on the low-frequency transition, a click on the T detector should project the spin into the $|\uparrow\rangle$ state.

4.2.1. Control sequence

We test our ability to project and retrieve the state of the electron spin from this Λ-scheme using a four stage pulse sequence (the bracketed duration labels the length of the optical input):

I. **Preparation (20 ns)** We drive the high-frequency transition to prepare the electron in $|\downarrow\rangle$. We can achieve this with a fidelity of $\sim$97%.

II. **Projection (160 ps)** We pulse the low-frequency transition. We look for a Raman photon through the etalon to project the spin to $|\uparrow\rangle$.

III. **Rotation (2+40+2 ps)** We coherently rotate the spin. This allows us to probe different state populations with the same readout pulse. We use a composite pair of rotation pulses separated by a period of free precession (see section 4.2.2).

IV. **Readout (7 ns)** We drive the high-frequency transition again. Fluorescence on any detector during this pulse corresponds to population in $|\uparrow\rangle$. The angle of rotation before determines whether this measure maps to $|\uparrow\rangle$, $|\downarrow\rangle$ or a coherent combination of the two.

This pulse sequence forms the basis for all the measurements presented in this chapter. The sequence is played by an Arbitrary Waveform Generator (AWG Tektronix 70002A), and converted to optical pulses with high-frequency waveguide electro-optic modulators. The coherent rotation pulses are picked using a 350-MHz AA Opto-Electronic acousto-optic modulator (AOM), switched by electrical pulses

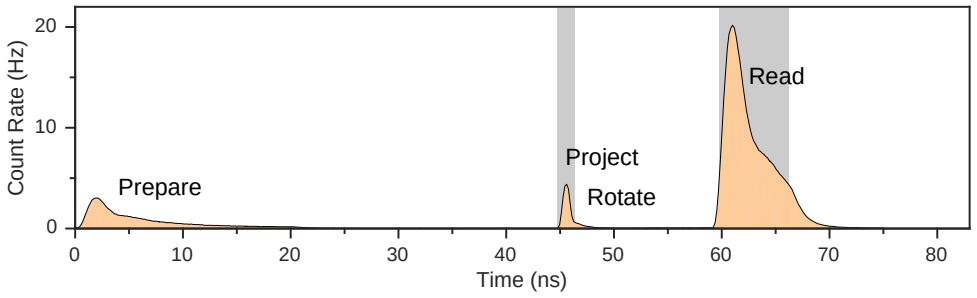

Figure 4.3.: **Quantum-dot pulse-sequence fluorescence** Time-correlated fluorescence from a single quantum dot during the project and read sequence. The prepare, project and read pulses all result in fluorescence, while the spin-rotation pulse generates no excited state population and is not visible here. The grey rectangles mark the regions of interest for registering fluorescence from the QD.

from a DG645 Digital Delay Generator, triggered by the AWG. The readout, preparation and state projection pulses are formed by waveguide electro-optic modulators, as in previous chapters. As for the coherent spin control experiments, the whole pulse sequence is locked to the repetition frequency of the modelocked spin rotation laser. Finally, a clock signal every 364 pulse repetitions (∼210 kHz) provides a reference for a time-to-digital converter. More details can be found in appendix A.

The quantum dot fluorescence during the control sequence correlated with the sequence clock is displayed in figure 4.3, with the positions of the four stages marked. The low amplitude exponential decay at zero-time is the spin preparation which pumps the population remaining after the previous sequence for the next repetition. Fluorescence from the 160-ps state-projection pulse at 46 ns is lifetime-limited. The spin-rotation arrives 1.1 ns after the short pulse. This delay is set such that sensitive coherences are mapped into robust population before the spin state has dephased. The decaying exponential signal fourteen nanoseconds later is the spin readout pulse. We use a power at the saturation intensity to maximise signal while limiting laser background and off-resonant driving of the other transitions. This produces an average of 1.6 photons for a spin-up state.

The two detection regions for spin projection and readout are marked as the grey

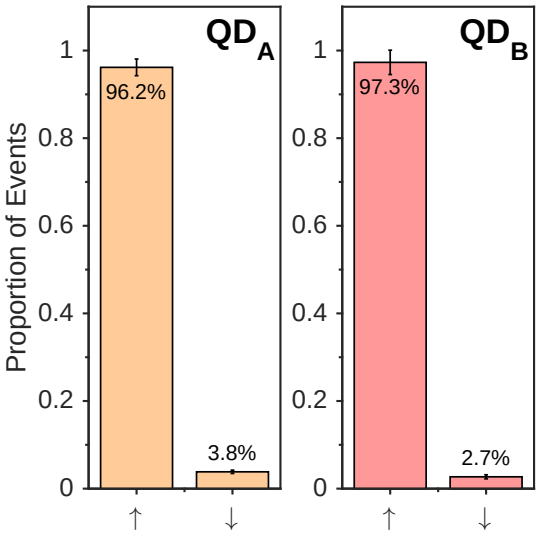

Figure 4.4.: **Raman-photon spin heralding** Two-photon coincidence events distributed according to the measured spin basis for the quantum dots studied in this chapter (QD_1 & QD_2). The error bars show one standard deviation in the state population due to the poissonian statistics of the coincidence events.

rectangles in figure 4.3. We only consider spin readout from sequence repetitions that contained a Raman detection event in the 1.2-ns wide state-projection window. We can then reconstruct the conditional spin state by observing the distribution of 2-photon project-and-read coincidences over the two spin basis states, which we cycle through by setting the angle spin-rotation to 0 or π on alternate repetitions and probing the final spin-up population.

4.2.2. Single spin recovery.

Figure 4.4 shows the distribution of two-photon coincidences recorded with this sequence for the two quantum dots we aim to entangle (QD_1 and QD_2). These two histograms show that, conditioned on a Raman photon, we recover spin up with a fidelity of 96.1±1.9% for QD_1 and 97.3±2.7% for QD_2. The errors are drawn from the statistical uncertainty of 2657 and 1260 two-photon events.

This recorded fidelity is a comprehensive measure of the filtering provided by the etalon, the fidelity of the spin rotations and the suppression of laser scattering

during the read pulse, all of which would diminish this figure. At the same time, it is worth noting that conditioning on a Raman photon in this way provides no information on the fidelity of the initial state preparation, nor is this measurement sensitive to unintentional spin pumping between state rotation and readout. The former is checked in the two quantum dot measurement we present later, while the latter simply reduces the number of coincidences by a very small fraction ($\sim$1%), and has no effect on the recovered state.

One novel feature of these measurements is the use of composite spin rotations [129, 208]. As discussed in section 1.8.4, Larmor precession during the optical rotation pulse tilts the spin rotation axis away from the equator, preventing a complete state inversion. The rotation errors are sufficiently small for coherent control measurements but too large to perform the high-fidelity tomography required for spin state reconstruction. On an equivalent measurement to figure 4.4 with single π-rotation pulses, we record a maximum fidelity of 90-92%. The compound rotations consist of a pair of pulses separated by a single Larmor precession period (39.5 ps). The pulse amplitudes are set close to $\pi/2$ rotations, corresponding to the best approximation to a π rotation.

The ability to optically project and retrieve a single spin is central to the entanglement scheme described above, and the high fidelity of these measurements form a strong foundation that allows us to focus on the more subtle aspects of distributing entanglement between two spins.

4.3. Forming a network

With the spin-photon interface confirmed for individual quantum dots, we construct a model network and attempt to distribute entanglement between their confined spin-states.

As discussed, projecting a particular entangled state requires the mixing of the beam splitter input modes with a well-defined phase. A prerequisite for this con-

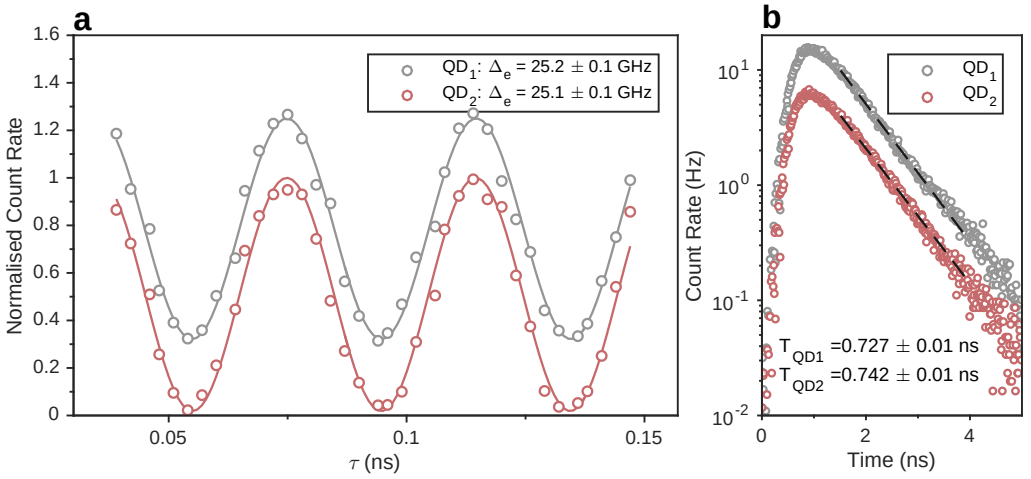

Figure 4.5.: **Matched quantum dot energetics. a** Ramsey interference measurements. The measurements were taken simultaneously under the exact conditions of the entanglement sequence, important for guaranteeing the absence of extra nuclear polarisation that would alter the spin splitting (section 4.6.1). The signal from QD_1 is offset for clarity. **b** Raman photon lifetime measurements extracted from the state-projection pulse. The signal from QD_1 is again offset for clarity. The dashed curves are single exponential fits.

dition is indistinguishability between the Raman photon modes from two quantum dots [209]. To achieve this we choose two quantum dots with overlapping charge-stability plateaus by scanning the sample positions and taking Photoluminescence spectra, and electrically shift their transition frequencies to a common resonance at 967.9 nm. With the correct magnetic fields applied to both (4 T to QD_1, 3.85 T to QD_2), the quantum dots present a spin splitting around 25.15 GHz. We confirm this through Ramsey interferometry measurements shown in figure 4.5a. As one would expect, nuclear-bath polarisation needs to be taken into account (more details are provided in section 4.6.1). Matching the spin splitting overlaps the central frequency of the Raman modes such that the optical phase is stationary [210, 211]. It also ensures that we generate a static entangled state.

Lifetime measurements of the Raman scattering from the two dots, as presented in figure 4.5b confirm complete overlap of the intrinsic spectral properties, with measured exponential excited-state decay times of 0.727 ± 0.01 ns (0.742 ± 0.01 ns) for QD_1 (QD_2). Stringent measures of Raman photon indistinguishability will be

presented in section 4.3.2.

The full setup containing all the necessary components to project and measure an entangled state is displayed in figure 4.6. The two identical quantum dots are housed in separate cryostats in the arms of a large fibre-based Mach-Zehnder interferometer. This architecture provides the required phase relationship between the Raman modes at the input of the second beam splitter. The entanglement pulse is common to the two quantum dots, split at the first beam splitter. In this way the combined phase of the optical excitations and paths from emitters to beam splitter can be controlled. To avoid path length drifts, the setup contains an optical phase reference: a detuned, non-interacting beam at 955 nm that is poorly suppressed by the crossed polarisers in the two microscopes. The laser scatter is split-off after the interferometer at two holographic diffraction gratings to provide a phase-dependent feedback signal. More details of this active phase protection this enables are discussed in section 4.3.1. The gratings also ensure that poorly suppressed spin-rotation pulses and the phonon sideband from each QD will not contribute to our measured coincidences.

The setup contains the additional optical inputs necessary to prepare, rotate and read the two spins. The readout and preparation pulses are added to each arm, with an 8-ns time delay to allow each spin to be read individually. The spin-rotation pulses are added at each microscope. At the outputs of the interferometer four superconducting nanowire single photon detectors (Quantum Opus Opus-One) cover the low ($R_{1/2}$) and high ($T_{1/2}$) frequency transitions, as well as two Avalanche Photodiodes (Excelitas SPCM-AQRH) for the detuned phase reference ($S_{1/2}$).

4.3.1. Interferometer delay

Controlling the propagation time delay between the two arms of the interferometer, Δt is essential for creating a well-defined nonlocal state between the two electron spins. Trivially, the case of $\Delta t = 0$ will always ensure projection into a well-defined state, however the state depends on the interferometer delay on the timescale of a single optical cycle. Setting and controlling the delay of an $\approx$ 10-m fibre-based

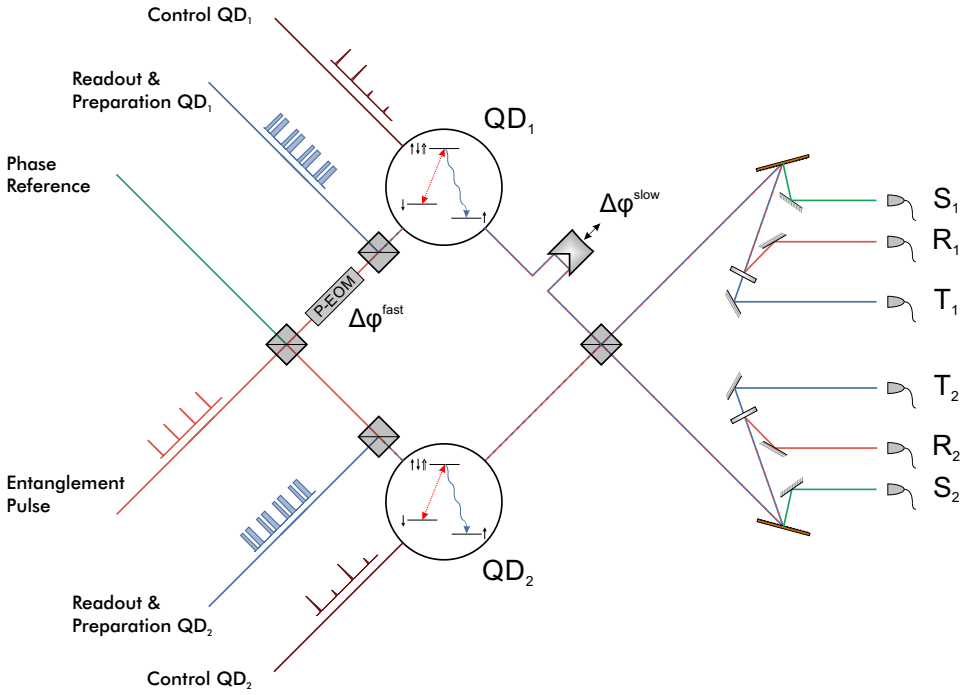

Figure 4.6.: **Entanglement setup** Each quantum dot sits in an arm of a large fibre-based Mach-Zehnder interferometer. Shown are all the required optical inputs and their pulse sequences for preparing, entangling and measuring the two spins. The outputs of the interferometer are spectrally separated into six single-photon detectors. Also shown is the detuned phase reference laser, which is used to provide a feedback signal to a piezo-mounted retroreflector ($\Delta\phi^{\text{slow}}$) and a phase-EOM (P-EOM, $\Delta\phi^{\text{fast}}$).

interferometer to this level is a continuous, involved process. By counting fringes we measure an interferometer-delay drift of 0.4 ps (150 fringes) on a timescale of 20 minutes. This is principally due to refractive index change and thermal expansion from sub-degree temperature cycles in the lab [212].

We monitor path length change with the interference of the stabiliser beam (green in figure 4.6), blue detuned from the optical resonances by 11 nm and detected by S_1 and S_2. The signal difference is passed to two PID controllers to control the position of a retroreflector on a piezo stack for slow, thermal drifts (< 10 Hz, $\Delta\phi^{\text{slow}}$ in figure 4.6), and the offset of a fibre-coupled phase-EOM for audio frequency noise (10-1500 Hz, $\Delta\phi^{\text{fast}}$ in figure 4.6). Locking the fringes to the midpoint (zero difference between the outputs) provides a linear error signal and limits the sensitivity to amplitude

changes in the two arms of the interferometer. This way the phase drift of the interferometer can be constrained to $< \pi/30$ for the duration of an experimental run.

Short-term change in the delay of the interferometer can be prevented to a very precise level. At the same time there are larger values within which we need to determine and set Δt. In particular, there are four key timescales over which a non-zero delay affects the operation of the experiment:

700 ps The quantum dot optical lifetime. Δt needed to be much less than this to ensure complete overlap of the Raman photons and interference between the two quantum dots.

40 ps The spin precession time. Delay changes on this timescale control the relationship between the spin state projection and the relative phase of the two arms at the excitation resonance frequency.

290 fs Set by the frequency difference of the stabiliser and the quantum dot resonances. The interferometer delay needs to be changed on this timescale to control the phase of the quantum dot scattering while stabilising at the midpoint of the phase reference signal

3 fs The optical cycle. This sets the phase of the interference, and therefore the spin state. Changes on this scale are effectively controlled against by the active feedback.

During the running of the experiment, Δt is kept constant to within 60 attoseconds by the active feedback. The relative phase of the stabiliser and the quantum dot fluorescence can be adjusted by stepping the offset voltage on the stabilising piezo-stack to alter the path length by $\sim$30 μm and the delay by $\sim$0.2 ps. The large frequency difference of these two tones ($>$ 3,000 GHz) ensures that this presents only a small correction to the delay relative to the larger timescales.

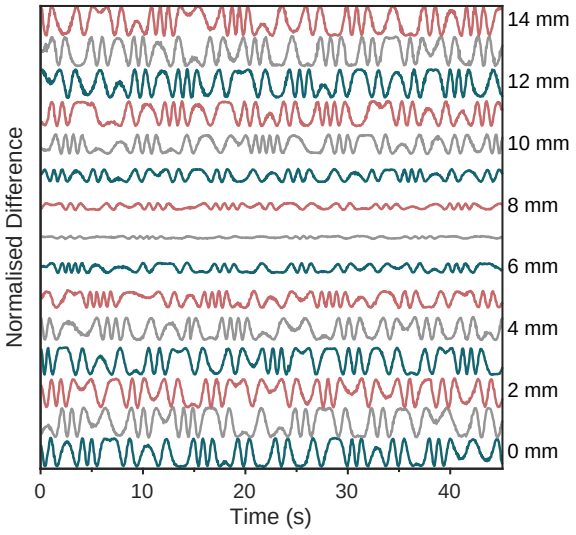

Figure 4.7.: **Interferometer-delay measurement traces** Normalised difference signal between the interference at two frequencies separated by 25 GHz for different positions of an offset stage. The interferometer delay modulo 40-ps can be extracted from the amplitude of the difference.

The interferometer delay can be measured by controllably allowing excitation photons to leak through the system to record a sizeable signal on the single-photon detectors. Sending through a 160-ps long optical pulse allows us to find and correct for the relative delay down to the time-jitter of the combined detector-TDC system, which provides $\sim$ 200 ps resolution. Controlling Δt to within this value provides large overlap between the Raman photons from the two quantum dots and good interference visibility. Nevertheless we need to establish this value to well within the 40-ps spin precession time, beyond the time resolution of the single-photon detectors.

The full detection setup provides us with methods to accurately determine the relative delay between the two interferometer arms. The free space etalons we use to split fluorescence from the two branches of the quantum dot lambda-system allow us to simultaneously monitor the interference of multiple frequencies. At $\Delta t = 0$ all frequencies will interfere with the same phase, but as the delay reaches the single-ps level, tones separated by > 1 GHz will beat with a measurable phase difference. Figure 4.7 shows the normalised difference between time-traces of interference fringes

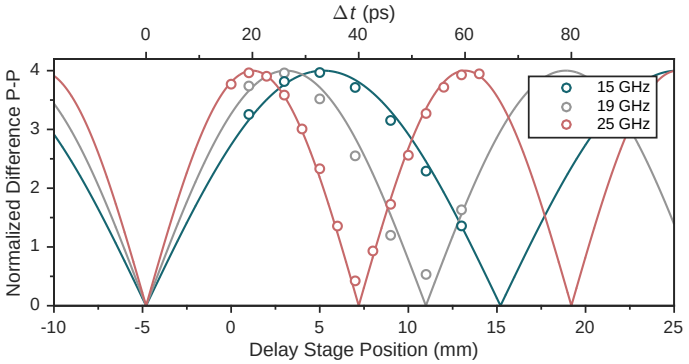

Figure 4.8.: **Reconstructed interferometer delay** Difference signal peak-to-peak values plotted against the stage offset for multiple frequency splittings. The curves are the expected signal-difference. The top axis marks the determined interferometer delay.

recorded for two beams at the Rayleigh (309703 GHz) and Raman (309728 GHz) frequencies. The curves are offset according to the position of a additional manual delay stage in one arm of the interferometer. The piezo stack we use to compensate for slow drifts is modulated with a triangle wave at 0.2 Hz to ensure that we evenly sample over the fringes. As the delay-offset is changed through 7 mm the two tones interfere with equal phase and the difference signal vanishes.

The phase difference between 25-GHz separated tones will only provide a measurement of Δt modulo 40 ps, and so we sweep the low-frequency signal and repeat the measurement for frequency pairs separated by 19 & 15 GHz. The extracted peak-to-peak values of the normalised difference for these three pairs are shown in figure 4.8. The combined measurements along with the 200-ps scale course estimation provide a unique determination of the interferometer delay with an accuracy up to the short-term thermal drift. As can be seen, a delay stage position of -4.8 mm provides a zero-delay interferometer.

4.3.2. Raman photon statistics

In section 4.2.2 we confirmed our ability to project a spin state at each quantum dot through detection of a spin-flipping Raman photon. In this section we use the statistics of Raman scattering events to determine the properties that will enable

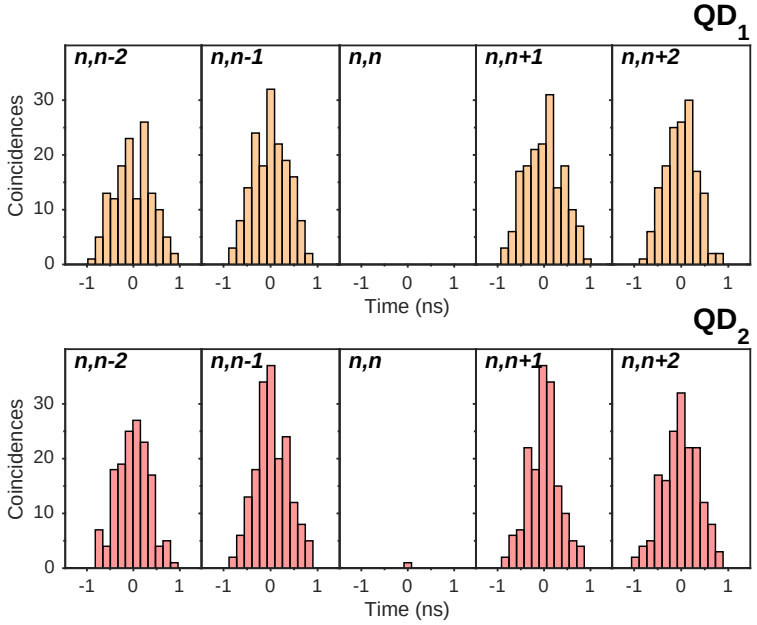

Figure 4.9.: **Raman photon intensity autocorrelation** The text marks the pulse sequence repetitions that contribute to the autocorrelation, where n is a free parameter. Each measurement lasts for three minutes.

entanglement distribution between the two systems.

The intensity autocorrelation, or $g^{(2)}$ function of the Raman scattering from each QD can be reconstructed by blocking an interferometer arm and running the pulse sequence described in section 4.2.1. The function is found from two-photon coincidences between Raman scattering events during the projection pulse. Figure 4.9 shows the distribution of these coincidences for the two identical quantum dots. The text in each panel marks the pulse sequence repetitions that the two photon event occurred in, where n is a free parameter. For both quantum dots, no two-photon events were recorded in the same sequence repetition, save for one count in the QD_2 measurement.

From our background count rate of ~ 10 Hz in the detection window, we expect to find one background coincidence for every 150 Raman photon coincidences, consistent with the single event at zero-delay in these two measurements. The absence of other coincidences in the central peak demonstrates how Raman scattering provides a mechanism for an ultra-high purity stream of single photons: the process is

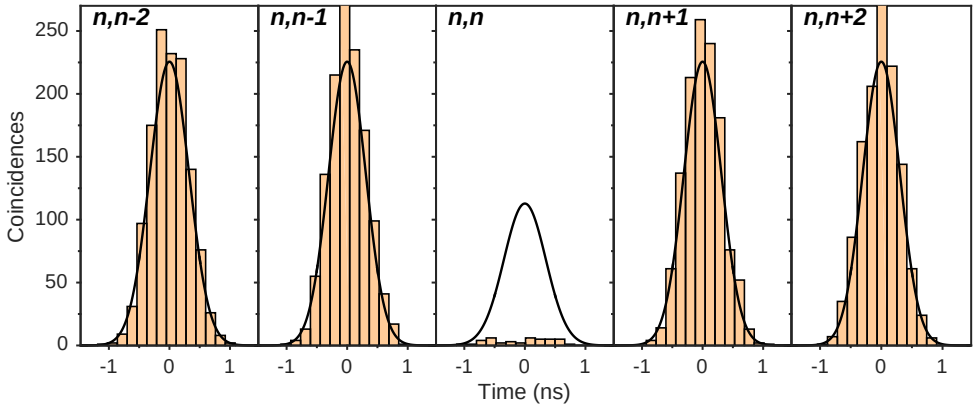

Figure 4.10.: **Hong-Ou-Mandel interference of Raman photons** As for figure 4.9 the inset text marks the sequence repetitions. The curves are Gaussian fits to the average satellite-peak. The central curve is half-amplitude, as expected for distinguishable photons.

self-limiting on the timescale of the ground state relaxation (up to milliseconds [96]), rather than the optical lifetime (sub-nanosecond) - the case for a two level system [213].

Having confirmed the single-photon nature of Raman scattering, the next issue to address is the extent to which photons from the two quantum dots share a common mode. This is required for the erasure discussed in section 4.1, and therefore crucial for distributing a quantum state. Quantum statistics provide a stringent method to access this quantity, as if two indistinguishable photons interfere, the symmetry of the possible output states causes them to bunch at one output [214]. This results in a dip in the rate of coincidences between opposite output ports within the coherence time of the two photons [215], an effect known as Hong-Ou-Mandel (HOM) interference. The amount of bunching is then directly related to the mode-overlap between the two inputs.

Figure 4.10 shows two-photon coincidences between the Raman-mode output ports T_1 & T_2 within the state-projection region of interest when the pulse sequence is run for both QDs simultaneously. As for the $g^{(2)}$ measurements, a pronounced loss of coincidences occur with the same sequence repetition. For distinguishable photons,

one would expect the central peak to contain half the area of the satellite peaks [139]: the satellite peaks can contain coincidences from the two dots in the combinations 1&2, 2&1, 1&1 and 2&2 while the single photon nature of the Raman scattering only allows coincidences of the form 1&2 and 2&1 within the same sequence repetition.

The suppression of this rate from half-height is due to photons bunching at the beam splitter. The indistinguishability of the photons is measured by the visibility of this reduction, extracted from the coincidence event distribution via:

$$V = 1 - \frac{2\Sigma g^{(2)}_{n=m}}{\Sigma g^{(2)}_{n\neq m}}, \tag{4.9}$$

where $\Sigma g^{(2)}_{n=m}$ are the number of counts in the central region, and $\Sigma g^{(2)}_{n\neq m}$ the average number of coincidences in the satellite peaks. We recover a value of V = 93.31 $\pm$ 1% over our 1.1-nanosecond state projection window.

This figure requires some context. In recording photon indistinguishability from a quantum dot, usually with the neutral exciton, a series of pulses are delayed and the fluorescence pattern is interfered with a time-lagged copy of itself via an asymmetrical Mach-Zehnder interferometer [216–219]. The optical delays here, realistically restricted to the sub μs regime are such that noise correlated on a longer timescale is not represented in the recorded visibility. Values as high as 99% have been recorded, however they neglect slow, environmental noise [82, 87], which would limit this figure. By interfering two independent sources, the figure recorded encapsulates these slow noise processes [139, 220] and yet a high degree of indistinguishability is still present.

An unavoidable limit to the indistinguishability of Raman scattering is the the ground-state coherence, T_2^* [140, 221, 222]. For confined electrons, the excited state lifetime takes up a non-negligible fraction of this value (0.7 ns compared to 1.9 ns). In any case the dephasing spin state requires that we only consider a window with a significantly smaller width than the dephasing time, filtering these processes. The window is set such that $\sim$60% of the emission is accepted. For comparison, if we

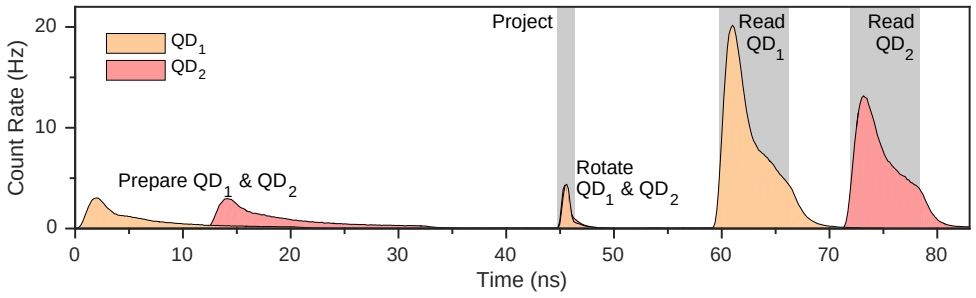

Figure 4.11.: **Entanglement pulse-sequence fluorescence** The sequence is identical for the two QDs, except for delayed readout for the QD_2. The rectangles mark the regions of interest for finding three-photon coincidences.

increase our window to 1.5 ns, we record a visibility of 91%. The high visibility we have presented here is a critically important result, as it bounds the available fidelity with which we can generate an entangled spin state.

4.4. State reconstruction

The measurements we have presented so far demonstrate that Raman scattering from the two quantum dots provides spin-state projection within a well-defined optical mode, suggesting its capability to distribute entanglement between the ground state spins. In this section, we discuss the projection and reconstruction of the joint spin state establishing the non-classicality of the state via spin-spin correlations.

4.4.1. Joint spin-state population

The first step towards full state reconstruction is to find the joint spin population conditioned on a single Raman photon detection. The pulse sequence for the two-spin system is identical to the scheme presented in section 4.2.2 with a delay in the QD_2 read and preparation pulses to distinguish the two spin readouts in time. Fluorescence emerging from the sequences for the two QDs are superimposed in figure 4.11. The spin state is reconstructed from three photon events in the three regions of interest marked in the figure (grey rectangles): the entanglement pulse

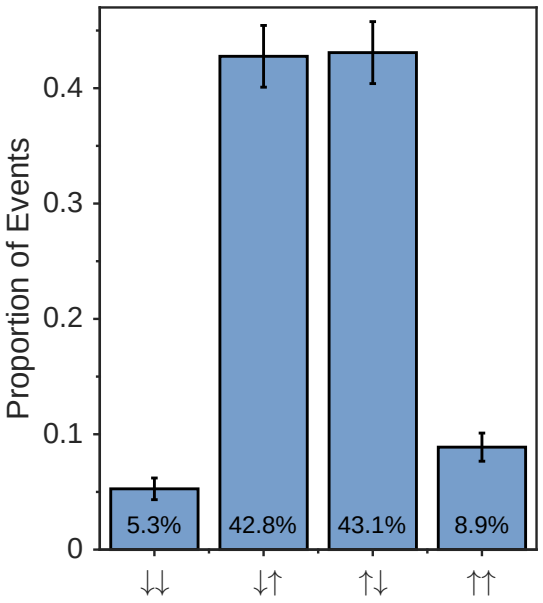

Figure 4.12.: **Joint spin-state population** 603 three-photon coincidences sorted according to basis state. Error bars show the uncertainty in the height of each bar, according to the number of contributing events.

common to both QDs, and the two spin readouts. The measurement cycles through the four basis states with independent spin rotations to cover $\{|\downarrow\downarrow\rangle, |\downarrow\uparrow\rangle, |\uparrow\downarrow\rangle, |\uparrow\uparrow\rangle\}$ in 367 ns before repeating.

To avoid events where both electrons change their spin state, which limits the available fidelity of the Bell-state, the spin flip probability is kept small for the two dots, at 5.0% (7.1%) for QD_1 (QD_2). The probabilities differ to compensate for different collection efficiencies in the two samples and match the Raman photon rates at the detectors. This results in an state projection rate of $\approx$ 7.3 kHz when attempting at 10.9 MHz, corresponding to a 0.07% success probability. The full three-photon project-and-read coincidence rate is then $\sim$ 100 mHz, taking into account the fact that two of the measurement bases should ideally produce very few three-fold coincidences.

Figure 4.12 contains the distribution of three-photon coincidences over the four two-spin basis states. The proportions of events show that, conditioned on a Raman

photon detection, we recover an antisymmetric spin population ($|\downarrow\uparrow\rangle$ or $|\uparrow\downarrow\rangle$) with a high probability. Taking into account the errors that emerge when reconstructing the state from 603 three photon coincidences, we find an overlap with a purely antisymmetric population of $85.8 \pm 3.8\%$. The even heights of the central bars are a consequence of the equal likelihood of detecting a Raman photon from each quantum dot.

Deviations from a perfect anti-symmetric state are present as the 14% of coincidences that occur in the $|\downarrow\downarrow\rangle$ and $|\uparrow\uparrow\rangle$ combinations. The origins of these events are well understood. Events in the $|\downarrow\downarrow\rangle$ measurement correspond to the imperfect spin heralding that was measured for each quantum dot individually in section 4.2.2. From equation 4.6 we expect the $|\uparrow\uparrow\rangle$ coincidence rate to follow the spin flip probability. This is indeed what we recover, with a slight correction owing to imperfect spin initialisation into $|\downarrow\downarrow\rangle$.

These measurements confirm that the Raman photon projection results in the desired anti-symmetric spin population: an effective test of our spin preparation and measurement setup. At the same time, measurements in other bases are needed to characterise the two-spin density matrix and confirm the presence of entanglement between the two spins.

4.4.2. Transverse spin measurements

Full reconstruction of the two-spin state would require 16 different measurements to determine the most-likely 4x4 density matrix [223]. At the same time, full tomography is not necessary to establish the presence of entanglement between the two spins, and as we will cover, deduce the Bell-state fidelity. The critical fact we need to determine is whether the population anticorrelations in figure 4.12 correspond to a statistical mixture or if indeed they reflect the populations of a well-defined entangled state. To achieve this we measure the transverse basis of the two-spin state, found through correlations between the spin projections on the equator of their respective Bloch spheres.

If we consider the pure, maximally entangled state $|\psi\rangle = 1/\sqrt{2}\left(|\uparrow\downarrow\rangle + e^{i\Delta\phi}|\downarrow\uparrow\rangle\right)$, its density matrix representation can be written in the $\{|\downarrow\downarrow\rangle, |\downarrow\uparrow\rangle, |\uparrow\downarrow\rangle, |\uparrow\uparrow\rangle\}$ basis as:

$$|\psi\rangle\langle\psi| = \frac{1}{2}\begin{pmatrix} 0 & 0 & 0 & 0 \\ 0 & 1 & e^{i\Delta\phi} & 0 \\ 0 & e^{-i\Delta\phi} & 1 & 0 \\ 0 & 0 & 0 & 0 \end{pmatrix} \tag{4.10}$$

To move to the transverse basis, we perform a $\pi/2$ rotation about the X axis on each spin, which corresponds to the transformation:

$$\begin{aligned} \hat{X}_{\pi/2}|\psi\rangle\langle\psi|\hat{X}^{\dagger}_{\pi/2} &= \frac{1}{8}\begin{pmatrix} 1 & -i & -i & -1 \\ -i & 1 & -1 & -i \\ -i & -1 & 1 & -i \\ -1 & -i & -i & 1 \end{pmatrix}\begin{pmatrix} 0 & 0 & 0 & 0 \\ 0 & 1 & e^{i\Delta\phi} & 0 \\ 0 & e^{-i\Delta\phi} & 1 & 0 \\ 0 & 0 & 0 & 0 \end{pmatrix}\begin{pmatrix} 1 & i & i & -1 \\ i & 1 & -1 & i \\ i & -1 & 1 & i \\ -1 & i & i & 1 \end{pmatrix} \\ &= \frac{1}{4}\begin{pmatrix} 1+\cos\Delta\phi & -\sin\Delta\phi & \sin\Delta\phi & 1+\cos\Delta\phi \\ -\sin\Delta\phi & 1-\cos\Delta\phi & \cos\Delta\phi - 1 & -\sin\Delta\phi \\ \sin\Delta\phi & \cos\Delta\phi - 1 & 1-\cos\Delta\phi & \sin\Delta\phi \\ 1+\cos\Delta\phi & -\sin\Delta\phi & \sin\Delta\phi & 1+\cos\Delta\phi \end{pmatrix}. \end{aligned} \tag{4.11}$$

The populations of the transformed state (highlighted in red) now follow the phase $\Delta\phi$ of the state, resulting in either correlated or anti-correlated spin populations if $\Delta\phi = 0$ or π.

Alternatively, if the spins are in a statistical mixture (ρ_{mix}), only the diagonal terms of the density matrix are non-zero (equivalent to a scrambling of the phase $\Delta\phi$) and after rotation all four populations exhibit an equal value of 1/4:

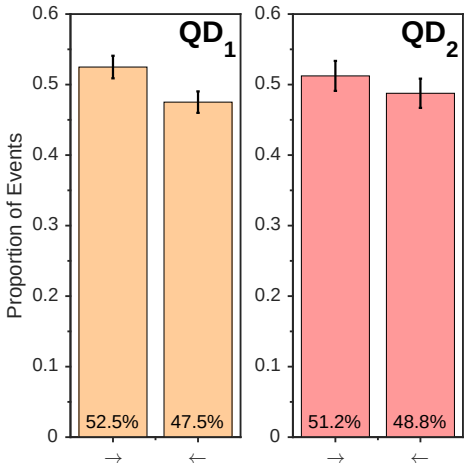

Figure 4.13.: **Single spin heralding in transverse basis** Measurement sequence identical to figure 4.4 with the rotation mapping $(0,\pi) \rightarrow (\pi/2, 3\pi/2)$.

$$\hat{X}_{\pi/2}\rho_{\mathrm{mix}}\hat{X}^{\dagger}_{\pi/2} = \frac{1}{8}\begin{pmatrix} 1 & -i & -i & -1 \\ -i & 1 & -1 & -i \\ -i & -1 & 1 & -i \\ -1 & -i & -i & 1 \end{pmatrix}\begin{pmatrix} 0 & 0 & 0 & 0 \\ 0 & 1 & 0 & 0 \\ 0 & 0 & 1 & 0 \\ 0 & 0 & 0 & 0 \end{pmatrix}\begin{pmatrix} 1 & i & i & -1 \\ i & 1 & -1 & i \\ i & -1 & 1 & i \\ -1 & i & i & 1 \end{pmatrix}$$
$$= \frac{1}{4}\begin{pmatrix} 1 & 0 & 0 & -1 \\ 0 & 1 & -1 & 0 \\ 0 & -1 & 1 & 0 \\ -1 & 0 & 0 & 1 \end{pmatrix} \tag{4.12}$$

The additional $\pi/2$ rotation is provided by mapping the state basis rotations (0, π) to ($\pi/2$, $3\pi/2$). With this additional rotation the states ($|\uparrow\rangle - i\,|\downarrow\rangle = |\rightarrow\rangle$, $|\uparrow\rangle + i\,|\downarrow\rangle = |\leftarrow\rangle$) are projected to ($|\uparrow\rangle$, $|\downarrow\rangle$). Figure 4.13 displays the distribution of coincidences for the same single quantum dot project and read sequence as in section 4.2.2 with the additional $\pi/2$ rotation. The matching coincidence rates show that this rotation effectively removes the spin-population information from our readout, and we measure the projection of the state $|\uparrow\rangle$ on the equator of the Bloch sphere.

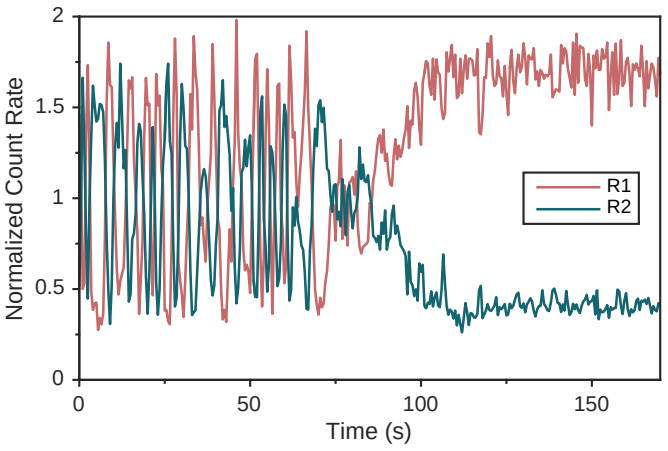

Figure 4.14.: **Stabilised Rayleigh photon interference** Extracted from time-averaged fluorescence within the state-projection window for 200-ms integration time. Interferometer stabilised at 75 s.

For these transverse measurements it is now essential that the phase of the interferometer is kept constant. The lower-frequency Rayleigh scattering during the projection pulse provides a measure of the interference at the quantum dot resonance. Figure 4.14 shows the interference of Rayleigh photons from the two quantum dots. For the first 75 s of the measurement the phase of the interferometer is left free-running, and the two outputs beat against one another as the interferometer path lengths drift. The incomplete visibility is due to high-frequency noise, incoherent scattering from the transitions, unequal Rayleigh photon rates from the two dots and the presence of background in the reflected channels from the projection pulse and spin rotation pulses. At 75 s the interferometer is stabilised and the scattering is predominantly directed towards output 1 (R_1), corresponding here to zero net phase accumulation in the interferometer. The stabiliser frequency is locked to a $\pi/2$ phase, with the difference provided by a sub-picosecond delay between the two arms.

Figure 4.15 shows the three-photon coincidences measured in the rotated basis. They are now sorted into two sets, depending on the output the state-projecting detection occurred in. These data are recorded for the interferometer phase set at either 0 or π, such that the Rayleigh scattering from the two dots is predominantly

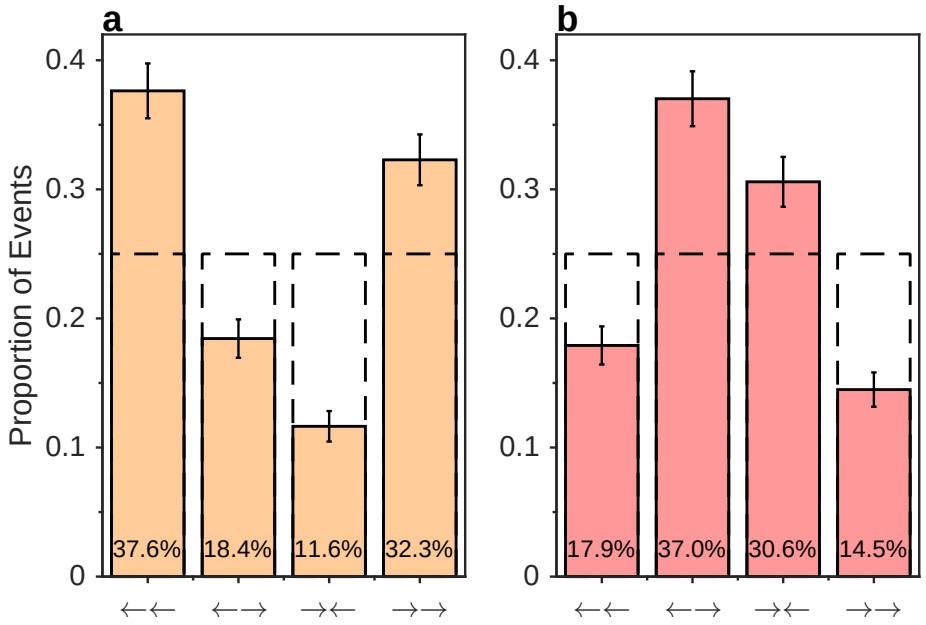

Figure 4.15.: **Transverse spin measurements** Three-photon coincidences for an interferometer phase of 0 or π, with a Raman detection event registered on the constructive (destructive) interference port in **a** (**b**). Dashed bars mark expected coincidences for classically correlated spins.

directed towards R_1 or R_2 respectively. The coincidence events are then sorted into whether the state-projecting Raman detection event occurred on the output that features constructive (4.15a) or destructive (4.15b) Rayleigh interference.

The two distributions reveal equal and opposite correlations in the spin populations. In the case of the constructive interference port the spins are now correlated with one-another, while the anti-correlation is preserved in the opposite port. As a guide to the eye, the figure includes the expected distribution if the two spins were only classically correlated (dashed lines). The recorded distribution in both cases show a clear deviation from this behaviour, establishing the non-classicality of the joint spin state. These measurements reveal a transverse visibility of 39.5±3.8% (-35.1±3.8%) for the two-spin state in figure 4.15a (4.15b).

The fidelity of a general two-spin density matrix with the Bell state $|\psi^{\pm}\rangle$ is $\langle\psi^{\pm}|\,\rho\,|\psi^{+}\rangle = 1/2(\rho_{22} + \rho_{33} \pm 2\Re(\rho_{23}))$. The two diagonal terms we can obtain from our initial measurement of the joint spin population, $\mathcal{F}_z$. For an arbitrary

density matrix, the visibility of the rotated population is $V_{\mathrm{Y}} = 2\Re(\rho_{23}) + 2\Re(\rho_{14})$. The density matrix, however is an average measure of the state we access and we can supplement our recovered values with knowledge of how the state evolves between projection and rotation. Specifically, the component $\rho_{14} = |{\downarrow\downarrow}\rangle\langle{\uparrow\uparrow}|$ evolves at twice our spin splitting, i.e. at ~ 50 GHz. The time-accuracy of our state retrieval is set by the difference between the single photon detection and the optical state rotation. The latter is stable to < 1 ps, however the former is limited by the jitter of our single-photon detection, which is constrained by the time-to-digital converter at ~ 120 ps. This ensures that $\Re(\rho_{14})$ is, on average, zero, and the visibility in our transverse basis measurement is directly set by the size of ρ_{23}, which evolves at the difference frequency between the two spins, controlled to be < 100 MHz.

Combining these two transverse basis measurements with the population measurement, we recover an average Bell-state state fidelity of $61.6 \pm 2.3\%$. This is 5.04 standard deviations above the 50% classical limit, clearly evidencing the entanglement in the two-spin state.

When we combine all the ways in which the state fidelity can be limited, we can understand the values we record. Double spin flips limit this state to 93% fidelity. Raman photon distinguishability measured in section 4.3.2 provides an additional factor of $1/2\,(1+V) = 0.95$. The joint state dephases at in a time of $T_2^*/\sqrt{2}$, where T_2^* is the dephasing time for a single spin. Integrating this Gaussian loss of coherence over our 1.1-ns collection window provides another factor of 0.87. We can also include our imperfect spin preparation and readout, each reducing our fidelity by a factor of 0.03 and 0.06 respectively. This predicts a fidelity of 70%. As we will describe in section 4.6.1, exactly predicting the spin splitting of the two dots is nontrivial due to nuclear polarisation, which will change to compensate electrical noise in the samples [110]. The entangled state will precess at the difference between the spin splittings. For a 150 MHz difference, a reasonable value that could be determined between each experimental run, an additional factor of 0.95 must be taken into account.

The optical path length is stable enough that we can neglect its contribution

to our imperfect fidelity. The phase response of the quantum dot transitions can drift due to sub-linewidth electrical noise in the two samples, however, which are mapped to the phase of the entangled spin-state. From the imperfect visibility of the Rayleigh scattering in figure 4.14, which, at 65% is 10% lower than the 75% limit owing to incoherent scattering, we estimate another factor of 0.95 in the state fidelity. This phase shift will be discussed further in section 4.6.2, where we cover how we select against large deviations in this value. Finally we note that many of the values we reference are figures taken in short calibration measurements. Finding enough three-photon coincidences requires integrating for multiple hours, over which time drifts can occur in the setup, limiting the interferometer visibility, background-free readout and the exact balance between the quantum dot rates. When one takes all of these factors into account, the relatively modest fidelity we record is easily understood.

4.5. Controllable entangled state generation

In using the a single photon to project an nonlocal spin state [194] we have direct access to the phase of the entangled state we generate via the interference of the Raman modes.

We demonstrate this capability in figure 4.16. This figure shows the extracted visibilities from transverse basis measurements for five different set-points of the entangled-state, which we find by examining the interference of Rayleigh scattering during the entanglement pulse. The visibilities are drawn from the relative coincidence rates displayed beneath. While the phase of the state follows the interferometer, the axis about which we perform tomography is fixed. In this way the different phases map into a coherently-changing visibility in the transverse measurement. We partition the coincidence events into the interferometer output that registered a Raman photon. For a zero-phase path-length difference, a detection on T_1 (T_2) projects the spins to $|\psi^+\rangle$ ($|\psi^-\rangle$), resulting in correlated (anti-correlated)

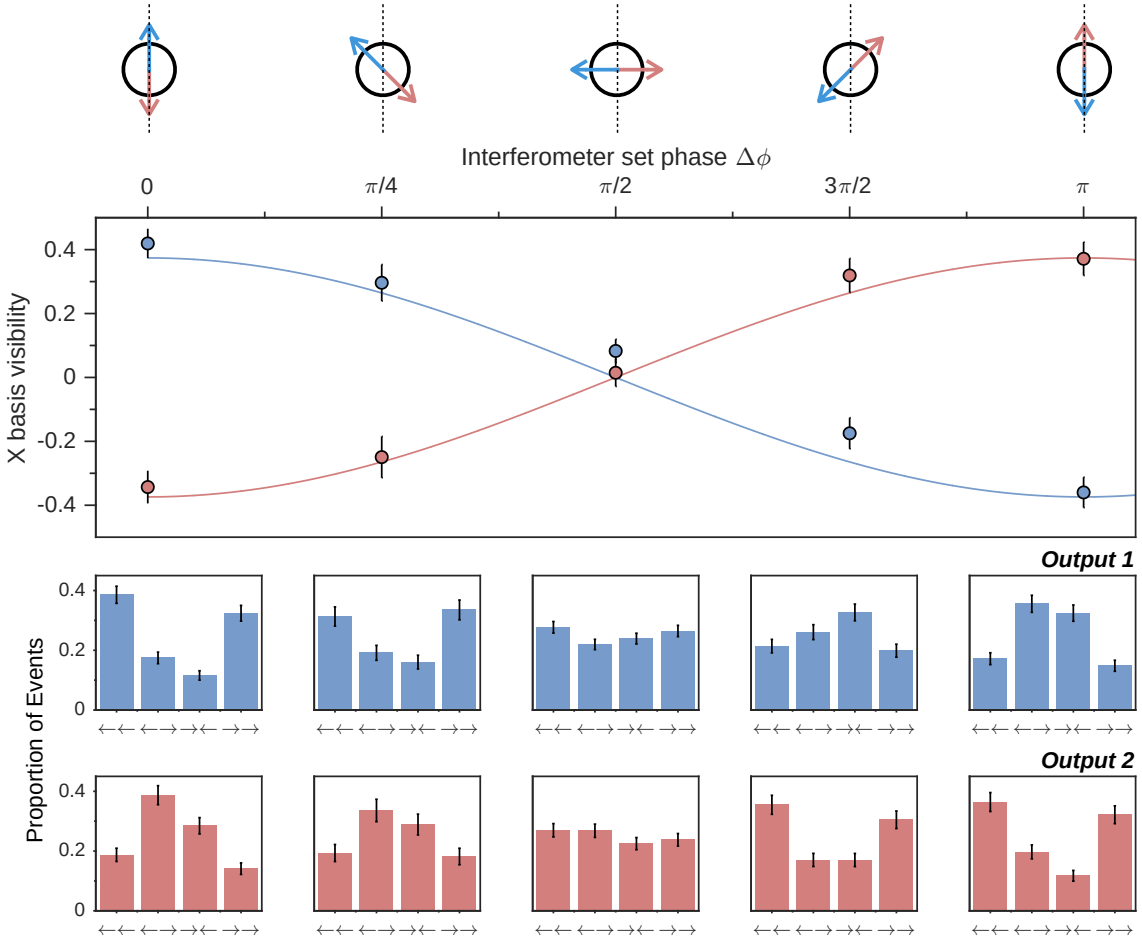

Figure 4.16.: **Controllable entangled state generation** Transverse basis visibilities for five interferometer set-points, drawn from the histograms at the base of the figure. Negative visibility corresponds to anticorrelated spins in the transverse basis. Curves are sinusoidal guides to the eye.

population in the transverse measurement. As we move to $\pi/2$ phase the conditional states are $\frac{1}{\sqrt{2}}(|\psi^+\rangle \pm |\psi^-\rangle)$ ($\Delta\phi = \pi/2$). Consequently these state exhibit no visibility, which our measurements confirm. At π-phase the role of the detectors is swapped, T_1 (T_2) projects $|\psi^-\rangle$ ($|\psi^+\rangle$) and the visibility along our measurement axis returns. The schematics above figure 4.16 sketch how the different spin states map onto the fixed angle we use to perform tomography. As the points project equally onto the measurement axis ($\delta\phi = \pi/2$), they show no visibility.

While any Bell state can be mapped to any other through a local $\hat{X}_\pi$ or $\hat{Z}_\pi$ rotation at one of the qubits, this demonstrates control over the entangled state at the point of generation. This is the core process of the experiment, in that through quantum erasure we map an optical phase onto the phase of a nonlocal spin state.

4.6. Experimental details

In projecting and recovering a well-defined entangled state between the two quantum dot spins, some particular features of both self-assembled quantum dots in general and the two QDs used in particular need to be taken into account. They are detailed here.

4.6.1. Dynamic nuclear spin polarisation

As with any experiment involving resonant optical interactions with a quantum dot under magnetic field, dynamic nuclear spin polarisation needs to be considered. Both quantum dots are resonant with the state-projection pulse over a small range of bias voltages, although through this range the spin splitting can change by over half a gigahertz as the nuclear bath becomes polarised to compensate the detuned readout and preparation pulse. If the splittings of the quantum dots differ the projected entangled state is non-stationary and evolves at the difference frequency. To control against this, we perform Ramsey interferometry on the two spins between each 20-minute measurement, and compensate for any difference with sub-millivolt

bias corrections. QD_2 in particular features an electrical environment that evolves on a millihertz timescale, large enough to bring the projection pulse off resonance, requiring a new gate voltage and spin-splitting measurement each time the resonance is lost.

4.6.2. Data filtering

Finding three-photon coincidences that correspond to successful spin state measurement from many hours of data-acquisition is a nontrivial task, and deserves to be discussed. The experiment produces single photon rates of 200 kHz, along with the 200 kHz clock. Each of these points are time-tagged with a 64 bit number, such that we generate an average data rate of 190 MB min^{-1}, from which we have to extract the 18 bits of data that represent which detector projected the state and the basis the $\approx$6 three-photon coincidences correspond to. First, the raw timestamps are correlated with the experiment clock, and a decision is made whether they sit in the regions of interest. The timing of the filtered events can then be compared to find the rare three-photon coincidences that occur within a single repetition. The work was the principle responsibility of Lukas Huthmacher, and the successful, efficient filtering of these significant data quantities is down to his expertise and persistence in optimising the operation of the code to compress and sort through the data.

In addition to the rare coincidences, the single-photon streams from the measurement continuously provide information on the condition of the two QDs. This then permits some low-level data filtering on the collected coincidences. The very low frequency noise QD_2 experiences causes it to fall off resonance on around a half-hour timescale. This can be seen as a drop in the average state projection rates from the two cryostats. Controlling against such an effect requires that we restart the experiment every 20 minutes with a reset gate voltage, but we additionally set a lower-threshold for the state-projection rate of 7 kHz to reject times when QD_2 had lost resonance. Similarly, for the transverse-basis measurement, we place a limit on the phase of the Rayleigh photons we record from the count rates on R_1 and

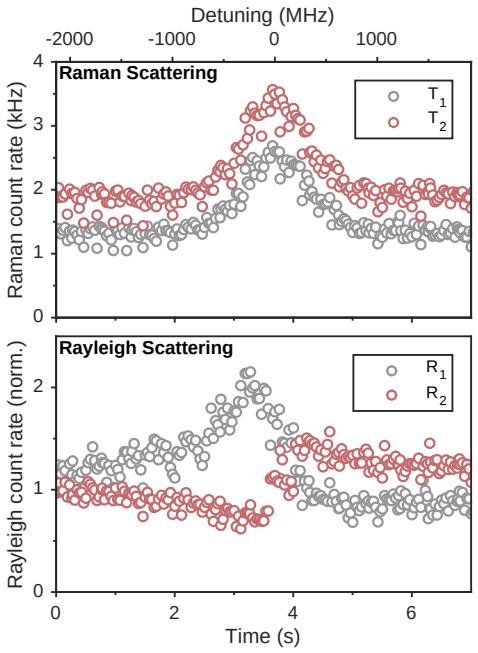

Figure 4.17.: **Detuned-quantum dot interference** Rayleigh and Raman scattering rates within the state-projection window for a controlled detuning introduced to QD_1 (top axis).

R_2 during entanglement pulse. Fluctuations in this phase are principally due to smaller-amplitude noise in the QD_2 environment. A generous bound of $\pm$ 20° avoids smaller resonance shifts which are resolvable in the phase rather than the amplitude of the count rates. We note that this filtering is only sensitive to fluctuations slower than the 1-second integration time we require to accurately determine the Rayleigh-scattering rates in the two outputs. This still leaves the state vulnerable to high-frequency phase shifts.

In figure 4.17 we show the effect of drive detuning on interference between the two quantum dots. We run the entanglement sequence and count the average photon rate in the state-projection region of interest on both the high and low frequency outputs. Simultaneously, we slowly (105 mHz) ramp the bias on QD_1 to introduce a detuning, which forms the top axis of the figure. The upper panel displays the Raman count rates from the two emitters, and the lower panel contains the Rayleigh scattering. As QD_1 is tuned past resonance (corresponding to the maximum rate of Raman scattering), the Rayleigh interference from the two quantum dots changes

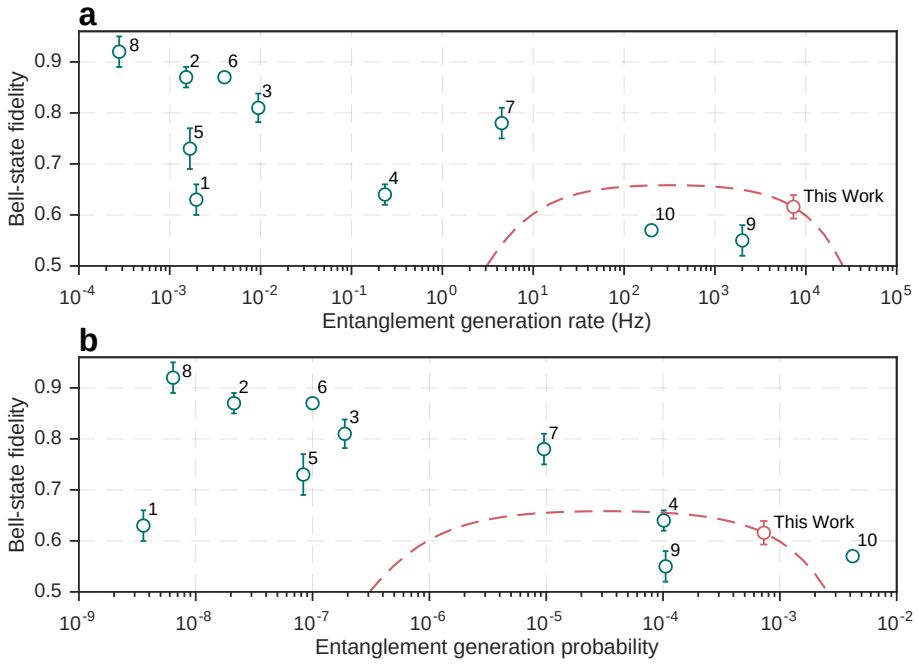

Figure 4.18.: **Entanglement comparison** Bell state fidelity against generation rate (**a**) and success probability (**b**). The numbered points are references: 1: [156], 2: [199], 3: [202], 4: [200], 5: [89], 6: [203], 7: [201], 8: [204], 9: [142], 10: [205]. We include our recovered fidelity and include a value that corrects for our imperfect spin readout detailed in figure 4.4. The dashed lines correspond to a projected fidelity for our demonstration with different operation rates.

phase. This corresponds to a changing phase in the coherent response of the QD_2 to the detuned driving field.

4.7. Conclusions & outlook

Distant entanglement has been reported in a variety of different physical systems, and it is important to contextualise the results presented in this chapter in order to understand the niche that entangled quantum-dot spins occupy. In figure 4.18a reported state fidelities are plotted against the entanglement generation rate for a number of physical systems: atomic qubits (points 1,2,3,4 & 6) [156, 199–202], NV centres (5,6, & 8) [89, 203, 204], confined hole spins in quantum dots (9) [142] and superconducting qubits (10) [205]. We plot our extracted fidelity and a figure corrected for our ∼3% readout error. The curves correspond to projected state

fidelities where we to alter our scattering probability. A lower rate suppresses double spin-flip events, increasing the Bell-state fidelity. As the scattering probability is decreased to the detector dark count rate ($\sim$ 1Hz), the fidelity decreases due to false heralds. The 7.3-kHz entanglement generation rate used in this chapter is the highest frequency entanglement generation reported for optically active qubits.

The exact generation rate has many instrumental conditions, including the need to intermittently cool atomic systems, and the oscillator strengths of the optical transitions. Both the continuous operation of confined spins and the strength of the excitonic transitions contribute to the high value we report here.

In figure 4.18b we control for the experimental protocol used by normalising against the attempt rate in each report to find the success probability of the scheme. This compresses the range of reported values by an order of magnitude. At 6.7×10^{-4}, the modest value we find here is again a highly competitive value. The only higher value reported is for two superconducting flux qubits which share a chip and operate in the microwave-frequency domain. The high success probability is principally due to two factors. First, the single photon heralding offers a clear advantage in the achievable rate, given the condition that the acceptable spin-flip probability is higher than the collection efficiency. Second, in comparison with other solid-state emitters, the high coherence of quantum dot transitions is such that $\sim$90% of emission processes can distribute a quantum state. These results along with those presented for holes [142] establish spins confined to self-assembled quantum dots as a high-frequency source of distant entanglement.

There are a number of clear steps forward from this demonstration. First, the fast dephasing of spins confined to self assembled dot is such that we are forced to measure the state before the state-projecting detection event. This perverse order is still an important test, as the state can be protected through local decoupling schemes at each site [224] as in chapter 3. This would allow us to extend the coherence of the two spins beyond the $\sim$100 ns time it takes for the scattering to reach our detectors, such that the state would be heralded. This is a relatively technical addition, and

the important component is the nonlocality demonstrated here.

Performance with respect to both axes of figure 4.18 could be improved by increasing the photon extraction efficiency from our samples. The single photon scheme we use ties the generation rate and fidelity together, such that an improved efficiency would provide higher fidelity at our 7.3-kHz rate, or a higher generation rate with the same fidelity.

Importantly, a demonstration of this style marks a point where the spin and optical properties of quantum dots can no longer be examined in isolation. Now the two are intimately linked, and both need to perform to a high standard. A clear next step beyond this work would be a demonstration of this style using devices that permit near-unity photon extraction, or on-chip routing [136]. To this end, the observation of entangled optical states from quantum dots in nanowires [225], indistinguishable photons from quantum dots in microcavities [217, 218] and spin-induced single photon nonlinearity in a waveguide [19] are encouraging results towards truly scalable creation of states distributed over a network of interconnected spin qubits.

CHAPTER

FIVE

DIRECT COUPLING OF A QUANTUM DOT TO A SINGLE ION

It is natural that large scale quantum networks were first envisaged as realisable through coupling together identical quantum systems [10]. As scalability requirements were considered and the particular strengths of individual systems assessed an exciting alternative has emerged in coupling different systems with unique and complementary attributes together.

The term 'hybrid quantum system' encompasses a wide range of proposals and experiments all of which share the same basic motivation: different quantum systems are particularly capable of different tasks, and if linked efficiently enough, their combination could outperform each individual constituent [25–27]. In the context of information processing one could think of the composite system straddling the DiVincenzo criteria without each part ever satisfying more than a subset [92].

The combinations are numerous and varied. To select a few there are hybrid systems built of different atomic isotopes [226], or different optical wavelengths, compatible with coherent stationary systems and low attenuation optical fibres [44, 227, 228]. The latter can be extending to interconversion between the microwave and optical regimes for interfacing distant superconducting circuits [229, 230]. Al-

ternatively, 'hybrid' could refer to the encoding of the quantum state, as in protocols featuring information in both continuous phase quadratures and a discrete photon-number representation [231, 232]. Beyond this, hybrid materials mixing spin degrees of freedom and superconductivity are a promising route towards computing with topologically-protected quantum states [233, 234].

The interpretations we focus on are coupled quantum systems that provide complementary qubit definitions. Experiments have demonstrated the coupling between spin ensembles and a superconducting flux qubit that share a common resonator [235, 236], and optical interactions between a molecule or quantum dot and neutral atomic vapours [237–239]. These demonstrations have relied on ensembles to achieve interaction between the systems. The work contributing to this chapter is focussed on a goal which had so far remained elusive, the coupling of two different, single quantum systems, which we achieve with an InGaAs quantum dot and a single ytterbium ion in a high-finesse Fabry-Perot cavity. These systems are of particular interest owing to the ultrafast operations possible and on-chip integration available with a single quantum dot, compared to the long coherence times states encoded in trapped ions experience, together with their shared interaction with near-infrared optical fields [240].

The challenge of any hybrid system is in the link: how to form a common mode between two systems presenting such desirable differences. In this chapter we first discuss the extent to which the atom and quantum dot share a common optical mode and the limitations provided by their differing bandwidths. We demonstrate a direct link between the systems by controllably changing the internal state of the ion with emission from the quantum dot and explore routes that circumvent the optical mismatch. We then present classical correlations between the quantum dot spin and the internal state of the ion, and discuss how this might be extended to achieve the significant goal of a hybrid entangled state shared between the two systems.

The work presented in this chapter is a collaborative effort between Prof. Atatüre's and Prof. Köhl's research groups, which includes Claire Le Gall on the quantum dot

side and Matthias Steiner and Hendrik Meyer on the atomic side.

5.1. A single $^{174}Yb^{+}$ ion

The atomic node of our hybrid system is formed of a single $^{174}Yb^{+}$ ion confined to a needle Paul trap. The ion is trapped by applying a high voltage (100 V amplitude) signal at 22 MHz to two very fine tungsten needles separated by 100 μm, creating a psuedo-potential minimum with a width of $2\pi\times$(1-3) MHz. Figure 5.1a shows the single fluorescing ion between the tungsten needles of the trap, surrounded by a fibre cavity. An important feature of this minimal trap geometry is the high numerical-aperture optical access to the ytterbium atom it allows.

The relevant atomic level structure for understanding our hybrid coupling experiment is displayed in figure 5.1b. The ion is Doppler-cooled with the 369 nm transition between the $^{2}S_{1/2}$ ground state and the $^{2}P_{1/2}$ excited state. The excited state decays into the metastable $^{2}D_{3/2}$ state with a branching ratio of 0.5% [241], which in turn decays back to the ground state in $\sim$ 50 ms [242]. The $^{2}D_{3/2}$ state is of particular interest to us, as it can be excited to $^{3}D[3/2]_{1/2}$ with light at 935 nm, within the typical range of InGaAs quantum dot transition frequencies. With a high probability interaction at 935 nm transfers population back down to the ground state, set by the free-space branching ratio of 98:2, which allows us to use ground state population as a probe for interaction between the ion and a resonant photon from the quantum dot.

Linking the ion to other single quantum systems requires operating at the single photon level. To access this regime, a high-finesse Fabry-Pérot cavity surrounding the trapped ion enhances the interaction between the weak $^{2}D_{3/2}$-$^{3}D[3/2]_{1/2}$ transition and the cavity mode. The interaction between a single excitation in the cavity mode and the ion can be encapsulated in the cavity cooperativity, $C = g^2/(2\kappa\gamma)$ [243]. In this expression, g is the coherent (reversible) coupling rate between the optical mode and the atom, γ the atomic dipole decay rate and κ the decay rate of

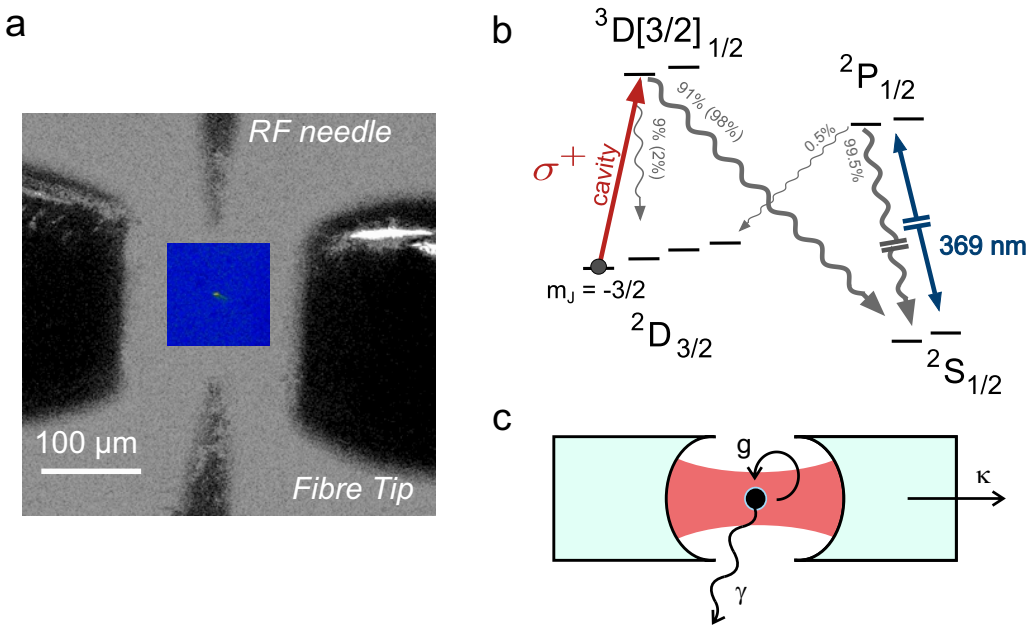

Figure 5.1.: **Single ^{174}Yb$^+$ ion in a fibre-based cavity a** Image of single ion confined in needle trap. Visible are the tungsten trap needles (top and bottom) and the sleeves of the fibre-tip cavity (left and right). **b** Level structure of single ^{174}Yb$^+$ ion. The highlighted transitions are the main cooling transition from the ground state at 369 nm, and the cavity coupled near-infrared transition at 935 nm. **c** Schematic showing the three processes that characterise the ion-cavity coupling, the coherent coupling strength, g, the dipole decay rate γ and the cavity-field decay rate κ.

the cavity field, as displayed in figure 5.1c. The coherent coupling rate, $g \propto 1/\sqrt{V}$, where V is the cavity mode volume, thus minimising the size of the cavity mode is a clear route to enhancing the cooperativity with the atomic transition.

Achieving small mode volumes around trapped ions presents a challenge, as large dielectric surfaces near to the trap disturb the electrostatic environment of the ion [244]. The key development here is to form the cavity from facets of single-mode fibres [245]. Curved faces are laser-machined into the fibre ends with radii of curvature of 250 ± 30 and 300 ± 20 μm, and coated to achieve transmissions of 10 and 100 parts-per-million [246]. The mode is then 170 ± 10 μm long with a waist of 6.1 ± 0.2 μm [247]. For this cavity the parameters (g;κ;γ) are found to be $2\pi\times$(1.6;25;2.1) MHz, with a cooperativity of 2.4 ± 0.5%. These values exist in the range referred to as the intermediate coupling regime, where the coherent coupling rate is compa-

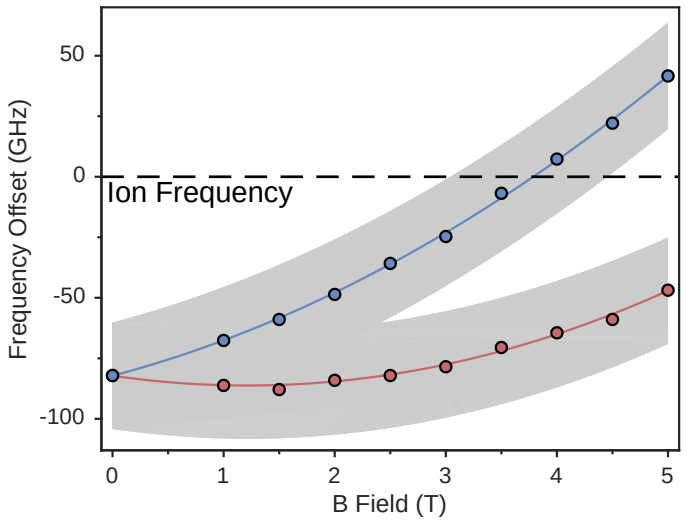

Figure 5.2.: **QD resonance magnetic field dependence** Resonance frequencies of the X^0 transition as a function of external magnetic field. The points correspond to the central frequencies of the Zeeman-split transitions. The curves are quadratic fits to the frequencies. The grey shading follows the width by which we can electrically tune the transitions. The dashed line at the ion frequency can be matched by the blue branch between 3 and 4.5 T external field.

rable to the dipole decay rate of the transition, rather than strong coupling where the coherent rate, g, exceeds all other processes. An advantage of this technique is the natural coupling to fibre-modes which provides an easy compatibility with fibre-based networking.

The successful realisation of this demanding atom-photon interface was the doctoral work of Dr Hendrik Meyer and Dr. Matthias Steiner. More details on the cavity coupling can be found in references [245, 247]. The high-coupling strengths and stable operation are manifestations of their hard work over multiple years of development.

5.2. A common resonance

The full optical characterisation of the quantum dot used for the hybrid coupling experiment is presented in section 1.6. Here, the simplest requirement is covered: the need for a common resonance between the systems. The ion presents a strict

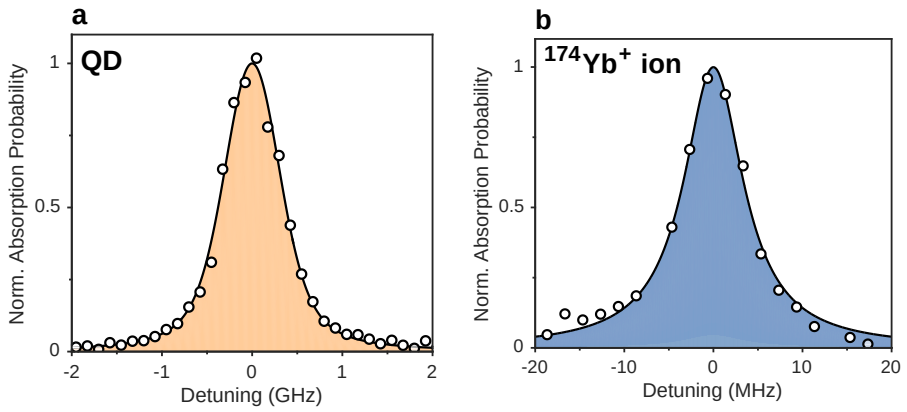

Figure 5.3.: **Resonant transitions** Absorption scans of the quantum dot (**a**) and trapped ion (**b**) transitions at 320572.2 GHz. The curve in **a** is a voigt fit revealing a width of 744 ± 42 MHz, the curve in (**b**) is a Lorentzian function with a width of 8 ± 0.44 MHz.

resonance frequency at 320572.2 GHz (935.18 nm), and it is the responsibility of the spectrally flexible quantum dot to match it. First, we find an emitter with the possibility of being resonant with the ion transition. We achieve this by performing above band-gap photoluminescence and manually raster-scanning the sample until we find a peak corresponding to an X^0 transition within 100 GHz of the ion resonance. Electrical tuning with the sample gate provides a range of $\sim$ 50 GHz for the quantum dot optical resonance, with additional range provided by coupling to an external magnetic field. The response of the quantum dot spectrum to the external fields, offset by the atomic resonance, is mapped out in figure 5.2. The curves are quadratic fits to the data and the grey shaded areas represent the estimated electric tuning range at each magnetic field. The magnetic field which couples to the excited states splits the transitions linearly through the Zeeman effect (split by 18.2 GHz T^{-1}) [248] and raises their frequency quadratically via the diamagnetic shift (2.6 GHz T^{-2}) [249]. With a field value between 3 and 4.5 Tesla the quantum dot can be electrically tuned to match the atomic transition. We work at an external field of 4.2 T, as the gate voltage selection is limited by electrical noise from a nearby voltage dependent charge trap in the sample.

Figure 5.3 contains normalised absorption measurements of the quantum dot and

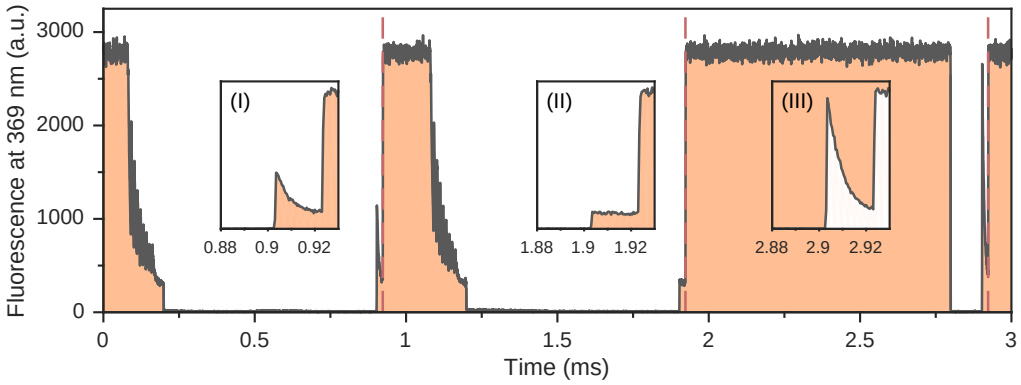

Figure 5.4.: **Pulse-sequence fluorescence trace** Average time-trace displaying the fluorescence at 369 nm from the ion during the sequence for coupling to photons from the quantum dot. The transients highlighted in the insets are the fluorescence from probing the ground state population due to (I) quantum dot photons, (II) no repumping and (III) full repumping.

ion around their common resonance (note the different x-scale in each panel). The quantum dot is fitted with a Voigt profile (more details in section 1.6), and the ion transition with a Lorentzian function. Lifetime measurements of the ion and quantum dot correspond to Fourier-limited linewidths of $2\pi\times4$ MHz and $2\pi\times250$ MHz respectively: a 60-fold discrepancy. In the two absorption scans, we recover widths of $2\pi\times8 \pm 0.44$ MHz for the ion, and $2\pi\times744 \pm 42$ MHz for the quantum dot. The broader linewidths are due to power broadening and spectral wandering of the transitions, such that we record a factor of 93 bandwidth mismatch. This large mismatch highlights the difficulty of forming a network containing both systems: defining a common mode that interacts efficiently with both. The bandwidth difference results in a loss of efficiency in direct coupling experiments, or a need to spectrally filter photons from the quantum dot (or temporally filter the atomic emission) to achieve indistinguishability in joint measurements.

5.3. A photonic link

The first experiment we perform is to establish an optical link between the quantum dot and the ion. Physically this is provided by two 50-m single-mode fibres, allowing us to pass fluorescence from the quantum dot cryostat to the ion-trapping lab, and use spectrally narrow, cavity locked lasers suitable for atomic transitions to excite the quantum dot. We then test the optical interface by observing a single photon stream from the quantum dot controllably change the internal state of the ion. The measurement sequence that allows us to measure this interaction is as follows:

A. We cool the ion. A repump at 935 nm ensures that the state of the ion is not shelved and the cooling continues as the state is recycled.

B. We remove the σ^+-polarised component of the 935 repump. This shelves the ion into the $m_J = -3/2$ level of the $^2\mathrm{D}_{3/2}$ manifold.

C. We drive the quantum dot transition resonantly for some time T and pass the resulting fluorescence to the ion. We excite the quantum dot at half saturation intensity ($I/I_{\mathrm{sat}} = 0.5$), such that the average excitonic population is 1/6.

D. We probe the atomic ground state population. An interaction with a quantum dot photon will have most probably transferred the ion to the $^2\mathrm{S}_{1/2}$ ground state, according to the cavity modified branching ratio of 92:8. The ground-state population then provides a conservative estimate of the ion-photon interaction.

In this way we use the ion population to probe interaction with quantum dot photons. The average 369 nm fluorescence from the ion accompanying the sequence is shown in figure 5.4. The high fluorescence regions are the ion cooling and the modulated decay follows the state preparation into $m_J = -3/2$. The low fluorescence regions the interaction time and the subsequent sharp decays, highlighted in the insets, the ground state population readout. As shown in the figure, we repeat

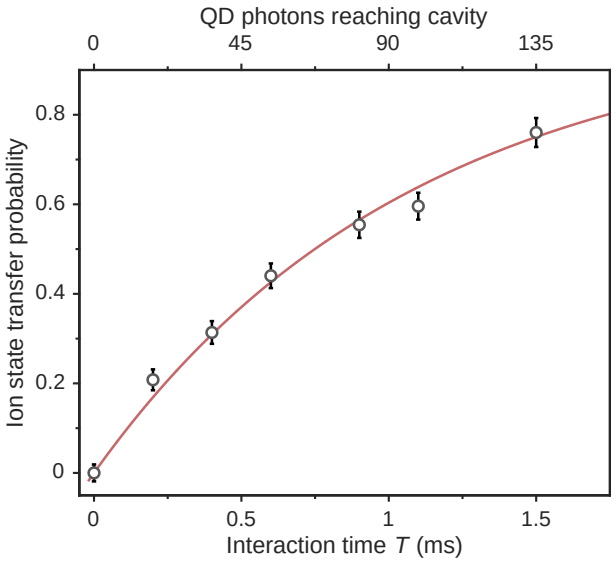

Figure 5.5.: **Atomic state transfer by quantum dot photons** State change probability dependence on quantum dot-ion interaction time, T. The curve is an exponential fit revealing a transfer time of 1.08 ± 0.04 ms. The top axis displays the number of quantum dot photons reaching the ion cavity during the interaction.

the whole sequence three times, with the single photon stream (I), no quantum dot photons (II) and with deterministic repumping to the ground state (III). This allows us to normalise the atomic fluorescence and gain a differential measure of the state transfer.

Figure 5.5 displays the state transfer probabilities we recover when we perform this sequence and sweep the interaction time T. The probability of changing the ion state saturates with the pulse length. Fitting the measured populations with a single exponential (curve in figure 5.5) we find a characteristic transfer time of $\tau = 1.08 \pm 0.04$ ms. During the experiment, we monitor the rate of quantum dot photons impinging on the ion cavity, which forms the top axis of the figure. This allows us to extract a per-photon state transfer probability, $p_{\text{abs}} = 1.0 \pm 0.2\%$.

With this initial experiment, we have been able to measure an optical link between the quantum dot and the ion, expressed via controllably changing the internal state of the ion. This satisfies the most basic aim of the experiment: a link between two different, single quantum systems. We can now extend this to explore and characterise the interaction between the two systems via the quantity p_{abs}.

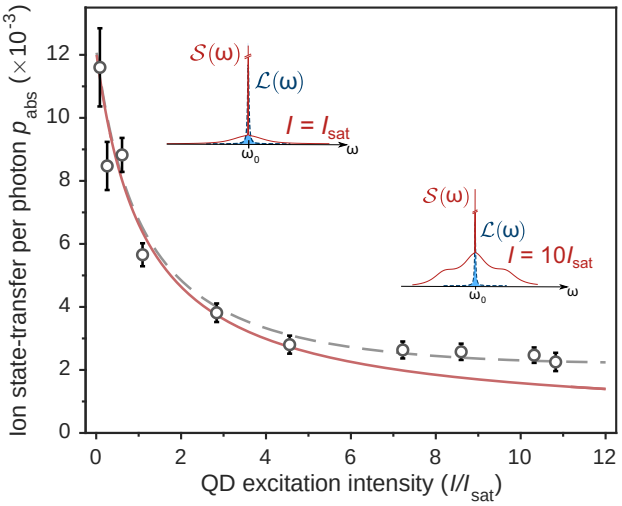

Figure 5.6.: **Ion state transfer dependence on QD driving intensity** Points are per-photon state change probabilites for two decades of variation in resonant quantum dot drive power. The solid curve is the normalised spectral overlap between the two systems, with the dashed curve containing the contribution from background laser light. The insets show the emission spectra of the quantum dot, $\mathcal{S}(\omega)$, the ion transition, $\mathcal{L}(\omega)$ and their overlap (shaded regions).

5.4. Interaction properties

Having successfully linked the two systems together, we want to understand to a greater extent the interaction between quantum dot photons and the atomic resonance, in particular the effect the optical mismatch presented in figure 5.3 has on efficiently linking the two systems.

In order to understand how the contrasting optical properties affect the efficiency of the interface, we measure the dependence of the ion-state per-photon transfer probability p_{abs} on the normalised QD excitation intensity (I/I_{sat}, defined in section 1.3). The measured values are displayed in figure 5.6. We observe a pronounced change between low and high power driving of the quantum dot, corresponding to a ratio of 5.0 ± 0.8 between the measured per-photon efficiencies. When we correct for the presence of stray photons from the drive laser, which contribute at the highest excitation intensities ($I \gg I_{\mathrm{sat}}$), we recover a ratio of 8.6 ± 0.8.

We fully understand this dependence from the overlap between the quantum dot emission spectra, $\mathcal{S}(\omega)$, and the 20-MHz wide cavity-broadened ion transition $\mathcal{L}(\omega)$.

We can calculate the quantum dot emission spectra directly from the density matrix describing the two-level exciton system, including dephasing due to phonon-induced decay between optically dressed states [22]. The solid curve in figure 5.6 is the expected state-transfer efficiency, p_{abs}, found from the normalised overlap between the two transitions:

$$p_{\mathrm{abs}} \propto \frac{\int \mathcal{S}(\omega)\mathcal{L}(\omega)\mathrm{d}\omega}{\int \mathcal{S}(\omega)\mathrm{d}\omega}. \tag{5.1}$$

Including the effect of the stray drive laser photons results in the dashed curve, reproducing our observed state transfer efficiencies. The overall scaling of the curve is set by the coupling of the ion to the optical cavity.

The two spectra and their overlap are shown for two different powers as insets in figure 5.6, both centred on the ion absorption frequency ω_0. At the saturation intensity ($I = I_{\mathrm{sat}}$), we predict that 46% of the emission from the quantum dot is coherent with the laser and follows the sub-linewidth spectrum of the optical drive [22], This emission has a high degree of overlap with the narrow ion transition. At higher powers, where the optical Rabi frequency exceeds the excitonic decay rate of the quantum dot ($I = 10I_{\mathrm{sat}}$ in the figure), we build up significant excited state population. In this limit the emission spectrum becomes dominated by spontaneous decay processes with coherence limited by the optical lifetime, as well as sidebands at the Rabi frequency due to modulation of the excitonic population. At these intensities, the mismatch now plays a significant role since all of these processes lead to a diminished overlap with the sharp atomic transition, resulting in the decreased state-transfer efficiency we observe.

In the low excitation limit we record per-photon state-transfer probabilities of 1.2 $\pm$ 0.2%. When we correct for the 13% of quantum dot emission which is phonon-assisted (see section 1.6) and does not interact with the ion we find an efficiency of 1.4 $\pm$ 0.2%. This is comparable to the highest recorded laser state-transfer probabilities for this cavity of 1.8 $\pm$ 0.2% [247]. In this way we show that coherent photon generation offers a route to circumvent the inherent mismatch between the optical

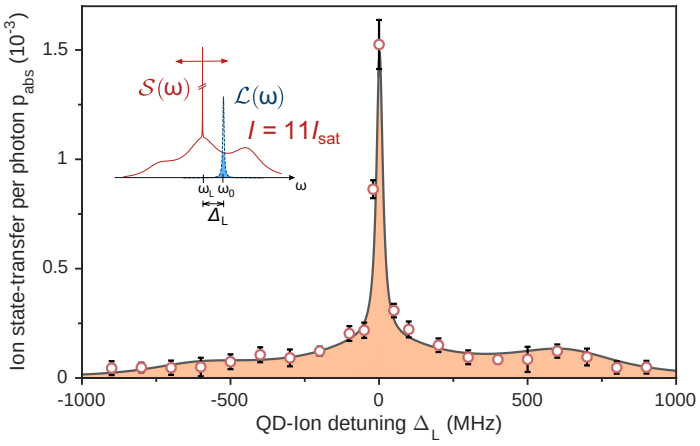

Figure 5.7.: **Spectral dependence of the per-photon ion state change probability** Measured at high excitation intensity for varying detuning Δ_L. The filled curve is the convolution between the quantum dot emission spectra and the 20-MHz wide cavity-coupled ion absorption. The inset contains a schematic of the joint spectral measurement process.

properties of the two systems.

Further insight into the bandwidth mismatch is provided by the joint spectrum of the two systems, presented in figure 5.7. We drive the quantum dot at a high intensity ($I = 11I_{sat}$), centred on frequency ω_L and find the per-photon ion state-transfer probability as we scan the emission across the atomic resonance at ω_0. The state-transfer probability arises from the convolution between the quantum dot emission spectra $\mathcal{S}(\omega)$ and the cavity-coupled atomic resonance $\mathcal{L}(\omega)$. The inset of figure 5.7 shows a schematic of the two spectra and their relative detuning $\Delta_L = \omega_0 - \omega_L$.

As we would expect from equation 5.1, the state-transfer efficiency follows the Mollow triplet emission spectra of the quantum dot. Around $\Delta_L = 0$ we find a sharp resonance feature with a width set by the cavity-coupled ion absorption spectra. At larger values of Δ_L we recover broad, low probability features. These are due to the incoherent decay processes in the quantum dot, reflecting the limited efficiency with which they can couple to the internal states of the ion.

The curve in figure 5.7 is the convolution between the modelled quantum dot emission at this high excitation intensity and the atomic linewidth, with the addition

of residual laser due to imperfect background suppression (this contributes 30% of the central peak height). The asymmetry in the emission spectrum we record is a consequence of nuclear spin polarisation in the quantum dot, which holds the excitation at a slight detuning from the exact excitonic resonance [109], and high-frequency dephasing at high driving intensity (as discussed in section 1.6.4) which result in asymmetric sideband areas under this condition [125].

5.5. Electron spin-ion state correlations

The optical link demonstrated in this chapter is the principal mechanism that would enable us to transfer a quantum state between the quantum dot and the ion. As an initial step towards this important end-goal we demonstrate classical correlations between the quantum dot spin and the internal state projection of the ion.

We find a quantum dot with a negatively charged trion (X^{1-}) resonant with the ion. We then define the ground state spin projection with an external magnetic field along the growth axis (Faraday geometry), which enables two, circularly polarised ($\sigma^{+/-}$), spin-conserving transitions split by 28.6 GHz T^{-1}, as in the level diagram of figure 5.8a. Diagonal spin-flipping Raman transitions are only weakly allowed ($\sim$ 1-2%) in this geometry by heavy-light hole mixing [250, 251]. The resonance fluorescence map of this quantum dot under a 0.7 T external field is shown in figure 5.8b, taken by sweeping the laser frequency and an applied bias voltage across the quantum dot to record the charging plateau. The map shows two transitions, mostly suppressed by spin pumping over the weakly allowed diagonal transitions [42]. The four bright regions at 0.4 and 0.57 V occur due to fast electron cotunneling with the nearby electron reservoir, which quickly recycles the spin state and restores the average fluorescence signal (as discussed in section 1.4.1). The horizontal line marks the atomic resonance at 320572.2 GHz, which is met by the high-frequency σ^+ transition at an applied gate voltage of 0.46 V.

Figure 5.8c displays the fluorescence when we hold a laser at the atomic resonance

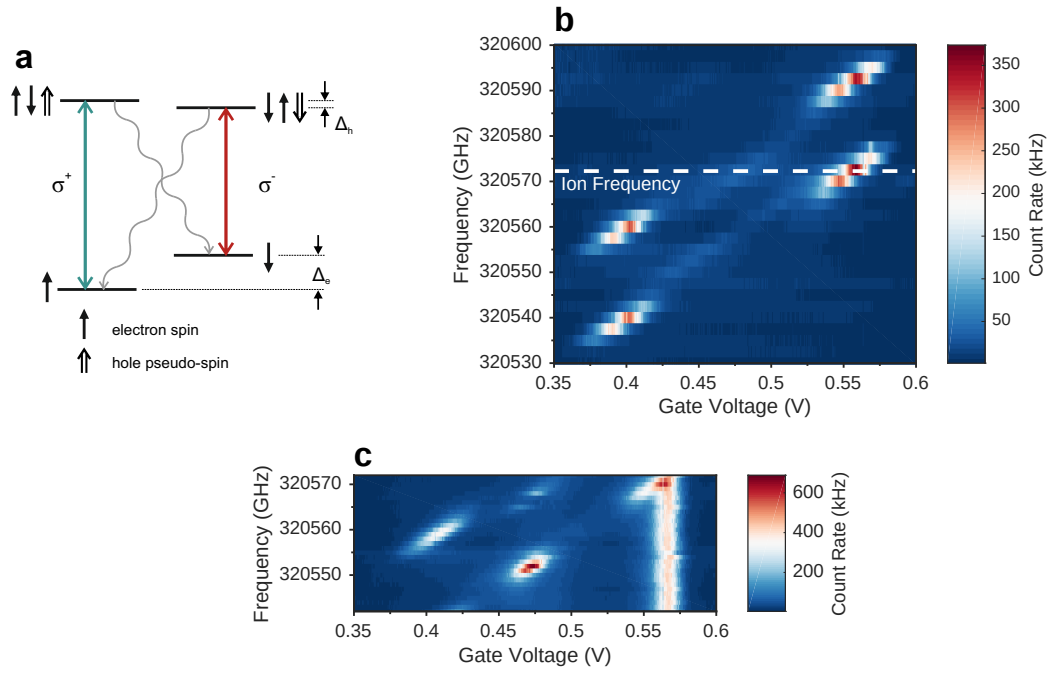

Figure 5.8.: **Quantum dot spin in Faraday geometry a** Level scheme for a charged quantum dot in Faraday geometry. The two vertical transitions are circularly polarised and the grey decays represent the weakly allowed diagonal transitions. **b** Single frequency map of quantum dot charging plateau, showing the suppressed fluorescence due to spin pumping and the restored fluorescence due to electron cotunneling. **c** Two frequency map of the quantum dot plateau. One probe is held at the ion resonance while the other laser is scanned through the quantum dot plateau.

and scan the frequency of a second probe. The bright stripe at 0.56 V corresponds to the fixed frequency laser driving the quantum dot in the cotunneling region, similarly for the scanning beam at 320560 GHz and 0.4 V. The central bright feature at 0.47 V and 320551 GHz is the double resonance of the quantum dot whereby the two beams, resonant with the $\sigma^{+/-}$ transitions, continuously repump the spin. The dimmer feature at 320568 GHz and 0.48 V is due to the scanning beam driving the weakly allowed diagonal transition.

We set the two lasers resonant with the $\sigma^{+/-}$ transitions, pulse these two frequencies with a pair of acousto-optic modulators and time resolve the fluorescence, resulting in the histogram shown in figure 5.9a. During the first pulse we drive the low-frequency σ^{-} transition for 3 μs at $I/I_{\mathrm{sat}} = 2$ and in the second the high-

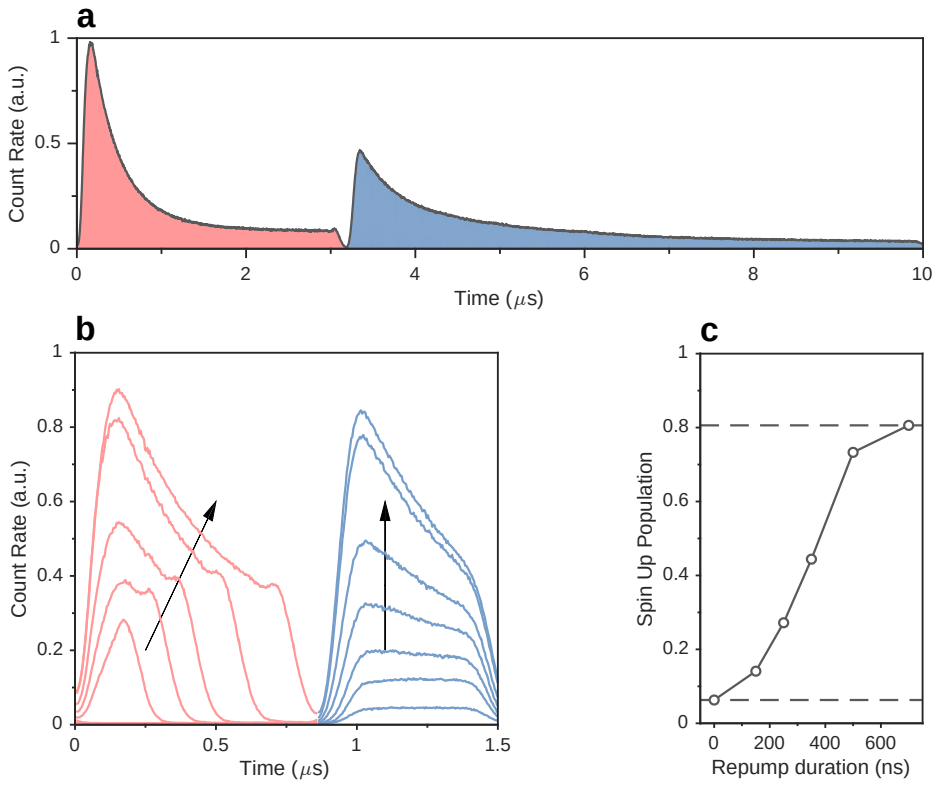

Figure 5.9.: **Spin pumping in Faraday geometry a** Fluorescence histogram from alternatively driving the two allowed transitions for 3 and 6.5 μs. **b** Histogram displaying variable spin preparation by changing length of the low frequency repump pulse from 0-700ns. The high-frequency pulse is held at a constant length of 600 ns. **c** Extracted spin up population $p_\uparrow$ from changing repump power.

frequency σ^+ transition for 6.5 μs at $I/I_{\text{sat}} = 0.5$. As the quantum dot spin is shelved the fluorescence decays with timescales of 351 $\pm$ 1 and 613 $\pm$ 14 ns, respectively, set by the average excited state population, the transition lifetime and the small branching ratio. From this we determine preparation fidelities of 92.2 $\pm$ 0.2% (92.8 $\pm$ 0.2%) for the state $|\uparrow\rangle$ ($|\downarrow\rangle$). Compared to the transverse field used in previous chapters the near cycling transitions in this geometry can permit single-shot readout of the spin state if the detection efficiency is sufficiently high [117], at the expense of requiring many optical lifetimes to prepare a well-defined ground state population.

By repeating this alternating pulse sequence and varying the length of the low-frequency pulse we can create a well-defined time averaged spin mixture. The high-frequency fluorescence resulting from a constant-length pulse resonant with the σ^+-

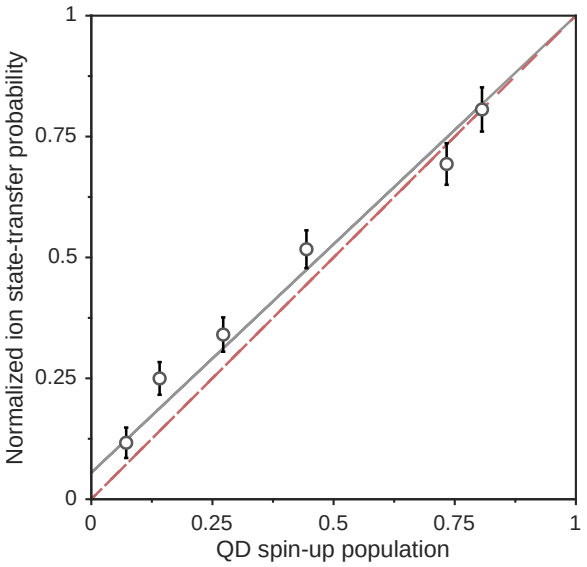

Figure 5.10.: **Ion state-transfer correlated to quantum dot spin** Normalised ion state-transfer probability in 0.7 ms plotted against prepared quantum dot spin mixture. The spin up projection is found from the analysing the time-resolved quantum dot fluorescence. The dashed (solid) curve represents the ideal (measured) correlation between the two systems.

polarised transition provides a linear measure of the ground state population directly beforehand. Figure 5.9b contains the correlated fluorescence histograms for holding the high-frequency pulse length constant at 550 ns, and sweeping the length of the low-frequency pulse from 0 to 700 ns. By fitting the fluorescence areas and the contrast of the exponential decays we can extract the population of the spin mixture $p_\uparrow |\uparrow\rangle \langle\uparrow| + (1 - p_\uparrow) |\downarrow\rangle \langle\downarrow|$. The values of $p_\uparrow$ are plotted in figure 5.9c, showing that for this sequence we can produce values between 6.3% and 80.6%, limited by state preparation fidelities and the maximum length of our low-frequency repump pulse.

Combining this spin preparation and readout scheme with the QD-ion photonic link allows for the realisation of classical correlations between the system ground states. We link the two systems as in figure 5.5 with a stream of quantum dot photons 0.7 ms long, however during that sequence we run the spin-preparation and measurement sequence at 670 kHz (469 repeats per interaction time). The resulting ion state transfer probability, normalised against the maximum state transfer rate of 318 Hz, is plotted against the prepared QD spin population in figure 5.10. The

constant length of the resonant pulse and the spectral detuning of the repump pulse ensures that any change in the state-transfer of the ion is a result of a different spin mixture in the quantum dot. These results show that to within an uncertainty of 3.8% we can faithfully reproduce the quantum dot spin population in the form of $^2S_{1/2}$ internal state projection in the atomic node. The dashed curve in figure 5.10 represents the ideal correlation between the systems, while the solid curve follows our measured dependency, which slightly deviates due to the presence of laser photons leaking through the system.

5.6. Conclusions & outlook

In this chapter we have presented the realisation of a direct photonic link between a semiconductor quantum dot and a single Ytterbium ion, constituting the first link between wholly different single quantum systems. At the same time, coherently scattered photons from the quantum dot allow us to couple the systems with per-photon efficiencies that circumvent the inherent optical mismatch. In correlating the ion state with the quantum dot spin, we present the first communication between the internal ground states of the systems, albeit in the form of a classical mixture.

The next milestone is the transfer of a quantum state. This could be achieved either by mapping information in the QD spin to a photon and passing it to the ion, or by entangling the two systems and teleporting the information. Achieving either of these two would require changes to both the quantum dot and the ion. First, the magnetic field would need to be transverse to the QD growth direction, forming the spin-photon interface we use in chapter 4 to entangle two quantum dot spins. Second, the ion would need to be changed from the $^{174}Yb^+$ isotope to $^{171}Yb^+$. The non-zero nuclear spin of this isotope results in hyperfine levels, allowing us to employ the 'Rubidium toolkit' in exchanging a state between atomic levels and optical degrees of freedom [241, 252]. Quantum dot spin-photon entanglement could then be converted to hybrid entanglement with the ion, as in figure 5.11, following the

scheme demonstrated in neutral atoms in reference [157], with the potential addition of a few GHz frequency shift or frequency-to-polarisation conversion between the systems. A similar proposal has been examined in reference [240], whereby the two systems are entangled through measurement of indistinguishable photons which elastically scatter from an ion and dispersively interact with a cavity-coupled quantum dot.

Among the many challenges involved in realising hybrid distant entanglement, a direct mapping scheme would require coupling both spin-conserving Rayleigh and spin-flipping Raman scattering from the quantum dot to the ion. When adapting the work here, the ground state coherence of the quantum dot spin needs to be considered, as this sets a limit for the coherence of Raman photons [140, 146, 222]. The measured electron spin T_2^* of 1.74 ns we presented in chapter 2 corresponds to a linewidth of 91 MHz, limiting efficient interaction between Raman photons and an atomic transition. While the intrinsic limits to hole spin coherence are not fully understood, the immediate reduction of inhomogeneous dephasing rate by at least an order of magnitude due to the suppressed hyperfine interaction will allow for greater coupling of Raman scattering to the ion [180]. This spin qubit could also perform at smaller splittings, requiring less frequency conversion to match the atomic transitions, as quadrupolar broadening will play less of an effect than that observed in chapter 3.

A key requirement for hybrid state transfer and entanglement would be an increased node-to-node photon transfer efficiency. The scheme could operate with a herald for successful ion state change [253], however the success probability would still need to be sufficiently high to dominate false heralds and achieve high fidelity mapping.

In this chapter, the efficiencies presented were normalised to the photon rate impinging on the ion cavity, recording values $\sim$ 1-2%. This normalisation allows us to highlight the physics of interest in the hybrid coupling, and make the comparison with attenuated laser light. The total efficiency of the link, however is 5×10^{-6}. This

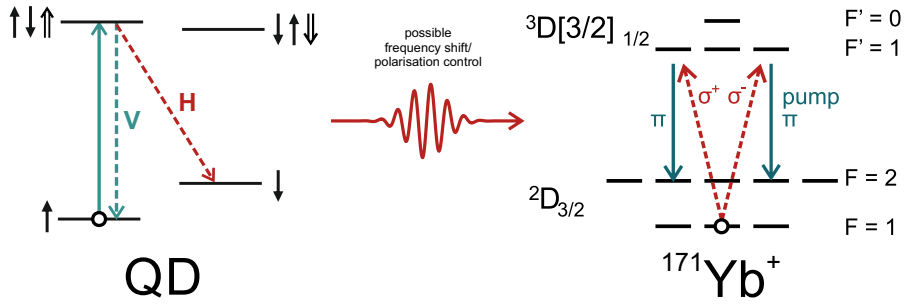

Figure 5.11.: **Hybrid entanglement from a direct interface** Spin-photon entanglement is realised at the quantum dot, as demonstrated in [43–45]. With the addition of some intermediate frequency conversion, polarisation modes can be mapped into internal hyperfine state projection at the ion with an additional pump field.

can be partitioned into three stages:

I. Quantum dot sample out-coupling - 3.5%

II. Transmission from the quantum dot sample to the ion cavity - 1.4%

III. Ion state transfer due to one intra-cavity photon - 1.0%

The low sample outcoupling effiency is chiefly a consequence of the high refractive index of gallium arsenide, and we discuss options to circumvent this in detail in the chapter 6. That being said, collection efficiencies consistent with a 20-fold improvement over this rate have been reported [217, 218, 254]. The 1.4% transmission from quantum dot sample to cavity is partially due to the need to monitor rates in situ to make measurements of per-photon ion coupling effiencies, as well as the modularity of the combined setup. Removing these elements would allow for a 10-fold improvement in the efficiency. A higher finesse cavity with a greater cooperativity would permit higher state transfer rates [255]. Combined, these improvements could offer 3-orders of magnitude improvement in our node-to-node coupling.

CHAPTER

SIX

COLLECTION EFFICIENCY STRATEGIES

As demonstrated in chapter 4, optical spin measurement is a key process for distributing entanglement within quantum networks. It is the process that enables two-qubit gates between non-interacting nodes [189, 199, 256], and forms the individual steps in cluster-state computing [14]. Although entanglement-by-measurement schemes provide an automatic herald, allowing for repeat-until-success strategies, achieving high probability state generation is a necessary step to forming scalable networks. For networked computing in particular, the entanglement generation rate must be at least comparable to the qubit decoherence time to ensure low-overhead fault-tolerance [12].

The single photon-heralding scheme we use in chapter 4 allows us to record a high success probability of $\sim 10^{-3}$, however this scheme is limited by the requirement that we must keep the photon generation probability low ($< 10\%$). For comparison, the highest reported generation rate with a two-photon scheme is currently $\sim 10^{-5}$ [201]. We find that 1% of decay processes contribute to our entanglement distribution, a factor that accumulates for each step in a higher-order process. This efficiency is the product of every loss channel between the excited-state decay and the registered detection event.

Advances in superconducting nanowire detectors (SNSPDs) have enabled detec-

tion efficiencies >80% through the near-infrared spectral range [257], a proportion inaccessible with conventional Silicon or InGaAs single photon detectors [258, 259]. Additionally, our polarisation filtering, which currently blocks 50% of the state-projection photons could be matched to the transition axes with the requirement of sharper spectral rejection of our circularly-polarised spin-control pulses. It is worth noting that the lack of significant phonon-assisted decay processes ($< 15\%$, see section 1.6.2) ensures that the majority of emission events occur within a well-defined spectral window. With these considerations, the major loss in the system is the coupling of the dipole emission from the quantum dot to the collection fibre, limited by the extraction from the high-refractive index sample (as discussed in section 1.4.3). Currently, we estimate that we are accessing ∼5-10% of the dipolar emission field at the first lens of the collection optics.

In this chapter we are concerned with methods to extract larger amounts of emission from our sample structures. We first discuss some of the routes currently available for buried solid-state emitters. We then consider a method to efficiently model the far-field of an oscillating dipole embedded in a semi-infinite one-dimensional stack of dielectric layers. The method is sympathetic to MBE growth, which can generate atomically-precise layers of varying refractive-index materials. We then use this semi-analytic method to study a quantum dot embedded above an under-etched air-gap in combination with a DBR reflector, a structure that should allow us to access large proportions of the dipole field. Finally, we consider the remaining limits to achieving such large efficiencies, and possible routes to circumvent them.

6.1. Dipole collection strategies

As discussed in section 1.4.3, with no collection strategy we lose 50% of the emission into the lower half space, and another 48% to total internal reflection at the GaAs-air interface (figure 6.1a). The remaining 2% is distributed over the 2π solid angle above the emitter [262].

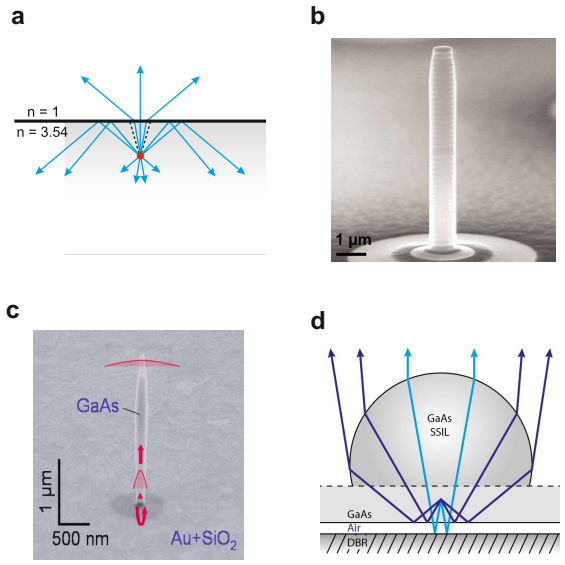

Figure 6.1.: **Collection efficiency strategies** Some of the strategies employed to extract photons from buried quantum dots. **a** Initial planar situation with a very small proportion of the emission escaping the dielectric. **b** Micropillar containing a solid state cavity formed by two DBR layers. **c** Photonic nanowire grown above a metallic reflecting surface. **d** Planar structure with a Solid Immersion Lens and a reflecting layers below the point source. **b** and **c** reproduced from references [260] & [261] respectively.

Attempts to access the full emission of a single dipole emitter can be roughly grouped into two main strategies. In the first, the local density of states is actively modified to ensure that emission into a single mode dominates over all other processes. For atomic systems, this is provided by free-space Fabry-Perot cavities [157] (as demonstrated in chapter 5) or by near field coupling to tapered optical fibres [263]. For quantum dots, this has been successfully realised by forming DBR cavities around the quantum dot layer, where the high oscillator strength enhances the cooperativity with the cavity mode [264]. A micropillar cavity is displayed in figure 6.1b, with the DBR stacks visible above and below the central layer containing the emitters.

A second option is to passively convert the near-isotropic dipolar field distribution into one suitable for single mode fibres. This is achieved in atomic systems through parabolic reflecting surfaces [265], or with high-aperture objectives [266, 267]. In

the solid state, the equivalent is the construction of a dielectric antenna, which passively funnels the 4-π emission into a small solid angle through the combination of a reflective surface and a solid immersion lens [268]. These antennas can permit near-unity collection efficiencies into limited numerical apertures [269, 270]. At the same time the designs generally require coupling from the emitter which is held in a moderately low refractive index material to a SIL which features a higher refractive index; a challenge for quantum dots in GaAs.

The most successful solutions to raise collection efficiency for InGaAs quantum dots have involved etching to form sub wavelength diameter GaAs photonic nanowires (figure 6.1c), which provide a broadband interface between the quantum dot emission and a single Gaussian mode [271, 272]. This way very high collection efficiencies have been recorded, at 72% of the quantum dot emission [273]. In order to have this strong effect on the mode distribution of the light, the sub-wavelength structures have large surface areas very close to the dot, which affect the quantum dot states due to trapped surface charges [274, 275]. Further perturbation occurs due to the mechanical motion of the structures as strain-induced spectral wandering [276].

As discussed, we require maximal amounts of the emission field to be funnelled into our collection optics. At the same time, our experiments demand a low noise electrical environment for the emitter, as well as sample gating. We want to find a collection strategy that is compatible with both these requirements.

6.2. A dipole in a 1D heterostructure

This section covers the basic steps by which we can find the far field of a Hertzian dipole embedded in a one-dimensional stack of dielectric layers. The form of the structure is presented in figure 6.2. The stack varies in the z-direction, parallel to which vertical dipoles are oriented. In general, the dipole is assumed to lie in the x-z plane at an angle of θ_d, with $\theta_\mathrm{d} = 90°$ for a horizontal dipole.

The key to the method is that the field of an electric dipole at an arbitrary

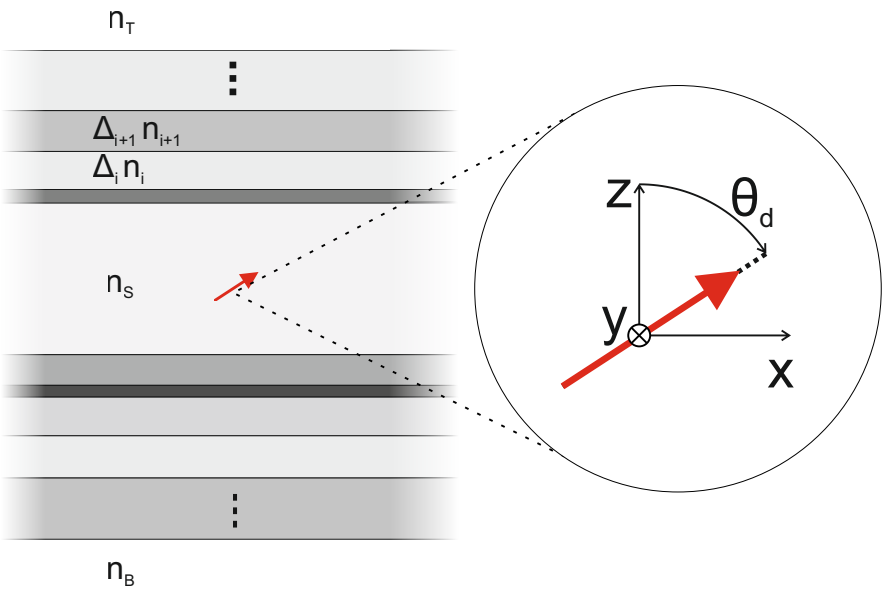

Figure 6.2.: **Dipole in 1-D dielectric stack** Dipole oscillating at angle θ_d in the x-z plane in source region with refractive index $\mathrm{n_s}$, surrounded by layers of thickness Δ_i with refractive index n_i.

orientation can be expressed as the sum of the fields due to vertical electric and magnetic dipoles. The highly symmetric emission of these dipoles contain only transverse-magnetic and transverse-electric polarised components respectively. In this way the two orthogonal polarisations with different boundary conditions are decoupled and the radiation patterns out of the stack can be found for each and then recombined.

This decoupling is made possible by using electric and magnetic Hertz vectors [277, 278] (sometimes referred to as polarisation potentials) to express the electromagnetic field. This representation considers an arbitrary field as due to a distribution of point-dipole sources, and so has a particularly simple form for the case of a single electric dipole. Electric dipoles are sources of an electric Hertz vector field ($\mathbf{\Pi}^e$), and magnetic dipoles give rise to a magnetic Hertz vector field ($\mathbf{\Pi}^m$). The electric Hertz vector at displacement $\mathbf{r}$ from a single electric dipole oscillating at frequency ω at angle θ_d:

$$\mathbf{\Pi}^e(\mathbf{r}) = p_0 \frac{e^{in_i k_0 r}}{4\pi r} \left(\sin\theta_\mathrm{d}\hat{e}_x + \cos\theta_\mathrm{d}\hat{e}_z\right), \tag{6.1}$$

where p_0 is the dipole moment of the source, $k_0 = \omega/c = k_i/n_i$ is the wavevector of the oscillation in vacuum, $n_i = \sqrt{\epsilon_i}$ the refractive index of the medium, ϵ_i the relative permittivity and $\hat{e}_{x/z}$ unit vectors in the x and z directions.

The electric and magnetic fields, ($\mathbf{E}$ & $\mathbf{H}$) in medium i due to this dipole can be then found as:

$$\mathbf{E} = \frac{1}{\epsilon_0 \epsilon_i} \left[\nabla \left(\nabla \cdot \mathbf{\Pi}^e\right) + k_i^2 \mathbf{\Pi}^e\right] + i\omega \nabla \times \mathbf{\Pi}^m \tag{6.2}$$

$$\mathbf{H} = -i\omega \nabla \times \mathbf{\Pi}^e + \frac{1}{\mu_0 \mu_i} \left[\nabla \left(\nabla \cdot \mathbf{\Pi}^m\right) + k_i^2 \mathbf{\Pi}^m\right] \tag{6.3}$$

The dipole can then be split into the vertical electric and magnetic dipoles (VED & VMD) by comparing the electric and magnetic fields from the three different sources. More details are provided in appendix B.

6.2.1. Boundary conditions

Having decoupled the dipole into orthogonal polarisations, the next step is to propagate the dipole field through the layers of the dielectric stack. We do this by taking the two-dimensional Fourier transform of the spherical dipole wave, which re-expresses it as an infinite sum of plane-waves. For a cylindrically symmetric system this transformation is equivalent to the Sommerfeld identity:

$$\frac{e^{ik_0 r}}{r} = \int_0^\infty dk_\rho \left\{ \frac{k_\rho}{k_z} J_0\left(k_\rho \rho\right) e^{ik_z |z|} \right\} \tag{6.4}$$

This identity expresses the spherical wave as a product of plane waves in the z-direction with wavevector k_z wighted by cylindrical transverse waves (encapsulated in the zeroth-order Bessel function $J_0\left(k_\rho \rho\right)$) with wavevector $k_\rho = \sqrt{k_x^2 + k_y^2}$ ($\rho = \sqrt{x^2 + y^2}$). The wavevectors are linked by $k_i = \sqrt{k_\rho^2 + \left(k_z^i\right)^2}$, including both travelling ($k_\rho < k_i$) and evanescent ($k_\rho > k_i$) contributions.

Plane wave boundary conditions can be applied to each contribution to the inte-

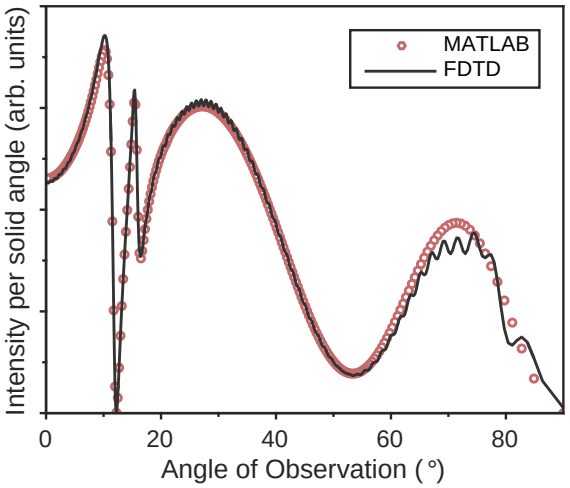

Figure 6.3.: **Dipole far-field comparison** Points are calculated from the semi-analytic model. Curve found through FDTD simulation (Lumerical). Intensity owing to structure discussed in section 6.3.1

gral, ensuring the conservation of the transverse wavevector across the boundaries. The total boundary conditions for the heterostructure can then be found using 2x2 plane wave matrix methods, in a method similar to chapter 5 in reference [81]. Again, full details can be found in appendix B.

6.2.2. Far-field approximations

Plane wave boundary conditions provide us with integral expressions for the dipole potentials at each point in the structure, however they are not directly soluble. While the dielectric structures may contain features in the near-field of the optical dipole, we are only concerned with the field at far distances where $rk_i \gg 1$. In this limit the integral can then be approximated to first order through the method of stationary phase [279]. The fast oscillation of the integrand phase ensures that only plane waves with wavevectors parallel to the direction of observation contribute to the far-field [280]. The fields and Poynting vectors due to the buried dipoles can then be found from the far-field potentials and the orthogonal polarisations recombined to obtain the full dipole field.

The two-stage decomposition of the dipole field and the analytic far-field approx-

imations form a light-weight method to model a stack of arbitrary dielectrics, where the only computationally difficult step is the calculation of the boundary conditions for a many-layered structure at each observation angle. The full-force method of finite-difference time-domain (FDTD) simulation is always available, although is generally a much more computationally intensive procedure. To check the implementation of the method, figure 6.3 displays a comparison of the Poynting Vector distribution with FDTD simulation for the quantum dot sample structure we will discuss in section 6.3.1. The semi-analytical model shows good agreement with the full simulation, while taking $\sim 1/300$ of the time to perform.

We implement this technique to determine structures that could maximise the outcoupling of quantum dot samples, however it applies to any buried two-level system, such as molecules or NV-centres [269, 270], and can predict effects such as radiative emission enhancement or suppression owing to the modified local density of states [281–284] (up to the strong coupling regime, where a full QED treatment is required).

6.3. Quantum dot device structure

In section 1.4.3 we introduced the methods we have in place to try and access a significant proportion of the quantum dot emission distribution. With a Zirconia SIL and a DBR stack, we still estimate from recorded count rates that at the first collection lens we are only accessing 5-10% of the full field.

To understand how we can maximise the amount of collected radiation from the quantum dot, we can examine the DBR reflectivity in more detail. Figure 6.4a shows the plane wave reflectivity for our DBR stack as a function of incident angle for both TE and TM radiation at 950 nm. For small angles the interference condition provides near-unity reflectivity, however above 20°, the larger effective length of the alternating layers prevents constructive interference, and the reflectivity drops to a low value. Above 65° total internal reflection between the layers causes the stack to

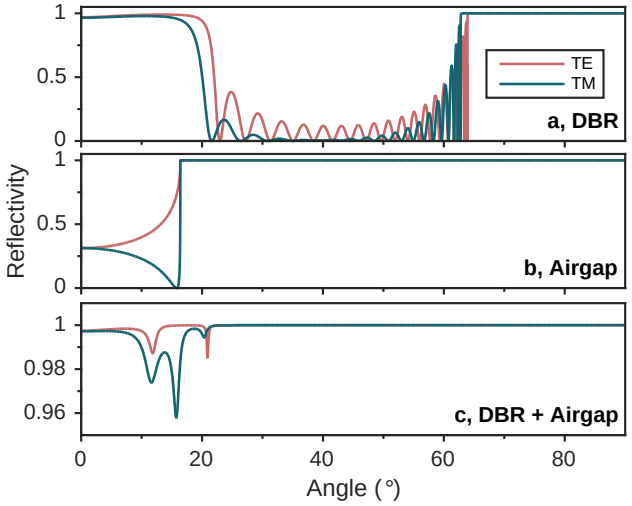

Figure 6.4.: **Sub-quantum dot reflections a** DBR Stack for TE & TM waves at 950 nm. **b** $3\lambda/4$ air-gap. **c** Both layers, separated by 110 nm.

become reflective again.

As a comparison, if we consider an air-gap in the sample with a $3\lambda/4$ thickness, we recover the reflectivity plotted in figure 6.4b. The air-gap is only partially reflective at small angles, however above 17°, total internal reflection ensures a complete return of the incident field.

Figure 6.4c displays the combined reflectivity of the DBR and air-gap, set at a 110-nm distance to ensure constructive interference in the reflected fields. Now the complementary behaviours of the two layers act together to realise a near unity reflectivity for all incident angles.

6.3.1. Structure design

We can find the far-field dipole intensity distributions due to the air-gap DBR combination by the method outlined in section 6.2. We model the quantum dot excitation as a horizontal dipole with a 950-nm wavelength, and take the refractive index of gallium arsenide at 3.44, taken from cryogenic measurements [74, 75]. The doped layer is neglected as its effect on the refractive index of the material is expected to

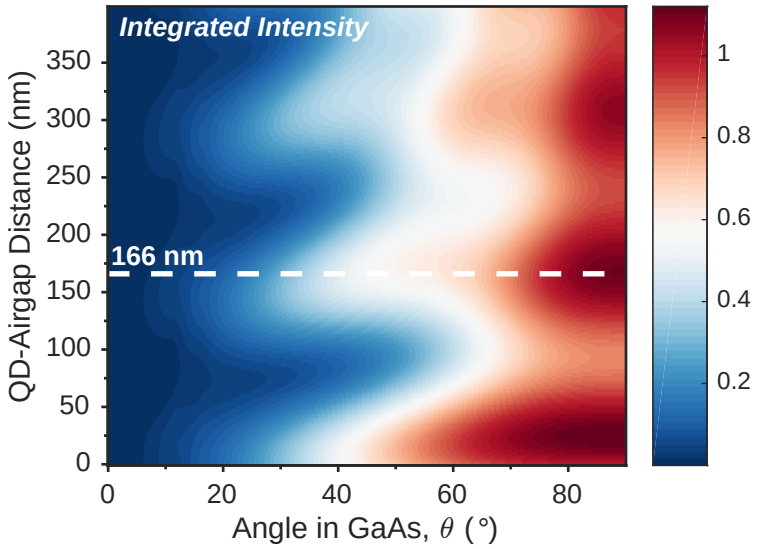

Figure 6.5.: **Integrated dipole intensities** Upper half-space intensities integrated up to angle θ for changing distance from QD to air-gap. Intensities normalised to dipole in bulk GaAs.

be small [285].

We consider a structure where the dipole sits at a certain distance from a $3\lambda/4$ air-gap (710 nm), which is in turn 110 nm from a 20-layer AlAs/$Al_{0.3}Ga_{0.7}As$ DBR stack above a GaAs substrate. We then find the radiation into an upper half-space of GaAs. This is motivated by the use of a GaAs SIL, which, in matching the sample index, provides the highest collection efficiencies.

Figure 6.5 shows the integrated dipole intensity up to angle θ for varying distance between the quantum dot and the reflective air-gap. This allows us to determine the distance that will ensure constructive interference between the source and reflective fields and a maximum photon rate from the sample. This is provided by a distance of 166 nm, marked in the figure (we require a minimum QD-air-gap distance of 75 nm to host the tunnel barrier and doped layer). This distance generates the Poynting vector distribution in figure 6.3, averaged over the azimuthal angle.

The total intensities are normalised to the 4π emission into bulk GaAs. For the correct geometry, values slightly exceeding unity (1.1 for $\theta = 90°$ at 166nm)

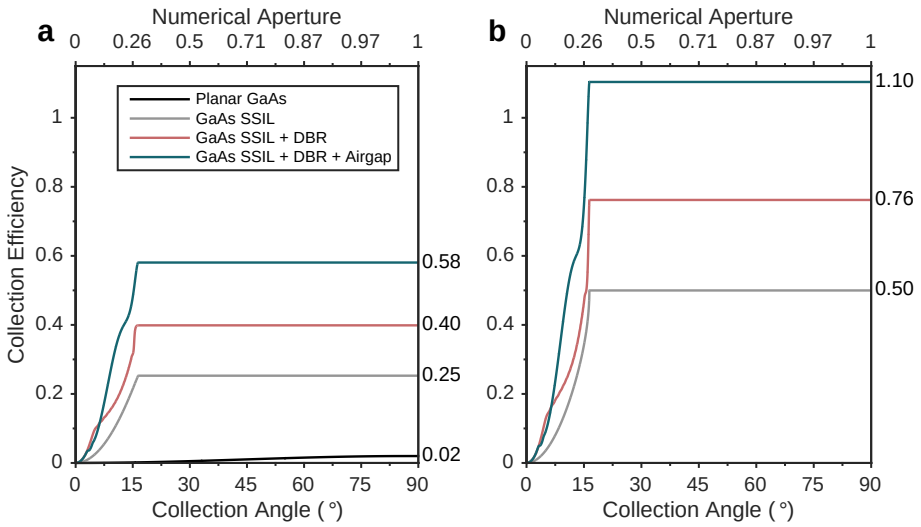

Figure 6.6.: **Free-space collection efficiencies** Dipole fields within collection angle outside super-hemispherical GaAs SIL assuming **a**, all reflected fields lost at surface of SIL, **b** no surface losses at SIL.

are expected. This is enhancement of the radiative rate due to the constructive interference of the emitted fields [281], occuring at interface distances consistent with studies on self-assembled QD emission rates near air-interfaces reported in reference [286].

By propagating the intensity through a super-hemispherical SIL, set by the geometry in section 1.4.3, we can find the free-space collection efficiency of the structure. Two estimates are displayed in figure 6.6. We plot the collection efficiency as a function of collection angle or numerical aperture (NA) for the air-gap-DBR combination, a DBR only structure and a featureless substrate. The super-hemispherical SIL funnels the dipole field to within an NA of 0.3. The two panels in the figure correspond to two limits of the SIL operation. In panel a, we assume full interface losses at the surface of the lens (set by the Fresnel coefficients in figure 6.4b). In panel 6.6b, we assume that all of the light is transmitted through the lens surface. For all the structures, we find a factor of ~ 2 difference between the extremes. With anti-reflection coating, we would recover in some intermediate case between these two situations [287].

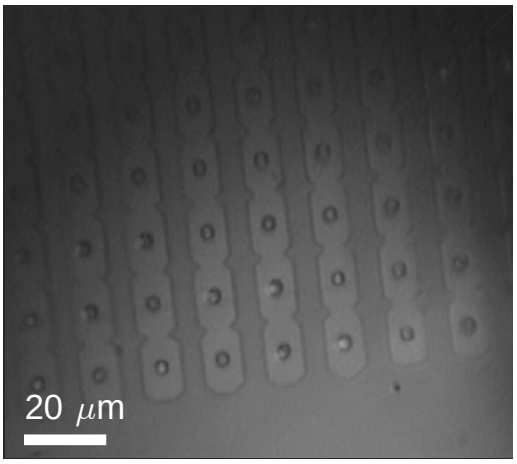

Figure 6.7.: **Partially under-etched sample** Holes spaced by 15μm. Lighter areas correspond to under-etching.

6.3.2. Device construction

To define the air-gap we grow a sacrificial layer of $Al_{0.8}Ga_{0.2}As$ between the DBR and the n-doped layer. In the sample processing stage, we etch down to this layer at an array of points separated by 15 μm with a dilute mixture of sulphuric acid and hydrogen peroxide, and then use a selective etch of dilute hydrogen fluoride to remove the aluminium rich regions of the sample structure. With the correct exposure time to the etchant we are left with a thin membrane containing the Schottky diode structure supported at various points between the etch-holes. Figure 6.7 displays an image of the partially under-etched taken through a Zironia solid-immersion lens, showing the holes around which the sample has been etched and the remaining support areas.

In figure 6.8 we show some preliminary characterisation of these samples. Both panels contain photoluminescence spectra of X^{1-} peaks with those in panel a from six dots on non-etched regions, and in panel b from six in under-etched areas. All studied dots show a similar pickup of extracted fluorescence. We record an average three-fold increase between the two sets of dots. In moving to resonance fluorescence, the sample of dots studied here were found to suffer from significant spectral wandering, featuring noise on the scale of the transition linewidth in the tens of

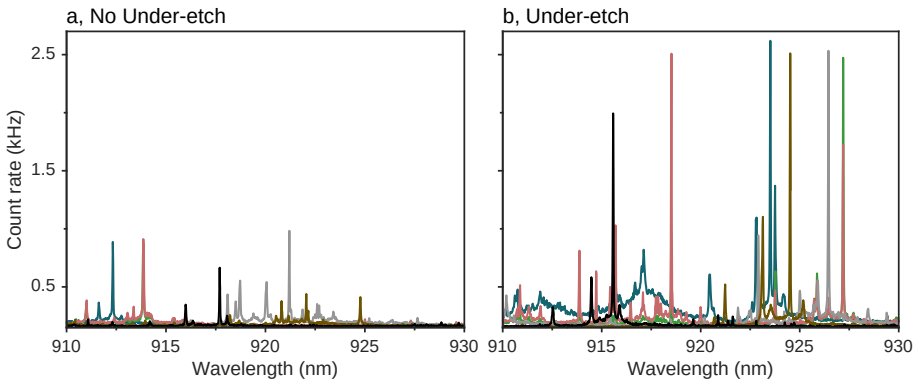

Figure 6.8.: **Under-etched Photoluminescence** PL spectra for dots within the same sample on **a** non-underetched regions and **b** underetched regions.

μs timescale. These fluctuations are probably caused to some extent by the under-etched surface. A newer generation of samples featuring thicker doped layers should help to ameliorate this issue.

6.4. Conclusions & outlook

With the air-gap-DBR combination we now have access to the total emission of the quantum dot in the upper half of the sample, which, with the addition of a SIL can in principle be funnelled into a reasonable numerical aperture.

In the absence of any reflecting surface, figure 6.6 shows that we should be able to extract a large amount (25-50%) of the dipole field into a far-sub unity numerical aperture. These efficiencies require that the SIL is in close contact with the sample surface to counter total-internal reflection at all angles of incidence. Deviations from this ideal-immersion condition emerge on the sub-wavelength level owing to the long optical path high-angle beams experience [288]. To understand this effect, in figure 6.9 we estimate the proportion of the emission inside the immersion lens for increasing sample-SIL mounting-gap distance. To avoid any cavity effects that may emerge we consider the mounting gap as a pure source of loss and neglect the reflected fields. Owing to the loss of high-angle fields the proportion decreases rapidly as a gap is introduced between the sample and the lens. The loss of collection

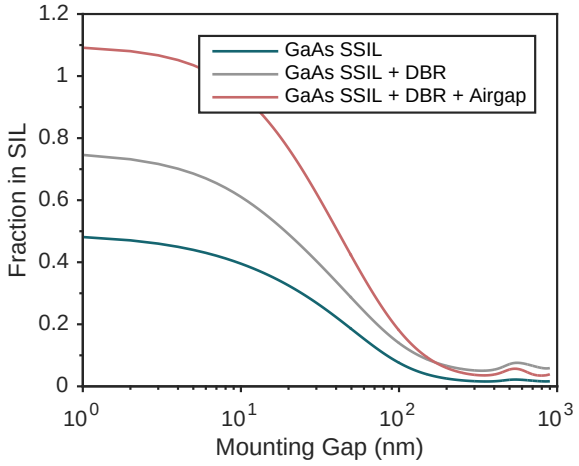

Figure 6.9.: **SIL mounting-gap collection efficiency** Proportion of dipole emission transmitted into GaAs SIL for varying mounting gap distance.

over the 10-100 nm range is critical, particularly in comparing these length scales with typical tolerances of polished spherical lenses.

A powerful new alternative is the creation of deterministically placed microlenses around individual quantum dots in a hybrid spectroscopy and lithography process [219]. These lenses are formed directly from the GaAs substrate without the contacting issue of macroscopic lenses [289], and work is ongoing to combine this technique with our Schottky devices. One particular challenge of this approach will be the small feature size of the microlense with respect to our excitation laser focal spot. This introduces mode distortion to the scattered beam: a potential challenge to our highly mode dependent polarisation-based laser rejection technique.

A clear extension to the techniques in this chapter would be to express the dipole emitted field in terms of the Gaussian mode that couples well into our collection fibre. For instance, the field in the focal spot of our microscope could be expressed in a multipole expansion [290], or alternatively, the overlap found between the field distribution after the focussing lens and the gaussian fibre mode. This should provide sample designs specifically suited to single-mode fibre coupling.

CONCLUSIONS & FURTHER WORK

The work contributing to this thesis has achieved three main goals: a full understanding of the evolution of electron spin coherence in self-assembled quantum dots, the high-frequency entanglement of two distant electron spins and the demonstration of an optical link between two distinctly different quantum systems: a self-assembled quantum dot and a single ytterbium ion.

In chapter 3 we linked the evolution of electron spin coherence to the distinct material properties of InGaAs quantum dots. In showing that the nuclear spin interaction with inhomogeneous strain fields is the critical parameter in determining the storage of a quantum state in the electron spin, we hope to motivate the investigation of spin coherence in other quantum dot varieties that feature tailored strain properties.

The entanglement of distant electron spins presented in chapter 4 is to some extent a culmination of our work on both coherent light-matter interaction and spin control. Its demonstration, however opens the door to using entangled electron spins in these structures as a resource. One limiting factor for higher-order entanglement demonstrations in these systems is the lack of single-shot ground state readout through optical pumping. Proposals to change the basis of the spin [118] or the use of spin to charge conversion are available [119, 291], which will allow us to characterise the entangled state at rates approaching its distribution.

The entanglement scheme we demonstrated in chapter 4 is inherently probabilistic, and if we want to connect larger numbers of qubits, we must be able to protect

the state during our repeated attempts at forming the next link. This has been demonstrated in NV centres, where the entangled state is mapped onto local nuclear spins in a way that is protected against decoherence due to the optically driven NV [292]. A local memory could be provided if we move from single quantum dots to coupled quantum dot molecules. Here, the two spins can either form a singlet-triplet qubit [293], or the second spin can act as a memory for the first [294]. In another proposal the optically active QD is capacitively coupled to an electrostatically-defined quantum dot [295], which takes advantage of the longer decoherence times for electron spins in the latter [144].

A particular task that spins in self-assembled quantum dots could excel at is the generation of entangled optical states [296]. In these schemes, determining the spin population is the final step necessary to decouple the resident spin from the generated photon string [158]. In this way the high-oscillator strength and single-mode coupling of quantum dot transitions provide an advantage against similar optically active systems, even in the absence of single-shot population readout. Furthermore, entanglement between distant electron spins could then be mapped to entangled photon generation [297].

The use of a single spin confined to a self-assembled dot as an entangler for a chain of scattered photons is a very promising application as described in reference [158]. In this case, spin-photon entanglement is extended to produce a chain of entangled photons by alternating between periods of free precession and excitation. For the scheme outlined in this reference the successful generation of long strings of photons requires a strict hierarchy between the excited state decay rate Γ_{exc}, the ground state precession rate Δ_e and the dephasing time T_2: $1/T_2 \ll \Delta_e \ll \Gamma_{\text{exc}}$. To ensure at least a stable electron spin population, the 30-mT width of the Overhauser field demands a minimum spin splitting of $\sim$ 600 MHz, which approaches the exciton decay rate. One route could be to controllably alter the spin precession through application of high Rabi frequency detuned optical pulses. Alternatively, the weaker hole-spin hyperfine coupling could allow for a stable spin state at sufficiently small

splittings. Additionally, cavity coupling would increase the decay rate of the exciton [298], separating its timescale from the spin precession. As discussed in chapter 2, we expect nuclear polarisation to play an important role in these schemes. Here, this polarisation could be advantageous, extending the dephasing time by reducing fluctuations in the nuclear bath [148]. An alternative route to realising this scheme has been demonstrated with the dark exciton as a qubit [299].

The development of a hybrid quantum network is an important long-term goal, which the work in chapter 5 provides some first steps towards. A promising current route is the work on strain-free quantum dots at 780 nm, matched to the $D2$ transitions in rubidium [300]. The recent reports on coherent optical transitions in these systems enables the same bandwidth matching with the atomic transition as demonstrated here [186].

Sample out-coupling plays a key role in all of these demonstrations, particularly the generation of high-number entangled photonic states. At the current state of the art, research groups can now combine gated samples with DBR cavities [217, 218], enabling the resonant generation of indistinguishable photons. These strongly-coupled systems are particularly interesting as they permit new types of interaction with the optical field based on dispersive coupling to the transition [301, 302]. This ability to switch the polarisation of an incident photon provides another route to overcome the bandwidth mismatch with single atoms [240].

As research into InGaAs quantum dots reaches maturity a target of the experimental work contributing to this thesis has been the continual development of atomic physics-style experiments in the solid state. This has resulted in a flexible experimental setup capable of manipulating and characterising electron spin states in multiple quantum dots as well as interfering their scattering with a controlled phase. On a technical level, the knowledge developed in how the timescales of external hardware and intrinsic processes intersect provides the technological groundwork for further networking demonstrations using these optically manipulated spins.

APPENDIX

A

PULSE SEQUENCE CONSTRUCTION

For the coherent spin control and entanglement experiments, synchronising the spin readout and preparation with the repetition of the modelocked laser is essential for constructing meaningful control sequences. The modelocked laser itself is not clocked to any external reference, so we convert a pick-off of the optical signal to an electrical pulse via high frequency photodiodes. This 76 MHz signal provides a clock and start trigger for driving the optical modulators for continuous-wave sources, as well as picking rotation pulses.

For basic schemes, such as single pulse spin-Rabi oscillations and free-induction decay measurements, the integrated readout signal provides the time-averaged spin state information. However for more complex schemes such the alternating Ramsey interference, Hahn-echo and spin-spin entanglement, the modelocked clock is also passed to a time-to-digital converter (TDC). This trigger provides a reference for finding readout regions of interest within the sequence.

For all the single spin measurements, the modelocked laser (MIRA-900) is split at the output into two distinct arms: 'moving' and 'stationary', which are recombined before reaching the microscope. The moving arm contains a Nanomotion stepper stage to scan the delay between the arms. In addition, four passes of a metre-long optical rail provide a controllable delay between the pulses from 0 to 6.5 ns. The

readout pulses are formed with electro-optic modulators (EOM), which suppress the laser with a waveguide Mach-Zehnder interferometer. The interferometer phase requires active stabilisation against thermal drifts, which we provide an optical pick-off after the modulator and a stabilisation board (Photline MBC-DG board).

A historical note: as the complexity of the experiments increased, so did the equipment available. Accordingly, the earlier setups used were set by the limited pulse sources and modulators available, and the later schemes could take advantage of greater flexibility in the modulation of our different optical sources. In general, the later setups are capable of providing the functionality of earlier iterations, especially when we include an arbitrary waveform generator, which was introduced for the demanding distant entanglement experiment.

A.1. Version 1 - Basic readout suppression

In the simplest case, sketched in figure A.1, we ensure that the readout laser is suppressed during the rotation-sequence to prevent unwanted spin pumping. To do this we monitor the modelocked laser with a 150-MHz bandwidth photodiode (Thorlabs PDA10A). This generates 3-ns broad bandwidth-limited pulses following the pulse train. We then amplify this signal with a MiniCircuits ZFL-1000H+ amp and pass the resulting envelope to the readout laser EOM.

The timing of the modulation is controlled through the length of coaxial cable between the amplifier and the modulator, and the 18 cm ns^{-1} propagation speed of the signal in the coaxial dielectric. The three curves in the left panel of figure A.2 show the overlap between the readout modulation and two control pulses, separated by 0.5 ns, for different coaxial lengths. The right panel displays the final, 127 cm length used that centres the readout modulation on the Ramsey sequence. The traces here are recorded with a Picoscope 9200 sampling oscilloscope.

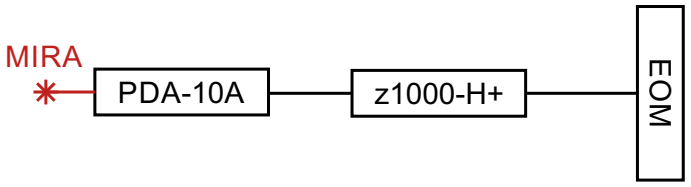

Figure A.1.: **Basic pulse sequence for modulating readout.** The amplifier gain is set to match the photodiode voltage to the maximum-extinction voltage of the electro-optic amplitude modulator.

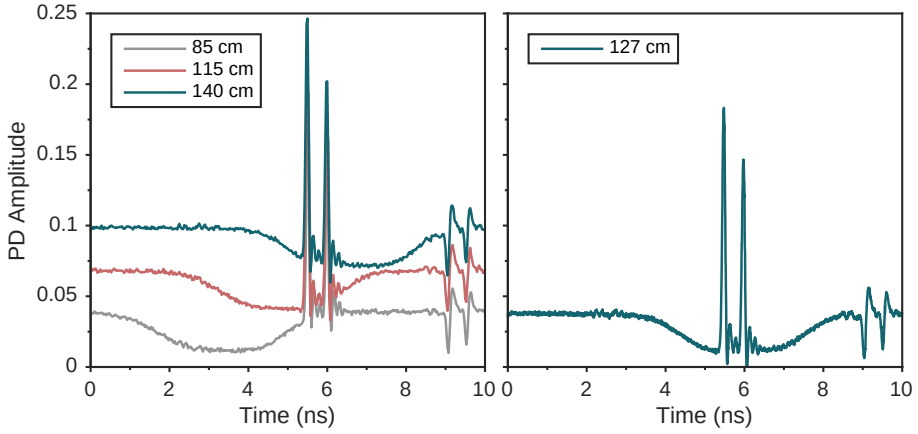

Figure A.2.: **Delay tuning of the Version 1 pulse sequence** Two modelocked pulses seperated by 0.5 ns and the modulated readout laser are shown. By altering the length of coaxial between the photodiode and the modulator, the suppression window is centred on the rotations.

A.2. Version 2 - Modulation > 76 MHz

An extension to the minimal sequence is possible with an Anritsu MP1763C Pulse Pattern Generator (PPG), which provides arbitrary square-wave modulation at frequencies up to 12.5 GHz. The PPG constructs the sequence out of bins with the same repetition frequency as a square or sinusoidal clock input. In order to pulse the readout laser between the modelocked repetition cycle, the 76 MHz signal from the high frequency photodiode has to be upconverted. This can be achieved in more than one way, either by filtering out and amplifying a high harmonic of a high frequency photodiode output, or through directly converting the signal. We choose the latter, using a home-made phase-locked loop (PLL) to convert a band-passed signal from the photodiode at 76 MHz up to 2.43 GHz. This then provides a clock

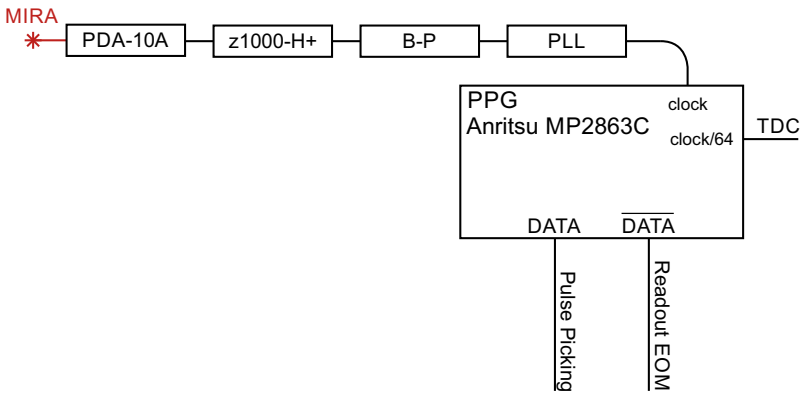

Figure A.3.: **PLL-triggered PPG.**Pulse sequence for providing sub-13 ns pulsing by up-converting the modelocked laser photodiode signal to provide a high-frequency clock for the PPG.

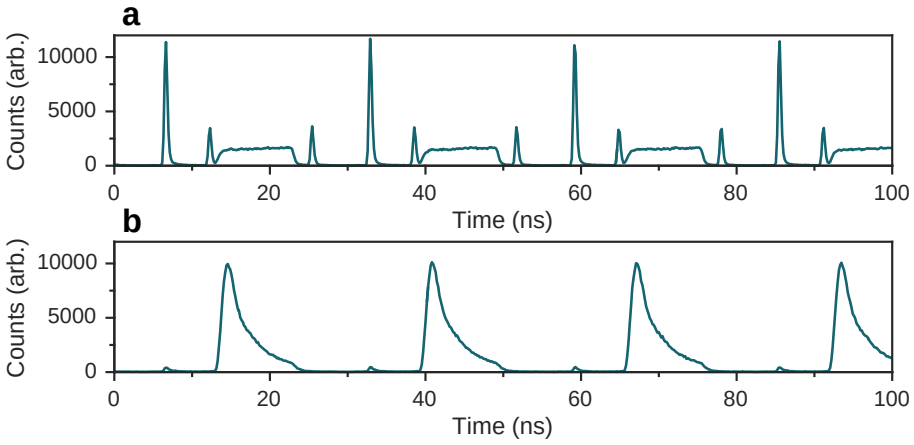

Figure A.4.: **PPG pulse sequence and fluorescence. a** Readout pulse and rotations for a 13.1 ns Hahn-echo sequence.**b** Corresponding fluorescence from the quantum dot. Traces are recorded from single photon detection events correlated with the sequence clock with a time-to-digital converter.

for the PPG with 32 bins per pulsed-laser repetition. The PPG can play an arbitrary square wave sequence containing up to 8,388,608 steps and can output both the original and inverse sequences. The scheme is displayed in figure A.3, which includes the amplifier and band-pass filter required to provide a sinusoidal input to the PLL. Finally, a 1/64 clock output from the PPG allows us to synchronise the spin-readout to the control sequence.

With a single EOM in the path of the combined arms of the modelocked laser, this setup can also perform initial Hahn-echo measurements. We achieve this by passing the main output of the PPG to the readout-laser modulator (on for 24 of 64 bins) and the inverted signal to the rotation-pulse picker (on for 40 of 64 bins). An example of the pulse sequence from this setup is shown in figure A.4. Panel a displays the readout pulses and the Hahn-echo rotations. Panel b displays the readout signal from the quantum dot. The inputs are suppressed with polarisation and only the signal from the spin readout every 26 ns remains. Allowing us to operate at the repetition rate of the pulsed laser is particularly important when measuring the de-polarisation of nuclear spins, as the long waiting times needed to depolarise the bath limit the amount of useful signal we can extract.

A.3. Version 3 - High suppression

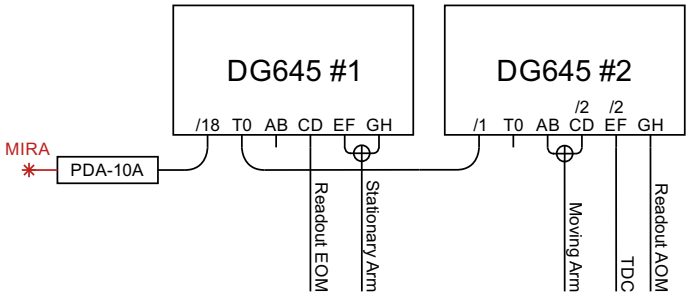

Figure A.5.: **Hahn-echo hardware.** Two SRS DG645 delay generators with outputs combined through radio-frequency splitters.

For the Hahn-echo measurements in chapter 3, we have independent pulse picking of both the moving and stationary arms of the split-modelocked laser. Additionally,

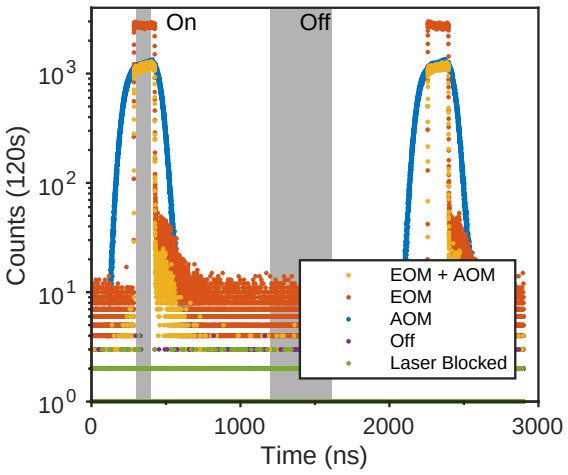

	Suppression
EOM	516
AOM	3687
EOM + AOM	6321

Figure A.6.: **Long time readout suppression.** Correlated laser scatter with variety of modulation: AOM, EOM or both. The table displays the extracted suppression ratio between the marked regions in the figure.

operating at the highest repetition rate is not crucial as the alternating sequence does not require that the nuclear bath relax. For these experiments, we use two Stanford Research Systems DG645 Digital Delay Generators, as displayed in figure A.5. The delay generators require a dead-time of $\sim 100ns$ per loop, yet by combining the pulses together with radio frequency splitters used in reverse ($\oplus$ symbols), we can pick multiple rotation pulses and drive the readout EOM. Additional dividers on individual channels (marked in the figure) allow us to perform alternating measurements with an additional π-rotation every second repeat to prevent nuclear polarisation.

These experiments require long off-times of the readout laser ($> 1\mu s$). In order to combat against residual spin-pumping we add an Acousto-optic modulator (AOM) to the readout laser path, which provides additional suppression during non-read times. Figure A.6 shows correlated background counts from this sequence for a variety of modulator combinations. By adding an AOM to the path we increase the suppression ratio from $\sim$ 500:1 to $\sim$ 6000:1. Combining this enhanced suppression with a sub-saturation readout power prevents optical pumping during the long spin

storage times.

A.4. Version 4 - Spin-spin entanglement

Entangling distant electron spins presents the most demanding requirements of any pulse sequence, as both quantum dots require independent rotation, readout and preparation, cycling through 4 permutations of spin readout per repetition of the experiment. At the same time, the need to find rare three-photon coincident events requires that the scheme was run at the highest repetition rate possible.

Figure A.7 contains a schematic of the electrical setup we use. The central component to the experiment is a Tektronix 70002A arbitrary waveform generator (AWG) that produces square voltage pulses for entanglement (160 ps) and readout (5 + 15 ns). These are amplified to the voltages we require for maximum EOM extinction. The sequence runs on a loop, triggered from a DG645 which subdivides the signal from the modelocked laser. A filtered signal from the modelocked source at 76 MHz provides a clock to synchronise the AWG.

Pulse picking is performed by a pair of DG645 pulse delay generators, triggered by the AWG. The configuration shown is used for the X basis measurement, where alternating $\pi/2$ and $3\pi/2$-rotations are sent to the quantum dots 0.9 nanoseconds after the entanglement pulse. Four $\pi/2$ pulses are formed from the combinatorial output at the back of each delay generator, two of which are boosted up to $3\pi/2$-rotations by the front panel outputs. Unlike the Hahn-echo experiments, the rotation pulses are now picked by 350 MHz AOMs, which provide a bandwidth sufficient to distinguish 13.15 ns-separated optical pulses. This sequence allows us to run one prepare-entangle-read cycle in 6 repetitions of the modelocked laser (78.8 ns) with a 52.56 ns pause every four measurements for the dead-time of the DG645 delay generators. A clock pulse every 56 cycles provided a reference for the TDC.

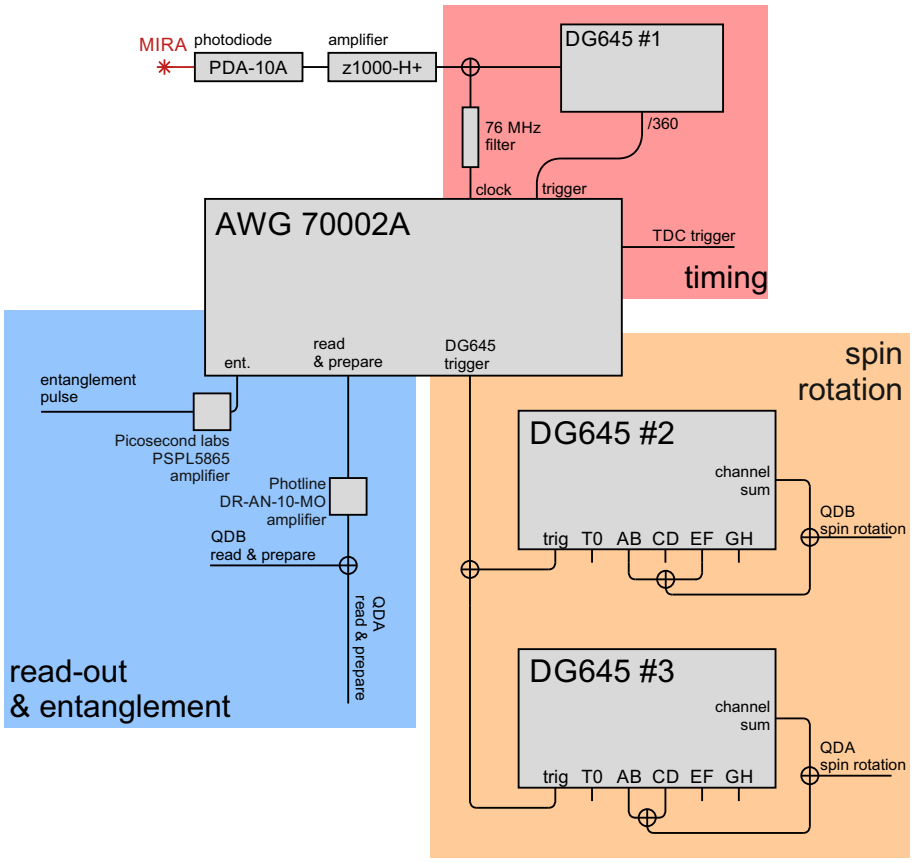

Figure A.7.: **Entanglement experiment electrical hardware** The setup can be divided into three main parts, responsible for the overall timing, the modulation of spin readout and entanglement pulses, and the pulse picking of the modelocked laser for coherent spin rotations.

APPENDIX

B

BURIED DIPOLE BOUNDARY CONDITIONS

This appendix shows in slightly more depth how the effect of a one-dimensional heterostructure of planar dielectrics upon the far field of a buried dipole's emission pattern can be calculated.

B.1. Polarisation decoupling

The method of decoupling an arbitrary dipole into symmetric vertical electric and magnetic dipoles was introduced by Lukosz [303, 304] and explored in depth by Brueck [305]. With the general dipole Hertz vector given by (6.1), the two decoupled electric and magnetic vectors are taken as:

$$\mathbf{\Pi}^E = (0, 0, \phi) \quad \mathbf{\Pi}^H = (0, 0, \psi)\,, \tag{B.1}$$

which only contain z-components due to the orientation of the decoupled dipoles.

In equation 6.4, we introduced the Sommerfeld identity, which expresses the spherical vector field owing to a vertical electric dipole as an integral of weighted plane waves ($k_\rho < k$) and evanescent contributions ($k_\rho > k$). The identity is the two-dimensional Fourier transform of a spherical wave, which is more generally for a function Φ:

$$\Phi = \iint_{-\infty}^{\infty} \tilde{\Phi}\left(k_x, k_y\right) e^{i(k_x x + k_y y + k_z z)} \mathrm{d}k_x \mathrm{d}k_y. \tag{B.2}$$

We perform this operation with our symmetric vertical-dipole Hertz vectors:

$$\phi = \iint_{-\infty}^{\infty} \tilde{\phi} e^{i(k_x x + k_y y + k_z z)} \mathrm{d}k_x \mathrm{d}k_y, \tag{B.3}$$

$$\psi = \iint_{-\infty}^{\infty} \tilde{\psi} e^{i(k_x x + k_y y + k_z z)} \mathrm{d}k_x \mathrm{d}k_y. \tag{B.4}$$

By comparing the fields of the vertical dipoles with the electric dipole at angle θ_d in the x-z plane (see figure 6.2), the values of $\tilde{\phi}$ and $\tilde{\psi}$ can be found [280]:

$$\tilde{\phi}_{\pm} = \frac{ip_0}{8\pi^2}\left(\frac{\cos\theta_d}{k_z} \mp \frac{k_x}{k_x^2 + k_y^2}\sin\theta_d\right), \tag{B.5}$$

$$\tilde{\psi} = \frac{-i\mu_0 p_0 \omega k_y}{8\pi^2 k_z\left(k_x^2 + k_y^2\right)}\sin\theta_d. \tag{B.6}$$

Note the $\mp$ sign in the expression for $\tilde{\phi}$. This sign depends on whether the field is evaluated above ($\tilde{\phi}_+$) or below ($\tilde{\phi}_-$) the emitter, owing to the phase change in transforming from an oscillating electric dipole with some horizontal component ($\theta_\mathrm{d} \neq 0$) to a vertical dipole.

B.2. Trial solutions

Having decoupled the polarisations of the dipole emission, we form trial solutions for the potentials in the source and outer layers (S, T & B):

$$\phi_\mathrm{T} = \iint_{-\infty}^{\infty} \tilde{\phi}_\mathrm{T} e^{i(k_x x + k_y y + k_z z)} \mathrm{d}k_x \mathrm{d}k_y, \tag{B.7}$$

$$\phi_{\mathrm{S}} = \phi_{\pm} + \iint_{-\infty}^{\infty} \tilde{\phi}_{\mathrm{S}_+} e^{i(k_x x + k_y y + k_z z)} \mathrm{d}k_x \mathrm{d}k_y + \iint_{-\infty}^{\infty} \tilde{\phi}_{\mathrm{S}_-} e^{i(k_x x + k_y y - k_z z)} \mathrm{d}k_x \mathrm{d}k_y, \quad \text{(B.8)}$$

$$\phi_{\mathrm{B}} = \iint_{-\infty}^{\infty} \tilde{\phi}_{\mathrm{B}} e^{i(k_x x + k_y y - k_z z)} \mathrm{d}k_x \mathrm{d}k_y. \quad \text{(B.9)}$$

The top region contains waves travelling in the positive z direction and the bottom region waves in the negative direction. The source region contains both the terms directly due to the dipole ($\phi_{\pm}$) and the reflected positive- and negative-travelling waves ($\tilde{\phi}_{\mathrm{S}_+}$ & $\tilde{\phi}_{\mathrm{S}_-}$). The next step is to link these solutions with boundary conditions at each layer to find their value for each k_x & k_y.

B.3. Matrix methods

With the dipole potential now fully disassembled into orthogonal components we can now introduce the dielectric structure to determine the form of the trial solutions in equations B.7, B.8 & B.9. At a dielectric interface in the heterostructure between layer i and layer $i+1$ the z-components of electric and magnetic Hertz vectors must satisfy the following boundary conditions (assuming a non-magnetic material):

$$\phi_i = \phi_{i+1}; \quad \frac{1}{\epsilon_i}\frac{\partial \phi_i}{\partial z} = \frac{1}{\epsilon_{i+1}}\frac{\partial \phi_{i+1}}{\partial z}; \quad \psi_i = \psi_{i+1}; \quad \frac{\partial \psi_i}{\partial z} = \frac{\partial \psi_{i+1}}{\partial z} \quad \text{(B.10)}$$

As each layer (except for the top and bottom regions) contains both outgoing and incoming plane waves in the z-direction, the derivatives in the boundary conditions can be simplified such that the conditions in (B.10) can be cast in matrix form:

$$\mathbf{D_i^{TM}} \begin{pmatrix} \tilde{\phi}_i^{OUT} \\ \tilde{\phi}_i^{IN} \end{pmatrix} = \mathbf{D_{i+1}^{TM}} \begin{pmatrix} \tilde{\phi}_{i+1}^{OUT} \\ \tilde{\phi}_{i+1}^{IN} \end{pmatrix}, \tag{B.11}$$

$$\begin{pmatrix} 1 & 1 \\ \frac{k_z^i}{\epsilon_i} & -\frac{k_z^i}{\epsilon_i} \end{pmatrix} \begin{pmatrix} \tilde{\phi}_i^{OUT} \\ \tilde{\phi}_i^{IN} \end{pmatrix} = \begin{pmatrix} 1 & 1 \\ \frac{k_z^{i+1}}{\epsilon_{i+1}} & -\frac{k_z^{i+1}}{\epsilon_{i+1}} \end{pmatrix} \begin{pmatrix} \tilde{\phi}_{i+1}^{OUT} \\ \tilde{\phi}_{i+1}^{IN} \end{pmatrix}, \tag{B.12}$$

$$\mathbf{D_i^{TE}} \begin{pmatrix} \tilde{\psi}_i^{OUT} \\ \tilde{\psi}_i^{IN} \end{pmatrix} = \mathbf{D_{i+1}^{TE}} \begin{pmatrix} \tilde{\psi}_{i+1}^{OUT} \\ \tilde{\psi}_{i+1}^{IN} \end{pmatrix}, \tag{B.13}$$

$$\begin{pmatrix} 1 & 1 \\ k_z^i & -k_z^i \end{pmatrix} \begin{pmatrix} \tilde{\psi}_i^{OUT} \\ \tilde{\psi}_i^{IN} \end{pmatrix} = \begin{pmatrix} 1 & 1 \\ k_z^{i+1} & -k_z^{i+1} \end{pmatrix} \begin{pmatrix} \tilde{\psi}_{i+1}^{OUT} \\ \tilde{\psi}_{i+1}^{IN} \end{pmatrix}, \tag{B.14}$$

where ϕ_i^{OUT} and ϕ_i^{IN} are the incoming and outgoing parts of the Hertz Vector. We also include matrices for the phase accumulated by propagation of the potential through each layer:

$$\begin{pmatrix} \tilde{\phi}_i^{OUT} \\ \tilde{\phi}_i^{IN} \end{pmatrix} = \mathbf{P_i^{TM}} \begin{pmatrix} \tilde{\phi}_i^{OUT} \\ \tilde{\phi}_i^{IN'} \end{pmatrix} = \begin{pmatrix} e^{-ik_z^i \Delta_i} & 0 \\ 0 & e^{ik_z^i \Delta_i} \end{pmatrix} \begin{pmatrix} \tilde{\phi}_i^{OUT} \\ \tilde{\phi}_i^{IN} \end{pmatrix}, \tag{B.15}$$

where Δ_i is the thickness of each layer. Combining these two forms of matrix together way we can find a single transformation that describes the structure above our below the emitter:

$$\begin{aligned} \begin{pmatrix} \phi_S^{OUT} \\ \phi_S^{IN} \end{pmatrix} &= \mathbf{D_{TOT}^{TM}} \begin{pmatrix} \phi_T^{OUT} \\ \phi_T^{IN} \end{pmatrix}, \\ &= \left(\mathbf{D_S^{TM}}\right)^{-1} \prod_i \left\{ \mathbf{D_i^{TM}} \mathbf{P_i^{TM}} \left(\mathbf{D_i^{TM}}\right)^{-1} \right\} \mathbf{D_T^{TM}} \begin{pmatrix} \phi_T^{OUT} \\ \phi_T^{IN} \end{pmatrix}, \end{aligned} \tag{B.16}$$

where the product is over all the layers between the source region and the structure exterior. Of key interest is the field in the top region outside the structure. We solve for the boundary conditions with the condition that the top and bottom layers only contain out-going waves. As a result the value of $\tilde{\phi}_{\mathrm{T}}$ (and $\tilde{\psi}_{\mathrm{T}}$) can be expressed in terms of the transfer-matrix elements and the source field $\phi_{\pm}$:

$$\tilde{\phi}_{\mathrm{T},+} = \frac{\frac{1}{D_U^{11}}\left(\tilde{\phi}_+ + \tilde{\phi}_- \frac{D_L^{21}}{D_L^{11}}\right)}{1 - \frac{D_L^{21}}{D_L^{11}}\frac{D_U^{21}}{D_U^{11}}}. \tag{B.17}$$

The subscripts U&L correspond to total matrices for the layers above and below the dipole, respectively. This has a simple physical interpretation, as the ratio $\frac{D^{21}}{D^{11}}$ is linked to the reflectivity of a collection of layers, and the value of $\frac{1}{D^{11}}$ related to the transmission through those layers. Importantly, equation B.17 includes positive ($\tilde{\phi}_+$) and negative travelling ($\tilde{\phi}_-$) source terms as the correct phase relationship in equation B.5 needs to be taken into account. The same relationship can be found for the magnetic dipole, $\psi_{\mathrm{T},+}$.

Having found these values the integral can be approximated according to methods in references [280] and [305], the far field expressions for ϕ and ψ can be found and the Poynting vectors determined for the original dipole.

REFERENCES

1. Deutsch, D & Jozsa, R. Rapid Solution of Problems by Quantum Computation. *Proceedings of the Royal Society of London Series A-Mathematical Physical and Engineering Sciences.* **439,** 553–558 (1992).

2. Shor, P. Polynomial-Time Algorithms for Prime Factorization and Discrete Logarithms on a Quantum Computer. *SIAM Journal on Computing* **26,** 1484–1509 (1997).

3. Bennett, C. H. & Brassard, G. Quantum cryptography: Public key distribution and coin tossing. *International Conference on Computers, Systems & Signal Procmputers, Systems & Signal Processing* **1,** 175 –179 (1984).

4. Ekert, A. K. Quantum cryptography based on Bell's theorem. *Physical Review Letters* **67,** 661 (1991).

5. Feynman, R. P. Simulating physics with computers. *International Journal of Theoretical Physics* **21,** 467–488 (1982).

6. Shor, P. W. Scheme for reducing decoherence in quantum computer memory. *Physical Review A* **52,** 2493–2496 (1995).

7. Steane, A. M. Error Correcting Codes in Quantum Theory. *Physical Review Letters* **77,** 793–797 (1996).

8. Kitaev, A. Anyons in an exactly solved model and beyond. *Annals of Physics* **321,** 2–111 (2006).

9. Fowler, A. G., Mariantoni, M., Martinis, J. M. & Cleland, A. N. Surface codes: Towards practical large-scale quantum computation. *Physical Review A* **86,** 032324 (2012).

10. Kimble, H. J. The quantum internet. *Nature* **453,** 1023–1030 (2008).

11. Nickerson, N. H., Li, Y. & Benjamin, S. C. Topological quantum computing with a very noisy network and local error rates approaching one percent. *Nature communications* **4,** 1756 (2013).

12. Monroe, C. *et al.* Large-scale modular quantum-computer architecture with atomic memory and photonic interconnects. *Physical Review A* **89,** 022317 (2014).

13. Childress, L, Taylor, J. M., Sørensen, A. S. & Lukin, M. D. Fault-tolerant quantum repeaters with minimal physical resources and implementations based on single-photon emitters. *Physical Review A* **72,** 052330 (2005).

14. Raussendorf, R. & Briegel, H. J. A One-Way Quantum Computer. *Physical Review Letters* **86,** 5188–5191 (2001).

15. Schön, C., Solano, E., Verstraete, F., Cirac, J. I. & Wolf, M. M. Sequential Generation of Entangled Multiqubit States. *Physical Review Letters* **95,** 110503 (2005).

16. Cirac, J. I., Zoller, P., Kimble, H. J. & Mabuchi, H. Quantum State Transfer and Entanglement Distribution among Distant Nodes in a Quantum Network. *Physical Review Letters* **78,** 3221–3224 (1997).

17. Schneider, C. *et al.* Lithographic alignment to site-controlled quantum dots for device integration. *Applied Physics Letters* **92,** 183101 (2008).

18. Mouradian, S. L. *et al.* Scalable Integration of Long-Lived Quantum Memories into a Photonic Circuit. *Physical Review X* **5,** 031009 (2015).

19. Javadi, A. *et al.* Single-photon non-linear optics with a quantum dot in a waveguide. *Nature Communications* **6,** 8655 (2015).

20. Reithmaier, G. *et al.* On-Chip Generation, Routing, and Detection of Resonance Fluorescence. *Nano Letters* **15,** 5208–5213 (2015).

21. Press, D., Ladd, T. D., Zhang, B. & Yamamoto, Y. Complete quantum control of a single quantum dot spin using ultrafast optical pulses. *Nature* **456,** 218–221 (2008).

22. Matthiesen, C., Vamivakas, A. N. & Atatüre, M. Subnatural Linewidth Single Photons from a Quantum Dot. *Physical Review Letters* **108,** 093602 (2012).

23. Schulte, C. H. H., Hansom, J., Jones, A. E., Matthiesen, C., Le Gall, C. & Atatüre, M. Quadrature squeezed photons from a two-level system. *Nature* **525,** 222–225 (2015).

24. Matthiesen, C. *et al.* Phase-locked indistinguishable photons with synthesized waveforms from a solid-state source. *Nature Communications* **4,** 1600 (2013).

25. Wallquist, M., Hammerer, K., Rabl, P., Lukin, M. & Zoller, P. Hybrid quantum devices and quantum engineering. *Physica Scripta* **T137,** 014001 (2009).

26. Morton, J. J. & Lovett, B. W. Hybrid Solid-State Qubits: The Powerful Role of Electron Spins. *Annual Review of Condensed Matter Physics* **2,** 189–212 (2011).

27. Kurizki, G. *et al.* Quantum technologies with hybrid systems. *Proceedings of the National Academy of Sciences* **112,** 3866–3873 (2015).

28. Yoffe, A. D. Low-dimensional systems: quantum size effects and electronic properties of semiconductor microcrystallites (zero-dimensional systems) and some quasi-two-dimensional systems. *Advances in Physics* **42,** 173–262 (1993).

29. Murray, C. B., Sun, S., Gaschler, W., Doyle, H., Betley, T. A. & Kagan, C. R. Colloidal synthesis of nanocrystals and nanocrystal superlattices. *IBM Journal of Research and Development* **45,** 47–56 (2001).

30. Kastner, M. A. The single-electron transistor. *Reviews of Modern Physics* **64,** 849–858 (1992).

31. Singleton, J. *Band Theory and Electronic Properties of Solids* ISBN: 978-0-19-850644-7 (Oxford University Press, 2001).

32. Yu, P. Y. & M, C. *Fundamentals of Semiconductors* ISBN: 3-540-25470-6 (Springer-Verlag Berlin Heidelberg, 2005).

33. Stranski, I. N. & Krastanow, L. Berichtigung zur Arbeit. *Monatshefte für Chemie* **72,** 76–76 (1939).

34. Shchukin, V. A. & Bimberg, D. Spontaneous ordering of nanostructures on crystal surfaces. *Reviews of Modern Physics* **71,** 1125–1171 (1999).

35. Pimpinelli, A. & Villain, J. *Physics of Crystal Growth* ISBN: 978-0-511-62252-6 (Cambridge University Press, 1998).

36. Leonard, D., Krishnamurthy, M., Reaves, C. M., Denbaars, S. P. & Petroff, P. M. Direct formation of quantum-sized dots from uniform coherent islands of InGaAs on GaAs surfaces. *Applied Physics Letters* **63,** 3203–3205 (1993).

37. Bulutay, C. Quadrupolar spectra of nuclear spins in strained InxGa(1-x)As quantum dots. *Physical Review B* **85,** 115313 (2012).

38. Leonard, D, Pond, K & Petroff, P. M. Critical layer thickness for self-assembled InAs islands on GaAs. *Physical Review B* **50,** 11687–11692 (1994).

39. Leon, R, Kim, Y., Jagadish, C, Gal, M, Zou, J & Cockayne, D. J. H. Effects of interdiffusion on the luminescence of InGaAs/GaAs quantum dots. *Applied Physics Letters* **69,** 1888 (1996).

40. McFarlane, J. *et al.* Gigahertz bandwidth electrical control over a dark exciton-based memory bit in a single quantum dot. *Applied Physics Letters* **94,** 093113 (2009).

41. Bayer, M. *et al.* Fine structure of neutral and charged excitons in self-assembled In(Ga)As/(Al)GaAs quantum dots. *Physical Review B* **65,** 195315 (2002).

42. Atatüre, M., Dreiser, J., Badolato, A., Hogele, A., Karrai, K. & Imamoglu, A. Quantum-Dot Spin-State Preparation with Near-Unity Fidelity. *Science* **312,** 551–553 (2006).

43. Gao, W. B., Fallahi, P, Togan, E, Miguel-Sanchez, J & Imamoglu, A. Observation of entanglement between a quantum dot spin and a single photon. *Nature* **491,** 426–430 (2012).

44. De Greve, K. *et al.* Quantum-dot spin-photon entanglement via frequency downconversion to telecom wavelength. *Nature* **491,** 421–425 (2012).

45. Schaibley, J. R. *et al.* Demonstration of Quantum Entanglement between a Single Electron Spin Confined to an InAs Quantum Dot and a Photon. *Physical Review Letters* **110,** 167401 (2013).

46. Gywat, O., Krenner, H. J. & Berezovsky, J. *Spins in Optically Active Quantum Dots* ISBN: 78-3-527-40806-1 (Wiley-VCH, Weinheim, Germany, 2009).

47. Foot, C. *Atomic Physics* 144. ISBN: 0-19-850696-1 (Oxford University Press, 2006).

48. Johansen, J. *et al.* Size dependence of the wavefunction of self-assembled InAs quantum dots from time-resolved optical measurements. *Physical Review B* **77,** 073303 (2008).

49. Olmschenk, S. *et al.* Measurement of the lifetime of the 6p2Po1/2 level of Yb+. *Physical Review A* **80,** 022502 (2009).

50. Glass, R. Evaluation of the resonance oscillator strength of calcium. *Journal of Physics B: Atomic and Molecular Physics* **18,** 4047–4053 (1985).

51. Kuhlmann, A. V. *et al.* Transform-limited single photons from a single quantum dot. *Nature Communications* **6,** 8204 (2015).

52. Cohen-Tannoudji, C., Dupont-Roc, J. & Grynberg, G. *Atom-Photon Interactions* 353–405. ISBN: 9783527617197 (Wiley-VCH Verlag GmbH, 2008).

53. Meystre, P. & Sargent, M. *Elements of Quantum Optics* ISBN: 9783540742098 (2007).

54. Dagenais, M. & Mandel, L. Investigation of two-time correlations in photon emissions from a single atom. *Physical Review A* **18,** 2217–2228 (1978).

55. Loudon, R. *The Quantum Theory of Light* 2nd, 290–307. ISBN: 978-0-198-50176-3 (Oxford University Press, 1983).

56. Konthasinghe, K *et al.* Coherent versus incoherent light scattering from a quantum dot. *Physical Review B* **85,** 235315 (2012).

57. Autler, S. H. & Townes, C. H. Stark effect in rapidly varying fields. *Physical Review* **100,** 703–722 (1955).

58. Schabert, A., Keil, R. & Toschek, P. E. Dynamic stark effect of an optical line observed by cross-saturated absorption. *Applied Physics* **6,** 181–184 (1975).

59. Mollow, B. R. Power Spectrum of Light Scattered by Two-Level Systems. *Physical Review* **188,** 1969–1975 (1969).

60. Wu, F. Y., Grove, R. E. & Ezekiel, S. Investigation of the spectrum of resonance fluorescence induced by a monochromatic field. *Physical Review Letters* **35,** 1426–1429 (1975).

61. Flagg, E. B. *et al.* Resonantly driven coherent oscillations in a solid-state quantum emitter. *Nature Physics* **5,** 203–207 (2009).

62. Nick Vamivakas, A., Zhao, Y., Lu, C.-Y. & Atatüre, M. Spin-resolved quantum-dot resonance fluorescence. *Nature Physics* **5,** 198–202 (2009).

63. Neave, J. H., Dobson, P. J., Harris, J. J., Dawson, P. & Joyce, B. A. Silicon doping of MBE-grown GaAs films. *Applied Physics A Solids and Surfaces* **32,** 195–200 (1983).

64. Drexler, H, Leonard, D, Hansen, W, Kotthaus, J. P. & Petroff, P. M. Spectroscopy of Quantum Levels in Charge-Tunable InGaAs Quantum Dots. *Physical Review Letters* **73,** 2252–2255 (1994).

65. Warburton, R. J. *et al.* Optical emission from a charge-tunable quantum ring. *Nature* **405,** 926–929 (2000).

66. Smith, J. M. *et al.* Voltage Control of the Spin Dynamics of an Exciton in a Semiconductor Quantum Dot. *Physical Review Letters* **94,** 197402 (2005).

67. Dreiser, J., Atatüre, M., Galland, C., Müller, T., Badolato, A. & Imamoglu, A. Optical investigations of quantum dot spin dynamics as a function of external electric and magnetic fields. *Physical Review B* **77,** 075317 (2008).

68. Latta, C., Srivastava, A. & Imamoglu, A. Hyperfine Interaction-Dominated Dynamics of Nuclear Spins in Self-Assembled InGaAs Quantum Dots. *Physical Review Letters* **107,** 167401 (2011).

69. Fry, P. W. *et al.* Inverted Electron-Hole Alignment in InAs-GaAs Self-Assembled Quantum Dots. *Physical Review Letters* **84,** 733–736 (2000).

70. Mowbray, D. J. & Skolnick, M. S. New physics and devices based on self-assembled semiconductor quantum dots. *Journal of Physics D: Applied Physics* **38,** 2059–2076 (2005).

71. Schulhauser, C. *et al.* Giant permanent dipole moments of excitons in semiconductor nanostructures. *Physica E: Low-Dimensional Systems and Nanostructures* **13,** 161–164 (2002).

72. Hansom, J., Schulte, C. H. H., Matthiesen, C., Stanley, M. J. & Atatüre, M. Frequency stabilization of the zero-phonon line of a quantum dot via phonon-assisted active feedback. *Applied Physics Letters* **105,** 172107 (2014).

73. Prechtel, J. H. *et al.* Fast electro-optics of a single self-assembled quantum dot in a charge-tunable device. *Journal of Applied Physics* **111,** 043112 (2012).

74. Marple, D. T. F. Refractive Index of GaAs. *Journal of Applied Physics* **35,** 1241 (1964).

75. Reynolds, D. C., Bajaj, K. K., Litton, C. W., Peters, G., Yu, P. W. & Parsons, J. D. Refractive index, n, and dispersion, dn/dλ, of GaAs at 2 K determined from Fabry Perot cavity oscillations. *Journal of Applied Physics* **61,** 342 (1987).

76. Zwiller, V. & Bjork, G. Improved light extraction from emitters in high refractive index materials using solid immersion lenses. *Journal of applied physics* **92,** 660–665 (2002).

77. Mansfield, S. M. & Kino, G. S. Solid immersion microscope. *Applied Physics Letters* **57,** 2615 (1990).

78. Nickolas Vamivakas, A. *et al.* A case study for optics: The solid immersion microscope. *American Journal of Physics* **76,** 758 (2008).

79. Serrels, K. A. *et al.* Solid immersion lens applications for nanophotonic devices. *Journal of Nanophotonics* **2,** 21829–21854 (2008).

80. Ippolito, S. B., Goldberg, B. B. & ÜNlü, M. S. Theoretical analysis of numerical aperture increasing lens microscopy. *Journal of Applied Physics* **97,** 053105 (2005).

81. Yeh, P. *Optical Waves in Layered Media* 118–134. ISBN: 978-0-471-73192-4 (Wiley, 2005).

82. Thoma, A. *et al.* Exploring Dephasing of a Solid-State Quantum Emitter via Time- and Temperature-Dependent Hong-Ou-Mandel Experiments. *Physical Review Letters* **116,** 033601 (2016).

83. Bayer, M., Walck, S. N., Reinecke, T. & Forchel, A. Exciton binding energies and diamagnetic shifts in semiconductor quantum wires and quantum dots. *Physical Review B* **57,** 6584–6591 (1998).

84. Nick Vamivakas, A., Zhao, Y., Lu, C.-Y. & Atatüre, M. Spin-resolved quantum-dot resonance fluorescence. *Nature Physics* **5,** 198–202 (2009).

85. Kuhlmann, A. V. *et al.* Charge noise and spin noise in a semiconductor quantum device. *Nature Physics* **9,** 570–575 (2013).

86. Matthiesen, C., Stanley, M. J., Hugues, M., Clarke, E. & Atatüre, M. Full counting statistics of quantum dot resonance fluorescence. *Scientific Reports* **4,** 4911 (2014).

87. Stanley, M. J. *et al.* Dynamics of a mesoscopic nuclear spin ensemble interacting with an optically driven electron spin. *Physical Review B* **90,** 195305 (2014).

88. Besombes, L., Kheng, K., Marsal, L. & Mariette, H. Acoustic phonon broadening mechanism in single quantum dot emission. *Physical Review B* **63,** 155307 (2001).

89. Bernien, H. *et al.* Heralded entanglement between solid-state qubits separated by three metres. *Nature* **497,** 86–90 (2013).

90. Kimble, H. J., Dagenais, M. & Mandel, L. Photon antibunching in resonance fluorescence. *Physical Review Letters* **39,** 691–695 (1977).

91. Matthiesen, C. *Coherent photons from a solid-state artificial atom* PhD thesis (University of Cambridge, 2013).

92. DiVincenzo, D. P. The physical implementation of quantum computation. *Forschritte der Physik-Progress of Physics* **48,** 771–783 (2000).

93. Khaetskii, A. V. & Nazarov, Y. V. Spin-flip transitions between Zeeman sublevels in semiconductor quantum dots. *Physical Review B* **64,** 125316 (2001).

94. Woods, L. M., Reinecke, T. L. & Kotlyar, R. Hole spin relaxation in quantum dots. *Physical Review B* **69,** 125330 (2004).

95. Hanson, R., Kouwenhoven, L. P., Petta, J. R., Tarucha, S. & Vandersypen, L. M. K. Spins in few-electron quantum dots. *Reviews of Modern Physics* **79,** 1217–1265 (2007).

96. Kroutvar, M. *et al.* Optically programmable electron spin memory using semiconductor quantum dots. *Nature* **432,** 81–84 (2004).

97. Amasha, S. *et al.* Electrical Control of Spin Relaxation in a Quantum Dot. *Physical Review Letters* **100,** 046803 (2008).

98. Lu, C.-Y. *et al.* Direct measurement of spin dynamics in InAs/GaAs quantum dots using time-resolved resonance fluorescence. *Physical Review B* **81,** 035332 (2010).

99. Golovach, V. N., Khaetskii, A. & Loss, D. Phonon-Induced Decay of the Electron Spin in Quantum Dots. *Physical Review Letters* **93,** 016601 (2004).

100. Yang, W. & Sham, L. J. General theory of feedback control of a nuclear spin ensemble in quantum dots. *Physical Review B* **88,** 235304 (2013).

101. Abe, E. *et al.* Electron spin coherence of phosphorus donors in silicon: Effect of environmental nuclei. *Physical Review B* **82,** 121201 (2010).

102. De Lange, G, Wang, Z. H., Riste, D., Dobrovitski, V. V. & Hanson, R. Universal Dynamical Decoupling of a Single Solid-State Spin from a Spin Bath. *Science* **330,** 60–63 (2010).

103. Fermi, E. Über die magnetischen Momente der Atomkerne. *Zeitschrift für Physik* **60,** 320–333 (1930).

104. Urbaszek, B. *et al.* Nuclear spin physics in quantum dots: An optical investigation. *Reviews of Modern Physics* **85,** 79–133 (2013).

105. Gammon, D *et al.* Electron and Nuclear Spin Interactions in the Optical Spectra of Single GaAs Quantum Dots. *Physical Review Letters* **86,** 5176–5179 (2001).

106. Merkulov, I. A., Efros, A. L. & Rosen, M. Electron spin relaxation by nuclei in semiconductor quantum dots. *Physical Review B* **65,** 205309 (2002).

107. Koppens, F. H. L. Control and Detection of Singlet-Triplet Mixing in a Random Nuclear Field. *Science* **309,** 1346–1350 (2005).

108. Hansom, J. *et al.* Environment-assisted quantum control of a solid-state spin via coherent dark states. *Nature Physics* **10,** 725–730 (2014).

109. Högele, A. *et al.* Dynamic Nuclear Spin Polarization in the Resonant Laser Excitation of an InGaAs Quantum Dot. *Physical Review Letters* **108,** 197403 (2012).

110. Latta, C *et al.* Confluence of resonant laser excitation and bidirectional quantum-dot nuclear-spin polarization. *Nature Physics* **5,** 758–763 (2009).

111. Welander, E., Chekhovich, E., Tartakovskii, A. & Burkard, G. Influence of Nuclear Quadrupole Moments on Electron Spin Coherence in Semiconductor Quantum Dots, 36–40 (2014).

112. Chekhovich, E., Hopkinson, M., Skolnick, M. & Tartakovskii, A. Suppression of nuclear spin bath fluctuations in self-assembled quantum dots induced by inhomogeneous strain. *Nature Communications* **6,** 6348 (2015).

113. Waeber, A. M. *et al.* Few-second-long correlation times in a quantum dot nuclear spin bath probed by frequency-comb nuclear magnetic resonance spectroscopy. *Nature Physics* **12,** 688–693 (2016).

114. Haupt, F., Imamoglu, A. & Kroner, M. Single Quantum Dot as an Optical Thermometer for Millikelvin Temperatures. *Physical Review Applied* **2,** 024001 (2014).

115. Xu, X. *et al.* Fast Spin State Initialization in a Singly Charged InAs-GaAs Quantum Dot by Optical Cooling. *Physical Review Letters* **99,** 097401 (2007).

116. Emary, C., Xu, X., Steel, D. G., Saikin, S. & Sham, L. J. Fast Initialization of the Spin State of an Electron in a Quantum Dot in the Voigt Configuration. *Physical Review Letters* **98,** 047401 (2007).

117. Delteil, A., Gao, W.-b., Fallahi, P., Miguel-Sanchez, J. & Imamoglu, A. Observation of Quantum Jumps of a Single Quantum Dot Spin Using Submicrosecond Single-Shot Optical Readout. *Physical Review Letters* **112,** 116802 (2014).

118. Flagg, E. B. & Solomon, G. S. Optical spin readout method in a quantum dot using the ac Stark effect. *Physical Review B* **92,** 245309 (2015).

119. Bechtold, A. *et al.* Three-stage decoherence dynamics of an electron spin qubit in an optically active quantum dot. *Nature Physics* **11,** 1005–1008 (2015).

120. Jelezko, F., Gaebel, T., Popa, I., Gruber, A. & Wrachtrup, J. Observation of Coherent Oscillations in a Single Electron Spin. *Physical Review Letters* **92,** 076401 (2004).

121. Pla, J. J. *et al.* A single-atom electron spin qubit in silicon. *Nature* **489,** 541–545 (2012).

122. Brion, E, Pedersen, L. H. & Mølmer, K. Adiabatic elimination in a lambda system. *Journal of Physics A: Mathematical and Theoretical* **40,** 1033–1043 (2007).

123. Quilter, J. H. *et al.* Phonon-Assisted Population Inversion of a Single InGaAs/GaAs Quantum Dot by Pulsed Laser Excitation. *Physical Review Letters* **114,** 137401 (2015).

124. Ramsay, A. J. *et al.* Damping of Exciton Rabi Rotations by Acoustic Phonons in Optically Excited InGaAs/GaAs Quantum Dots. *Physical Review Letters* **104,** 017402 (2010).

125. Ulhaq, A. *et al.* Detuning-dependent Mollow triplet of a coherently-driven single quantum dot. *Optics Express* **21,** 4382 (2013).

126. Barends, R *et al.* Superconducting quantum circuits at the surface code threshold for fault tolerance. *Nature* **508,** 500–503 (2014).

127. Barends, R. *et al.* Rolling quantum dice with a superconducting qubit. *Physical Review A* **90,** 030303 (2014).

128. Yamamoto, Y *et al.* Optically controlled semiconductor spin qubits for quantum information processing. *Physica Scripta* **T137,** 014010 (2009).

129. Levitt, M. H. Composite pulses. *Progress in Nuclear Magnetic Resonance Spectroscopy* **18,** 61–122 (1986).

130. *Quantum Dots Optics, Electron Transport and Future Applications* (ed Tartakovskii, A.) ISBN: 978-1-107-01258-5 (Cambridge University Press, 2012).

131. Warburton, R. J. Self-assembled semiconductor quantum dots. *Contemporary Physics* **43,** 351–364 (2002).

132. Skolnick, M. & Mowbray, D. Self-Assembled semiconductor quantum dots: Fundamental Physics and Device Applications. *Annual Review of Materials Research* **34,** 181–218 (2004).

133. Warburton, R. J. Single spins in self-assembled quantum dots. *Nature Materials* **12,** 483–493 (2013).

134. Chekhovich, E. A. *et al.* Nuclear spin effects in semiconductor quantum dots. *Nature Materials* **12,** 494–504 (2013).

135. De Greve, K., Press, D., McMahon, P. L. & Yamamoto, Y. Ultrafast optical control of individual quantum dot spin qubits. *Reports on progress in physics. Physical Society (Great Britain)* **76,** 092501 (2013).

136. Lodahl, P., Mahmoodian, S. & Stobbe, S. Interfacing single photons and single quantum dots with photonic nanostructures. *Reviews of Modern Physics* **87,** 347–400 (2015).

137. Warburton, R. J. *et al.* Optical emission from a charge-tunable quantum ring. *Nature* **405,** 926–929 (2000).

138. Press, D. *et al.* Ultrafast optical spin echo in a single quantum dot. *Nature Photonics* **4,** 367–370 (2010).

139. Flagg, E., Muller, A., Polyakov, S., Ling, A., Migdall, A. & Solomon, G. Interference of Single Photons from Two Separate Semiconductor Quantum Dots. *Physical Review Letters* **104,** 137401 (2010).

140. He, Y. *et al.* Indistinguishable Tunable Single Photons Emitted by Spin-Flip Raman Transitions in InGaAs Quantum Dots. *Physical Review Letters* **111,** 237403 (2013).

141. Gao, W. *et al.* Quantum teleportation from a propagating photon to a solid-state spin qubit. *Nature Communications* **4,** 2744 (2013).

142. Delteil, A., Sun, Z., Gao, W., Togan, E., Faelt, S. & Imamoglu, A. Generation of heralded entanglement between distant hole spins. *Nature Physics* **12,** 218–223 (2015).

143. Viola, L. & Lloyd, S. Dynamical suppression of decoherence in two-state quantum systems. *Physical Review A* **58,** 2733–2744 (1998).

144. Bluhm, H. *et al.* Dephasing time of GaAs electron-spin qubits coupled to a nuclear bath exceeding 200 μs. *Nature Physics* **7,** 109–113 (2011).

145. Ladd, T. D. *et al.* Quantum computers. *Nature* **464,** 45–53 (2010).

146. Sun, Z., Delteil, A., Faelt, S. & ImamoÄ§lu, A. Measurement of spin coherence using Raman scattering. *Physical Review B* **93,** 241302 (2016).

147. Ladd, T. D. *et al.* Nuclear Feedback in a Single Electron-Charged Quantum Dot under Pulsed Optical Control. arXiv: `1008.0912` (2010).

148. Xu, X. *et al.* Optically controlled locking of the nuclear field via coherent dark-state spectroscopy. *Nature* **459,** 1105–1109 (2009).

149. Greilich, A *et al.* Nuclei-Induced Frequency Focusing of Electron Spin Coherence. *Science* **317,** 1896–1899 (2007).

150. Le Gall, C., Brunetti, A., Boukari, H. & Besombes, L. Electron-nuclei spin dynamics in II-VI semiconductor quantum dots. *Physical Review B* **85,** 195312 (2012).

151. Dyakonov, M. I. & Perel, V. I. in *Optical Orientation* (eds Meier, F & Zakharchenya, B. P.) 11–71 (Elsevier, 1984).

152. Greilich, A. Mode Locking of Electron Spin Coherences in Singly Charged Quantum Dots. *Science* **313,** 341–345 (2006).

153. Onur, A. R., de Jong, J. P., O'Shea, D., Reuter, D., Wieck, A. D. & van der Wal, C. H. Stabilizing nuclear spins around semiconductor electrons via the interplay of optical coherent population trapping and dynamic nuclear polarization. *Physical Review B* **93,** 161204 (2016).

154. Sousa, R. D. Electron spin as a spectrometer of nuclear-spin noise and other fluctuations. *Topics Appl. Physics* **115,** 183 (2009).

155. Braun, P.-F. *et al.* Direct Observation of the Electron Spin Relaxation Induced by Nuclei in Quantum Dots. *Physical Review Letters* **94,** 116601 (2005).

156. Moehring, D. L. *et al.* Entanglement of single-atom quantum bits at a distance. *Nature* **449,** 68–71 (2007).

157. Ritter, S. *et al.* An elementary quantum network of single atoms in optical cavities. *Nature* **484,** 195–200 (2012).

158. Lindner, N. H. & Rudolph, T. Proposal for Pulsed On-Demand Sources of Photonic Cluster State Strings. *Physical Review Letters* **103,** 113602 (2009).

159. Bylander, J. *et al.* Noise spectroscopy through dynamical decoupling with a superconducting flux qubit. *Nature Physics* **7,** 565–570 (2011).

160. Hahn, E. L. Spin Echoes. *Physical Review* **80,** 580–594 (1950).

161. Chekhovich, E., Hopkinson, M., Skolnick, M. & Tartakovskii, A. Suppression of nuclear spin bath fluctuations in self-assembled quantum dots induced by inhomogeneous strain. *Nature Communications* **6,** 6348 (2015).

162. Waeber, A. M. *et al.* Few-second-long correlation times in a quantum dot nuclear spin bath probed by frequency-comb nuclear magnetic resonance spectroscopy. *Nature Physics* **12,** 688–693 (2016).

163. Viola, L., Knill, E. & Lloyd, S. Dynamical Decoupling of Open Quantum Systems. *Physical Review Letters* **82,** 2417–2421 (1999).

164. Szwer, D. J., Webster, S. C., Steane, A. M. & Lucas, D. M. Keeping a single qubit alive by experimental dynamic decoupling. *Journal of Physics B: Atomic, Molecular and Optical Physics* **44,** 025501 (2011).

165. Cywiński, L., Witzel, W. M. & Das Sarma, S. Pure quantum dephasing of a solid-state electron spin qubit in a large nuclear spin bath coupled by long-range hyperfine-mediated interactions. *Physical Review B* **79,** 245314 (2009).

166. Neder, I., Rudner, M. S., Bluhm, H., Foletti, S., Halperin, B. I. & Yacoby, A. Semiclassical model for the dephasing of a two-electron spin qubit coupled to a coherently evolving nuclear spin bath. *Physical Review B* **84,** 035441 (2011).

167. Biercuk, M. J., Doherty, a. C. & Uys, H. Dynamical decoupling sequence construction as a filter-design problem. *Journal of Physics B: Atomic, Molecular and Optical Physics* **44,** 154002 (2011).

168. Klauder, J. & Anderson, P. Spectral Diffusion Decay in Spin Resonance Experiments. *Physical Review* **125,** 912–932 (1962).

169. Cywiński, L., Lutchyn, R. M., Nave, C. P. & Das Sarma, S. How to enhance dephasing time in superconducting qubits. *Physical Review B* **77,** 174509 (2008).

170. Uhrig, G. S. Exact results on dynamical decoupling by π pulses in quantum information processes. *New Journal of Physics* **13,** 059504 (2011).

171. Cywiński, Ł. Dynamical-decoupling noise spectroscopy at an optimal working point of a qubit. *Physical Review A* **90,** 042307 (2014).

172. Ajoy, A., Álvarez, G. A. & Suter, D. Optimal pulse spacing for dynamical decoupling in the presence of a purely dephasing spin bath. *Physical Review A* **83,** 032303 (2011).

173. Newland, D. *An Introduction to Random Vibration, Spectral & Wavelet Analysis* Third Ed., 41. ISBN: 0-582-21584-6 (Longman Scientific & Technical, 1993).

174. Wüst, G. *et al.* Role of the electron spin in determining the coherence of the nuclear spins in a quantum dot. *Nature Nanotechnology,* 1–6 (2016).

175. Bulutay, C., Chekhovich, E. A. & Tartakovskii, A. I. Nuclear magnetic resonance inverse spectra of InGaAs quantum dots: Atomistic level structural information. *Physical Review B* **90,** 205425 (2014).

176. Botzem, T., McNeil, R. P. G., Mol, J.-M., Schuh, D., Bougeard, D. & Bluhm, H. Quadrupolar and anisotropy effects on dephasing in two-electron spin qubits in GaAs. *Nature Communications* **7,** 11170 (2016).

177. Malinowski, F. K. *et al.* Notch filtering the nuclear environment of a spin qubit. *Nature Nanotechnology* **12,** 16–20 (2016).

178. Rowan, L., Hahn, E. & Mims, W. Electron-Spin-Echo Envelope Modulation. *Physical Review* **137,** A61–A71 (1965).

179. Mims, W. B. Envelope Modulation in Spin-Echo Experiments. *Physical Review B* **5,** 2409–2419 (1972).

180. Brunner, D. *et al.* A Coherent Single-Hole Spin in a Semiconductor. *Science* **325,** 70–72 (2009).

181. De Greve, K. *et al.* Ultrafast coherent control and suppressed nuclear feedback of a single quantum dot hole qubit. *Nature Physics* **7,** 872–878 (2011).

182. Godden, T. M. *et al.* Coherent Optical Control of the Spin of a Single Hole in an InAs/GaAs Quantum Dot. *Physical Review Letters* **108,** 017402 (2012).

183. Carter, S. G. *et al.* Strong hyperfine-induced modulation of an optically driven hole spin in an InAs quantum dot. *Physical Review B* **89,** 075316 (2014).

184. Prechtel, J. H. *et al.* Decoupling a hole spin qubit from the nuclear spins. *Nature Materials* **15,** 981–986 (2016).

185. Keizer, J. G., Bocquel, J., Koenraad, P. M., Mano, T., Noda, T. & Sakoda, K. Atomic scale analysis of self assembled GaAs/AlGaAs quantum dots grown by droplet epitaxy. *Applied Physics Letters* **96,** 062101 (2010).

186. Jahn, J.-P. *et al.* An artificial Rb atom in a semiconductor with lifetime-limited linewidth. *Physical Review B* **92,** 245439 (2015).

187. Sallen, G. *et al.* Nuclear magnetization in gallium arsenide quantum dots at zero magnetic field. *Nature Communications* **5,** 3268 (2014).

188. Bennett, C. H., Brassard, G., Crépeau, C., Jozsa, R., Peres, A. & Wootters, W. K. Teleporting an unknown quantum state via dual classical and Einstein-Podolsky-Rosen channels. *Physical Review Letters* **70,** 1895–1899 (1993).

189. Barrett, S. D. & Kok, P. Efficient high-fidelity quantum computation using matter qubits and linear optics. *Physical Review A* **71,** 060310 (2005).

190. Nickerson, N. H., Fitzsimons, J. F. & Benjamin, S. C. Freely Scalable Quantum Technologies Using Cells of 5-to-50 Qubits with Very Lossy and Noisy Photonic Links. *Physical Review X* **4,** 041041 (2014).

191. Wootters, W. K. Quantum entanglement as a quantifiable resource. *Philosophical Transactions of the Royal Society A: Mathematical, Physical and Engineering Sciences* **356,** 1717–1731 (1998).

192. Plenio, M. B. & Virmani, S. S. in *Quantum Information and Coherence* 1,2, 173–209 (Springer International Publishing, Cham, 2014). ISBN: 1533-7146.

193. Nielsen, M & Chuang, I. *Quantum Computation and Quantum Information* 25. ISBN: 9781107002173 (Cambridge University Press, 2000).

194. Cabrillo, C, Cirac, J. I., García-Fernández, P. & Zoller, P. Creation of entangled states of distant atoms by interference. *Physical Review A* **59,** 1025–1033 (1999).

195. Leibfried, D *et al.* Experimental demonstration of a robust, high-fidelity geometric two ion-qubit phase gate. *Nature* **422,** 412–5 (2003).

196. Browne, D. E., Plenio, M. B. & Huelga, S. F. Robust Creation of Entanglement between Ions in Spatially Separate Cavities. *Physical Review Letters* **91,** 067901 (2003).

197. Duan, L.-M. & Kimble, H. J. Efficient Engineering of Multiatom Entanglement through Single-Photon Detections. *Physical Review Letters* **90,** 253601 (2003).

198. Feng, X.-L., Zhang, Z.-M., Li, X.-D., Gong, S.-Q. & Xu, Z.-Z. Entangling Distant Atoms by Interference of Polarized Photons. *Physical Review Letters* **90,** 217902 (2003).

199. Maunz, P., Olmschenk, S., Hayes, D., Matsukevich, D. N., Duan, L.-M. & Monroe, C. Heralded Quantum Gate between Remote Quantum Memories. *Physical Review Letters* **102,** 250502 (2009).

200. Slodička, L., Hétet, G., Röck, N., Schindler, P., Hennrich, M. & Blatt, R. Atom-Atom Entanglement by Single-Photon Detection. *Physical Review Letters* **110,** 083603 (2013).

201. Hucul, D *et al.* Modular entanglement of atomic qubits using photons and phonons. *Nature Physics* **11,** 37–42 (2014).

202. Hofmann, J. *et al.* Heralded Entanglement Between Widely Separated Atoms. *Science* **337,** 72–75 (2012).

203. Pfaff, W *et al.* Unconditional quantum teleportation between distant solid-state quantum bits. *Science* **345,** 532–535 (2014).

204. Hensen, B. *et al.* Loophole-free Bell inequality violation using electron spins separated by 1.3 kilometres. *Nature* **526,** 682–686 (2015).

205. Narla, A. *et al.* Robust Concurrent Remote Entanglement Between Two Superconducting Qubits. *Physical Review X* **6,** 031036 (2016).

206. Zippilli, S., Olivares-Rentería, G. a., Morigi, G., Schuck, C., Rohde, F. & Eschner, J. Entanglement of distant atoms by projective measurement: the role of detection efficiency. *New Journal of Physics* **10,** 103003 (2008).

207. Kok, P. & Lovett, B. W. *Introduction to optical quantum information processing* ISBN: 978-0-521-51914-4 (Cambridge University Press, Cambridge, 2010).

208. Kempsell, P. Radiofrequency Pulse Sequences Which Compensate Their Own Imperfections. *Journal of Magnetic Resonance* **38,** 453–479 (1980).

209. Vittorini, G., Hucul, D., Inlek, I. V., Crocker, C. & Monroe, C. Entanglement of distinguishable quantum memories. *Physical Review A* **90,** 040302 (2014).

210. Legero, T., Wilk, T., Hennrich, M., Rempe, G. & Kuhn, A. Quantum Beat of Two Single Photons. *Physical Review Letters* **93,** 070503 (2004).

211. Zhao, T.-M. *et al.* Entangling Different-Color Photons via Time-Resolved Measurement and Active Feed Forward. *Physical Review Letters* **112,** 103602 (2014).

212. Hocker, G. B. Fiber-optic sensing of pressure and temperature. *Applied optics* **18,** 1445–1448 (1979).

213. Barros, H. G., Stute, A., Northup, T. E., Russo, C., Schmidt, P. O. & Blatt, R. Deterministic single-photon source from a single ion. *New Journal of Physics* **11,** 103004 (2009).

214. Gerry, C. & Knight, P. *Introductory Quantum Optics* 217. ISBN: 0-521-82035-9 (2005).

215. Hong, C. K., Ou, Z. Y. & Mandel, L. Measurement of subpicosecond time intervals between two photons by interference. *Physical Review Letters* **59,** 2044–2046 (1987).

216. Santori, C., Fattal, D., Vucković, J., Solomon, G. S. & Yamamoto, Y. Indistinguishable photons from a single-photon device. *Nature* **419,** 594–597 (2002).

217. Ding, X. *et al.* On-Demand Single Photons with High Extraction Efficiency and Near-Unity Indistinguishability from a Resonantly Driven Quantum Dot in a Micropillar. *Physical Review Letters* **116,** 020401 (2016).

218. Somaschi, N *et al.* Near-optimal single-photon sources in the solid state. *Nature Photonics* **10,** 340–345 (2016).

219. Gschrey, M *et al.* Highly indistinguishable photons from deterministic quantum-dot microlenses utilizing three-dimensional in situ electron-beam lithography. *Nature communications* **6,** 7662 (2015).

220. Patel, R. B., Bennett, A. J., Farrer, I., Nicoll, C. A., Ritchie, D. A. & Shields, A. J. Two-photon interference of the emission from electrically tunable remote quantum dots. *Nature Photonics* **4,** 632–635 (2010).

221. Santori, C., Fattal, D., Fu, K.-M.M. C., Barclay, P. E. & Beausoleil, R. G. On the indistinguishability of Raman photons. *New Journal of Physics* **11,** 123009 (2009).

222. Fernandez, G., Volz, T., Desbuquois, R., Badolato, A. & Imamoglu, A. Optically Tunable Spontaneous Raman Fluorescence from a Single Self-Assembled InGaAs Quantum Dot. *Physical Review Letters* **103,** 087406 (2009).

223. James, D. F. V., Kwiat, P. G., Munro, W. J. & White, A. G. Measurement of qubits. *Physical Review A* **64,** 052312 (2001).

224. Lo Franco, R., D'Arrigo, a., Falci, G., Compagno, G. & Paladino, E. Preserving entanglement and nonlocality in solid-state qubits by dynamical decoupling. *Physical Review B* **90,** 054304 (2014).

225. Versteegh, M. A. M. *et al.* Observation of strongly entangled photon pairs from a nanowire quantum dot. *Nature Communications* **5,** 5298 (2014).

226. Ballance, C. J. *et al.* Hybrid quantum logic and a test of Bell's inequality using two different atomic isotopes. *Nature* **528,** 384–386 (2015).

227. Zaske, S. *et al.* Visible-to-Telecom Quantum Frequency Conversion of Light from a Single Quantum Emitter. *Physical Review Letters* **109,** 147404 (2012).

228. Lenhard, A. *et al.* Telecom-heralded single-photon absorption by a single atom. *Physical Review A* **92,** 063827 (2015).

229. Andrews, R. W. *et al.* Bidirectional and efficient conversion between microwave and optical light. *Nature Physics* **10,** 321–326 (2014).

230. Hisatomi, R. *et al.* Bidirectional conversion between microwave and light via ferromagnetic magnons. *Physical Review B* **93,** 174427 (2016).

231. Takeda, S., Mizuta, T., Fuwa, M., van Loock, P. & Furusawa, A. Deterministic quantum teleportation of photonic quantum bits by a hybrid technique. *Nature* **500,** 315–318 (2013).

232. Andersen, U. L., Neergaard-Nielsen, J. S., van Loock, P. & Furusawa, A. Hybrid discrete and continuous variable quantum information. *Nature Physics* **11,** 713–719 (2015).

233. Krogstrup, P *et al.* Epitaxy of semiconductorâĂŞsuperconductor nanowires. *Nature Materials* **14,** 400–406 (2015).

234. Albrecht, S. M. *et al.* Exponential Protection of Zero Modes in Majorana Islands. *Nature* **531,** 206–209 (2016).

235. Zhu, X. *et al.* Coherent coupling of a superconducting flux qubit to an electron spin ensemble in diamond. *Nature* **478,** 221–224 (2011).

236. Kubo, Y. *et al.* Hybrid Quantum Circuit with a Superconducting Qubit Coupled to a Spin Ensemble. *Physical Review Letters* **107,** 220501 (2011).

237. Akopian, N., Wang, L., Rastelli, A., Schmidt, O. G. & Zwiller, V. Hybrid semiconductor-atomic interface: slowing down single photons from a quantum dot. *Nature Photonics* **5,** 230–233 (2011).

238. Akopian, N. An artifical atom locked to natural atoms. arXiv: 1302.2005 (2013).

239. Siyushev, P., Stein, G., Wrachtrup, J. & Gerhardt, I. Molecular photons interfaced with alkali atoms. *Nature* **509,** 66–70 (2014).

240. Waks, E. & Monroe, C. Protocol for hybrid entanglement between a trapped atom and a quantum dot. *Physical Review A* **80,** 062330 (2009).

241. Olmschenk, S, Younge, K. C., Moehring, D. L., Matsukevich, D. N., Maunz, P & Monroe, C. Manipulation and detection of a trapped Yb+ hyperfine qubit. *Physical Review A* **76,** 052314 (2007).

242. Yu, N. & Maleki, L. Lifetime measurements of the 4f5d metastable states in single ytterbium ions. *Physical Review A* **61,** 022507 (2000).

243. Kimble, H. J. Strong Interactions of Single Atoms and Photons in Cavity QED. *Physica Scripta* **T76,** 127 (1998).

244. Harlander, M., Brownnutt, M., Hänsel, W. & Blatt, R. Trapped-ion probing of light-induced charging effects on dielectrics. *New Journal of Physics* **12,** 093035 (2010).

245. Steiner, M., Meyer, H. M., Deutsch, C., Reichel, J. & Köhl, M. Single Ion Coupled to an Optical Fiber Cavity. *Physical Review Letters* **110,** 043003 (2013).

246. Hunger, D., Steinmetz, T., Colombe, Y., Deutsch, C., Hänsch, T. W. & Reichel, J. A fiber FabryâĂŞPerot cavity with high finesse. *New Journal of Physics* **12,** 065038 (2010).

247. Steiner, M, Meyer, H. M., Reichel, J & Köhl, M. Photon Emission and Absorption of a Single Ion Coupled to an Optical-Fiber Cavity. *Physical Review Letters* **113,** 263003 (2014).

248. Hogele, A. *et al.* Spin-selective optical absorption of singly charged excitons in a quantum dot. *Applied Physics Letters* **86,** 221905 (2005).

249. Kuther, A *et al.* Zeeman splitting of excitons and biexcitons in single In0.60Ga0.40 As/GaAs self-assembled quantum dots. *Physical Review B* **58,** R7508–R7511 (1998).

250. Koudinov, A. V., Akimov, I. A., Kusrayev, Y. G. & Henneberger, F. Optical and magnetic anisotropies of the hole states in Stranski-Krastanov quantum dots. *Physical Review B* **70,** 241305 (2004).

251. Eble, B. *et al.* Hole-Nuclear Spin Interaction in Quantum Dots. *Physical Review Letters* **102,** 146601 (2009).

252. Specht, H. P. *et al.* A single-atom quantum memory. *Nature* **473,** 190–193 (2011).

253. Kurz, C., Schug, M., Eich, P., Huwer, J., Müller, P. & Eschner, J. Experimental protocol for high-fidelity heralded photon-to-atom quantum state transfer. *Nature Communications* **5,** 5527 (2014).

254. Dousse, A. *et al.* Ultrabright source of entangled photon pairs. *Nature* **466,** 217–220 (2010).

255. Ballance, T. G., Meyer, H. M., Kobel, P., Ott, K., Reichel, J. & Köhl, M. Cavity-induced back-action in Purcell-enhanced photoemission of a single ion in an ultraviolet fiber-cavity. *arXiv,* 1609.04997 (2016).

256. Lim, Y. L., Beige, A. & Kwek, L. C. Repeat-until-success linear optics distributed quantum computing. *Physical Review Letters* **95,** 1–4 (2005).

257. Marsili, F. *et al.* Detecting single infrared photons with 93% system efficiency. *Nature Photonics* **7,** 210–214 (2013).

258. Hadfield, R. H. Single-photon detectors for optical quantum information applications. *Nature Photonics* **3,** 696–705 (2009).

259. Zhang, J., Itzler, M. A., Zbinden, H. & Pan, J.-W. Advances in InGaAs/InP single-photon detector systems for quantum communication. *Light: Science & Applications* **4,** e286 (2015).

260. Reitzenstein, S & Forchel, A. Quantum dot micropillars. *Journal of Physics D: Applied Physics* **43,** 33001 (2010).

261. Gerard, J. M., Claudon, J, Munsch, M, Bleuse, J & Gregersen, N. *Recent advances for high-efficiency sources of single photons based on photonic nanowires* in *2012 14th International Conference on Transparent Optical Networks (ICTON)* (IEEE, 2012), 1–5.

262. Barnes, W. L. *et al.* Solid-state single photon sources: light collection strategies. *The European Physical Journal D - Atomic, Molecular, Optical and Plasma Physics* **18,** 197–210 (2002).

263. Vetsch, E., Reitz, D., Sagué, G., Schmidt, R., Dawkins, S. T. & Rauschenbeutel, A. Optical Interface Created by Laser-Cooled Atoms Trapped in the Evanescent Field Surrounding an Optical Nanofiber. *Physical Review Letters* **104,** 203603 (2010).

264. Reithmaier, J. P. *et al.* Strong coupling in a single quantum dot semiconductor microcavity system. *Nature* **432,** 197–200 (2004).

265. Maiwald, R. *et al.* Collecting more than half the fluorescence photons from a single ion. *Physical Review A* **86,** 043431 (2012).

266. Tey, M. K. *et al.* Interfacing light and single atoms with a lens. *New Journal of Physics* **11** (2009).

267. Gerber, S. *et al.* Quantum interference from remotely trapped ions. *New Journal of Physics* **11** (2009).

268. Lee, K. G. *et al.* A planar dielectric antenna for directional single-photon emission and near-unity collection efficiency. *Nature Photonics* **5,** 166–169 (2011).

269. Chen, X.-W., Götzinger, S. & Sandoghdar, V. 99% efficiency in collecting photons from a single emitter. *Optics Letters* **36,** 3545 (2011).

270. Chu, X.-L. *et al.* Experimental realization of an optical antenna designed for collecting 99% of photons from a quantum emitter. *Optica* **1,** 203 (2014).

271. Friedler, I, Sauvan, C, Hugonin, J. P., Lalanne, P, Claudon, J & Gérard, J. M. Solid-state single photon sources: the nanowire antenna. *Opt. Express* **17,** 2095–2110 (2009).

272. Munsch, M. *et al.* Dielectric GaAs Antenna Ensuring an Efficient Broadband Coupling between an InAs Quantum Dot and a Gaussian Optical Beam. *Physical Review Letters* **110,** 177402 (2013).

273. Claudon, J. *et al.* A highly efficient single-photon source based on a quantum dot in a photonic nanowire. *Nature Photonics* **4,** 174–177 (2010).

274. Yeo, I. *et al.* Surface effects in a semiconductor photonic nanowire and spectral stability of an embedded single quantum dot. *Applied Physics Letters* **99,** 233106 (2011).

275. Wang, C. F. *et al.* Optical properties of single InAs quantum dots in close proximity to surfaces. *Applied Physics Letters* **85,** 3423 (2004).

276. Montinaro, M. *et al.* Quantum dot opto-mechanics in a fully self-assembled nanowire. *Nano Letters* **14,** 4454–4460 (2014).

277. Essex, E. A. Hertz vector potentials of electromagnetic theory. *American Journal of Physics* **45,** 1099–1101 (1977).

278. Jackson, J. D. *Classical Electrodynamics* 3rd ed. ISBN: 978-0-471-30932-1 (John Wiley & Sons, Inc., 1998).

279. Chew, W. C. *Waves and Fields in Inhomogeneous Media* (ed 1) ISBN: 978-0-780-34749-6 (Van Nostrand Reinhold, 1990).

280. Lukosz, W. Light emission by multipole sources in thin layers I Radiation patterns of electric and magnetic dipoles. *Journal of the Optical Society of America* **71,** 744 (1981).

281. Drexhage, K. Influence of a dielectric interface on fluorescence decay time. *Journal of Luminescence* **1-2,** 693–701 (1970).

282. Chance, R. R., Miller, A. H., Prock, A. & Silbey, R. Fluorescence and energy transfer near interfaces: The complete and quantitative description of the Eu+3/mirror systems. *The Journal of Chemical Physics* **63,** 1589–1595 (1975).

283. Dowling, J. P. Spontaneous emission in cavities: How much more classical can you get? *Foundations of Physics* **23,** 895–905 (1993).

284. Novotny L. & Hecht, B. *Principles of Nano-Optics* (Cambridge University Press, 2006).

285. Sell, D. D., Casey, H. C. & Wecht, K. W. Concentration dependence of the refractive index for n - And p -type GaAs between 1.2 and 1.8 eV. *Journal of Applied Physics* **45,** 2650–2657 (1974).

286. Stobbe, S., Johansen, J., Kristensen, P. T., Hvam, J. M. & Lodahl, P. Frequency dependence of the radiative decay rate of excitons in self-assembled quantum dots: Experiment and theory. *Physical Review B* **80,** 155307 (2009).

287. Lee, C. C. *Thin film optical coatings* 3–33. ISBN: 978-1-4200-7302-7 (CRC Press, Taylor & Francis Group, 2015).

288. Baba, M., Sasaki, T., Yoshita, M. & Akiyama, H. Aberrations and allowances for errors in a hemisphere solid immersion lens for submicron-resolution photoluminescence microscopy. *Journal of Applied Physics* **85,** 6923 (1999).

289. Ma, Y, Ballesteros, G, Zajac, J. M., Sun, J & Gerardot, B. D. Highly directional emission from a quantum emitter embedded in a hemispherical cavity. *Optics Letters* **40,** 2373 (2015).

290. Sheppard, C. J. R & Torok, P. Efficient calculation of electromagnetic diffraction in optical systems using a multipole expansion. *Journal of Modern Optics* **44,** 803–818 (1997).

291. Bechtold, A. *et al.* Quantum Effects in Higher-Order Correlators of a Quantum-Dot Spin Qubit. *Physical Review Letters* **117,** 027402 (2016).

292. Reiserer, A. *et al.* Robust Quantum-Network Memory Using Decoherence-Protected Subspaces of Nuclear Spins. *Physical Review X* **6,** 021040 (2016).

293. Weiss, K. M., Elzerman, J. M., Delley, Y. L., Miguel-Sanchez, J. & ImamoÄ§lu, A. Coherent Two-Electron Spin Qubits in an Optically Active Pair of Coupled InGaAs Quantum Dots. *Physical Review Letters* **109,** 107401 (2012).

294. Kim, D., Carter, S. G., Greilich, A., Bracker, A. & Gammon, D. Ultrafast optical control of entanglement between two quantum dot spins. *Nature Physics* **7,** 24 (2011).

295. Kim, D., Kiselev, A. A., Ross, R. S., Rakher, M. T., Jones, C. & Ladd, T. D. Optically Loaded Semiconductor Quantum Memory Register. *Physical Review Applied* **5,** 024014 (2016).

296. Beige, A., Liang Lim, Y. & Schön, C. Multi-photon entanglement from distant single photon sources on demand. *Journal of Modern Optics* **54,** 397–407 (2007).

297. Economou, S. E., Lindner, N. & Rudolph, T. Optically Generated 2-Dimensional Photonic Cluster State from Coupled Quantum Dots. *Physical Review Letters* **105,** 093601 (2010).

298. Englund, D. *et al.* Controlling the Spontaneous Emission Rate of Single Quantum Dots in a Two-Dimensional Photonic Crystal. *Physical Review Letters* **95,** 013904 (2005).

299. Schwartz, I *et al.* Deterministic generation of a cluster state of entangled photons. *Science* **354,** 434–437 (2016).

300. Huo, Y. H., Rastelli, A. & Schmidt, O. G. Ultra-small excitonic fine structure splitting in highly symmetric quantum dots on GaAs (001) substrate. *Applied Physics Letters* **102,** 152105 (2013).

301. Arnold, C. *et al.* Macroscopic rotation of photon polarization induced by a single spin. *Nature Communications* **6,** 6236 (2015).

302. Androvitsaneas, P. *et al.* Charged quantum dot micropillar system for deterministic light-matter interactions. *Physical Review B* **93,** 241409 (2016).

303. Lukosz, W & Kunz, R. E. Light emission by magnetic and electric dipoles close to a plane interface. I. Total radiated power. *JOSA* **67,** 1607–1615 (1977).

304. Lukosz, W. Theory of optical-environment-dependent spontaneous-emission rates for emitters in thin layers. *Physical Review B* **22,** 3030–3038 (1980).

305. Brueck, S. R. J., Smagley, V. A. & Eliseev, P. G. Radiation from a dipole embedded in a multilayer slab. *Physical Review E* **68,** 036608 (2003).